Development of a cryogenic refrigerator for a compact superconducting cyclotron in a hospital environment

Zur Erlangung des akademischen Grades
Doktor der Ingenieurwissenschaften
von der KIT-Fakultät für Maschinenbau
Karlsruher Institut für Technologie (KIT)

genehmigte

DISSERTATION

von

Dipl.-Ing. Daniel Alexander Berkowitz Zamora

Development of a cryogenic refrigerator for a compact superconducting cyclotron in a hospital environment

D. Berkowitz Zamora

Doctoral thesis, Karlsruhe Institute of Technology, Germany

2019

DOI: 10.5445/IR/1000099481

Kurzfassung

Tieftemperaturkühlung ist unverzichtbar für den Betrieb von medizischen Anlagen, die durch die Verwendung von supraleitenden Komponenten ein leistungsfähigeres und kompakteres System erreichen sollen. Obwohl kryogene Refrigeratoren im Handel erhältlich sind, ist manchmal die Entwicklung maßgeschneiderter Lösungen aufgrund spezieller Systemanforderungen unvermeidlich. Dies ist der Fall für AMIT's Teilchenbeschleuniger; ein hochkompaktes supraleitendes Zyklotron für die Einzeldosisherstellung von radiopharmazeutischen Substanzen in einer Krankenhausumgebung. Zur Erzeugung des Magnetfeldes verwendet das Zyklotron ein Paar supraleitender Magnete, die eine isotherme Kühlung bei 4,5 K im Wattbereich und eine wärmere nicht-isotherme Kühlung zur thermischen Abschirmung erfordern. Die größten Herausforderungen bei der Kühlung ergeben sich aus der begrenzten Platzverfügbarkeit, der schädlichen radioaktiven Umgebung, den strengen Sicherheitsaspekten, und der Anforderung eines kontinuierlichen und unterbrechungsfreien Betriebs.

In dieser Dissertation wird ein neues Kühlsystem vorgestellt, welches einen handelsüblichen Kryokühler als Kältequelle verwendet, und mittels einer erzwungenen Durchströmung mit kaltem Helium aus der Distanz kühlen kann. Die Studie untersucht fünf Prozessvarianten eines Kaskadenkühlschemas unterschiedlicher Kühlleistung und Komplexität. Die technisch einfachste und thermodynamisch effizienteste Variante wird zum Entwurf und zur Herstellung des Kryo-Versorgungssystems verwendet; ein kleiner kryokühlerbasierter Refrigerator mit 1,66 W isothermer Kühlleistung bei 4,5 K, und 24,32 W nicht-isothermer Kühlleistung von 40 K bis 70 K. Die verbleibenden Varianten sind komplexer und leistungsfähiger, und dienen somit als Grundlage für zukünftige Designiterationen, die, theoretisch, eine isotherme Kühlleistung von bis zu 11 W erreichen könnten.

Das neue Kühlsystem wird in einem angrenzenden Raum neben dem Zyklotron aufgestellt, wodurch eine äußerst kompakte Bauweise des Zyklotrons ermöglicht wird. Die Fähigkeit, isotherme kryogene Kühlung aus einem entfernten geschlossenen Kleinrefrigerator bereitzustellen, könnte es einer Vielzahl anderer medizinischer Geräte, wie z. B. MRI-Scannern, ermöglichen, eine kleinere Größe zu erreichen.

Abstract

Cryogenic refrigeration is indispensable for the operation of medical devices that employ superconducting components, in order to obtain a more powerful and compact system. Although cryogenic refrigerators are commercially available, the development of tailor-made solutions is sometimes unavoidable due to special system requirements. This is the case for AMIT's particle accelerator; a highly compact superconducting cyclotron for the single-dose production of radiopharmaceutical substances in a hospital environment. The cyclotron has a pair of superconducting magnets that require isothermal refrigeration at 4.5 K in the Watt-range, and a warmer non-isothermal refrigeration for thermal shielding. Major refrigeration challenges derive from the limited space availability, the damaging radioactive environment, the stringent safety aspects, and the requirement for continuous and uninterrupted operation.

This dissertation presents a new refrigerator system that employs a commercial cryocooler as the cold source, and that is capable of cooling at a distance by means of helium forced-flow. The study examines five process variants of a cascade cooling scheme with different performance and complexity. The technically simplest and thermodynamically most efficient variant is used to design and manufacture the Cryo-Supply System; a small-scale cryocooler based refrigerator system with 1.66 W of isothermal cooling power at 4.5 K, and 24.32 W of non-isothermal cooling power from 40 K to 70 K. The remaining variants are more complex and powerful, thus serving as the basis for future design iterations that could, theoretically, reach an isothermal cooling power of up to 11 W.

The new refrigerator will be located in a room adjacent to the cyclotron, thus allowing for a highly compact design of the cyclotron itself. The ability to provide isothermal cryogenic refrigeration from a distant small-scale closed system could allow a variety of other medical devices, such as MRI scanners, to attain smaller sizes.

Eidesstattliche Erklärung

Hiermit erkläre ich, dass ich die vorliegende Arbeit selbständig angefertigt und keine anderen als die angegebenen Quellen und Hilfsmittel benutzt sowie die wörtlich und inhaltlich übernommenen Stellen als solche kenntlich gemacht und die Satzung des KIT zur Sicherung guter wissenschaftlicher Praxis in der jeweils gültigen Fassung beachtet habe.

Die Arbeit wurde bisher weder im Inland noch im Ausland in gleicher oder ähnlicher Form als Dissertation eingereicht und ist als Ganzes auch noch nicht veröffentlicht.

Daniel Alexander Berkowitz Zamora

Karlsruhe, den 9. August 2019

Acknowledgments

I owe my deepest gratitude to my university advisor, Professor Robert Stieglitz, for his great support throughout the course of this work and for accepting me as a remote doctoral student. I am also very thankful to Professor Mathias Noe for being my second reviewer. I am deeply thankful to my CERN supervisor, Friedrich Haug, for his trust and day-to-day guidance during the duration of the project. It was a great pleasure to work closely together.

This work would not have been possible without the very hard work of an incredible team of young engineers. Many thanks to Jonas Schmid, Andreas Striebel, Wolfgang Herberger, Matthias Michels, Manuel Diez, Andreas Krüger, Ruben Gomez Bosch, Markus Keh, and Daniel Österle. Few of them stayed for longer than a year, but their strong commitment and dedication were fundamental for *our* system to become a reality. It was a lot of fun to work with all of them. Matthias also deserves my special gratitude for taking over the lead of our small team after my departure, and for successfully leading the validation campaigns.

My sincere thanks are due to all members of CERN, but notably to the members of the Cryogenics Group, the Cryogenics Workshop, the Cryogenics Laboratory, and the Main Workshop for providing their technical expertise which greatly assisted this work.

I would like to express my sincere thanks and appreciation to our partners in Spain for all the good work together. At our in-kind partner CIEMAT, to Jose Manuel Pérez, Luis García-Tabarés, Fernando Toral, Javier Munilla, and Diego Obradors. At our industrial partner ANTEC S.A., to Rafael Iturbe and Leire Minguez.

I thank the Wolfgang Genter Programme of the German Federal Ministry of Education and Research for the three-year scholarship at CERN and Michael Hauschild, the coordinator of the program, for his assistance and advice. My deepest gratitude is due to my friend Moritz Guthoff for introducing me to that program back at our home university.

Many thanks to all my friends for their motivation, inspiration, and great laughs. They were crucial in making CERN a unique and joyful experience. Particular thanks go to Lea Kicherer and Cristhian Valerio-Lizarraga for their exceptional support and encouragement during my "busy times". Also many thanks to Thomas Birtwistle for all the hours spent proof reading this document.

Finally I would like to thank my mother, my two sisters, and their families for all their love, support, and encouragement during this incredible journey.

Contents

Abbreviations

Abbreviation	Denotation
AMIT	Advanced Molecular Imaging Technologies
CERN	European Organization for Nuclear Research
c.f.	Abr.: *compare* (latin: *confer*). Refers to other material for comparison.
CIEMAT	Centro de Investigaciones Energéticas, Medioambientales y Tecnológicas
CSS	Cryo-Supply System
COP	Coefficient of performance
DC	Direct current
D.I.C.	Differential inversion curve
FOM	Figure of merit
GHe	Gaseous Helium
GM	Gifford-McMahon
HP	High pressure
HT-SC	High-temperature superconductor
HX	Heat exchanger
IP	Inner pipe
JT	Joule-Thomson
JTHX	Joule-Thomson heat exchanger
LHe	Liquid Helium
LP	Low pressure
LT-SC	Low-temperature superconductor
MEG	Magnetoencephalography
MP	Medium pressure
MRI	Magnetic resonance imaging
NIST	National Institute of Standards and Technology
OP	Outer pipe
PET	Positron Emission Tomography
SC	Superconductor
SQUID	Superconducting quantum interference device
TFL	Transfer line

Subscripts	Denotation corresponds to
$—_0$	Evaluation set-point of a variable
$—_{1st}$	First stage
$—_{2nd}$	Second stage
$—_a$	Ambient (normal) conditions
$—_c$	Colder stream or fluid
$—_{calc}$	Calculation error of a quantity
$—_{com}$	Comparison error of a quantity
$—_{crit}$	Liquid-vapour critical point (for helium: T_{crit}=5.20 K; p_{crit}=2.27 bar)
$—_{cs}$	Colder side of a heat exchanger
$—_{CB}$	Connector box
$—_{Cyc}$	Cyclotron
$—_{data}$	Experimental-data error of a quantity
$—_{hs}$	Hotter side of a heat exchanger
$—_h$	Hotter stream or fluid
$—_{IN}$	Inlet stream
$—_{input}$	Input error of a quantity
$—_{INV}$	Applies to an inversion state
$—_{lam}$	Laminar zone
$—_m$	Mean value
$—_{model}$	Model error of a quantity
$—_{num}$	Numerical error of a quantity
$—_{obs}$	Observed quantity
$—_{OUT}$	Outlet stream
$—_{tran}$	Transition zone
$—_{true}$	True-value of a quantity
$—_{turb}$	Turbulent zone
$—_R$	Refrigeration
$—_{surr}$	Heat-in-leak coming from the surroundings
$—_{val}$	Validation error of a quantity
$—_{wall}$	Applies to the wall of the heat exchanger

Superscripts	Denotation corresponds to
$—^{eq}$	Equivalent system in terms of exergy
$—^{rev}$	Reversible process
$—^I, —^{II}$	Applies to Circuit I; II
$—^{(0.1.2)}$	Error identification number
$\widehat{—}$	Evaluation mean of a variable

Nomenclature	Denotation	Dimensions
A	Heat exchange surface area	m^2
A_{cross}	Cross-sectional area of a channel, tube or body	m^2
$\vec{B}$	Magnetic field	T
c_{p}	Heat capacity at a given pressure	J/(g·K)
c_X	Asymmetry expression of a standard uncertainty interval $\pm u_X$	-
$\dot{C}$	Heat capacity rate	J/(K·s)
$\dot{C}_{\text{min}}; \dot{C}_{\text{max}}$	Smaller; larger heat capacity rate between two streams	J/(K·s)
$\dot{C}^*$	Heat capacity rate ratio	-
D_h	Hydraulic diameter ($= 4A_{\text{cross}}/O$)	m
e	Specific exergy	J/g
E	Exergy	J
$\dot{E}_{\text{d}}$	Destroyed exergy	W
F_X	Asymmetry factor of an expanded uncertainty interval $\pm U_X$	-
$\vec{F}_{\text{L}}$	Lorentz Force	N
h	Specific enthalpy	J/g
h_{evap}	Specific evaporation enthalpy	J/g
H	Enthalpy	J
k	Technical pipe roughness.	mm
k_{r}	Relative pipe roughness ($= k/D_h$)	-
L	Length	m
L_{M}	Manufacturing length of a heat exchanger	m
LM	Lower limit of a probability distribution	-
L_0	Characteristic length of a channel	m
$\dot{m}$	mass flow rate	g/s
MF	Magnification factor	-
MPL	Most probable point of a probability distribution	-
NTU	Number of transfer units	-
Nu	Nusselt number	-
O	Perimeter of a channel/tube	m
p_{sat}	Saturation pressure	bar
Pe	Péclet number	-
Pr	Prandtl number	-
q	Elementary charge	e
Q	Heat	J
$\dot{Q}$	Heat power	W
R_{UA}	Heat transfer resistance	K/W
Re	Reynolds number	-
s	Specific entropy	J/(g·K)
S	Entropy	J/K
S_{irr}	Entropy created in an irreversible process	J/K
t	thickness	m
T	Temperature	K
u_X	Standard uncertainty of a variable X	-
$u_{X,Y}$	Covariance between two variables (X and Y)	-
U	Local overall heat transfer coefficient	W/(K·m^2)
UL	Upper limit of a probability distribution	-
U_m	Mean overall heat transfer coefficient	W/(K·m^2)
UMF	Uncertainty magnification factor	-
UPC	Uncertainty percentage contribution	-
U_X	Expanded uncertainty of a variable X	-
W	Work	W
y_{LHe}	Condensate yield	-
%_	Variable normalised by the evaluation set-point (i.e. %$u_X = u_X/X_0$)	-

Greek Symbols	Denotation	Dimensions
ξ	Darcy-Weisbach flow friction factor; Relative position	-
α	Local heat transfer coefficient	W/(K·m²)
γ	Intermittency factor	-
δT	Local temperature difference at a heat exchanger	K
δT_m	Mean temperature difference	K
Δp_f	Frictional pressure loss	bar
ε	Effectiveness (heat exchangers); emissivity (heat radiation)	-
ϵ_X	Error of a variable X (deviation from the unknown true value)	-
ζ	Exergetic efficiency	-
η_C	Carnot factor	-
$\theta_{P,X}$	Absolute sensitivity coefficient (=$\partial P/\partial X$)	-
λ	heat conduction coefficient	W/(K·m)
Λ	Dimensionless longitudinal conduction parameter	-
μ	Dynamic fluid viscosity	kPa·s
μ_{JT}	Adiabatic JT coefficient	K/kPa
ρ	Density	kg/m³
σ_b	Boltzmann´s constant ($1.380\ 649 \cdot 10^{-23}$ J/K)	J/K
v_m	Mean fluid velocity	m/s

1   Introduction

Cryogenic refrigeration, the refrigeration at temperatures below 120 K, is indispensable for a variety of applications. For example, it allows the exploitation of quantum effects such as superconductivity and superfluidity, the substantial reduction of thermal noise or vapour pressure, the separation and liquefaction of so-called permanent gases such as nitrogen and helium, and the preservation of biological samples. [1], [2]

The type of application determines many of the requirements and constraints of the refrigeration system. In particular, the application is what often defines the required refrigeration power and temperature (Figure 1.1). This has a profound impact in the selection of the technical solution, leading to a variety of cryogenic systems. [3] [4]

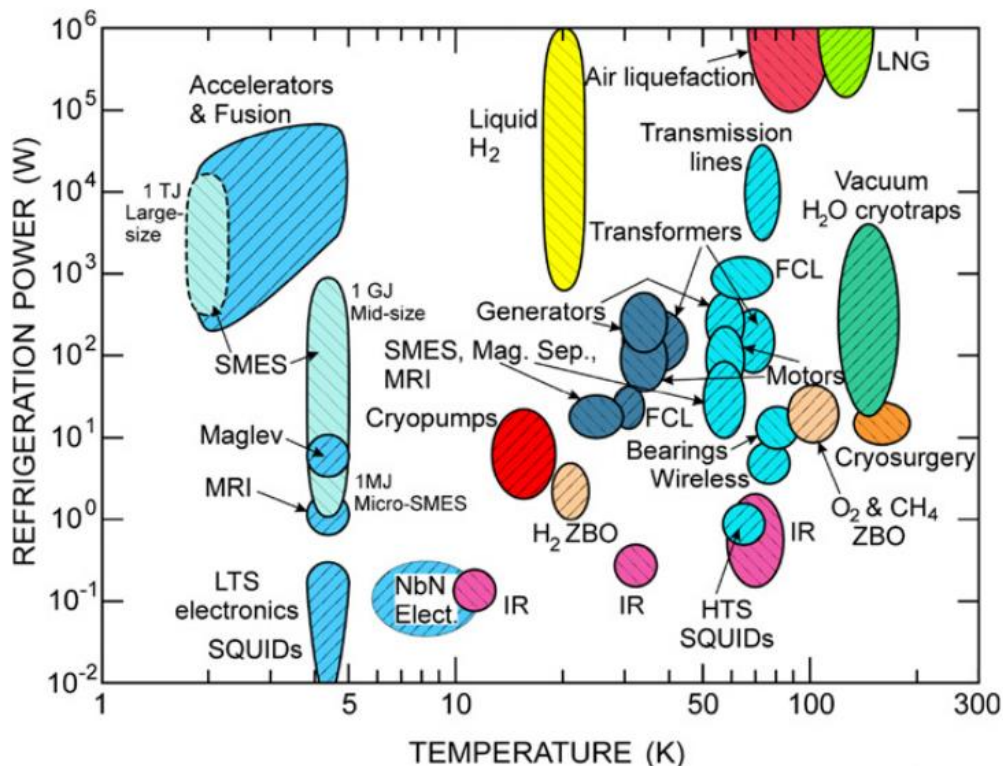Figure 1.1. Map of cryogenic applications in the plane of refrigeration power versus temperature [3].

Some cryogenic systems are directly connected to a refrigerator providing the required cooling power. Others are connected to a reservoir containing cold liquid at cryogenic temperatures which is then used as the coolant. The latter, however, requires the employment of trained personnel to handle and replenish the stored liquid. [2]

Cryogenic refrigerators are commercially available in a variety of types. However, the development of tailor-made solutions is, in some cases, unavoidable due to special system requirements.

1.1 Production of radiopharmaceuticals for Positron Emission Tomography (PET)

Particle accelerators are machines capable of propelling a beam of charged particles to higher speeds and energies, and are used in a wide range of disciplines, from particle physics research to practical applications in industry.

The business of producing and employing accelerators for commercial purposes is extensive. According to estimations, over 25 000 accelerators are used in industrial and medical applications worldwide. They are used for such activities as non-destructive inspection of equipment, particle therapy for oncological treatment or radioisotope production for medical diagnostics. [5], [6]

Positron Emission Tomography (PET) is a molecular imaging technic used for medical diagnostics that relies on the production of positron-emitting radioisotopes, which are previously introduced into the patient's body in the form of a radiopharmaceutical substance [7]. The system is able to reconstruct body images by detecting pairs of gamma-photons produced indirectly by the radioisotopes decay. The emitted positrons annihilate with nearby electrons releasing a pair of gamma-photons with the same energy, moving on opposite directions (Figure 1.2). [8]
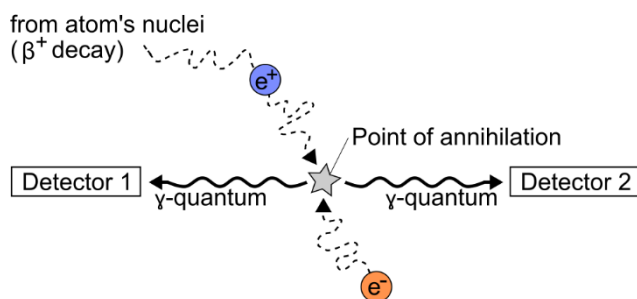
Figure 1.2. Detection of two back-to-back gamma-photons released by the annihilation of a positron emitted by a decaying radioisotope and a nearby electron. [8].

The radioisotopes ^{18}F and ^{11}C, considered of great importance for medical PET, are normally produced using the particle beam of a cyclotron, a type of particle accelerator, to bombard a target substance and generate the required output. Shortly after, the radioisotopes are synthetised in specialised laboratories into a radiopharmaceutical substance and delivered to the patient for immediate use. The main substances for oncological PET are fluorine desoxyglucose and methionine, based on ^{18}F and ^{11}C, respectively. [8], [9]

The use of medical radioisotopes and the demand for cyclotrons to produce them is increasing, promoting a range of new developments in various domains. Before the 1980s, cyclotron systems for radionuclide production were large and complicated requiring considerable physics expertise for operations and maintenance. More recently, however, a newer generation of smaller and user-friendly systems is commercially available. Some companies opt to reduce the size of the cyclotron itself by using superconducting magnets, which require cryogenic refrigeration, but, are both smaller and more powerful than

conventional ones [10]. Other companies adopt new methods for single-patient dose production, allowing them to provide an entire PET production lab in a 30 sq. meter room [11]. Based on these trends, some experts predict that in the future a new generation of small table-top cyclotron systems will be able to produce single doses on demand [12][13].

The use of radiopharmaceutical substances for medical PET demands time-efficient production methods and logistics due to the relatively short half-life of the radioisotopes ($\sim$110 min. for ^{18}F; $\sim$20 min for ^{11}C). The fact that there is no way to stop the radioisotope decay during the production and delivery time results in the need of higher production throughputs in order to compensate for the losses, which leads to larger equipment and higher costs. [9]

The centralised production of ^{18}F-based Fludeoxyglucose in large specialised centres, comprising of both a cyclotron complex and a radiopharmaceutical laboratory, is considered cost-efficient for populated areas. In most cases, the cyclotrons produce relatively large batches equivalent to 1000 times of a patient dose per run. However, ^{11}C-based substances have an even shorter half-life time, raising the logistical demands considerably. [12][14][15]

There is a growing interest in bringing production facilities and patients closer together in order to minimize the delivery distances. Shorter delivery times, in combination with new methods for single-patient dose production, can reduce the throughput requirements, potentially leading to smaller facilities and a higher production efficiency. [13][14][15][16][17][18]

To cover this demand, a consortium of several institutes and companies launched a research and development (R&D) program in 2010, called AMIT (Advanced Molecular Imaging Technologies). Within this program, the Spanish institute CIEMAT is leading the development of a highly compact superconducting cyclotron capable of producing ^{18}F and ^{11}C, so that it can be used in the single-dose production of radiopharmaceutical substances for medical PET in a hospital environment. The European Organization for Nuclear Research (CERN) is involved in the research phase as part of a technology transfer program, due to its expertise in various technologies in the particle accelerator domain, cryogenics being its main contribution. [13]

1.2   Motivation and objective

Cryogenics is identified as a key technology for the AMIT program, due to the necessity of a suitable cryogenic system for the cyclotrons refrigeration. The refrigeration system shall present a cryocooler as its cold source, and be able to provide both isothermal refrigeration at 4.5 K in the Watt-range, and a warmer non-isothermal refrigeration sufficient for thermal shielding. In addition, the cryogenic system shall exclusively use helium as a coolant. General constraints derive from the radiation environment, the general safety aspects, and the space availability imposed by the cyclotron design. Unfortunately, such a refrigerator system is not commercially available and hence a tailor-made solution is required.

The objective of this work is, first, to define a small-scale closed refrigeration cycle capable of providing isothermal 4.5 K cooling to AMITs superconducting cyclotron by means of remote helium forced-flow, and then, to design and manufacture the demonstrator of such a refrigerator system to prove the viability of the chosen approach.

In order to achieve this goal, current design principles and thermodynamic fundamentals of refrigeration at 4.5 K are reviewed, focusing on cryocoolers and cryocooler-based refrigerators with a cooling power in the Watt-range. The general requirements and constraints

deriving from the cyclotron system are also considered. Based on this information, a novel refrigeration concept is proposed, and variations of its thermodynamic cycle are analysed. The acquired insights are then used to select the variation to be implemented for the demonstrator system; the more complex and powerful variations are identified but withheld for future design iterations. The design and manufacturing of the demonstrator system is based on the chosen variation and foresees the refrigeration of the cyclotron with operating beam at CIEMATs premises.

The content of this work precedes the commissioning and validation tests of the built demonstrator system, and provides the theoretical foundation for future design upgrades. The prototype development of a fully autonomous refrigerator system is envisaged at a later stage.

1.3   Scope of the work

The fundamentals of refrigeration at 4.5 K are introduced in chapter 2 "Principles of cryogenic refrigeration". The chapter presents operational concepts for selected types of cryocoolers and cryocooler-based refrigerators, as well as thermodynamic principles needed for the later evaluation of refrigeration cycles.

Due to their relevance in this work, chapter 3 "Fundamentals of recuperative heat exchangers" is dedicated entirely to this type of components. It describes the heat-exchange process in detail, and elaborates on thermodynamic principles and equations. It establishes the theoretical basis for the later definition and characterization of the heat exchangers.

Chapter 4 "AMIT's compact superconducting cyclotron" presents the conceptual design of the cryogenic system. It provides the general requirements and constraints to be considered in the design and manufacturing of the demonstrator system.

Chapter 5 "Thermodynamic analysis of possible refrigeration cycles" concentrates on the theoretical evaluation of configuration schemes that are proposed for the demonstrator system. The different schemes are assessed individually, and then, compared to each other.

The final design of the demonstrator system is presented in chapter 6 "Design of the Cryo Supply System" and is based on the insights gained in the previous chapter. The main focus is the thermal and manufacturing design of the heat exchangers.

Chapter 7 "Assessment of the overall cryogenic system" defines the nominal working point of the system and gives an estimation of the expected refrigeration power. The evaluation is based on the conceptual design introduced in chapter 4 and the manufacturing design defined in chapter 6.

Chapter 8 "Evaluation of the calculation uncertainty" estimates the confidence on the results reported in chapters 5 to 7. The evaluation identifies error sources in the employed methodology and quantifies their effect on the calculation results.

A summary and outlook are provided in chapter 9.

2 Principles of cryogenic refrigeration

Refrigeration is provided when heat is extracted at temperatures below that of the environment [1]. A cryogenic refrigerator is a device capable of extracting heat from cryogenic temperatures, which are generally described to be temperatures less than 120 K ([1], [19]). This work focuses on the refrigeration close to 4.5 K, which corresponds to the temperature of boiling helium at a pressure of 130.26 kPa. Helium is often referred to as a cryogenic fluid because its boiling point is at cryogenic temperatures, for which it is widely used as a cryogenic refrigerant, also called cryogen.

This chapter presents the principles of cryogenic refrigerators at 4.5 K focussing on the operational concepts of closed-cycle mechanical devices known as cryocoolers. It also introduces thermodynamic fundamentals concerning the isenthalpic expansion and energy flow in a refrigeration cycle.

Within this work, all physical properties of helium are obtained from the specialised library HePak© [20], and the thermal properties of solid materials from the equations available at the database of the National Institute of Standards and Technology (NIST) [21]. The terms *ambient temperature* and *ambient pressure* are defined as

$$T_a \equiv 293.15 \, K = 20 \, °C \tag{2.1}$$

and

$$p_a \equiv 101.325 \, kPa \quad , \tag{2.2}$$

according to the NIST definition of *normal conditions*.

2.1 Low-capacity refrigerators at 4.5 K

A thermodynamic process that provides refrigeration is capable of transporting heat from a lower to a higher temperature. As shown in Figure 2.1, refrigerators are devices that use work W to absorb an amount of heat Q_R at the refrigeration temperature T_R and reject the heat Q_a at the ambient temperature T_a. The amount of work W required by a refrigerator does not only depend on the amount of heat Q_R that is extracted, but also on the refrigeration temperature T_R. In fact, the required work W increases when the refrigeration temperature T_R decreases (more in chapter 2.3). Consequently, the refrigeration temperature T_R also defines, to a great extent, the technological solution chosen for a given system and needs to be specified when referring to a refrigerator.
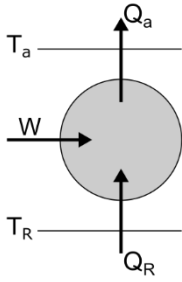
Figure 2.1. Schematic diagram of a refrigerator. Work W is required to absorb the heat Q_R at the refrigeration temperature T_R and reject the heat Q_a at the ambient temperature T_a.

The cooling power of refrigerators at 4.5 K can range by several orders of magnitude depending on the particular system, from a few watts for commercial cryocoolers [22] to tens of kilowatts for large-scale refrigerators [23]. However, there is no generally accepted classification for refrigerators concerning their cooling power. For example, Walker and Bingham [19] arbitrarily define 1 kW or less of refrigeration power at 80 K as "low-capacity cryogenic refrigeration". For this reason, and in a similar way, the category of "low-capacity refrigerators at 4.5 K" is arbitrary defined in this work for systems providing a cooling power in the range of 0.5 to 10 W at a refrigeration temperature of 4.5 K. Starting from this category, and based on [19], the systems are further classified in Figure 2.2. The two principal subcategories are the open and the closed-cycle systems, which differ in the way the cryogen is used. For example, a common method for open-cycle systems is the use of stored, cold, liquid cryogen, which is removed from the system after its use. For this reason, the stored cryogen in an open-cycle system is considered "expendable" and has to be replenished from time to time, while in a closed-cycle system the cryogen is re-cooled to be used indeterminately.

According to the classification in Figure 2.2, cryocoolers are low-capacity closed-cycle cryogenic mechanical refrigerators and are sub-categorised into regenerative and non-regenerative systems. [19]
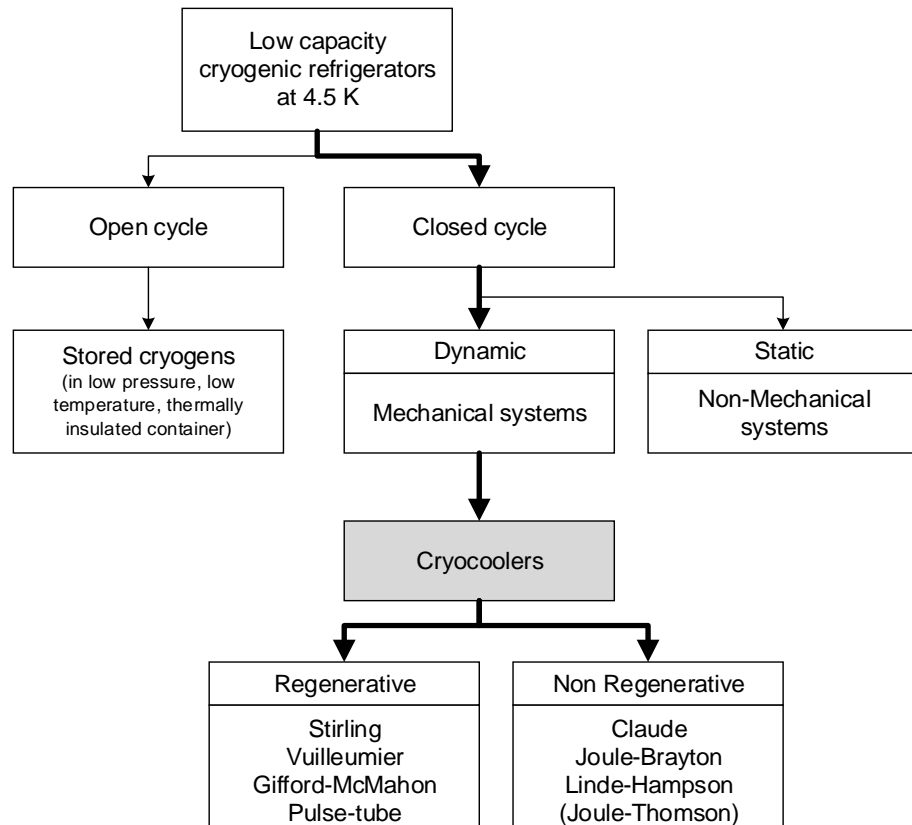
Figure 2.2. Classification of low-capacity cryogenic refrigerators at 4.5 K (c.f. [19]). The list is non-exhaustive.

A regenerative cryocooler comprises a regenerative heat exchanger and provides a pulsatile reversing flow. Regenerative heat exchangers, also called *regenerators*, are normally a porous matrix of finely divided material that operates on the principle of heat storage in an intermittent heat exchange process (Figure 2.3a). In a first step, the porous matrix acts as the storage mass, which absorbs the heat from the cryogen when it is passing at a higher temperature. In a subsequent step, the storage mass rejects the heat to the cryogen when it passes back at a lower temperature. [19]

Non-regenerative cryocoolers have a recuperative, but not regenerative, heat exchanger and provide a steady continuous flow. Recuperative heat exchangers, also called *recuperators*, have independent channels for each cryogen stream where the colder stream is used to extract the heat of the warmer one in a continuous heat exchange process (Figure 2.3b). Recuperators can be further classified according to their flow arrangements (e. g. counterflow, parallelflow, crossflow, etc.). [19][25]
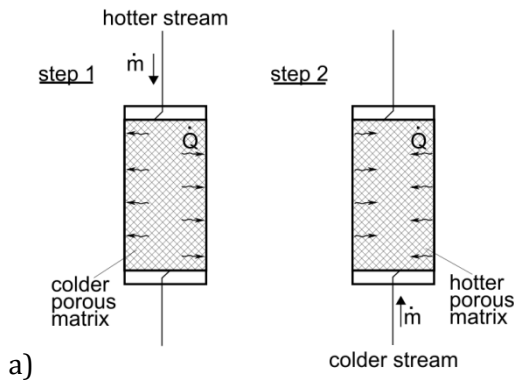
Regenerator   **Recuperator**
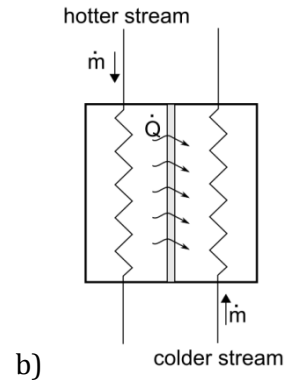
Figure 2.3. Principle of regenerative (a) and recuperative (b) heat exchange. In both cases, the heat rejected by the hotter stream is absorbed by the colder stream. Regenerators store the heat temporarily and recuperators exchange the heat continuously.

The operational principles of selected mechanical cryocoolers (both regenerative and non-regenerative) are described in the following subchapter. Due to their relevance in this work, the fundamentals of heat exchangers, particularly of recuperators, are introduced in chapter 3.

2.1.1 Cryocoolers

Three commonly used cryocooler types are the Gifford-McMahon, the Pulse-Tube and the Brayton cryocooler [3] (Figure 2.4). Each cryocooler operates using different principles, but all rely on compression and expansion of a gas to generate the temperature changes. The mechanical arrangement normally consists of reciprocating pistons (b) or displacers (c). Pistons (b) are elements that transfer work from and to the cryogen, withstanding large pressure differences across them. In contrast, displacers (c) are elements that displace the cryogen from one space to another (each at a different temperature level) without performing any work. The mechanical arrangements also include a cold stage (d) to absorb heat at the refrigeration temperature T_R. The compression work generated at room temperature is normally extracted to the ambient by an aftercooler (e). The Gifford-McMahon (GM) and the Pulse-Tube cryocoolers are regenerative systems, while the Brayton cryocooler is recuperative. [1] [2] [3] [26]

Regenerative Cycles   **Recuperative Cycle**

Gifford-McMahon (GM)   Pulse-Tube   Brayton
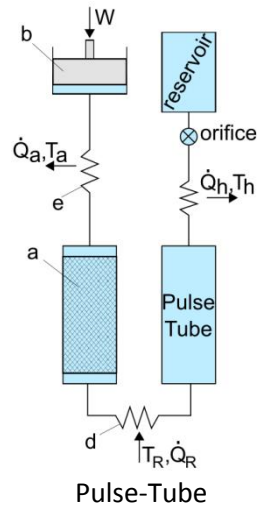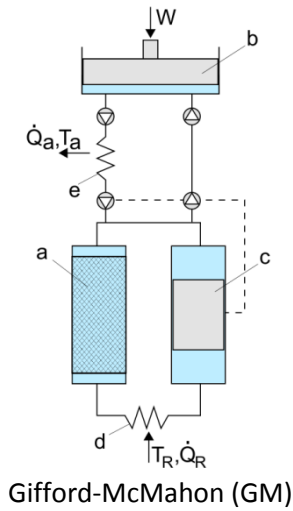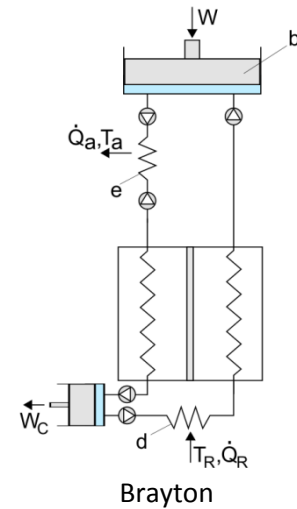
Figure 2.4. Schematics of three common types of cryocoolers. (c.f. [3])
a) regenerator; b) piston; c) displacer; d) cold (refrigeration) stage; e) aftercooler

Regenerative Systems

The regenerative cryocoolers shown in Figure 2.4 operate with oscillating flow and pressure, analogous to AC electrical systems. The presented Pulse-Tube system is characterised by the method of fluid flow control by volume changes and is therefore generally classified as a Stirling engine*. In contrast, the presented GM system is characterised by the method of fluid flow control by valves and is therefore classified as an Ericsson engine [26]. In GM cryocoolers, the displacer moves most of the gas to the hot end during the compression process, and to the cold end during the expansion process. In the case of Pulse-Tube cryocoolers, an oscillating flow through an orifice at the warm end moves the gas in a similar phase relationship as it would be provided by a displacer, but without the requirement of a moving part. This potentially results in lower system vibrations in comparison to GM cryocoolers. The orifice can also be a long capillary, which is called inertance tube. On both cryocoolers, heating and cooling occurs as the pressure increases or decreases, respectively. [2] [3]

Multi-stage cryocoolers have more than one cold stage and each of them absorbs heat at a different temperature. They are realised by the use of several displacers and the connection of regenerators in series. As an example, the mechanical arrangement of a 2-stage GM cryocooler is shown in Figure 2.5a. The arrangement comprises of a cold head (a) connected to a compressor unit (b). An aftercooler (c) integrated at the exhaust of the compressor (d) is used to cool the gas back to ambient temperature. The cold head (a) contains two regenerators connected in series (e, f), which together also act as the displacer. The gas flow through the cold head is controlled by a high-pressure (HP) and a low-pressure (LP) valve. The cold head is

---

* Note the word "cycle" is not used. [26]

comprised of two cold stages, with the first stage always at a higher temperature than the second stage.

The 4-step operation of the cryocooler is shown schematically in Figure 2.5b. In step 1, the LP valve is closed and the HP valve is opened, allowing high-pressure gas at room temperature to fill the regenerators and the space above the displacer. In the next step, the displacer moves to the upper position, forcing the high-pressure gas to pass through the colder regenerator. Consequently, the high-pressure gas is cooled isobarically, filling the space below the displacer. In step 3, the HP valve is closed and the LP valve is opened, allowing the gas inside the cold head to undergo expansion. This results in a cooling effect that is used for refrigeration when heat is absorbed at the cold stages. In the fourth step, the displacer moves back to its lowest position, forcing the low-pressure gas to pass through the warmer regenerator. Consequently, the low-pressure gas is warmed isobarically, filling the space above the displacer.

Mechanical arrangement   **Schematic operation**
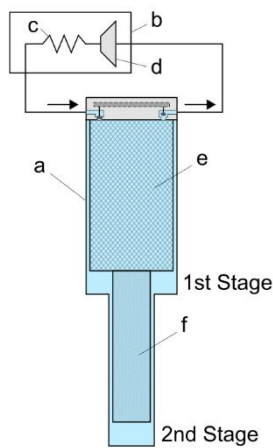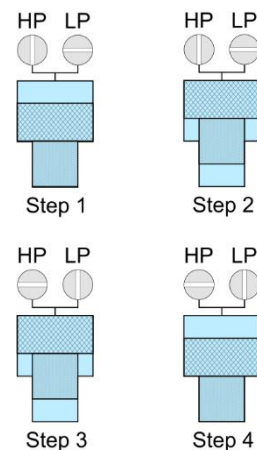
a)   b)

Figure 2.5. Mechanical arrangement (a) and schematic operation principle (b) of a 2-stage Gifford-McMahon cryocooler. (c.f. [27])
a) cold head; b) compressor unit; c) aftercooler; d) compressor; e) first regenerator; f) second regenerator.

To date, commercially available two-stage cryocoolers are capable of providing a refrigeration power of 2.0 W at a refrigeration temperature of 4.2 K on the colder stage. Two examples are the GM cryocooler (model RDE-418D4) from Sumitomo HI Ltd. and the Pulse-Tube cryocooler (model PT420) from Cryomech Inc. (Figure 2.6). [28], [29]

Gifford-McMahon   **Pulse-Tube**

a)   b)
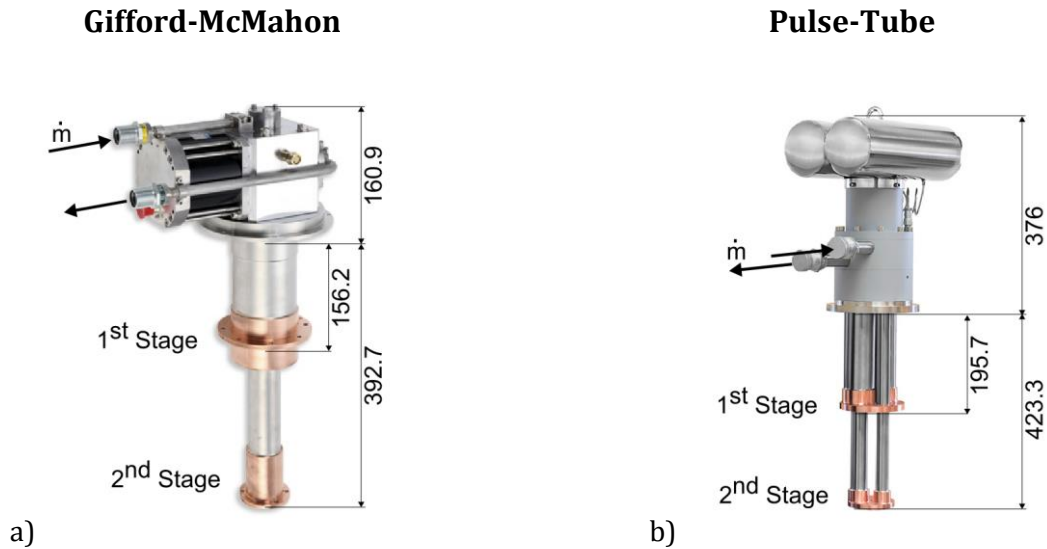
Figure 2.6. Cold heads of commercially available two-stage cryocoolers with a refrigeration power of 2.0 W at a refrigeration temperature of 4.2 K on the colder stage. Dimensions are in millimetres.
a) Cold head, model RDE-418D4 from Sumitomo HI Ltd. [28];
b) Cold head, model PT420 from Cryomech Inc. [29].

Recuperative Systems

The Brayton cryocooler in Figure 2.4 provides a continuous flow and steady pressure, analogous to DC electrical systems. The steady pressure in the system allows the presence of large gas volumes, which makes the transport of the expanded cold gas to any number of distant locations possible. In the Brayton refrigeration cycle, the gas is heated during compression and cooled during expansion, where the expansion engine is generally an expansion turbine.

2.1.2 Cryocooler-based refrigerators

A cascade refrigeration cycle consists of two or more refrigeration cycles that are thermally connected in series, in such a way that the previous cycle is used to pre-cool the subsequent one. Using this principle, cryocooler-based refrigerators are defined in this work as systems that employ a cryocooler device to pre-cool a subsequent refrigeration cycle. Then, the cooling power generated by the subsequent cycle is used for refrigeration.

One example of cryocooler-based refrigerators is the combination of a cryocooler device with a Joule-Thomson (JT) expansion cycle (Figure 2.7). In this specific example, the schematic shows the previously introduced 2-stage GM cryocooler, although there is no particular constraint on the cryocooler type to be implemented. The JT expansion cycle comprises of a compressor unit with integrated aftercooler (a), two types of heat exchanger (b, c) and a JT expansion valve (d). The recuperators (b) are used to pre-cool the high-pressure (HP) stream with the colder, low-pressure (LP) return stream. In addition to this, the HP stream is cooled further by thermalisation heat exchangers (c) attached to each one of the cold stages of the cold head (d). It is through these heat exchangers that both cycles are thermally connected, since heat power ($\dot{Q}_{1st}$, $\dot{Q}_{2nd}$) is transferred from one cycle to the other. After this, the cold HP stream is isenthalpic expanded by means of a JT valve, and thus cooled-down further. Finally, the

expanded LP stream is at its coldest temperature and is used to absorb the refrigeration power $\dot{Q}_R$. [27] [30]
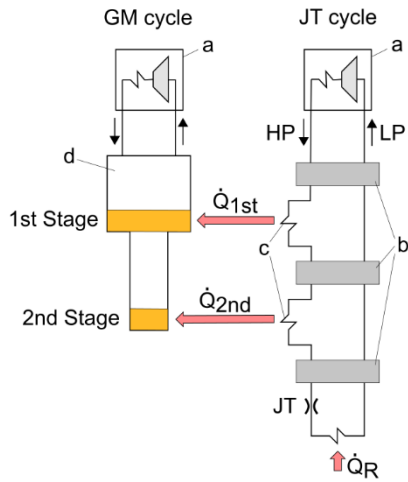
Figure 2.7. Schematics of a cryocooler-based refrigerator consisting of a 2-stage GM cryocooler thermally connected to a Joule-Thomson (JT) expansion cycle. The high-pressure (HP) stream is pre-cooled by the cryocoolers cold head prior its isenthalpic expansion at the JT valve. [27][30]
a) compressor unit; b) recuperator; c) thermalisation heat exchanger; d) cold head.

Figure 2.8 shows the cold head of a commercially available cryocooler-based refrigerator from the company Sumitomo HI Ltd (model CG310SC). The system combines a two-stage GM cryocooler (a) with a JT expansion cycle (b). The three-stage cold head can absorb, isothermally, 4.2 W at 4.3 K at its colder stage using the latent heat of helium. [22] [30] [31]

Gifford-McMahon Joule-Thomson
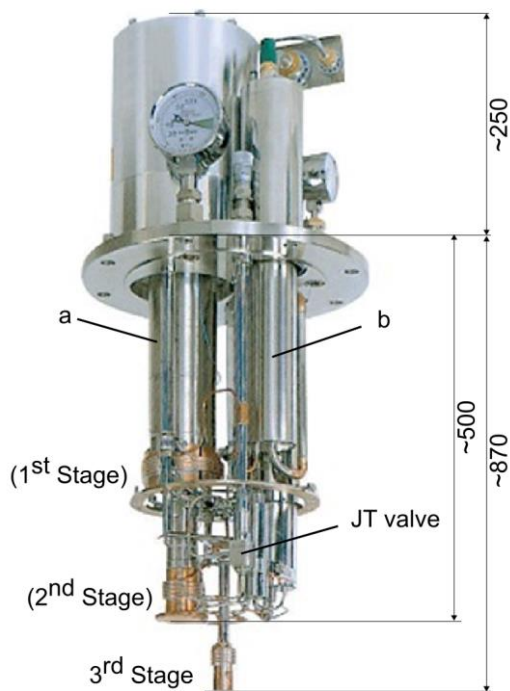
Figure 2.8. Cold head of commercially available refrigerator based on a two-stage GM cryocooler (a) with a JT cycle (b) from the company Sumitomo HI Ltd. (model CG310SC). The device can provide at its colder (3rd) stage an isothermal refrigeration power of 4.2 W at 4.3 K using the latent heat of helium. Dimensions are in millimetres. [22] [30] [31]

2.2 Isenthalpic Joule-Thomson expansion

The Joule-Thomson (JT) effect is the change of temperature under isenthalpic expansion per pressure drop [33]. The differential measure of this effect is the adiabatic JT coefficient μ_{JT} defined as

$$\mu_{JT} \equiv \left(\frac{\partial T}{\partial p}\right)_h = \mu_{JT}[p, T] \quad . \tag{2.3}$$

An ideal gas experiences no change of temperature during an isenthalpic expansion ($\mu_{JT} = 0$). In contrast, the JT coefficient μ_{JT} for a real gas can be positive, negative or zero. The inversion state marks the gradual and continuous transition of the JT coefficient from a positive to a negative value, or vice versa, and where $\mu_{JT} = 0$. The extended inversion states are additional states where the JT coefficient changes sign without passing through zero. [27] [33] [32]

Figure 2.9 shows isenthalpic curves for helium on a temperature-pressure diagram as calculated with the specialised library HePak© [20]. The loci of all inversion states comprise the differential inversion curve (D.I.C.), which presents the following features:

- By definition, the D.I.C passes through the peak of the isenthalps at the corresponding inversion pressure p_{INV} and inversion temperature T_{INV}.
- There is a highest inversion temperature (point A), the value of which is characteristic on each gas (here estimated at 38.92 K, 0.5 mbar). Above this temperature, no cooling is obtainable under isenthalpic expansion, independent of the pressure.
- There is a highest inversion pressure (point B), the value of which is characteristic on each gas (here estimated at 39.42 bar, 22.75 K). Above this pressure and at any temperature, the differential isenthalpic expansion always result in a temperature increase. The D.I.C. can be subdivided at point B into an upper and a lower part.
- For each inversion pressure there are two corresponding inversion temperatures. Each of these temperatures are situated at the upper and the lower part of the D.I.C.
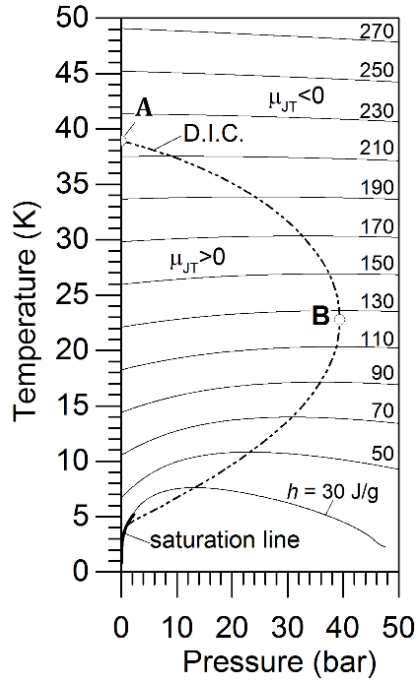
Figure 2.9. The differential inversion curve (D.I.C.) of helium is the location of the peaks of constant enthalpy trajectories. Fluid state values according to the specialised library HePak© [20].

2.3 Entropy, exergy and equivalent refrigeration power

Refrigerators require work to move heat from a lower to a higher temperature as a consequence of the second law of thermodynamics. Based on the previous refrigerator schematic (Figure 2.1), the first law of thermodynamics states

$$\dot{W} + \dot{Q}_R - \dot{Q}_a = 0 \ . \tag{2.4}$$

In addition, the second law states that any heat flow $\dot{Q}$ across a system boundary is inevitably accompanied by an entropy flow $\dot{S}_Q$, which is defined as

$$\dot{S}_Q \equiv \frac{\dot{Q}}{T} \ , \tag{2.5}$$

where T is the temperature at the corresponding system boundary. In contrast, work transported across system boundaries does not carry entropy [34]. Therefore, the entropy balance of the refrigerator dictates that

$$\frac{\dot{Q}_R}{T_R} - \frac{\dot{Q}_a}{T_a} + \dot{S}_{irr} = 0 \ , \tag{2.6}$$

where $\dot{S}_{irr} \geq 0$ is the entropy generated in the system due to irreversibilities. The combination of equations (2.4) and (2.6) gives

$$\dot{W} = \dot{Q}_R \left(\frac{T_a}{T_R} - 1 \right) + T_a \cdot \dot{S}_{irr} \geq 0 \ , \tag{2.7}$$

showing that for a given amount of cooling power the increase in losses ($\dot{S}_{irr}$) or the reduction of the refrigeration temperature T_R results in a higher requirement of work power. For the

theoretical case of an idealised refrigerator, which provides a reversible cycle and therefore no losses ($\dot{S}_{\text{irr}} = 0$), the required work power is still greater than zero

$$\dot{W}^{\text{rev}} = \dot{Q}_{\text{R}} \left(\frac{T_{\text{a}}}{T_{\text{R}}} - 1 \right) \geq 0 \ , \tag{2.8}$$

confirming the previous statement that all refrigerators require work to move heat from lower to higher temperatures.

The *quality* of the energy flow in a refrigerator can be specified using the concept of *exergy*, which describes the maximum available energy that can be obtained from a system in a given state. The concept of exergy is a consequence of the first and second law of thermodynamics. Due to energy conservation, when exergy is said to be destroyed, it is actually converted to its counter-part form, *anergy*. However, anergy cannot be converted back to exergy. [25] [34]

The exergy per unit of mass, or specific exergy e, as a function of state is defined as

$$e \equiv h - T_{\text{a}} \cdot s \ , \tag{2.9}$$

where h and s are enthalpy and entropy per unit of mass. Hence, the change in specific exergy Δe between two states (1→2) can be described as

$$\Delta e = \int_{1}^{2} (dh - T_{\text{a}} \cdot ds) = \Delta h - T_{\text{a}} \cdot \Delta s \ . \tag{2.10}$$

The work and electrical power $\dot{W}$ transported across system boundaries consist of pure exergy $\dot{E}_{\text{W}}$. Therefore,

$$\dot{E}_{\text{W}} = \dot{W} \ . \tag{2.11}$$

In contrast, and in analogy to Eq. (2.5), the exergy flow $\dot{E}_{Q}$ that accompanies any heat flow $\dot{Q}$ across a system boundary can be calculated as

$$\dot{E}_{Q} = \left(1 - \frac{T_{\text{a}}}{T} \right) \cdot \dot{Q} = \eta_{\text{C}} \cdot \dot{Q} \ , \tag{2.12}$$

where T is the temperature at the corresponding system boundary and η_{C} is the so-called Carnot factor, which corresponds to the thermal efficiency of a reversible heat engine producing mechanical power from a heat source [34]

$$\eta_{\text{C}}[T] = 1 - \frac{T_{\text{a}}}{T} \ . \tag{2.13}$$

Note that for a given ambient temperature T_{a}, the Carnot factor η_{c} is a function of the temperature T at the system boundary, and adopts negative values when heat is exchanged at temperatures below ambient (Figure 2.10). Consequently, for those cases the exergy flow is in the opposite direction to the heat flow.
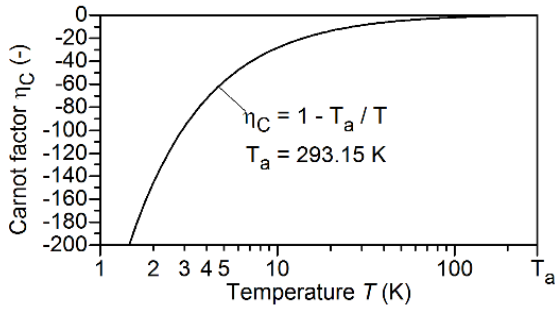
Figure 2.10. The Carnot factor η_c adopts negative values for temperatures T below the ambient temperature T_a.

Based on the energy balance of Eq. (2.4), the exergy balance states

$$\dot{E}_W + \dot{E}_R - \dot{E}_a - \dot{E}_d = 0 \quad , \tag{2.14}$$

where $\dot{E}_d$ is the "destroyed" exergy converted to anergy in the system (hence the negative sign). Combining Eq. (2.14) with Eq. (2.11) and Eq. (2.12) yields

$$\dot{E}_d = \dot{W} + \underbrace{\eta_C[T_R]}_{<1} \cdot \dot{Q}_R - \underbrace{\eta_C[T_a]}_{=0} \cdot \dot{Q}_a \ , \tag{2.15}$$

and using Eq. (2.7) results in

$$\dot{E}_d = T_a \cdot \dot{S}_{irr} \geq 0 \ , \tag{2.16}$$

showing that the destroyed entropy is directly related to the rate of entropy generation $\dot{S}_{irr}$. Moreover, exergy is destroyed if entropy is generated. It can be shown, that for the theoretical case of an idealised refrigerator ($\dot{S}_{irr} = 0$), the entire work power $\dot{W}^{rev}$ applied to the refrigerator is rejected in the form of an exergy flow $\dot{E}_R$ at the refrigeration temperature T_R

$$\dot{E}_R = \eta_C \cdot \dot{Q}_R = -\dot{W}^{rev} \ . \tag{2.17}$$

The heat, entropy and exergy flow in a refrigerator system are illustrated in Figure 2.11a, and the darker flow paths are related to the irreversibilities of the system. As shown so far, it is possible to describe a refrigeration cycle in terms of exergy. Consequently, different refrigerators can be compared to each other from the exergetic point of view, even if their working points are at different temperatures. To facilitate the comparison, a system can be represented by its equivalent system, which is a system equal in terms of exergy but working at the equivalent refrigeration temperature T_R^{eq} (Figure 2.11b). For this, the exergy balance of the refrigerator is used to calculate the energy and entropy balance of the equivalent system. For example, based on Eq. (2.12), the equivalent refrigeration power $\dot{Q}_R^{eq}$ can be calculated as

$$\dot{Q}_R^{eq} = \frac{\dot{E}_R^{eq}}{\eta_C[T_R^{eq}]} = \frac{\dot{E}_R}{\eta_C[T_R^{eq}]} = \frac{\eta_C[T_R]}{\eta_C[T_R^{eq}]} \cdot \dot{Q}_R \quad , \tag{2.18}$$

and the equivalent refrigeration entropy rate $\dot{S}_R^{eq}$ as

$$\dot{S}_R^{eq} = \frac{\dot{Q}_R^{eq}}{T_R^{eq}} = \frac{T_R}{T_R^{eq}} \cdot \frac{\eta_C[T_R]}{\eta_C[T_R^{eq}]} \cdot \dot{S}_R = \frac{T_a - T_R}{T_a - T_R^{eq}} \cdot \dot{S}_R \quad . \tag{2.19}$$

Refrigerator   *Equivalent* **refrigerator**
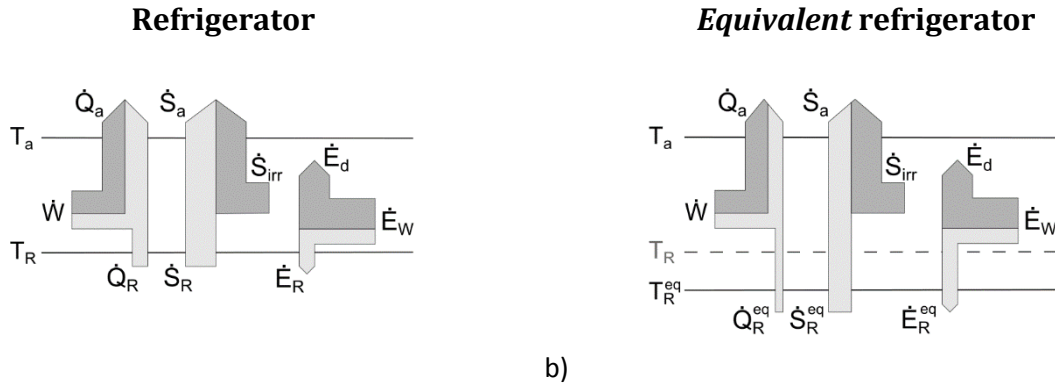
Figure 2.11. Heat, entropy and exergy flow in a refrigerator ($T_a = 2\,T_R$, $\dot{S}_{irr} = \dot{S}_R$) (a) and its *equivalent* system (b), which is equal in terms of exergy ($\dot{E}_R^{eq} = \dot{E}_R$) but has a different refrigeration temperature ($T_R^{eq} = 2/3\,T_R$). The darker flow paths are related to the thermodynamic losses of an irreversible system ($\dot{S}_{irr} > 0$).

The coefficient of performance (COP) is commonly used to quantify the capability of a refrigerator to extract heat from a lower temperature in relation to the required work to do so [1]. Therefore, the COP in a refrigeration system is defined as

$$\text{COP} \equiv \frac{\text{refrigeration power}}{\text{net work power input}} = \frac{\dot{Q}_R}{\dot{W}} \quad . \tag{2.20}$$

Using Eq. (2.7) and Eq. (2.13), the COP can be calculated as

$$\text{COP} = \left[-\eta_C(T_R) + \frac{T_a \cdot \dot{S}_{irr}}{\dot{Q}_R} \right]^{-1} \quad . \tag{2.21}$$

It can be shown that the highest theoretical COP is only achieved by reversible cycles, which present no losses ($\dot{S}_{irr} = 0$). The COP of those idealised refrigerators is calculated as

$$\text{COP}^{rev} = -\frac{1}{\eta_C[T_R]} = \frac{T_R}{T_a - T_R} \quad , \tag{2.22}$$

which only depends on the specified temperature levels. Then, in order to compare the COP of real refrigerators to idealised refrigerators, the performance criterion known as figure of merit (FOM) is used.

$$FOM \equiv \frac{\text{COP}}{\text{COP}^{rev}} \quad . \tag{2.23}$$

The reversible cycle of an ideal refrigerator is often represented by the Carnot refrigeration cycle, due to its convenience and familiarity [1]. It comprises of two isothermal and two isentropic processes, where the external heat exchange occurs only at the upper and lower temperature limits of the cycle (Figure 2.12). The cycle starts with an isentropic compression (①→②) where the temperature rises from the lower (refrigeration) temperature T_R to the upper (ambient) temperature T_a. The heat rejected during the isentropic compression is recovered and absorbed by the isentropic expansion (③→④). Then, at this upper temperature, the fluid is compressed isothermally (②→③) and the heat $\dot{Q}_a$ is rejected to the ambient. During the isentropic expansion of the fluid (③→④), the temperature of the

fluid drops back to the refrigeration temperature T_R. Lastly, at this lower temperature, the fluid is expanded isothermally (④→①) and heat $\dot{Q}_R$ is absorbed. [26]
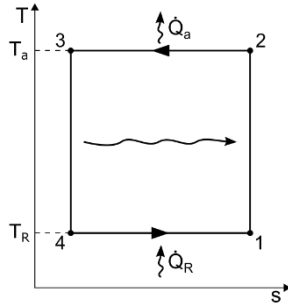
Figure 2.12. Temperature-entropy diagram of the Carnot refrigeration cycle.

The exergetic efficiency ζ of a system can be defined in general terms as

$$\zeta \equiv \frac{\text{usable exergy}}{\text{exergy effort}} \leq 1 \quad , \tag{2.24}$$

where the definition of usable exergy and exergy effort varies according to the purpose of a given system. For a refrigerator, the purpose is to provide cooling power and the effort is the work required to accomplish this. Therefore,

$$\zeta = \frac{\text{refrigeration power}}{\text{net work power input}} = \frac{\dot{E}_R}{\dot{E}_W} = 1 - \frac{\dot{E}_d}{\dot{E}_W} \leq 1 \quad . \tag{2.25}$$

Consequently, the exergetic efficiency ζ in a refrigerator quantifies, in terms of exergy, its capability of providing cooling power in relation to the required exergy to do so [34]. Only for the theoretical case of a reversible refrigerator ($\dot{E}_d = 0$), does the exergetic efficiency ζ reach its maximum value of one.

3 Fundamentals of recuperative heat exchangers

Recuperative heat exchangers, or recuperators, are devices able to transfer heat power $\dot{Q}_{HX}$ from a hotter to a colder stream in a continuous exchange process (Figure 3.1). This work concentrates exclusively on recuperators with a counterflow arrangement, due to their thermodynamic superiority compared to any other flow arrangement. [25], [35]
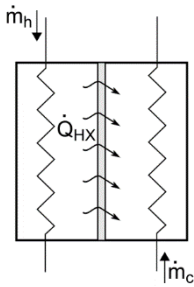
Figure 3.1. Schematic diagram of a recuperator in counterflow arrangement. The heat power $\dot{Q}_{HX}$ is transferred from the hotter to the colder stream in a continuous exchange process.

This chapter elaborates on the fundamentals of heat exchangers, focussing on recuperators with two streams in counterflow arrangement. First, the heat exchange process is described in terms of a flow of thermal energy across a solid wall, and the corresponding heat transfer equations are introduced. The energy balance within a recuperator is used to establish the heat power transmitted between both fluids and the resulting temperature profile along the flow paths. These concepts are then employed to define parameters that characterize the thermal performance of recuperators. Relevant sources of thermo-hydraulic losses and basic construction types of recuperators are introduced at the end.

3.1 Heat exchange process and heat transfer equations

The heat exchange process is illustrated in Figure 3.2. Note that the symbol "δ" is used in this work to denominate the local temperature <u>difference</u> between the hot and the cold stream of a heat exchanger. Therefore, δT is defined as

$$\delta T \equiv (T_h - T_c)_{\text{local}} \geq 0 \ , \tag{3.1}$$

where the subscripts h and c correspond to the hotter and the colder stream, respectively. The local temperature difference δT is also referred to as the temperature driving potential or force of heat transfer. [25]

In analogy to chapter 2.3, and based on Eq. (2.6), it can be shown that

$$d\dot{S}_{irr} = d\dot{Q}_{\text{HX}} \cdot \frac{\delta T}{T_h \cdot T_c} \geq 0 \ , \tag{3.2}$$

where $d\dot{Q}_{\text{HX}}$ is the locally transferred heat across an infinitesimally small surface area dA. Then, combining Eq. (2.13) with Eq. (3.2) gives the rate of destroyed exergy as

$$d\dot{E}_d = T_a \cdot d\dot{S}_{irr} = T_a \cdot \frac{\delta T}{T_h \cdot T_c} \cdot d\dot{Q}_{\text{HX}} \geq 0 \ , \tag{3.3}$$

or in terms of the Carnot factor $\eta_{\text{C}}[T]$,

$$d\dot{E}_d = (\ \eta_{\text{C}}[T_h] - \eta_{\text{C}}[T_c]\ ) \cdot d\dot{Q}_{\text{HX}} \geq 0 \ . \tag{3.4}$$

As shown by Eq. (2.12), heat and exergy flow in opposite directions when heat is exchanged at temperatures below ambient. Therefore, exergy is transferred from the cold to the hot stream, where part of this exergy is destroyed during the irreversible process. In other words, the increase in the exergy rate of the hotter stream is accomplished at the expense of the decrease in the exergy rate of the colder stream. For this reason, recuperators are often described as devices able to "recover" the exergy from a colder stream and transfer it to a hotter stream.
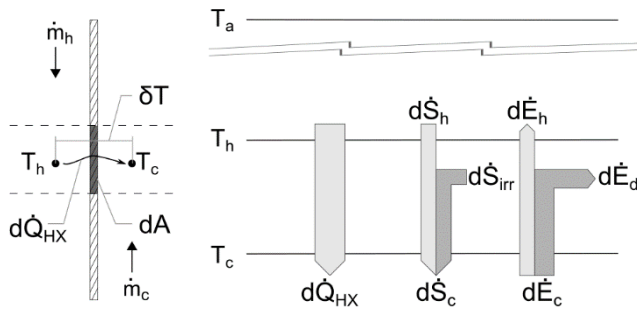
Figure 3.2. Heat, entropy and exergy flow resulting from the locally transferred heat power $d\dot{Q}_{\text{HX}}$ across an infinitesimal surface area dA. The local temperature difference between both streams is defined as $\delta T = T_h - T_c$. The path proportions are valid for $T_a = 5\,T_h = 10\,T_c$ and the darker flow paths are related to the thermodynamic losses of an irreversible heat exchange ($\dot{S}_{\text{irr}}$>0 since δT>0).

Heat is transferred between the two streams via the solid wall that is dividing them (Figure 3.3). Therefore, at a local point, the heat has to pass a certain heat transfer resistance dR_{UA} in order to flow from the hot to the cold side. Analogous to electrical circuits, the reciprocal value of this unit of resistance is defined as the local thermal conductance of the heat exchanger [25]:

$$d(U \cdot A) \equiv \frac{1}{dR_{UA}} \ , \tag{3.5}$$

where U is the local overall heat transfer coefficient and A is the heat exchange surface area. Consequently, the heat power $d\dot{Q}$ that is locally transferred over the surface area dA can be calculated as

$$d\dot{Q} = \frac{\delta T}{dR_{\text{UA}}} = \delta T \cdot d(U \cdot A) \ . \tag{3.6}$$

Note that both the local overall heat transfer coefficient U and the local temperature difference δT, can vary significantly along a heat exchanger. In addition, the heat transfer resistance dR_{UA} presented in Figure 3.3 neglects longitudinal heat conduction along the solid wall. This effect is introduced later in chapter 3.4.

The total heat flux at the heat exchanger can be obtained by integrating Eq. (3.6) over the entire heat exchanger surface. The resulting equation is also known in the literature as the heat transfer rate equation [25]

$$\dot{Q} = \int_A d\dot{Q} = \int_A \delta T \cdot d(U \cdot A) = U_m \cdot A \cdot \delta T_m \ , \tag{3.7}$$

where U_m and δT_m are the mean overall heat transfer coefficient and the mean temperature difference of the heat exchanger, respectively. Both expressions are defined as follows [25]:

$$\frac{1}{\delta T_m} \equiv \frac{1}{\dot{Q}} \int_{\dot{Q}} \frac{d\dot{Q}}{\delta T} \ , \tag{3.8}$$

$$U_m \equiv \frac{1}{A} \int_A d(U \cdot A) \ . \tag{3.9}$$

The local overall heat transfer coefficient U is the result of a convection-conduction heat transfer phenomenon between both streams and the solid wall (Figure 3.3). In analogy to an electrical circuit, it is calculated as the combination of two convection resistances ($R_{\alpha,h}, R_{\alpha,c}$) and one conduction resistance (R_{wall}) in series

$$\frac{1}{d(U \cdot A)} = dR_{\text{UA}} = dR_{\alpha,h} + dR_{\text{wall}} + dR_{\alpha,c} \ , \tag{3.10}$$

with

$$dR_{\alpha,h} + dR_{\text{wall}} + dR_{\alpha,c} = \frac{1}{\alpha_h \cdot dA_h} + \frac{t_{\text{wall}}}{\lambda_{\text{wall}} \cdot dA_{\text{wall}}} + \frac{1}{\alpha_c \cdot dA_c} \ , \tag{3.11}$$

where α_h and α_c are local heat transfer coefficients of the hot and cold stream to the solid wall, λ_{wall} is the local heat conduction coefficient of the wall, and t_{wall} is the local wall thickness.
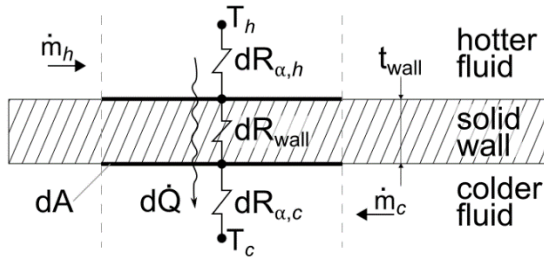
Figure 3.3. The local heat transfer resistance dR_{UA} is composed by the addition of the resistances $dR_{\alpha,h}$, dR_{wall} and $dR_{\alpha,c}$ as the result of a convection-conduction heat transfer phenomenon between both streams and the solid wall.

The calculation of the local heat transfer coefficient α leads back to the determination of the dimensionless Nusselt number Nu which gives the ratio of convective to conductive heat transfer across the boundary between the fluid and the wall. Therefore, a large Nusselt number Nu indicates that the heat transfer is dominated by convection. It is given by:

$$Nu = \frac{\text{"convective heat-transfer"}}{\text{"conductive heat-transfer"}} = \frac{\alpha \cdot L_0}{\lambda} \ , \tag{3.12}$$

where L_0 is the characteristic length of the channel and λ is the heat conduction coefficient of the fluid. The hydraulic diameter D_h is the characteristic length of a channel with inside flow ($L_0 = D_h$) and can be calculated as

$$D_h = \frac{4 \cdot A_{\mathrm{cross}}}{O} \ , \tag{3.13}$$

where A_{cross} and O are the cross sectional fluid domain area and the wetted perimeter of the channel.

The Nusselt number Nu is estimated using the empirical correlations from literature [35]; where each correlation is specific for certain boundary conditions. Most of the correlations are constructed as a function of two dimensionless quantities: the Reynolds number Re and the Prandtl number Pr. The Reynolds number Re quantifies the ratio of inertial to viscous forces within the flow, and the Prandtl number Pr gives the relative importance of the mass flow (momentum) over the thermal diffusion for the heat transport [32]. The quantities are given by:

$$Re = \frac{\text{"inertial forces"}}{\text{"viscous forces"}} = \frac{\rho \cdot v_m \cdot L_o}{\mu} = \frac{\dot{m} \cdot L_o}{\mu \cdot A_{\mathrm{cross}}} \tag{3.14}$$

and

$$Pr = \frac{\text{"momentum diffusivity"}}{\text{"thermal diffusivity"}} = \frac{\mu \cdot c_p}{\lambda} \ , \tag{3.15}$$

where ρ is the fluid density, $v_m = \dot{V}/A_{\mathrm{cross}}$ is the mean fluid velocity, μ is the dynamic fluid viscosity, and c_p is the heat capacity of the fluid at constant pressure. The equations show that the Prandtl number Pr only depends on the fluid state of helium, as opposed to the Reynolds number Re which is also a function of the channels dimension. For helium at $T \geq 20$ K, the Prandtl number Pr approaches asymptotically the ideal-gas value of 2/3 [32]. Its value increases two orders of magnitude in the vicinity of the critical point ($Pr \approx 30$ at p_{crit} = 2.27 bar and T_{crit} = 5.20 K; see Annex A4).

The selection of a suitable correlation for the Nusselt number Nu requires the consideration of several factors to establish whether the range of parameters is appropriate for a particular fit. Arguably the two most important factors are the *regime* and the *development* of the flow.

The flow regime is determined using the Reynolds number Re. The flow is *laminar* for Re<2300 and (with certainty) *turbulent* for Re>10^4. In the intermediate region (2300<Re<10^4), the so-called *transition zone*, the flow regime is unstable and can change between laminar and turbulent depending on the boundary conditions.

The flow development is evaluated based on the velocity and temperature profiles of the flowing fluid. The profiles develop in the direction of the flow, where the *hydrodynamic development* begins at the flow entrance and the *thermal development* starts at the beginning of the heat-exchange area. Each profile stabilises after a certain distance and remains unchanged afterwards. The flow is fully developed when both profiles reach their stable state. At $T \geq 20$ K, the Prandtl number Pr is close to unity for helium, and therefore, both developments are expected to occur at a similar rate. The relative importance of the developing region decreases with increasing channel length L. Therefore, for long channels ($L/D_h > 100$), the flow is assumed to be fully developed along the entire channel. [32]

The correlations used for the calculation of the Nusselt number Nu are introduced in Table 3.1 and are specific for the flow regime. The equations are valid for a flow that is thermally and hydrodynamically fully developed; as is always the case in this work, since chapter 6.1

shows that $L/D_h > 100$. The standard uncertainty of the employed correlations is estimated below 10 %.

The Nusselt number Nu_{lam} for laminar flow is constant when the flow is fully developed. This value is 3.66 for a constant wall-temperature ($\partial T_{\text{wall}}/\partial x=0$) or 4.364 for a constant heat-flux ($\partial \dot{q}/\partial x=0$) in the direction of the flow (x). A constant wall-temperature is usual for condensers and evaporators, since the heat transfer occurs isothermally due to the phase change of the fluid. A constant heat-flux is common for electrically heated pipes. As shown in Eq. (3.16), this work uses $Nu_{\text{lam}}= 3.66$ as a conservative approach, since this is also the smallest possible value of Nu. The Nusselt number Nu_{turb} for a turbulent flow is calculated using the empirical correlation in Eq. (3.18), which is independent from the conditions of "constant wall-temperature" and "constant heat-flux". For the transition zone, Eq. (3.17) assumes a periodic change between laminar and turbulent flow, hence using an intermittency factor γ to describe a linear and continuous development of the flow regime.

Table 3.1. Employed equations for the calculation of the Nusselt number Nu in a fully developed flow. [36]

Flow Regime	Equation	Eq.
Laminar flow: ($Re \leq 2300$)	$Nu_{\text{lam}} = 3.66$	(3.16)
Transition zone: ($2300 < Re < 10^4$)	$Nu_{\text{tran}} = (1-\gamma)\ Nu\big|_{Re=2300} +\gamma \cdot Nu\big|_{Re=10^4}$ with $\gamma = \dfrac{Re-2300}{10^4-2300}$ and $0 \leq \gamma \leq 1$	(3.17)
Turbulent flow: ($10^4 \leq Re \leq 10^6$)	$Nu_{\text{turb}} = \dfrac{(\chi/8)Re\cdot Pr}{1+12.7\sqrt{\chi/8}(Pr^{2/3}-1)}\left[1 + \left(\dfrac{D_h}{L}\right)^{2/3}\right]$ with $\chi = (1.8\log_{10} Re - 1.5)^{-2}$	(3.18)

D_h: Hydraulic diameter [m]; L: Total pipe length [m]; Pr: Prandtl number [-]; Re: Reynolds number [-];γ: intermittency factor [-].

Based on Eqs. (3.11) to (3.18), the local heat transfer coefficient α is pressure and temperature dependent through the physical fluid properties λ, μ and ρ, geometry dependent through L_0, and velocity dependent through Re. Consequently, the local heat transfer coefficient α of a stream j can be reduced to a function of its pressure, temperature and mass flow, as well as of its corresponding channel geometry:

$$\alpha_j = f\ [\ \underbrace{p_j, T_j, \dot{m}_j}_{\substack{\text{flow} \\ \text{properties}}}\ ,\ \underbrace{L_{0,j}}_{\substack{\text{channel} \\ \text{geometry}}}\ ]\ . \tag{3.19}$$

In analogy, the dependency of the local overall heat transfer coefficient U can be reduced to the pressure, temperature and mass flow of each stream, the local heat conduction coefficient of the solid wall, and the heat exchangers geometry:

$$U = f\ [\ \underbrace{p_h, p_c, T_h, T_c, \dot{m}_h, \dot{m}_c}_{\substack{\text{flow} \\ \text{properties}}},\ \underbrace{\lambda_{\text{wall}}}_{\substack{\text{wall} \\ \text{property}}},\ \underbrace{L_{0,h}, L_{0,c}, t_{\text{wall}}}_{\substack{\text{exchangers} \\ \text{geometry}}}\ ]\ . \tag{3.20}$$

3.2 Energy balance and temperature profile

The enthalpy rate $\dot{H}$ that accompanies a mass flow $\dot{m}$ can be calculated as

$$\dot{H} = \dot{m} \cdot h \quad . \tag{3.21}$$

Consequently, the energy balance for the heat power transmitted from the hotter to the colder stream gives

$$d\dot{Q} = \dot{m}_h \cdot dh_h = \dot{m}_c \cdot dh_c \quad , \tag{3.22}$$

where $d\dot{Q}$ is the net heat power that is exchanged by the fluids at a given incremental length dx within a control volume k, and dh is the enthalpy change resulting from it (Figure 3.4). Note that Eq. (3.22) considers the same reference direction x for both fluids, which is downstream for the mass flow $\dot{m}_h$ and upstream for the mass flow $\dot{m}_c$. The equation is also known as the enthalpy rate equation and is based on the first law of thermodynamics for an open non-adiabatic system with a single flow stream [25].
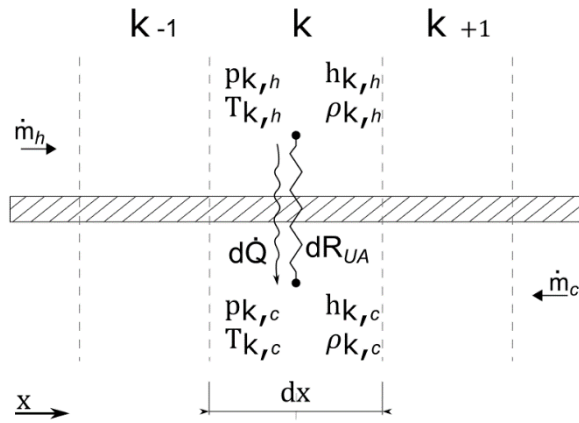
Figure 3.4. Control volume k for the energy balance of a recuperator.

For the isobaric heat exchange of single-phase fluids, the enthalpy change can be calculated as

$$dh = c_p[T] \cdot dT \quad , \tag{3.23}$$

where $c_p[T]$ is the temperature dependent heat capacity at a given constant pressure defined as

$$c_p \equiv \left(\frac{\partial h}{\partial T} \right)_p \quad . \tag{3.24}$$

The heat capacity rate $\dot{C}$ that accompanies a mass flow $\dot{m}$ is calculated as

$$\dot{C} = \dot{m} \cdot c_p \tag{3.25}$$

and consequently, the energy balance of Eq. (3.22) expressed in terms of the capacity rate can be calculated as

$$d\dot{Q} = \dot{C}_h \cdot dT_h = \dot{C}_c \cdot dT_c \quad . \tag{3.26}$$

The ratio between both heat capacity rates is denominated by the heat capacity rate ratio $\dot{C}^*$ and is defined in this work as

$$\dot{C}^* \equiv \frac{\dot{C}_h}{\dot{C}_c} \quad . \tag{3.27}$$

A heat exchanger is considered *balanced* when the heat capacity rate of both streams is equal ($\dot{C}^* = 1$).

It can be shown that the heat capacity rate of both streams influences the distribution of temperatures along the heat exchanger streams (Figure 3.5). This is derived from the changes in temperature and heat exchange area that result from the differential increment in the heat exchangers length [33].

A given incremental length dx in a heat exchanger results in the negative temperature change of both streams, dT_h and dT_c, so that

$$\frac{dT_h}{dx} \leq 0, \qquad \frac{dT_c}{dx} \leq 0 \quad ; \tag{3.28}$$

hence, and based on Eq. (3.26), the relative differential change is

$$\frac{dT_c}{dT_h} = \frac{\dot{C}_h}{\dot{C}_c} = \dot{C}^* \quad . \tag{3.29}$$

Thereafter, the change in local temperature difference δT over the temperature profile can be given as

$$\frac{d(\delta T)}{dT_c} = \frac{d(T_h - T_c)}{dT_c} = \frac{1}{\dot{C}^*} - 1 \tag{3.30}$$

and,

$$\frac{d(\delta T)}{dT_h} = 1 - \dot{C}^* \quad . \tag{3.31}$$

Consequently, the local temperature difference δT, and hence the driving force for the heat exchange mechanism, changes along the temperature profile as a function of the heat capacity rate ratio $\dot{C}^*$. It only remains constant for the special case of a balanced heat exchanger ($\dot{C}^* = 1$).

In the discrete model of a heat exchanger (Figure 3.4), a given incremental length dx results in the increase of the heat exchange area dA. Using Eq. (3.6) and Eq. (3.26), the change in temperature profile over the recuperators heat exchange area is given as

$$\frac{dT_j}{d(U \cdot A)} = -\frac{\delta T}{\dot{C}_j} \leq 0 \quad , \tag{3.32}$$

where the subscript j indicates either the hotter or the colder stream.

Therefore, the temperature profile of each stream along the exchangers length is defined by the local temperature difference δT and the heat capacity rate $\dot{C}$ of the given stream. Thus, the stream with the higher heat capacity rate $\dot{C}$ experiences the smaller temperature change during the heat exchange, and the temperature profiles of both streams are only equal for a balanced heat exchanger ($\dot{C}^* = 1$).

The change in the local temperature difference δT over the recuperators thermal conductance $U \cdot A$ is given as

$$\frac{\mathrm{d}(\delta T)}{\mathrm{d}(U \cdot A)} = \frac{\mathrm{d}(T_h - T_c)}{\mathrm{d}(U \cdot A)} = \delta T \cdot \left(\frac{1}{\dot{C}_c} - \frac{1}{\dot{C}_h}\right) \begin{cases} \geq 0 & \text{for } \dot{C}^* > 1 \\ = 0 & \text{for } \dot{C}^* = 1 \\ \leq 0 & \text{for } \dot{C}^* < 1 \end{cases}, \qquad (3.33)$$

showing that it varies according to the relationship between the heat capacity rate of both streams.

Based on the previous equations, the temperature profile of a recuperator is illustrated qualitatively in Figure 3.5, where the temperature variation of each stream is idealised as one-dimensional over the dimensionless length $\xi = x/L$ [25]. The profile is valid for single-phase fluids and the specific heat c_p on each fluid is treated as constant. Note that the local temperature difference δT decreases toward the cold side for $\dot{C}^* < 1$ and toward the hot side for $\dot{C}^* > 1$. Based on the shown reference direction of ξ, the temperature difference at each side of the recuperator is defined as follows:

$$\begin{cases} \delta T_{\mathrm{hs}} \equiv \delta T(\xi = 0) \\ \delta T_{\mathrm{cs}} \equiv \delta T(\xi = 1) \end{cases}, \qquad (3.34)$$

where δT_{hs} and δT_{cs} are the local temperature difference at the hot and the cold side, respectively.
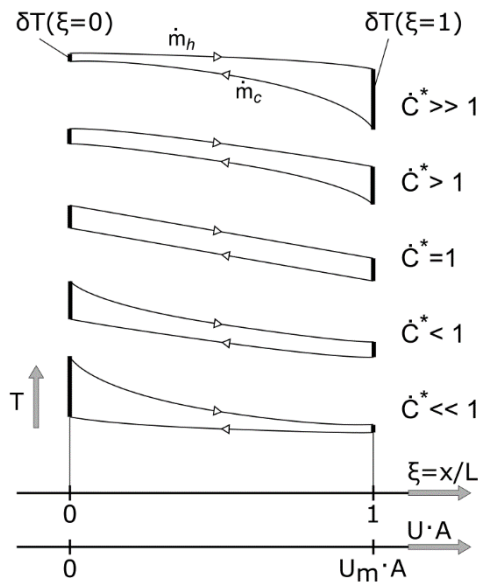
Figure 3.5. Longitudinal temperature profiles of a recuperator for different heat capacity rate ratios ($\dot{C}^* = \dot{C}_h/\dot{C}_c$). (c.f. [33])

3.3   Thermal performance

3.3.1 Effectiveness ε

The effectiveness ε, not to be confused with efficiency η, is widely used as a measure of the thermal performance of a heat exchanger. It is normally defined as the ratio of the actual heat power transfer $\dot{Q}$ to the maximum possible heat power transfer $\dot{Q}_{\mathrm{max}}$ that is thermodynamically permitted [25]:

$$0 \leq \varepsilon \equiv \frac{\dot{Q}}{\dot{Q}_{\max}} \leq 1 \ . \tag{3.35}$$

The introduction of the theoretical value $\dot{Q}_{\max}$ in Eq. (3.35) requires the concept of an "idealised heat exchanger with *infinitely* large thermal size" ($U_m A \to \infty$). The idealisation assumes no axial conduction, adiabatic behaviour to ambient and no frictional pressure loss (more in chapter 3.4). Such an idealised heat exchanger is only reversible in a balanced ($\dot{C}^* = 1$) counter-flow configuration, because only then the local temperature difference δT is practically zero along the entire heat exchanger (Figure 3.6). In contrast, exergy is destroyed for $\dot{C}^* \neq 1$ since δT only approaches zero at the cold side for $\dot{C}^* < 1$ and at the hot side for $\dot{C}^* > 1$. The reversible heat exchanger is capable of transfering the highest possible heat between two given temperatures. The heat and exergy flow of idealised recuperators with *infinite* thermal size ($U_m \cdot A \to \infty$) are illustrated qualitatively in Figure 3.7.

Based on Figure 3.6, the theoretical value $\dot{Q}_{max}$ can be calculated in terms of enthalpy change as:

$$\dot{Q}_{\max} = \begin{cases} \dot{m}_c \cdot \left(h_c[T_{h,\text{IN}}] - h_{c,\text{IN}} \right) & \text{for } \dot{C}^* \geq 1 \\ \dot{m}_h \cdot \left(h_{h,\text{IN}} - h_h[T_{c,\text{IN}}] \right) & \text{for } \dot{C}^* \leq 1 \end{cases} \ , \tag{3.36}$$

where $h[T]$ is the fluid enthalpy h at the temperature T.
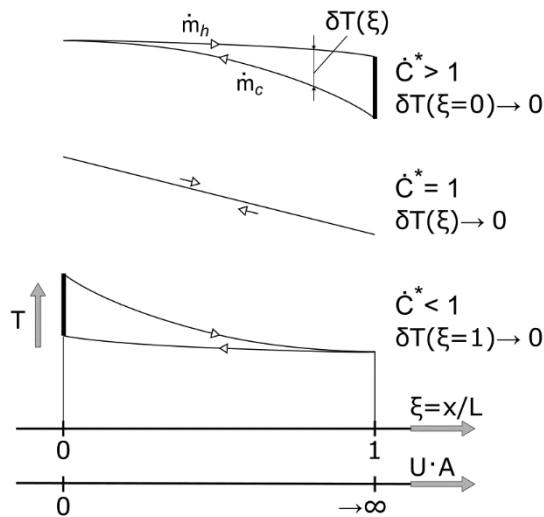
Figure 3.6. Longitudinal temperature profiles of the idealised recuperator with *infinite* thermal size ($U_m A \to \infty$) for different heat capacity rate ratios ($\dot{C}^* = \dot{C}_h / \dot{C}_c$).

Balanced Recuperator (C^*=1)
(reversible)
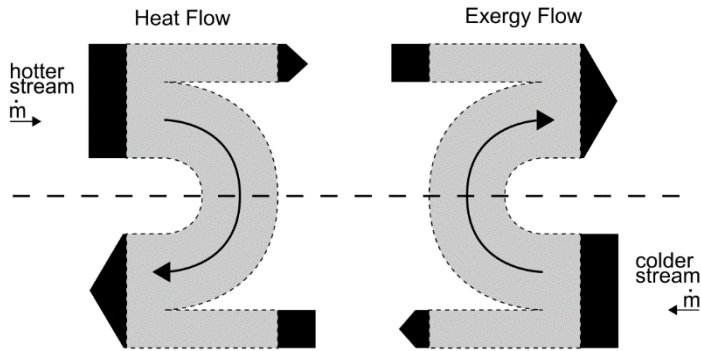
Unbalanced Recuperator ($C^* \neq 1$)
(irreversible)
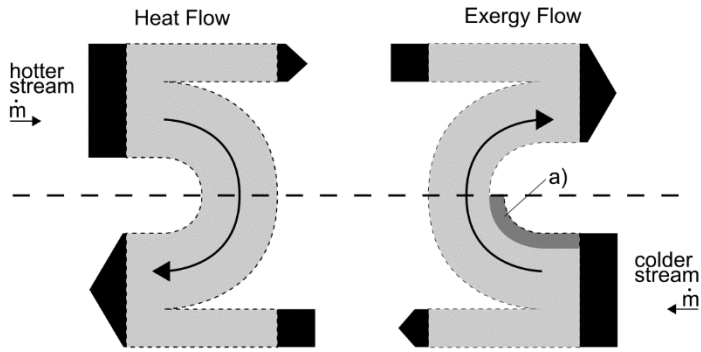
Figure 3.7. Qualitative heat and exergy flow on recuperators with *infinite* thermal size ($U_m \cdot A \to \infty$). The balanced recuperator is reversible, since no exergy is destroyed due to a local temperature difference approaching zero ($\delta T \to 0$). In contrast, exergy is destroyed (a) in the unbalanced recuperator.

Shah and Sekulić [25] refer to the definition of Eq. (3.35) as the "traditional meaning" of the heat exchanger effectiveness ε. It requires the concept of an idealised heat exchanger invoking the first law of thermodynamics explicitly and the second law of thermodynamics implicitly. In contrast, they refer to the following definition as the "true meaning" of effectiveness ε:

$$\varepsilon \equiv \begin{cases} \dfrac{T_{c,\text{OUT}} - T_{c,\text{IN}}}{T_{h,\text{IN}} - T_{c,\text{IN}}} \leq 1 & \text{for } \dot{C}^* \geq 1 \\[3mm] \dfrac{T_{h,\text{IN}} - T_{h,\text{OUT}}}{T_{h,\text{IN}} - T_{c,\text{IN}}} \leq 1 & \text{for } \dot{C}^* \leq 1 \end{cases} \quad . \tag{3.37}$$

This definition, which is the one used throughout this work, was derived by Sekulić [37] and uses the first law of thermodynamics only; without involving a priori more advanced thermodynamic concepts.

3.3.2 Number of Transfer Units (NTU)

The Number of Transfer Units (NTU), also referred to as the *nondimensional thermal size*, is defined as the ratio of the thermal conductance $(U \cdot A)$ to the smaller heat capacity rate between both streams $(\dot{C}_{\min} = \mathrm{MIN}[\dot{C}_h, \dot{C}_c])$:

$$\mathrm{NTU} \equiv \int_A \frac{U}{\dot{C}_{\min}} \cdot dA \quad . \tag{3.38}$$

Consequently, NTU can be interpreted as the relative magnitude of heat transfer rate to the rate of enthalpy change of the smaller heat capacity rate fluid. The physical size of a heat exchanger is not necessarily indicated by its NTU, but rather designated by its heat transfer surface area A. However, when comparing heat exchangers for a specific application, the relationship $U/C_{\min}$ can remain approximately constant, resulting in a direct relationship between NTU and physical size. [25]

As indicated in Eq. (3.20), the overall heat transfer coefficient U is an intricate function of stream and wall properties, as well as the exchangers geometry. Since NTU is a function of U, its value is also dependent on those parameters. For the constant mass flow of an ideal gas with constant heat capacity, however, the NTU definition can be simplified to

$$\mathrm{NTU} = \frac{U_m \cdot A}{\dot{C}_{\min}} \quad . \tag{3.39}$$

Shah and Sekulić [25] show that, based on Eq. (3.39), the functional relationship between effectiveness ε and NTU for a counterflow heat exchanger is as follows

$$\varepsilon = \frac{1 - \exp\left[-\mathrm{NTU}\left(1 - \frac{\dot{C}_{\min}}{\dot{C}_{\max}}\right)\right]}{1 - \frac{\dot{C}_{\min}}{\dot{C}_{\max}} \cdot \exp\left[-\mathrm{NTU}\left(1 - \frac{\dot{C}_{\min}}{\dot{C}_{\max}}\right)\right]} \quad , \tag{3.40}$$

where $\dot{C}_{\min}$ and $\dot{C}_{\max}$ are the smaller and larger heat capacity rates between both streams. The relationship has two limiting cases of special interest. First, the case of an evaporator or a condenser $(\dot{C}_{\min}/\dot{C}_{\max} \to 0)$ resulting in

$$\varepsilon = 1 - \exp[-\mathrm{NTU}] \quad , \tag{3.41}$$

and secondly, the case of a balanced recuperator $(\dot{C}_{\min}/\dot{C}_{\max} = 1)$ resulting in

$$\varepsilon = \frac{\mathrm{NTU}}{1 + \mathrm{NTU}} \quad . \tag{3.42}$$

The ε-NTU relationship of Eq. (3.40) is illustrated in Figure 3.8. For a specific heat capacity rate ratio $(\dot{C}_{\min}/\dot{C}_{\max})$, the effectiveness ε increases monotonically and at a diminishing rate with increasing values of NTU. For a specific NTU value, the effectiveness ε increases with decreasing values of $\dot{C}_{\min}/\dot{C}_{\max}$. For any heat capacity rate ratio, the effectiveness ε asymptotically approaches unity as NTU increases towards infinity.
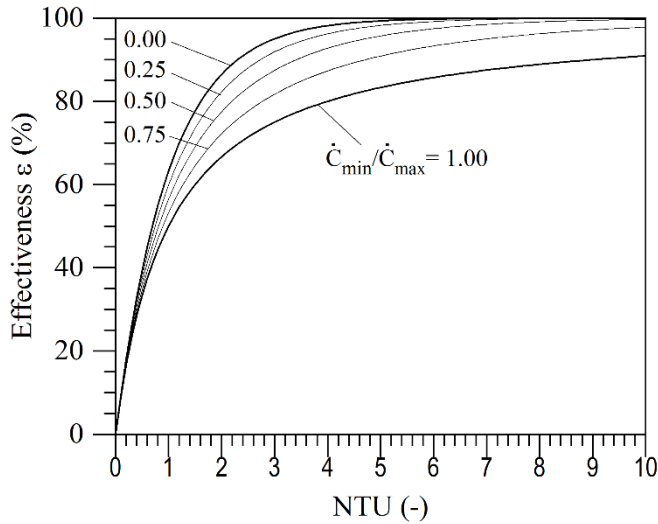
Figure 3.8. Recuperator effectiveness ε as a function of the Number of Transfer Units (NTU) for different heat capacity rate ratios ($\dot{C}_{min}/\dot{C}_{max}$). The relationship, based on Eq. (3.40), is valid for the constant mass flow of an ideal gas with constant heat capacity. (c.f. [25])

3.3.3 Exergetic efficiency ζ

The concept of efficiency quantifies the performance of a real system with respect to an ideal one. The term is generally restricted to the conversion between two types of energy, or the comparison from the energy point of view, between the performance of an actual system and an ideal system [25].

Exergetic efficiency ζ can be defined in many different ways and is also referred to as the second law efficiency, exergy efficiency or thermodynamic figure of merit. In this work, and based on Eq. (2.24), the exergetic efficiency ζ of a cryogenic recuperator is calculated as

$$\zeta = \frac{\dot{m}_h\left(e_{h,\text{OUT}} - e_{h,\text{IN}}\right)}{\dot{m}_c\left(e_{c,\text{IN}} - e_{c,\text{OUT}}\right)} \leq 1 \quad , \tag{3.43}$$

since the recuperators purpose is to increase the exergy rate of the hotter stream at the expense of the decrease in exergy of the colder stream.

Two heat exchangers with different exergetic efficiencies ζ could have the same effectiveness ε, because each term describes a different kind of thermal performance. Exergetic efficiency ζ refers to the performance of the heat exchange process itself with respect to a *reversible* reference. In contrast, effectiveness ε relates to the capability of performing a heat exchange duty $\dot{Q}$ with respect to a reference with infinite thermal size $U_m \cdot A$, regardless of whether this reference is *reversible or not*. In other words, exergetic efficiency ζ always relates to a *reversible* reference, while effectiveness ε does not. Figure 3.9 shows an example of two different heat exchangers (HX.a, HX.b) with identical heat exchange duty $\dot{Q}$ and inlet temperatures ($T_{h,\text{IN}}, T_{c,\text{IN}}$), but with distinct heat capacity rate ratios ($C^*_{\text{HXa}}=1$, $C^*_{\text{HXb}}=2$). The identical inlet temperatures and heat exchange duty result in the same outlet temperature $T_{c,\text{OUT}}$ on the colder stream, leading to equal values of effectiveness ε. In contrast, different heat capacity rate ratios require distinct thermal sizes $U_m \cdot A$ for the same heat exchange duty, leading to distinct temperature profiles, and therefore, to different values of exergetic efficiency ζ.

Since Eq. (2.12) stated that $\dot{E}=\eta_C\cdot\dot{Q}$, the areas spanned by the curves in the η_C-$\dot{Q}$ diagram correspond to the amount of exchanged exergy $(\dot{E}_h, \dot{E}_c)$ by the respective streams. Consequently, the area spanned between the curves of the hotter and the colder stream (dashed area) gives the amount of destroyed exergy $\dot{E}_d$ in the recuperator. [25], [38]
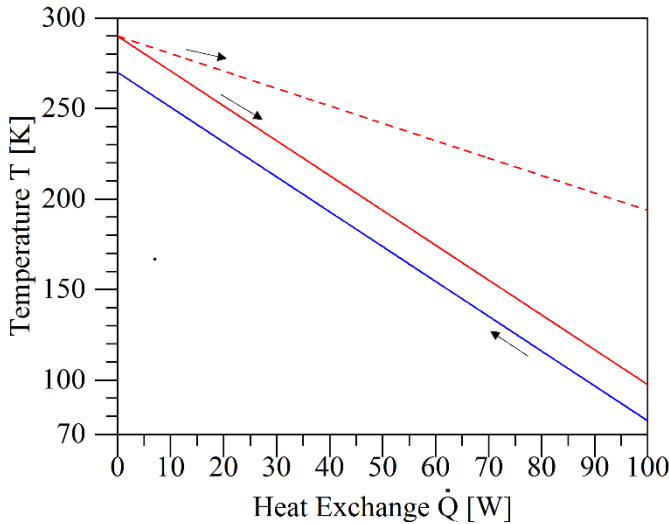
	HX.a	HX.b
Hotter Stream	——	- - -
Colder Stream	——	——
$\dot{E}_c - \dot{E}_h = \dot{E}_d$	/////	\\\\\
$\dot{E}_d$ [W]	24.1	63.7
$\dot{m}_h$ [g/s]	0.1	0.2
$\dot{m}_c$ [g/s]	0.1	0.1
T_h [K]	290-97.4	290-193.7
T_c [K]	270-77.5	270-77.5
C^* [-]	1.00	2.00
δT_m [K]	20.0	54.6
$U_m \cdot A$ [W/K]	5.0	1.8
$\dot{Q}$ [W]	100	100
ε [%]	90.59	90.59
NTU [-]	9.64	3.5
ζ [%]	73.27	25.35
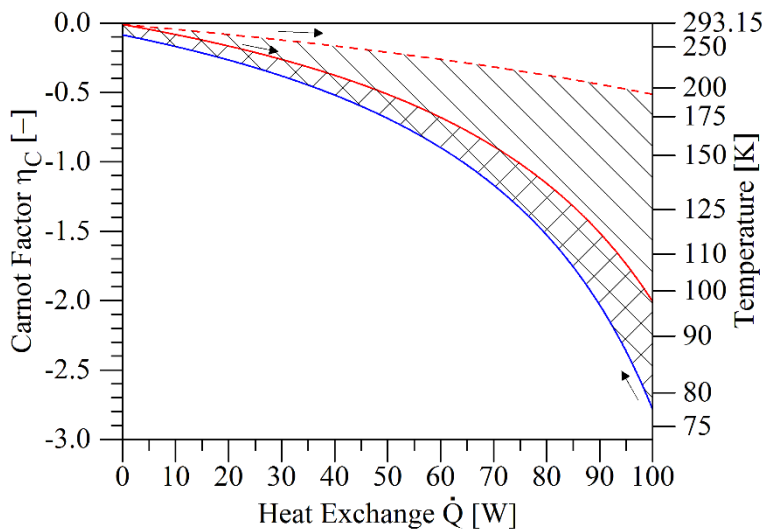
Figure 3.9. Comparison of two recuperators (HX.a, HX.b) with helium at a constant pressure of 130 kPa. Although both recuperators have identical heat exchange duty $\dot{Q}$ and effectiveness ε, their thermal size $U_m \cdot A$ and exergetic efficiency ζ are considerably different.

3.3.4 Heat and exergy flow

The heat and exergy flow of idealised recuperators with *finite* thermal size $(U_m A)$ is illustrated in Figure 3.10. The idealisation is analogous to the one used in Eq. (3.35) for the "infinitely large recuperator". For comparison, a dashed line indicates the flow in a recuperator with infinite thermal size (with the same inlet flow conditions). The darker flow paths relate to the process irreversibility (destroyed exergy $\dot{E}_d$). The respective longitudinal temperature profiles are

compared in Figure 3.11. Based on both illustrations, the following features are highlighted when comparing the *finite* recuperator to its *infinite* counterpart:

- Less heat and exergy is exchanged between both streams.
- The local temperature difference $\delta T(\xi)$ is always higher, and therefore, the mean temperature difference δT_m is also higher.
- Since less heat is exchanged, each stream experiences a lower temperature change per normalised unit of length $dT_j/d\xi$. Therefore, the temperature profile of the hotter stream $dT_h/d\xi$ is higher and the temperature profile of the colder stream $dT_c/d\xi$ is lower.
- Since less heat is exchanged, the total temperature change between inlet and outlet $\left(\Delta T_j = \left|T_{j,\text{OUT}} - T_{j,\text{IN}}\right|\right)$ is lower for each stream.
- The higher local temperature difference $\delta T(\xi)$ leads to a larger amount of destroyed exergy per unit of exchanged heat $d\dot{E}_d = \left(\eta_{\text{C,h}} - \eta_{\text{C,c}}\right) \cdot d\dot{Q}$.
- The colder stream absorbs less heat, leaving with a lower enthalpic flow rate $\dot{H}_c$. Accordingly, the colder stream rejects less exergy, leaving with a higher exergetic flow rate $\dot{E}_c$. For that reason, the colder stream leaves at a lower temperature $T_{c,\text{OUT}}$.
- The hotter stream rejects less heat, leaving with a higher enthalpic flow rate $\dot{H}_h$. Accordingly, the hotter stream absorbs less exergy, leaving with a lower exergetic flow rate $\dot{E}_h$. For that reason, the hotter stream leaves at a higher temperature $T_{h,\text{OUT}}$.
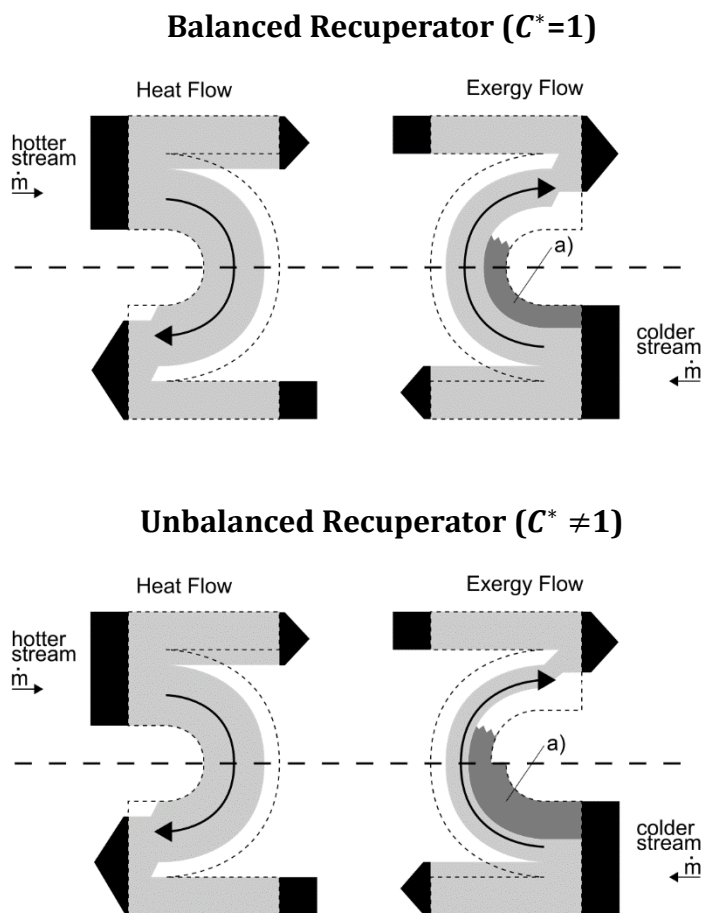
Figure 3.10. Qualitative heat and exergy flow on recuperators with *finite* thermal size $(U_m \cdot A)$. The dashed line indicates the flow for an *infinite* thermal size (Figure 3.7) and the darker path (a) corresponds to the destroyed exergy $\dot{E}_d$.
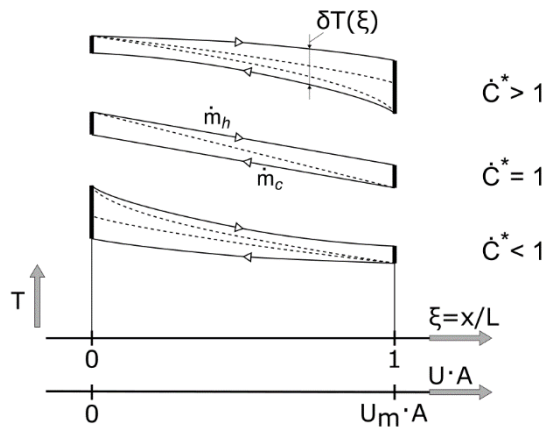
Figure 3.11. Comparison of longitudinal temperature profiles between recuperators with *finite* (solid line) and *infinite* (dashed line) thermal size ($U_m \cdot A$) for different heat capacity rate ratios ($\dot{C}^* = \dot{C}_h / \dot{C}_c$).

3.4 Thermo-hydraulic losses

3.4.1 Parasitic heat (heat-in-leaks)

The three basic heat transfer mechanisms responsible for the parasitic heat power coming from the surroundings $\dot{Q}_{\text{surr}}$ are conduction, radiation and convection.

The parasitic heat power due to conduction comes typically through the mechanical suspension of the heat exchanger. It can be calculated as

$$\dot{Q}_{\text{surr,conduction}} = \lambda[T] \cdot A \cdot \frac{dT}{dx} \ , \tag{3.44}$$

where $\lambda[T]$ is the temperature dependent heat conduction coefficient of the conducting material, A is its cross-sectional area, and dT/dx is the temperature gradient in direction of increasing conduction length x. [39]

Heat transmitted via convection can be drastically reduced by enclosing the cold components in a vacuum environment. However, since a real insulating vacuum is not perfect, small amounts of heat can be still transmitted by the residual gas within the vacuum. Nonetheless, this work assumes this heat source to be negligible as long as the residual gas pressure is lower than 10^{-7} mbar [40], which shall be then required by design:

$$\dot{Q}_{\text{surr,convection}} \approx 0 \quad . \tag{3.45}$$

Thermal radiation is exchanged between bodies even when they are separated by an absolute vacuum. The net amount of heat power transmitted between two bodies at different temperatures ($T_2 > T_1$) is calculated with

$$\dot{Q}_{\text{surr,radiation}} = \frac{\sigma_b \cdot A_1 \cdot (T_2{}^4 - T_1{}^4)}{\frac{1}{\varepsilon_1} + \frac{A_1}{A_2}\left(\frac{1}{\varepsilon_2} - 1\right)} \ , \tag{3.46}$$

where A_1 and A_2 are the surfaces exchanging radiation, ε_1 and ε_2 are their corresponding emissivity values, and σ_b is Boltzmann´s constant [39]. Based on NIST [24], the value of Boltzmann´s constant is

$$\sigma_b = 1.380\,649 \cdot 10^{-23} \text{ J/K} \; . \tag{3.47}$$

3.4.2 Longitudinal heat conduction

The temperature gradient along the heat exchanger (from the hotter to the colder side) results in heat being conducted by the heat-exchanger body and by the fluid itself. This longitudinal heat conduction can become very significant for heat exchangers with high effectiveness requirements, because it has the general effect of flattening the temperature distribution diminishing the heat exchangers effectiveness ε. The significance of this effect grows with the increase of heat exchange performance (i.e. Figure 3.12). In other words, the negative impact of longitudinal heat conduction in the heat exchangers effectiveness is higher with increasing performance. [25], [41]

The heat conducted axially (dx) by the fluid becomes of secondary importance when the heat transported to the fluid (enthalpy change $d\dot{H}/dx$) is far greater. The ratio of transported to conducted heat is expressed by the Péclet number Pe, which for fluids is equivalent to the product of the Reynolds and the Prandtl number [25]:

$$Pe = \frac{\text{"transported heat"}}{\text{"conducted heat"}} = Re \cdot Pr \; . \tag{3.48}$$

The effects of fluid heat-conduction become of secondary importance for $Pe > 10$ [25]. This is the case in this work, as later shown by chapter 6.1 ($Pr > 0.6$, $Re \gg 20$).

The heat conducted along the heat-exchanger wall $\dot{Q}_{\text{long}}$ can be estimated using the following equation

$$\dot{Q}_{\text{long}} = A_{\text{cross}}/L \cdot \int_{T_1}^{T_2} \lambda_{\text{wall}}[T] \cdot dT = A_{\text{cross}}/L \cdot \Theta_{T_1 \to T_2} \quad , \tag{3.49}$$

where $\lambda_{\text{wall}}[T]$ is the heat conduction coefficient of the conducting wall material, A_{cross} is its cross-sectional area, L is the longitudinal conduction length and Θ is the thermal conductivity integral [40]. To estimate whether longitudinal wall conduction is of concern, the dimensionless longitudinal conduction parameter Λ is used

$$\Lambda = \frac{\lambda_{\text{wall}} \cdot A_{\text{cross}}}{L \cdot \dot{C}_{\text{min}}} \; , \tag{3.50}$$

where $\dot{C}_{\text{min}}$ is the smaller heat capacity rate $\dot{C}$ between both fluid streams ([25], [39], [43], [44]).

As illustrated in Figure 3.12, the longitudinal wall conduction limits the highest possible effectiveness a heat exchanger could achieve. This is the case even if it would present otherwise idealised conditions, such as an infinite thermal size. This limit is expressed in the following equation for a balanced ($\dot{C}^* = 1$) counterflow heat exchanger [25]:

$$\varepsilon \leq 1 - \frac{\Lambda}{1 + 2\Lambda} \; , \tag{3.51}$$
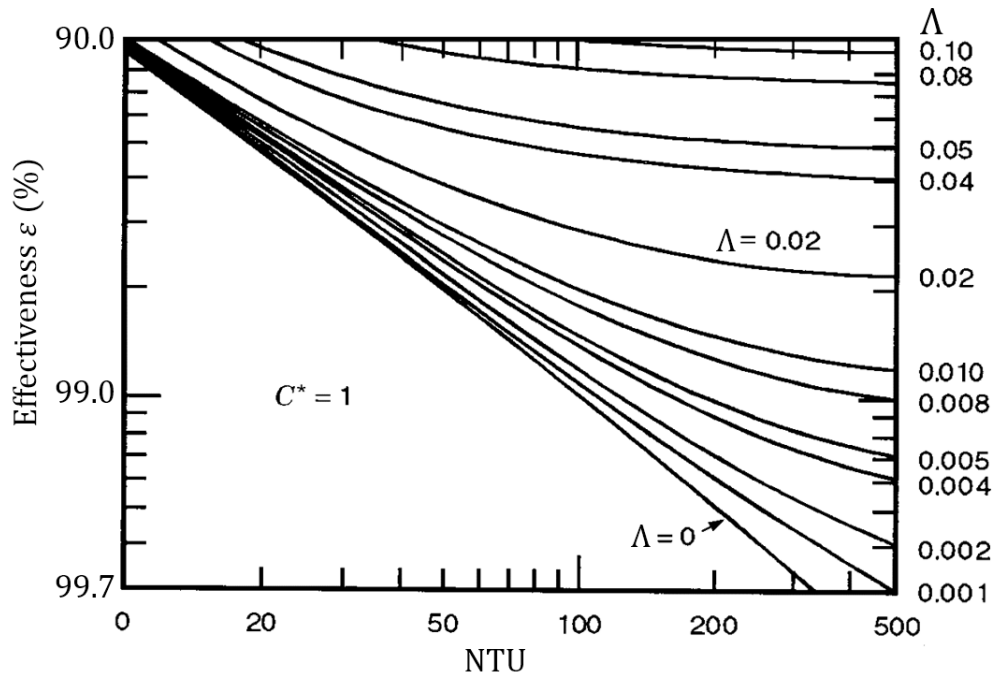
Figure 3.12. Relationship between effectiveness ε, thermal performance (in NTU) and dimensionless longitudinal conduction parameter Λ for a balanced ($\dot{C}^* = 1$) recuperator. Note the reverse order of the left ordinate scale. (c.f. [25], [44])

Based on the previous equation, Figure 3.13 shows the highest possible effectiveness ε as a function of the dimensionless longitudinal conduction parameter Λ. An effectiveness as high as 99 % is theoretically possible if the conduction parameter Λ is maintained at a value lower than 0.01.
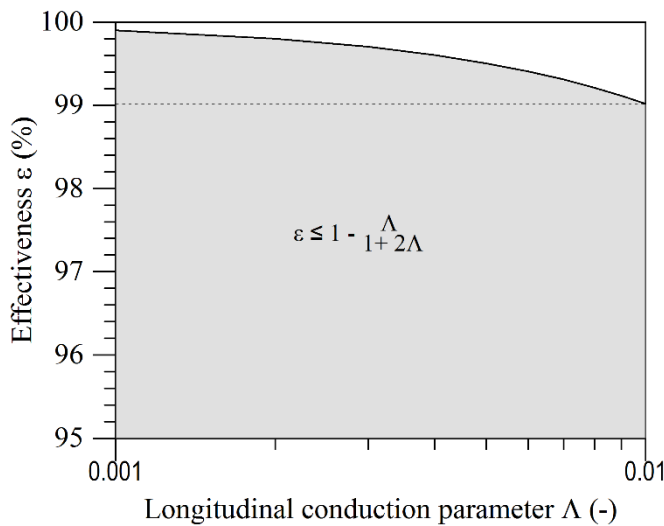
Figure 3.13. Highest possible recuperator effectiveness ε as a function of the longitudinal conduction parameter Λ for a balanced recuperator ($C^* = 1$).

3.4.3 Frictional pressure loss

The frictional pressure loss Δp_f experienced by a fluid inside a pipe can be estimated using the phenomenological equation known as the *Darcy-Weisbach equation*

$$\Delta p_f = \xi \cdot \frac{L}{D_h} \cdot \frac{\rho \cdot v_m^2}{2} \quad , \tag{3.52}$$

where ξ is the (Darcy-Weisbach) flow friction factor and $v_m = \dot{V}/A$ is the mean fluid velocity [45]. The equation predicts losses due to fluid friction on the pipe wall and fluid viscosity, without including losses at inlets, elbows or other fittings. When mass flow $\dot{m}$ and pipe cross-section A are given, the following variation of Eq. (3.52) can be more convenient

$$\Delta p_f = \xi \cdot \frac{L}{A^2 \cdot D_h} \cdot \frac{\dot{m}^2}{2\rho} \quad . \tag{3.53}$$

The equations to estimate the friction factor ξ are specific for the flow regime of the fluid and the relative surface roughness of the pipe k_r, which is defined as

$$k_r \equiv \frac{k}{D_h} \quad , \tag{3.54}$$

where k is the (technical) pipe roughness [46], [47].

Before introducing the actual equations to estimate the friction factor ξ, its relationship with the Reynolds number Re (hence flow regime) and relative surface roughness k_r is described based on the so-called Colebrook-diagram in Figure 3.14.

In the laminar region (Re<2300), any flow disturbance caused by protuberances is "smoothed out" by the influence of the fluid viscosity. Consequently, the friction factor ξ is a function of the Reynolds number and is independent of the relative surface roughness k_r.

In the turbulent region ($Re \geq 4000$), the turbulent boundary layer becomes thinner with increasing Reynolds number, so that protuberances are exposed in the sequence of their sizes. At lower Reynolds numbers, the boundary layer is considered to cover all protuberances, leading to a *hydraulic-smooth* pipe. Consequently, and as described by Prandtl's relation, the friction factor ξ in this region is a function of the Reynolds number only. The opposite is true at higher Reynolds numbers, where, as described by von Karman's relation, the friction factor ξ only depends on the relative surface roughness k_r. The monotonic transition of the friction factor ξ from the hydraulic-smooth regime (Prandtl) to the hydraulic-rough regime (von Karman), is described by the Colebrook equation.

In the transition region ($2300 < Re < 4000$), this work assumes a linear and continuous development in the friction factor ξ with increasing Reynolds number Re, from the laminar into the turbulent region. This conservative assumption clearly overestimates the values obtained with the relation by Blasius, which considers a hydraulic-smooth pipe at Reynold numbers up to 10^5. [46] [47] [36]
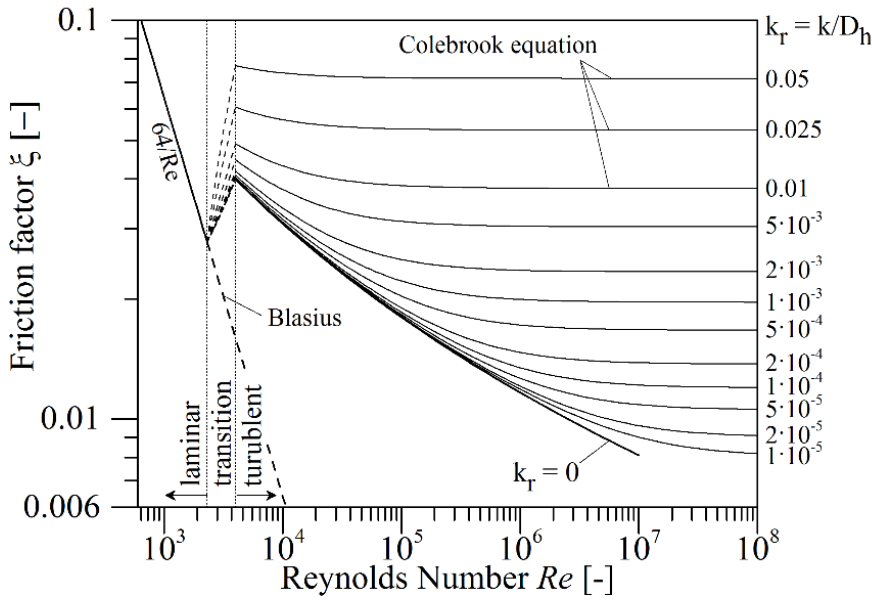
Figure 3.14. Colebrook-diagram for the friction factor ξ based on the equations introduced in this chapter.

The equations used for the estimation of the friction factor ξ are introduced in Table 3.2 and are specific for the flow regime. For the case of laminar flow ($Re \leq 2300$), the friction factor ξ_{lam} is calculated using Eq. (3.56) and is only a function of the Reynolds number Re. For a turbulent flow ($Re \geq 4000$), the friction factor ξ_{turb} is given by the Colebrook equation

$$\frac{1}{\sqrt{\xi_{\text{turb}}}} = -2 \cdot \log_{10} \left(\frac{2.51}{Re \cdot \sqrt{\xi_{\text{turb}}}} + \frac{k_r}{3.71} \right) . \tag{3.55}$$

However, this equation is implicit for an unknown friction factor ξ_{turb}, because the term is on both left and right-hand sides of the equation. Consequently, either the Colebrook equation is solved iteratively, or an explicit approximation is used instead. Due to its relative simplicity and high accuracy, this work uses the approximation in Eq. (3.58) as proposed by Buzzelli [48] for the range of $4000 \leq Re \leq 10^7$. Brkić [47] reviewed and compared over 20 explicit approximations available in the literature, and showed that Buzzelli's approximation has an estimated error of approximation lower than 0.14 % when compared with the implicit Colebrook equation, making it one of the most accurate approximations in the study*. For the transition zone ($2300 < Re < 4000$), Eq. (3.57) employs an intermittency factor γ to express the linear and continuous development of the friction-factor value; an approach analogous to Eq. (3.17) for the Nusselt number Nu. As shown in Figure 3.14, this assumption results in higher values than the Blasius relation ($0.316 \, Re^{-0.25}$), which considers a hydraulic-smooth pipe. [46]

---

* Estimated error of approximation for a parameter range of $10^{-6} \leq k_r \leq 10^{-1}$ and $10^4 \leq Re \leq 10^8$. [47]

Table 3.2. Employed equations for the calculation of the (Darcy-Weisbach) flow friction factor ξ. [36], [48]

Flow Regime	Equation	Eq.
Laminar flow: ($Re \leq 2300$)	$\xi_{\mathrm{lam}} = 64/Re$	(3.56)
Transition zone: ($2300 < Re < 4 \cdot 10^3$)	$\xi_{\mathrm{tran}} = (1-\gamma)\ Re\big|_{Re=2300} + \gamma \cdot Re\big|_{Re=4000}$ with $\gamma = \frac{Re-2300}{4000-2300}$ and $0 \leq \gamma \leq 1$	(3.57)
Turbulent flow: ($4 \cdot 10^3 \leq Re \leq 10^7$)	$\xi_{\mathrm{turb}} \approx \left(A - \frac{A+2\cdot\log_{10}(B/Re)}{1+(2.18/B)} \right)^{-2}$ where A and B are the functions: $A = \begin{cases} 0.774 \cdot \ln(Re) - 1.41 & \text{for } k_r = 0 \\ -2 \cdot \log\left(k_r/3.7 + 1.9 \cdot \frac{-2\cdot\log_{10}(k_r/3.7)}{Re}\right) & \text{for } 0 < k_r \leq 0.5 \end{cases}$ $B = (k_r \cdot Re/3.7) + 2.51 \cdot A$	(3.58)

k_r: Relative surface roughness of the pipe [-]; Re: Reynolds number [-]; γ: intermittency factor [-].

3.5   Construction types

Recuperators used to transfer heat between two fluids can have a variety of shapes, arrangements and other features. Figure 3.15 introduces a non-exhaustive list of heat exchangers categorised by their construction type. The three major subcategories are tubular, plate-type and extended surface, which differ in the type of components that constitute the bulk body of the heat exchanger.
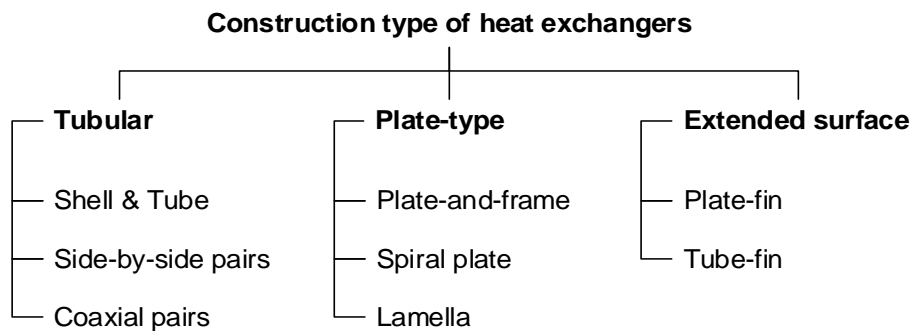
Figure 3.15. Classification of heat exchangers based on their construction type. (c.f. [25])

Tubular heat exchangers (Figure 3.16) are commonly built of circular tubes, although any other cross-sectional geometry can be used. The tubes can be arranged and bent in a variety of different ways. A bundle of parallel tubes can be used to split each stream and increase the heat exchange area across the tube walls. Shell-and-tube heat exchangers (a) consist of tubes routed through a shell, where one stream flows inside the tubes and the other stream passes outside of the tubes but inside of the shell. Other tubular heat exchangers consist of tubes that are arranged in pairs, either side-by-side or coaxially. In the side-by-side arrangement (b), each stream flows through one of the tubes, which are typically brazed together to provide mechanical stability and to reduce the thermal resistance between both streams. The heat is

transferred across the wall of both tubes and the filler material used for brazing. In the coaxial arrangement (c), one stream flows through the inner tube and the other stream flows through the annulus formed by the inner and outer tube. A spacer is often placed between both tubes to hold the inner tube in position and ensure a concentric arrangement. Coaxial heat exchangers are well known for their thermal simplicity since the heat is transferred across the wall of the inner tube only.

a) Shell-and-tube   **b) Side-by-side pairs**   **c) Coaxial pairs**
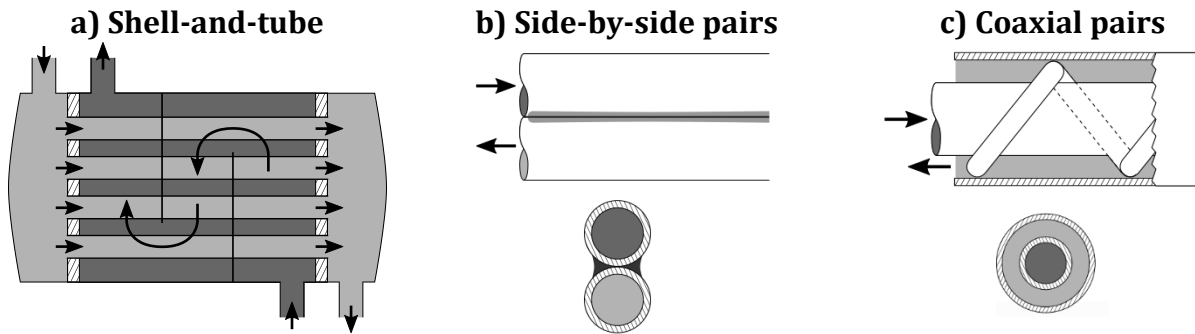
Figure 3.16. Schematics of tubular heat exchangers. (c.f. [25])

Plate-type heat exchangers (Figure 3.17) are built of thin plates that form flow channels and have a relatively large heat transfer area. The plates can have a smooth or a corrugated surface according to the desired level of turbulence. Plate-and-frame heat exchangers (a) consist of flat plates stacked together. In spiral plate heat exchangers (b), the plates are wound around an axis in order to achieve a more compact design. Lamella heat exchangers (c) are made of metal strips welded together to form narrow flow channels (lamellas). In all three cases, the heat is transferred across the plate walls.

a) Plate-and-frame   **b) Spiral plate**   **c) Lamella**
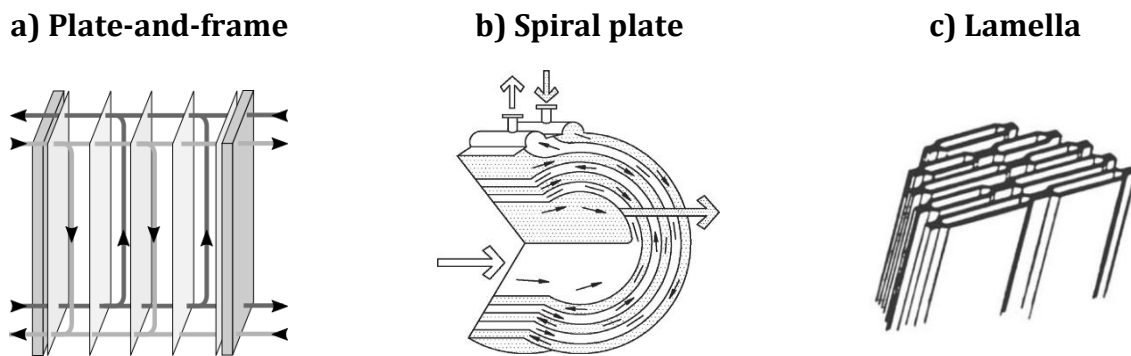
Figure 3.17. Schematics of plate-type heat exchangers. [25], [50]

Extended surface heat exchangers are built of tubes or plates that have additional appendages called *fins* in order to increase the heat transfer area. Fins do not separate the streams, but may form flow passages that merge and divide each of them. Fins can also be used to provide structural strength. Figure 3.18 illustrates the use of plate-fins (a) and tube-fins (b) in heat exchangers.

a) Plate-fins   **b) Tube-fins**
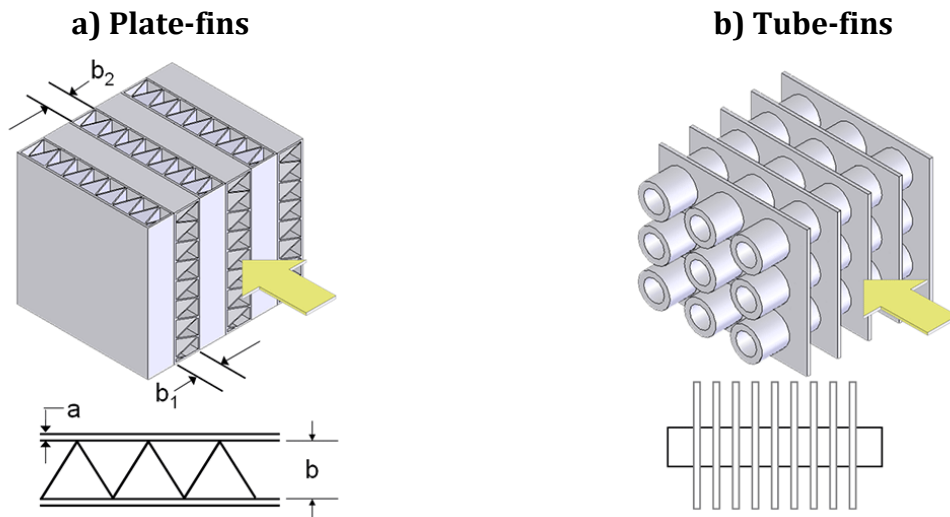
Figure 3.18. Use of fins in heat exchangers. [25], [49]

4 AMIT's compact superconducting cyclotron

This chapter presents the compact superconducting cyclotron that has been developed in the framework of the AMIT project to produce single-doses of radiopharmaceutical substances in a hospital environment. The cryogenic system (Figure 4.1) is divided into three parts: The *client* (c, d) to be cooled, the *cryogenic refrigerator* (a) providing the cooling power, and the *transfer line* (b) connecting both systems. The novel cryogenic refrigerator (a) is the main focus of this work.

First, the principle of particle acceleration is introduced in the following subchapter. Then, the conceptual design of the cryogenic system is described in more detail by showing technical models, providing flow schemes, and listing design requirements.
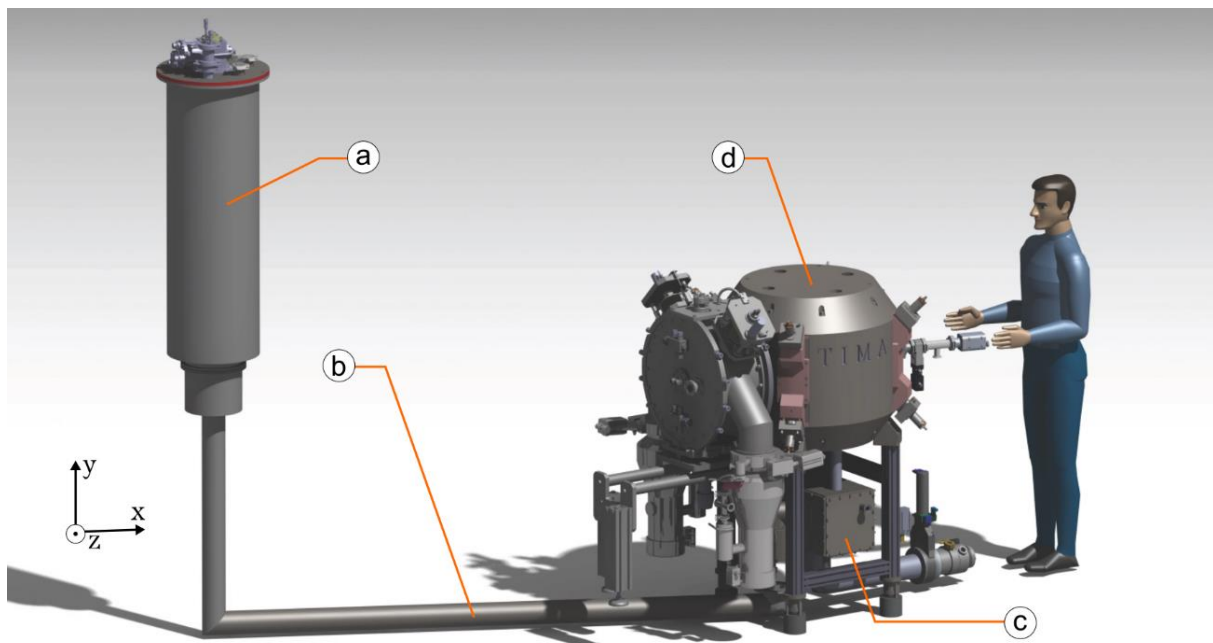
Figure 4.1. Technical model of AMITs compact superconducting cyclotron including cryogenic system. [51]
a) cryogenic refrigerator; b) cryogenic transfer line; c) interconnection box; d) cyclotron assembly.

4.1 Particle acceleration

The cyclotron is designed to accelerate hydrogen anions (^{1}H$^-$) at a current of 10 μA to a final energy of 8.5 MeV. Its working principle is illustrated in Figure 4.2. The particles are generated at the ion source (a) and then accelerated through an accelerating gap (b). This gap is the space between the two electrodes (c) called "dees" - due to their "D" shape - which are connected to a radio frequency alternating voltage generating an acceleration voltage of 60 kV at the accelerating gap (b). The particles are kept in a circular path (e) due to the Lorentz force F_L resulting from the charged particles (q = −1) moving with a velocity v in the presence of the magnetic field B (d):

$$\vec{F}_L = q \cdot \left(\vec{v} \times \vec{B} \right) . \tag{4.1}$$

A Helmholtz coil comprised of two superconducting solenoid electromagnets (f), aligned on the same vertical axis, generates a nearly uniform magnetic (d) field B of 4 T. The superconducting material used for the electromagnets is Niobium-Titanium (NbTi) and both magnets are operated with a current of 120 A at 4.5 K. The polarity of the dees (c) is inverted each time the particles return to the acceleration gap (b), accelerating the particles and increasing the radius of the particle path (e). The dees (c), the ion source (a), and the accelerating path (e) are all inside an acceleration chamber (g), which provides the required vacuum environment.
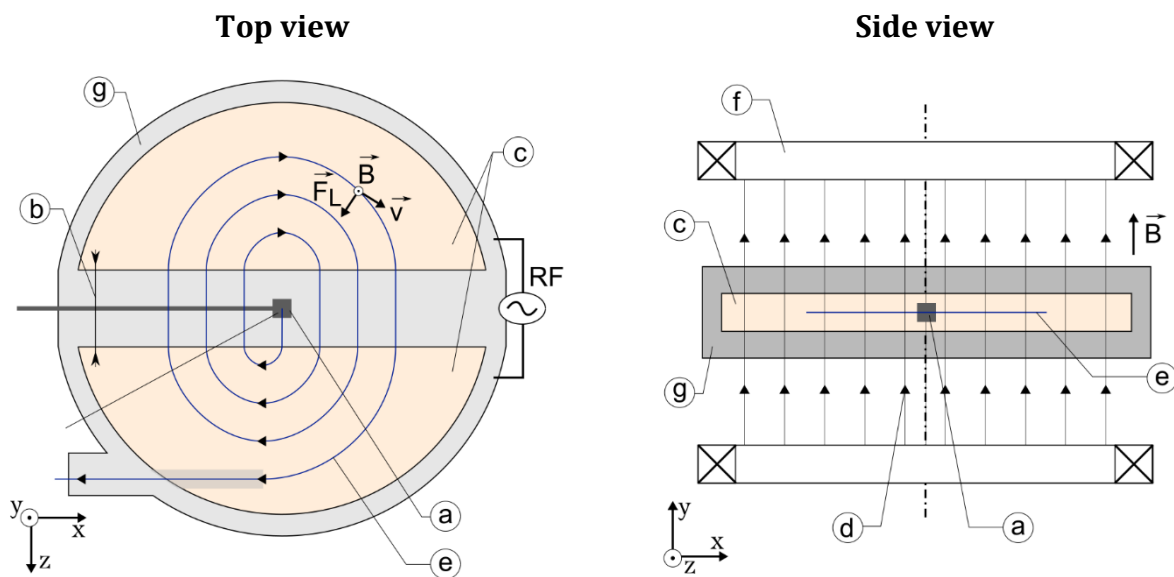
Figure 4.2. Principle of particle acceleration using a cyclotron (based on [52])
a) ion source; b) accelerating gap; c) dees (electrodes); d) magnetic field; e) particle path; f) superconducting electromagnets; g) acceleration chamber.

Figure 4.3 shows a horizontal and a vertical cross section of the cyclotron assembly. The particle acceleration takes place inside the acceleration chamber (g), which contains the ion source (d), the dees (c), and the RF resonator (b). The two superconducting magnets (f) at 4.5 K are inside a common cryostat (e) outside of the acceleration chamber (g). The magnetic iron yoke (a) is placed at room temperature around the magnets cryostat (e), considerably reducing

the amount of mass to be refrigerated. A lead shield is placed around the cyclotron assembly for radiation protection.

Horizontal Cross Section   **Vertical Cross Section**
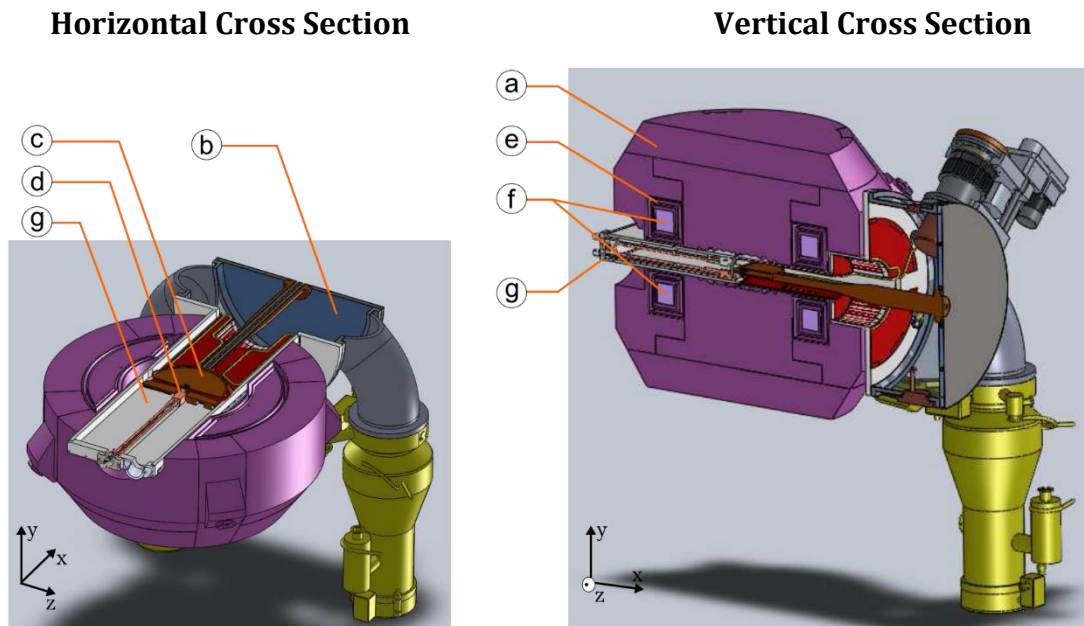
Figure 4.3. Cross-sectional views of the technical model of the cyclotron assembly. [53]
a) iron yoke; b) radio frequency resonator; c) dee; d) ion source; e) magnets cryostat; f) superconducting magnets; g) acceleration chamber.

4.2   Cryogenic system

The conceptual design of the cryogenic system considers general requirements and constraints deriving from the cyclotron system (Table 4.1). The superconducting magnets shall be refrigerated using the latent heat of 2-phase helium at 4.5 K in a closed refrigeration cycle. However, the amount of cold helium in the system shall be kept to a minimum, so that the system does not constitute a potential safety hazard to any person or equipment in the hospital environment. The refrigeration system shall be able to work uninterrupted and automatically for weeks, minimizing the presence of technical personal needed on site. The space inside the cyclotron's radiation shield is limited in order to minimize the shield's size and weight. This results in a part of the cryogenic system being placed outside of the radiation shield, facilitating the access to cryogenic components for operation and maintenance reasons, and reducing equipment and personnel exposure to ionisation radiation. Service holes are required to route the refrigeration pipes through the iron yoke. Their size shall be kept to a minimum to facilitate the realisation of uniform magnetic fields, required for the particle acceleration.

Table 4.1. General requirements and constraints of the cyclotron's cryogenic system.

Type	Description	
Requirements	I.	Magnet refrigeration temperature at 4.5 K.
	II.	Isothermal refrigeration with 2-phase fluid.
	III.	Closed refrigeration process.
	IV.	Non-stop refrigeration duty of several weeks.
	V.	No need of technical supervision during nominal operation.
Constraints (to minimize)	I.	Cold helium inventory.
	II.	Exposure of personnel and equipment to ionising radiation.
	III.	Space needed inside the cyclotrons radiation shield.
	IV.	Size and quantity of service holes through the iron yoke.

The cyclotron's cryogenic system (Figure 4.4) is divided into the *remote refrigerator* (A), located outside of the radiation shield (l), and the *client system* (B) located inside. A cryogenic transfer line (e) is used to connect both systems.

The client system (B) consists of the magnet's cryostat (k), as well as the interconnection box (i) for the magnet current leads (h) and refrigeration pipes. The remote refrigerator (A) provides two streams of cold helium, which are delivered to the client system (B) using the cryogenic transfer line (e). The colder stream (f) has two-phase helium at 4.5 K for the isothermal refrigeration of the superconducting magnets (j). The warmer stream (g) has gaseous helium at 40-50 K for the non-isothermal refrigeration of other components at the client's system, especially the current leads (h) and the thermal shield. Both streams (f, g) are part of a single helium circuit across the entire cryogenic system. A pump (a) generates the forced flow of helium through the entire circuit, ensuring its circulation without the need to rely on natural convection or the thermosiphon effect. The cold helium is generated at the remote refrigerator (A) using a two-stage cryocooler as the heat sink (b). The incoming stream is precooled by recuperators (c) and further thermalised by heat exchangers (d) attached to the cryocooler stages. The refrigeration cycle is described in more detail in chapter 5.
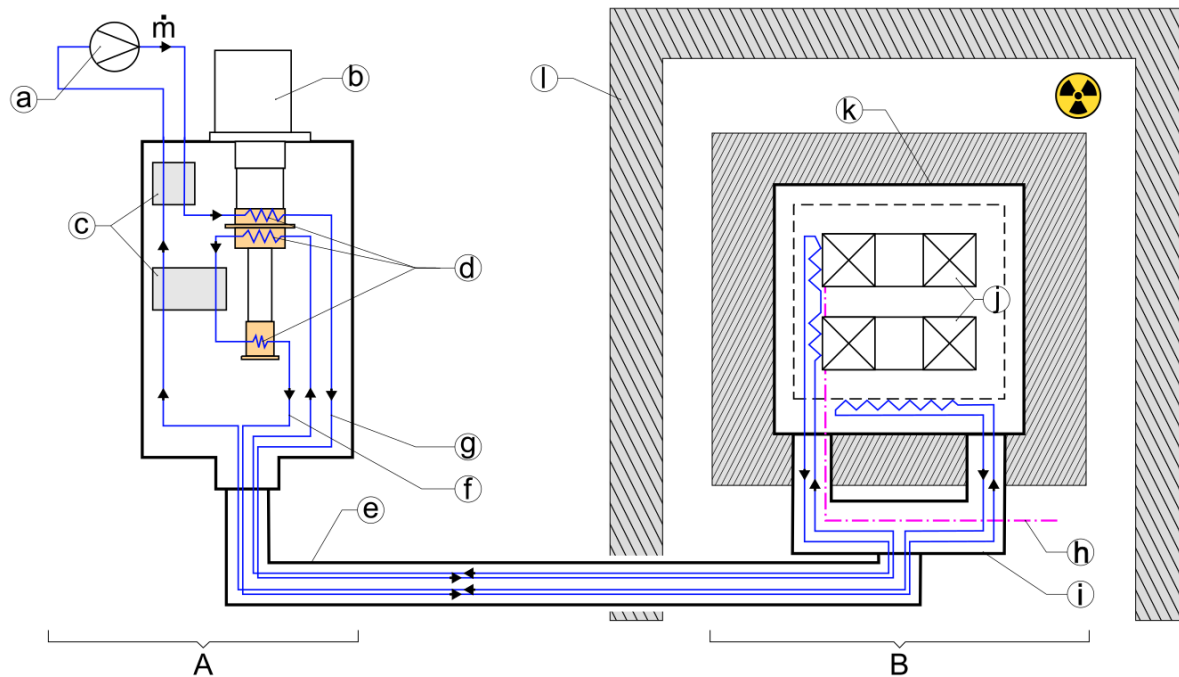
Figure 4.4. Schematics of the cyclotron's cryogenic system. The remote refrigerator (A) is placed outside of the radiation shield and generates two cold helium streams (f, g) using a room temperature circulation pump (a), a two-stage cryocooler (b) as the cold source, and various heat exchangers (c, d). The cold helium is used to refrigerate the client system (B) that is comprised of the superconducting magnets (j) inside their cryostat (k) and the magnet current leads (h) at the interconnection box (i). The helium is delivered through the radiation shield (l) using an optimised transfer line (e).

4.2.1 Client system

The cryostat containing the superconducting magnets is the main component of the client system (Figure 4.5). The magnetic interaction between both superconducting magnets (a), or between a single magnet and the iron yoke (e), can induce very high individual forces that need to be contained. For this reason, both magnets (a) are held together by a support structure (b) made of stainless steel. The structure, which also acts as a coil casing, has an aperture to allow the insertion of the cyclotrons accelerating chamber through it. The stream of two-phase helium is routed through a helical channel (i) inside the structure (b), providing isothermal refrigeration to the magnets (a). A thermal shield (c), made of copper, protects the support structure (b) from thermal radiation, and a stainless-steel vessel (d) enclosing the cold components (a-c) is used for vacuum insulation. Surrounding the cyclotron cryostat is the room-temperature iron yoke (e).

   The cold stainless steel structure (b) is supported by a set of 8 adjustable rods (f) anchored to the warm iron yoke (e). Once the system is cold, this set of support rods (f) allows the final alignment of the superconducting magnets (a) with respect to the iron yoke (e). The rods (f) are under tension, and are designed to support the system weight (~220 kg) and magnetic forces. They are made of Cryogenic Grade Glass Fiber Reinforced Polymer (GFRP-CR), due to its low thermal conductivity. Each one is split into two parts with the joint thermally attached to the thermal shield in order to reduce the heat conduction to the support structure. The two service holes (g) in the bottom of the iron yoke (e) are used to route the current leads

and the cold helium pipes coming from the interconnection box below. Due to symmetry reasons, the iron yoke (e) also has two dummy service holes (h) on the top. [51] [53] [54]

Support structure containing the superconducting magnets

Vacuum vessel of the magnets cryostat

Magnets cryostat surrounded by iron yoke
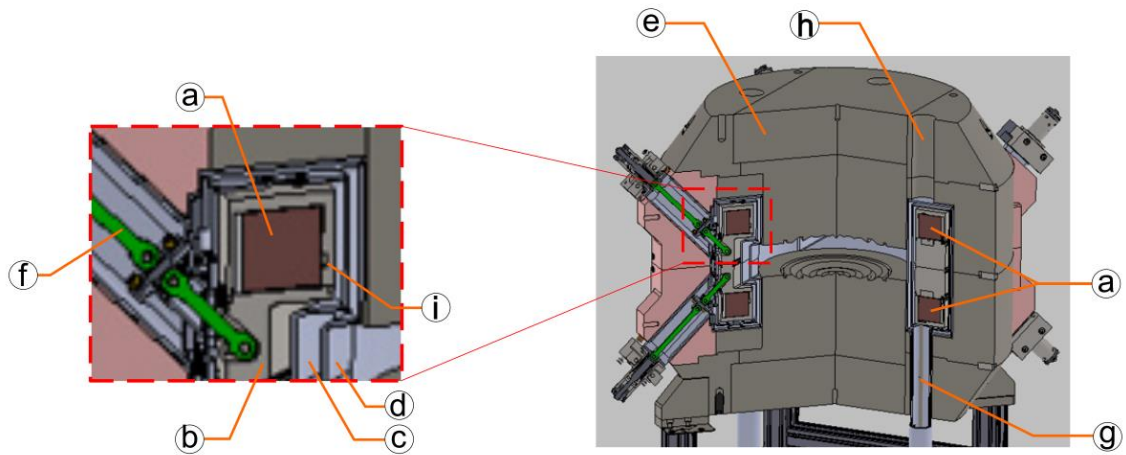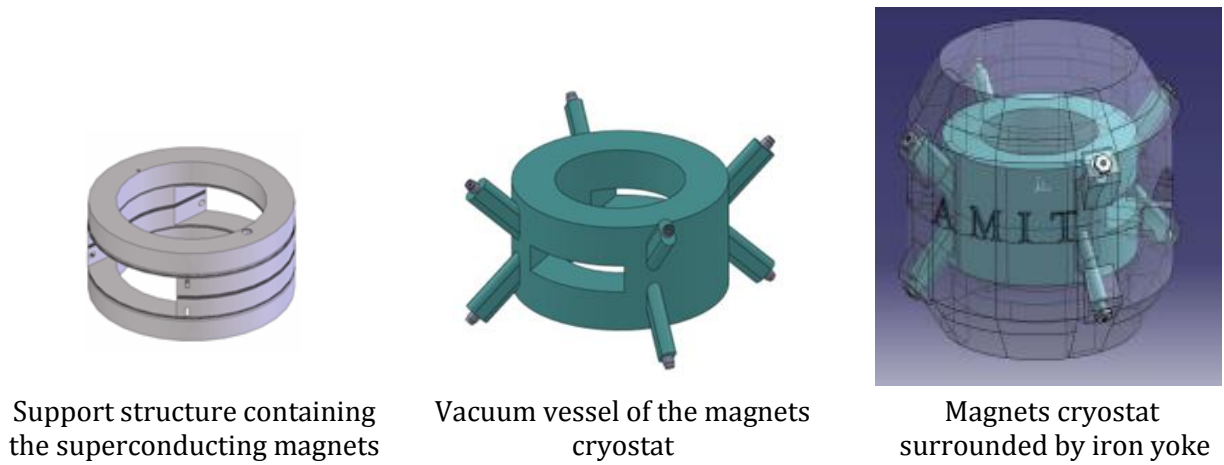
Cross-section of the magnets cryostat assembly including iron yoke

Figure 4.5. Overview of the components comprising the magnets cryostat assembly of the compact superconducting cyclotron. [53], [51]
a) superconducting magnet; b) support structure; c) thermal shield; d) vacuum vessel; e) iron yoke; f) support rod; g) service holes; h) dummy service hole; i) helical channel for two-phase stream.

The client system has two cooling circuits installed; each one for a different cold stream provided by the remote refrigerator (Figure 4.6). Circuit I is warmer and contains superheated gaseous helium for the non-isothermal refrigeration of components down to 40-50 K. Circuit II is colder, and contains two-phase helium for the isothermal refrigeration of components, especially the superconducting magnets, at 4.5 K. Each circuit is routed from the interconnection box to the magnets cryostat through a separate service hole and comprises a respective feed (g, i) and return (h, j) line.

The interconnection box (k) contains the interface for the refrigeration pipes coming from the transfer line, as well as most of the cryogenic instrumentation of the client system. The current leads are inserted at the interconnection box (e) and thermalised at two different points, where the lead material is changed accordingly to minimize heat loads. The first thermalisation point is at the feed line of Circuit I (g), and the copper current leads (l) are

changed to a high temperature superconducting (HT-SC) material (m). The second thermalisation point is at the return line of Circuit II (j), and the leads are changed to a low temperature superconducting (LT-SC) material (n). Afterwards, the LT-SC leads are inserted inside the feed line of Circuit II (i) and routed to the superconducting magnets (a).
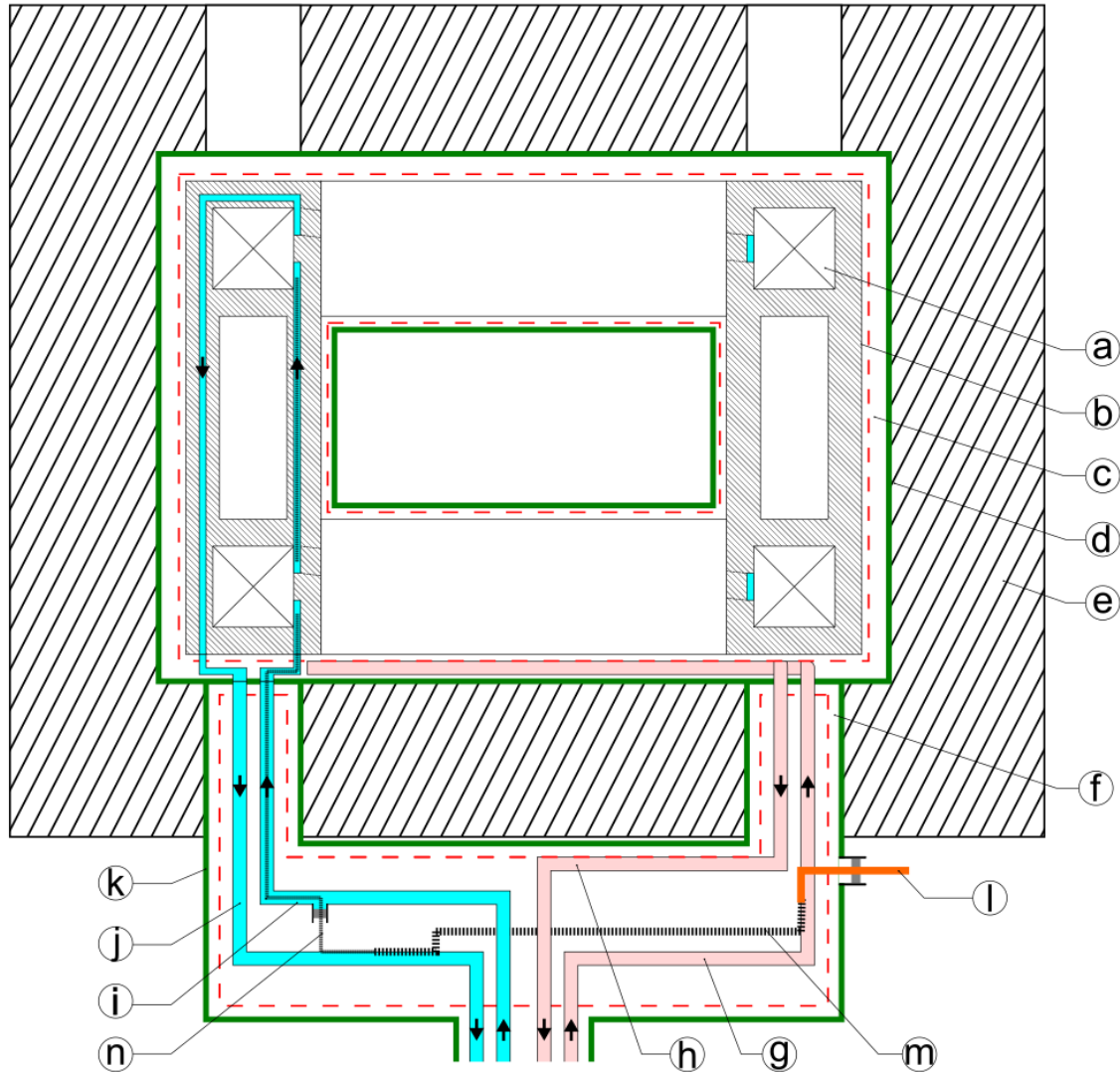
Figure 4.6. Simplified flow schematics of the client system consisting of two helium circuits at different temperatures for the isothermal refrigeration of the superconducting magnets and the thermalisation of the magnets current leads. (c.f. [51])
a) superconducting magnets; b) support structure; c) thermal shield; d) vacuum vessel; e) iron yoke; f) service holes; g) feed line Circuit I; h) return line Circuit I; i) feed line Circuit II; j) return line Circuit II; k) interconnection box; l) copper current leads; m) HT-SC current leads; n) LT-SC current leads.

The thermal budget of the different components is based on the presented configuration, with the resulting values having evolved over time (Table 4.2). In a preliminary stage, the remote refrigerator was required to provide a total cooling power of 15 W to Circuit I (≥50 K, non-isothermal) and 0.7 W to Circuit II (4.5 K, isothermal), leading to the thermal design of the remote refrigerator. Later on, first hardware tests indicated that the selected cryocooler device is able to provide a higher cooling power than anticipated by the supplier's specifications. This triggered the re-assessment of the thermal budget of the entire system in favour of simplifying

the client system design, which resulted in an increased refrigeration requirement of 21.84 W for Circuit I (≥40 K, non-isothermal) and 0.878 W for Circuit II (4.5 K, isothermal). As a consequence, the design working point of the remote refrigerator (chapter 6) differs from the nominal working conditions that derive from the overall system design (chapter 7). [55], [56]

The thermal budget is a design requirement for the client system, and dictates the lowest acceptable cooling-power to be provided by the external refrigerator. A possible deviation between the thermal budget and the actual thermal loads is not considered in this work; hence, the thermal budget is an "exact" criterion without uncertainty.

Table 4.2. Estimated cooling power required by the client system including the transfer line. Preliminary values, as used in the refrigerators design, are in parenthesis. [55], [56]

		Circuit I, Non-isothermal ≥40 K (≥50 K)	Circuit II, Isothermal 4.5 K (4.5 K)
Refrigeration temperature T_R			
Required cooling power [W]			
	Transfer Line	0.83	0.044
Client System	Interconnection Box	2.76	0.412
	Current Leads	10.60	0.032
	Cyclotron Cryostat	7.65	0.390
TOTAL		21.84 (15.00)	0.878 (0.700)

4.2.2 Transfer Line

The transfer line connects the helium circuits between the external refrigeration system and the client system. It has a thermally optimised design in order to preserve the limited cooling power provided by the refrigeration system [57].

Figure 4.7 shows the simplified arrangement of the four helium pipes (a-d) inside the larger vacuum pipe (e) of the transfer line. A thermal shield (f) and multi-layer insulation (g) are used to reduce thermal radiation loads. The two pipes corresponding to Circuit II (a, b) are inside the thermal shield (f), which is actively cooled by the return line of Circuit I (b). The two pipes of Circuit I (a, b) are routed between the thermal shield (f) and the vacuum pipe (e).
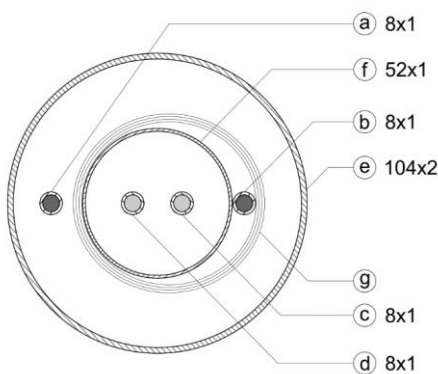
Figure 4.7. Simplified arrangement of the transfer line. Dimensions are in millimetres (pipe outer diameter; wall thickness)
a) feed line Circuit I; b) return line Circuit I; c) feed line Circuit II; d) return line Circuit II; e) vacuum pipe; f) thermal shield; g) multi-layer insulation.

The cold components of the transfer line (thermal shield and helium pipes) are held in position by thermally optimised spacers (Figure 4.8). The inner spacers (e) are used to keep the Circuit II pipes (d) in position with respect to the thermal shield (b). The outer spacers (f) support the thermal shield assembly and the feed line of Circuit I (c) to the vacuum pipe (a). No additional spacers are needed for the return line of Circuit I (c) because it is welded along the thermal shield. The spacer design foresees the relative displacement of components in the x-axis (a-d) due to thermal contraction. Consequently, all spacers are adapted in such a way that freedom of movement is given at the refrigerator side of the transfer line. The spacers are made of glass fiber reinforced polymer sheets (GFRP-CR), due to its low thermal conductivity. The rest of the components (a-d) are made of stainless steel AISI 316L, which minimises thermal stresses between joint components as they have the same thermal contraction coefficients. The transfer line has no vacuum barrier and connects the insulation vacuum of the client system with the remote refrigerator.
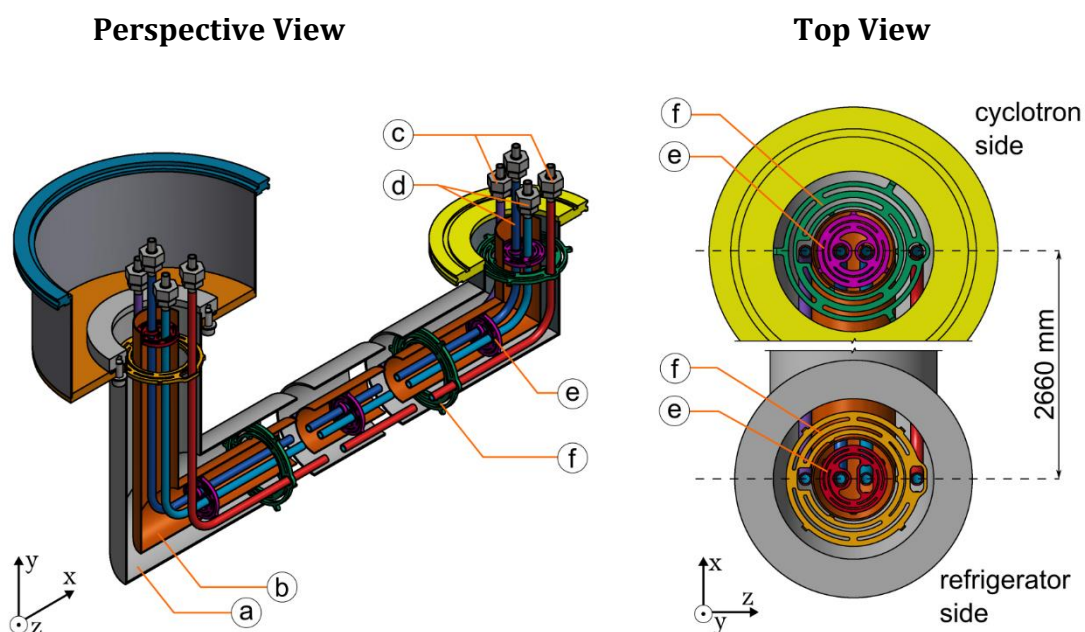
Figure 4.8. The thermally optimised spacers (e, f) hold the helium pipes (c, d) and the thermal shield (b) in position. Freedom of movement in the x-axis is given by the spacers at the refrigerator side of the transfer line.
a) vacuum pipe; b) active thermal shield; c) Circuit I pipes; d) Circuit II pipes; e) inner spacer; f) outer spacer

4.2.3 Remote refrigerator

The remote refrigerator is divided into two sub-systems (Figure 4.9). The first one is the circulation system (A), which generates the helium forced-flow using a circulation pump, (a) and is entirely at room temperature. The second one is the novel Cryo Supply System (CSS) (B), which is used to cool down the helium stream to the desired temperatures. The CSS comprises of a vacuum vessel (c) for thermal insulation, a two-stage cryocooler (b) as the cold source, and various heat exchangers (d, e) to extract heat from the incoming helium stream.
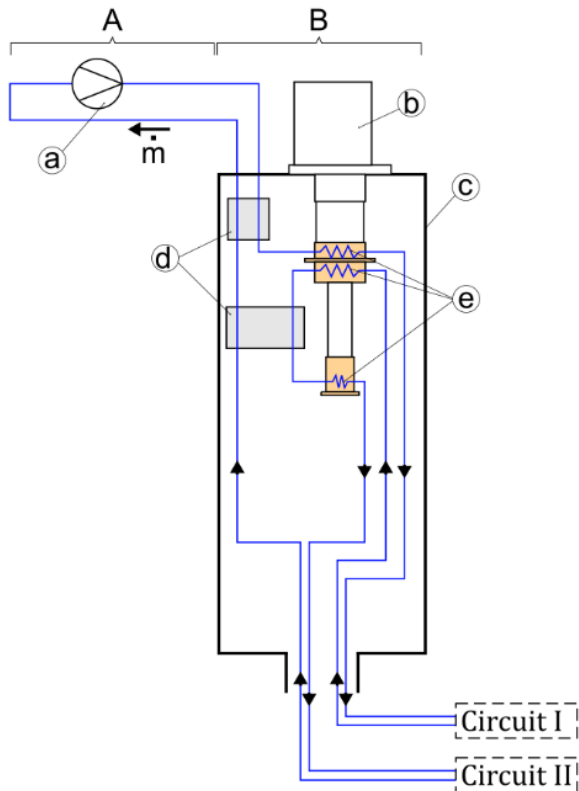
Figure 4.9. Remote refrigeration system comprised of the circulation system (A) and the Cryo Supply System (CSS) (B).
a) circulation pump; b) cryocooler; c) vacuum vessel; d) recuperative heat exchanger; e) thermalisation heat exchanger.

Table 4.3 lists the specific requirements of the remote refrigerator design, which are additional to the ones presented for the overall cryogenic system in Table 4.1. The refrigerator shall use an unmodified and commercially available two-stage cryocooler as the cold source. In order to simplify the overall refrigeration system, the need for an oil-removal system has to be avoided by using oil-free components only. In addition, and besides the cryocooler system, the use of cold moving components is strongly discouraged in order to increase the system robustness and reduce the risk of wearout problems. Consequently, the use of any type of expansion engine (i.e. turbines or pistons) is not allowed. Longitudinal heat conduction shall have a negligible effect on the recuperators effectiveness ε. This is assumed to be true for a longitudinal conduction parameter Λ with a value well below 0.01 (chapter 3.4.2). In order to avoid air leaking into the helium circuit, the static pressure at any cycle point shall remain above the ambient pressure p_a. In addition, the total frictional pressure loss shall be minimised, remaining well below a guidance value of 30 kPa. This particular requirement is not only meant to reduce exergetic losses, but also to provide sufficient design margin for any future upgrade [58] that might require a higher mass flow. Exempt from this requirement is the pressure drop resulting from a Joule-Thompson expansion step as part of the refrigeration cycle, as described later.

Table 4.3. Requirements and constraints of the remote refrigerator system.

Type	Description
Requirements	I. Use of an unmodified and commercially available two-stage cryocooler.
	II. Use of oil-free components only.
	III. No expansion engines (excluding the cryocooler system).
	IV. Negligible longitudinal heat conduction on recuperators. ($\Lambda \ll 0.01$)
	V. Process static pressure shall remain above ambient pressure ($p > p_a$ = 101.325 kPa).
	VI. Total frictional pressure loss well below 30 kPa (excluding any JT expansion step).

The selection of the cryocooler preceded this work and was driven by two main aspects. The cryocooler was required to have two cold stages and be commercially available. This resulted in the selection of a two-stage GM-Cryocooler (type SRDK-415D) from the company Sumitomo HI Ltd. (Figure 4.10), which comprises of a dedicated compressor unit (a), a helium gas line (b) and a cold head (c). The foreseen power line frequency for operation is 50 Hz. According to the supplier's data sheet [61], the device is capable of providing a refrigeration power of 1.5 W at 4.2 K on its 2nd stage, being at the time of purchase (August 2011) the most powerful GM-cryocooler on the market. The cold head itself weighs 18.5 kg. Cooldown time of the 2nd stage from ambient temperature to 4.2 K is approximately 60 min.
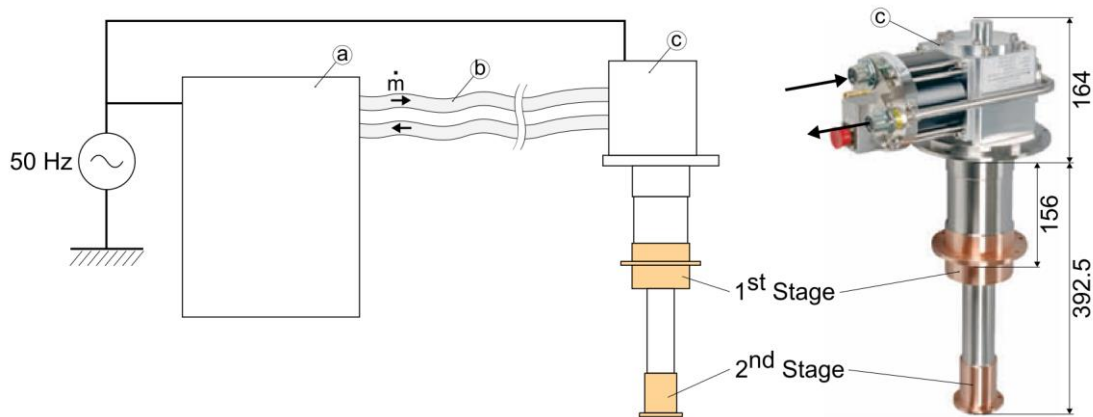
Figure 4.10. Selected GM-cryocooler from type SRDK-41D from the company Sumitomo. [61]
a) dedicated compressor unit; b) helium gas line; c) cold head

The interdependency of both cryocooler stages is illustrated by capacity maps. Figure 4.11 introduces the capacity map for a generic cryocooler of type SRDK-41D as published by the supplier, showing that each stage temperature (T_{1st} or T_{2nd}) is a function of the heat power ($\dot{Q}_{1st}$ and $\dot{Q}_{2nd}$) applied on both stages:

$$\left. \begin{array}{l} T_{1st} = f_1[\dot{Q}_{1st}, \dot{Q}_{2nd}] \\ T_{2nd} = f_2[\dot{Q}_{1st}, \dot{Q}_{2nd}] \end{array} \right\} . \tag{4.2}$$

The heat-power-dependency of a stage temperature is non-linear and the heat power increase on one stage can result in a temperature reduction on the other stage.
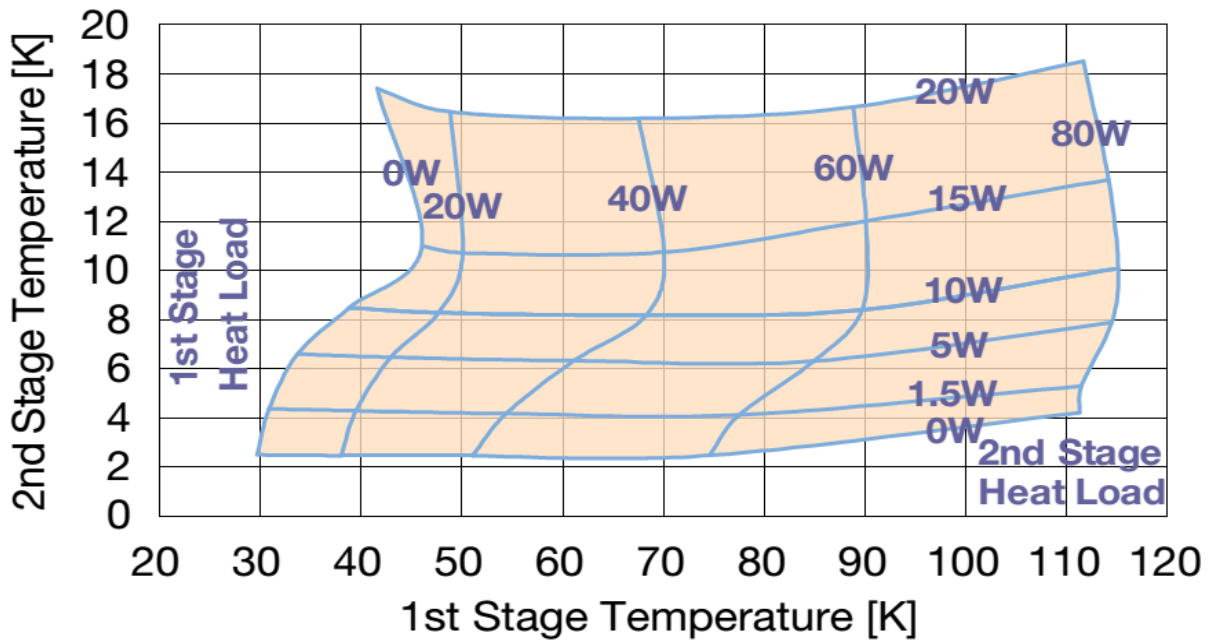
Figure 4.11. Capacity map of a generic GM-cryocooler of type SRDK-41D (Sumitomo HI Ltd.) connected to a main frequency of 50 Hz. The stage temperatures are a function of the applied heat loads. [22]

The capacity map on Figure 4.12 shows experimental data as published by the supplier for a generic cryocooler of type SRDK-41D. The data points indicate the temperature of the cryocooler stages (T_{1st}, T_{2nd}) when providing a given amount of cooling power ($\dot{Q}_{1st}$, $\dot{Q}_{2nd}$) in stationary conditions. For example, such a cryocooler can provide a cooling power of 30 W at 44 K on the first stage, and 1.5 W at 4.2 K on the second stage (data-point A).
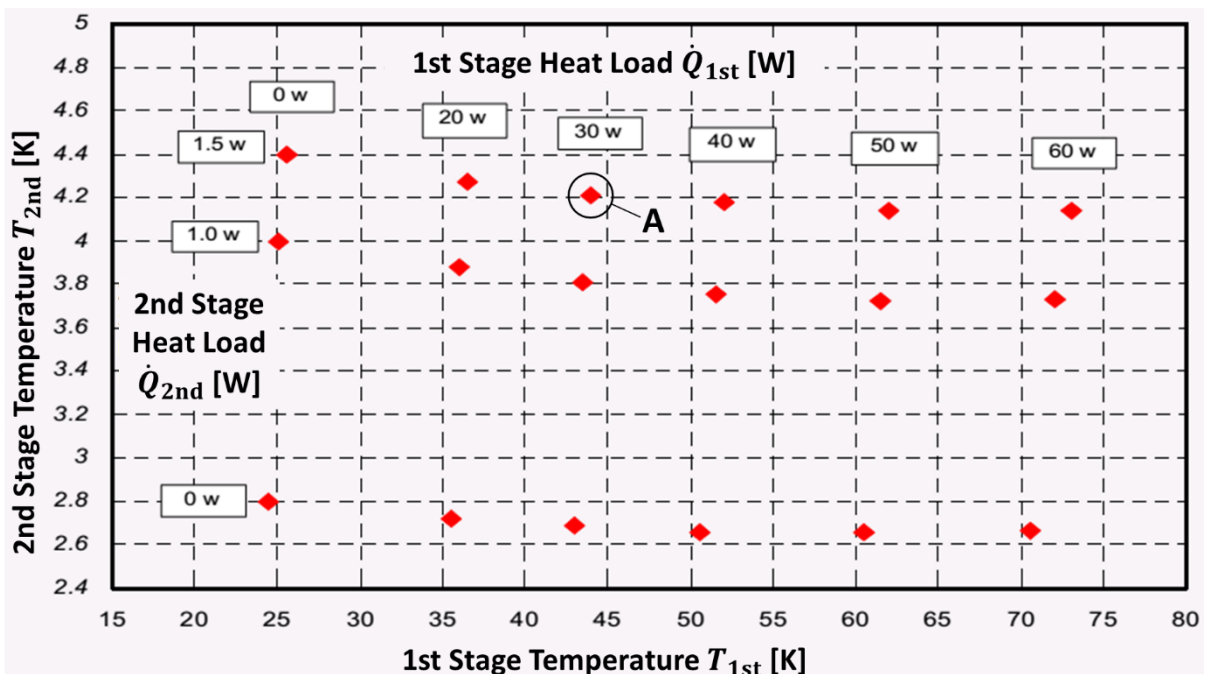
Figure 4.12. Capacity map of a generic GM-cryocooler from type SRDK-41D (Sumitomo HI Ltd.) connected to a main frequency of 50 Hz. Experimental data as published by the supplier on the cryocoolers`s data sheet [61]. Data-point A: 30 W at 44 K on the first stage and 1.5 W at 4.2 K on the second stage.

5 Thermodynamic analysis of possible refrigeration cycles

The assessment of possible refrigeration cycles is exploratory in nature and consists of the parametric study of various configuration schemes, in order to identify their possible advantages and limitations. Hence, it serves as the foundation for further evaluations. The assessment is constrained to the process analysis, without considering hardware limitations.

The analysis focuses on the novel remote refrigeration system and estimates the refrigeration power that could be delivered to a *generic* client with defined temperature requirements and undefined thermal budget; whether or not the refrigeration power is sufficient to cool such a client is not part of the assessment, since the thermal performance of the client system could also be improved to match the refrigerators capabilities. In general, increasing the refrigeration power for Circuit II (4.5 K, isothermal) has a higher priority than increasing the overall refrigerator efficiency, or increasing the refrigeration power for Circuit I (>50 K, non-isothermal).

First, the basic refrigeration cycle is described in detail and the terms used to quantify its efficiency are introduced. Then, the process evaluation is defined by specifying general assumptions and simplifications. The evaluation consists of the individual analysis of various configuration schemes that derive from the basic refrigeration cycle. Finally, all configurations are compared to each other and their relative advantages are provided.

5.1 Refrigeration cycle

The remote refrigerator is a novel cryocooler-based refrigerator capable of providing isothermal 4.5 K cooling by means of helium forced-flow. It consists of a 2-stage GM cryocooler thermally coupled to a closed helium cycle. The flow diagram in Figure 5.1a corresponds to the *basis configuration*, from which more complex systems with potentially higher refrigeration power are possible (more in chapter 5.2.3). The temperature diagram in Figure 5.1b introduces qualitatively the temperature distribution of the fluid over the components relative position $\xi = x/L$.

This description of the thermodynamic cycle starts with helium exiting the circulation system at ambient temperature (①). First, the recuperator HX1 transfers heat from the incoming (①→②) to the returning stream (⑨→⑩). Then, the stream is cooled further by passing through the heat exchanger HX1stA (②→③) and transferring its heat to the cryocooler. This step thermalises the stream close to the 1st stage temperature, since the heat exchanger, or *thermalisator,* is thermally attached to the cryocooler's 1st stage. Afterwards, the cold gaseous stream flows through Circuit I providing the non-isothermal refrigeration

power $\dot{Q}_R^I$, hence returning at a higher temperature (③→④). The stream is then thermalised once again to the cryocooler's 1st stage (④→⑤), although this time by thermalisator HX1stB, transferring roughly all heat collected at Circuit I to the cryocooler. Next, recuperator HX2 cools the stream even further (⑤→⑥) by transferring the heat to the returning stream (⑧→⑨). Then, the stream passes through the thermalisator HX2nd so that heat is transferred to the cryocooler's 2nd stage (⑥→⑦). During this process, helium reaches its condensation temperature and 2-phase helium is generated. The 2-phase stream is then routed through Circuit II providing the isothermal refrigeration power $\dot{Q}_R^{II}$ (⑦→⑧). In this particular example, a stream of saturated gas is assumed to return from Circuit II. The returning stream (⑧→⑩) then passes through both recuperators (HX2, HX1) on its way back to the circulation system, warming up nearly to ambient temperature due to the absorbed heat. Finally, the stream passes through the circulation system (⑩→①), which comprises of a circulation pump and an aftercooler. In this last step, the stream is compressed and thermalised to ambient temperature, closing the cycle.

For convenience, the flow diagram is divided into five sectors: the room-tempearture circulation system (⑩→①), Circuits I and II of the client system (③→④; ⑦→⑧), and Regions I and II (①→⑤, ⑨→⑩; ⑤→⑨) at the remote refrigerator. This sectorisation will later allow the separate analysis of the warmer Region I and the colder Region II.

a) Flow diagram   b) Temperature distribution
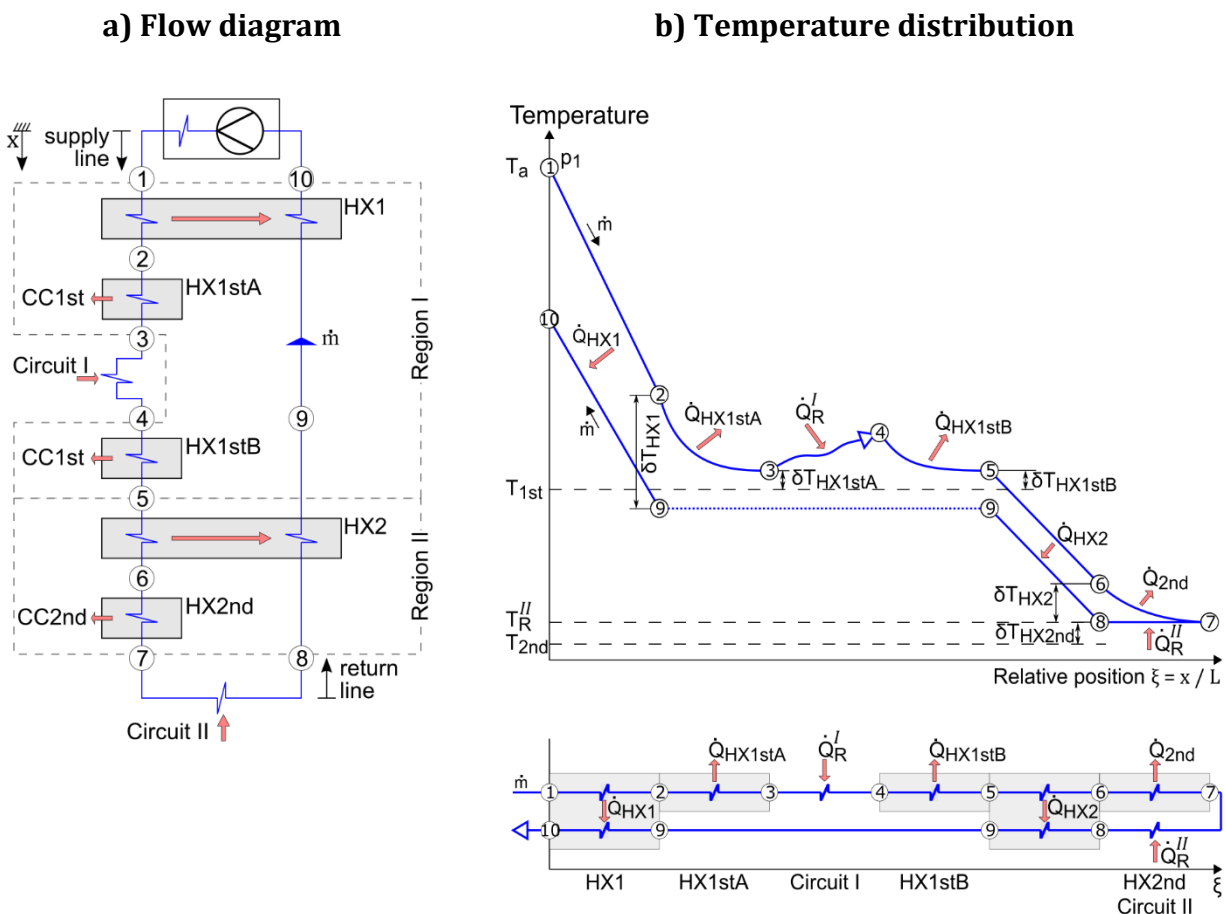
Figure 5.1. Flow diagram and qualitative temperature distribution of the remote refrigeration system in its basic configuration.

5.1.1 Supply-line thermalisation

The purpose of recuperators HX1 and HX2 is to pre-cool the incoming stream as much as possible by using the colder returning stream. This *supply-line thermalisation* would be best accomplished by a reversible recuperator ($\dot{C}^*$=1; $U_m \cdot A \rightarrow \infty$), able to cool the stream all the way down to the inlet temperature of the returning stream T_4 (Figure 5.2). However, the consideration of real recuperators imposes the need of a subsequent heat exchanger to cool the stream further (②→③) and reach the desired temperature ($T_3 = T_4 + \Delta T_{4 \rightarrow 3}$). This additional cooling, or *after-cooling,* is performed by a thermalisator (HX1stA or HX2nd), which transfers the heat to the cryocooler:

$$\dot{Q}_2 = \dot{m} \cdot (h_2 - h_3) \,. \tag{5.1}$$

It can be shown using the energy balance of the incoming stream that

$$\dot{H}_1 + \dot{Q}_{\text{surr}} - \dot{Q}_1 - \dot{Q}_2 - \dot{H}_3 = 0 \quad , \tag{5.2}$$

where $\dot{Q}_{\text{surr}}$ corresponds to parasitic heat-power coming from the surroundings. Using $\Delta \dot{H}_{4 \rightarrow 3} \approx \dot{m} \cdot \bar{c}_p \cdot \Delta T_{4 \rightarrow 3}$, under the assumption of an ideal-gas behaviour for that temperature range, it can be shown that

$$\dot{H}_1 + \dot{Q}_{\text{surr}} - \dot{Q}_1 - \dot{Q}_2 - (\dot{H}_4 + \dot{m} \cdot \bar{c}_p \cdot \Delta T_{4 \rightarrow 3}) \approx 0 \quad , \tag{5.3}$$

where $\bar{c}_p$ is the temperature <u>independent</u> heat capacity.

Based on Eq. (3.35), the effectiveness of the recuperator is

$$\varepsilon = \frac{\dot{Q}_1}{\dot{Q}_{1\text{MAX}}} = \frac{\dot{Q}_1}{\dot{H}_1 - \dot{H}_4} \,, \tag{5.4}$$

and substituting with Eq. (5.3) yields

$$\dot{Q}_2 \approx (1 - \varepsilon) \cdot \dot{Q}_{1\text{MAX}} + \dot{Q}_{\text{surr}} - \dot{m} \cdot \bar{c}_p \cdot \Delta T_{4 \rightarrow 3} \,, \tag{5.5}$$

showing that the amount of heat power to be absorbed by the cryocooler (after-cooling, $\dot{Q}_2$) depends upon the recuperator's effectiveness ε, the parasitic heat power coming from the surroundings $\dot{Q}_{\text{surr}}$, and the difference in fluid temperature between the cold inlet and the warm outlet $\Delta T_{4 \rightarrow 3}$. Consequently, recuperators with high effectiveness and efficient insulation solutions are essential to keep the required cooling power within an acceptable range.
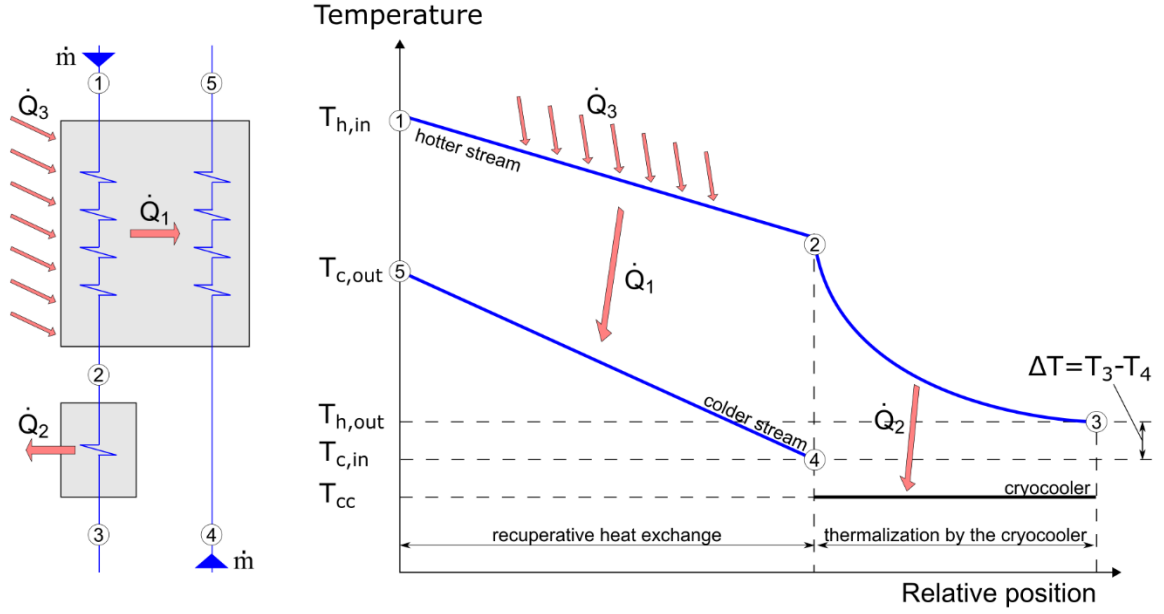
Figure 5.2. The supply line thermalisation (①→③) is accomplished with two heat exchangers connected in series. First, a recuperator transfers most of the heat from the warmer supply stream to the colder return stream. Then, a thermalisator transfers the remaining heat to the corresponding cryocooler stage.

5.1.2 Transmission and exergetic efficiency

The cooling power provided by the cryocooler stages corresponds to the total amount of heat that can be extracted from the system. This cooling power is gradually "used" along the refrigeration system, with the result that only a fraction remains available for the refrigeration of the cyclotron itself (Figure 5.3). The term transmission efficiency η is used to describe the percentage of cooling power that is passed from one subsystem to the next, and it is defined as the ratio of the cooling power output to input of a given subsystem i

$$\eta_i \equiv \frac{\dot{Q}_{\text{OUT},i}}{\dot{Q}_{\text{IN},i}} \leq 1 \quad . \tag{5.6}$$

First, the cooling power provided by the cryocooler $\left(\dot{Q}_{1\text{st}}, \dot{Q}_{2\text{nd}}\right)$ is partially used by the external refrigerator to compensate parasitic heat power on the CSS hardware $\left(\dot{Q}_{\text{CSS}}^{I}, \dot{Q}_{\text{CSS}}^{II}\right)$, diminishing the available cooling power for the thermodynamic process $\left(\dot{Q}_{\text{avail}}^{I}, \dot{Q}_{\text{avail}}^{II}\right)$. Once the losses of the thermodynamic process $\left(\dot{Q}_{\text{TP}}^{I}, \dot{Q}_{\text{TP}}^{II}\right)$ have been compensated, the remaining cooling power is "stored" in the helium streams in the form of sensible or latent heat, which corresponds to the cooling power provided by the refrigerator $\left(\dot{Q}_{\text{R}}^{I}, \dot{Q}_{\text{R}}^{II}\right)$. Then, a fraction of that power is used to compensate the static heat loads at the transfer line $\left(\dot{Q}_{\text{TFL}}^{I}, \dot{Q}_{\text{TFL}}^{II}\right)$. Finally, the remaining cooling power $\left(\dot{Q}_{\text{CS}}^{I}, \dot{Q}_{\text{CS}}^{II}\right)$ is used at the client system to refrigerate the connector box $\left(\dot{Q}_{\text{CB}}^{I}, \dot{Q}_{\text{CB}}^{II}\right)$ and the cyclotron $\left(\dot{Q}_{\text{Cyc}}^{I}, \dot{Q}_{\text{Cyc}}^{II}\right)$ components.
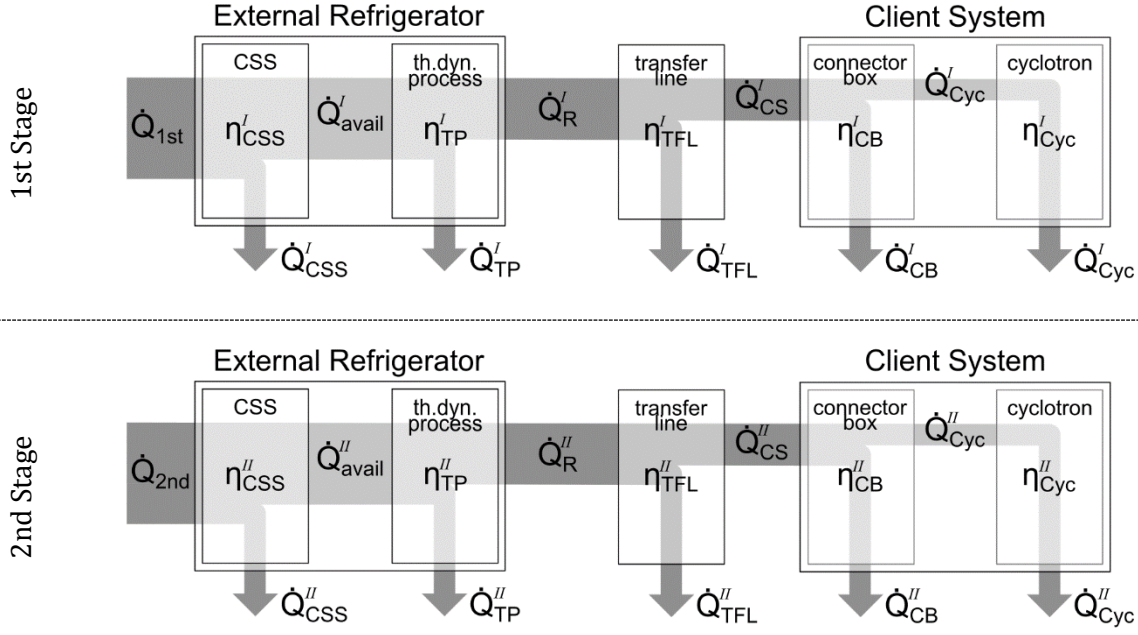
Figure 5.3. Allocation of the cooling power provided by the cryocooler stages. The efficiency η_i for each subsystem i represents the ratio of supplied to received cooling power.

The term *condensate yield* y_{LHe} quantifies the condensation capabilities of the thermodynamic cycle and is defined as the ratio of the latent heat power stored in the generated liquid over the available refrigeration power for its condensation:

$$y_{\text{LHe}} \equiv \frac{\dot{m}_{\text{LHe}} \cdot h_{\text{evap}}}{\dot{Q}^{II}_{\text{avail}}} = \frac{\dot{m} \cdot (1 - x) \cdot h_{\text{evap}}}{\dot{Q}^{II}_{\text{avail}}} \leq 1 \quad , \tag{5.7}$$

where h_{evap} is the evaporation enthalpy (latent heat) of the liquid and x the vapour quality of the fluid leaving the external refrigerator. In the special case that the refrigeration power $\dot{Q}^{II}_{\text{R}}$ comes exclusively from the entire latent heat of the produced liquid $\dot{m}_{\text{LHe}}$, the condensate yield y_{LHe} corresponds to the process efficiency η^{II}_{TP}:

$$\eta^{II}_{\text{TP}} = \frac{\dot{Q}^{II}_{\text{R}}}{\dot{Q}^{II}_{\text{avail}}} = y_{\text{LHe}} \quad , \text{when } \dot{Q}^{II}_{\text{R}} = \dot{m}_{\text{LHe}} \cdot h_{\text{evap}} \quad . \tag{5.8}$$

The transmission of cooling power from one subsystem to the other is also accompanied by a flow of exergy power. In contrast to the cooling power (Figure 5.3), part of the exergy power is not only gradually "used", but also destroyed due to process irreversibilities. Consequently, only a fraction of the exergetic power provided by the cryocooler stages arrives at the cyclotron itself (Figure 5.4). The exergetic efficiency ζ, as defined in Eq. (2.24), is used to quantify the percentage of exergy passed from one subsystem to the next

$$\zeta_i = \frac{\dot{E}_{\text{OUT},i}}{\dot{E}_{\text{IN},i}} \leq 1 \quad . \tag{5.9}$$
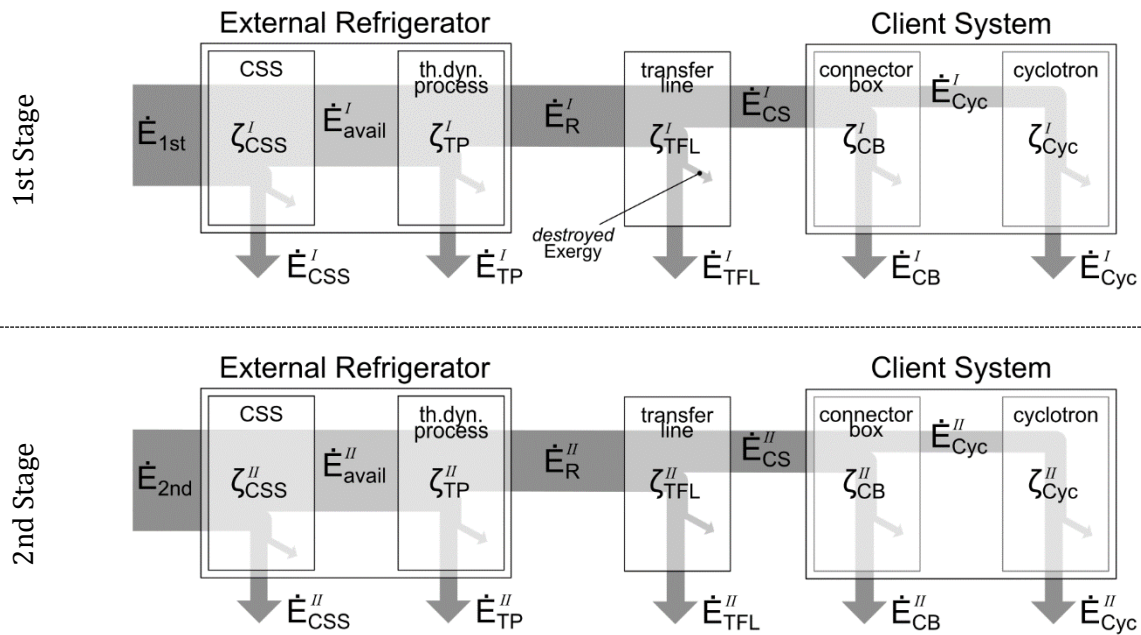
Figure 5.4. Exergy flow across the refrigeration system. The exergetic efficiency ζ_i for each subsystem i represents the ratio of supplied to received exergy.

5.2   Process evaluation

The following evaluation presents the thermodynamic analysis of various configuration schemes. It describes the relationship between process parameters and provides the criteria to determine process values. First, the framework of the evaluation is defined by introducing the general assumptions and simplifications. Then, a parametric study is performed for each configuration. Region I and Region II are evaluated separately; the configurations are identical at Region I, but differ at Region II. Flow schemes, equations and parameter values are provided in all cases to fully define the thermodynamic process.

5.2.1 General assumptions and simplifications

The process evaluation is limited to the general requirements and constraints of the cyclotron's cryogenic system (chapter 4.2). In addition to that, Table 5.1 lists the general assumptions and thermal-model simplifications made for the thermodynamic analysis. The entire system is assumed to be adiabatic and to operate in steady state conditions. In addition, a system design with negligible frictional pressure losses along its pipes is postulated. The physical properties of helium are obtained from the specialised library HePak© [20]. In a few cases, helium is assumed to behave as an ideal gas at temperatures above 20 K. This assumption simplifies the analysis and is mentioned explicitly when applied. All heat exchangers are calculated as idealised components with a finite thermal size; this requires a uniform velocity and temperature profile over the pipe cross-section for each fluid, and zero longitudinal heat conduction along the wall.

Table 5.1. Assumptions and simplifications made for the analysis of the CSS cycle.

Type	Description
General assumptions	I. System operation under steady state conditions (i.e. flow rates and temperatures are time independent). II. No additional heat sources or sinks from the surroundings (i.e. parasitic heat in leaks). III. Frictional pressure loss along the pipes is of secondary importance by design. Pressure drop at JT expansion steps are considered.

Thermal model simplifications	I. Physical properties of helium obtained from specialised libraries. Ideal-gas behaviour of Helium for T > 20 K is only assumed if needed to simplify the analysis.
	 II. Heat exchangers are idealised components with finite thermal size ($U_m \cdot A$). Hence, besides the general assumptions:
	   a) Velocity and temperature of each fluid is uniform over every cross section (i.e. no temperature gradient normal to flow direction).
	   b) No longitudinal heat conduction along the wall.

Process parameters and notation

The thermodynamic process is defined by a suitable set of parameter values, which are determined based on one of the following criteria:

- The value corresponds to a specified *boundary condition*.
- The value results from the simplification of the thermal model.
- The parameter is defined as a *design parameter*. Therefore, its value is chosen based on experience and/or expectations.
- The parameter is defined as a *free design parameter.* Therefore, its value can vary within a defined range, so that the optimal design conditions can be identified. Due to its relevance, this parameter is written in **orange font colour** for better readability.

The thermodynamic state at a given process point is fully defined by a suitable parameter set of state quantities. Therefore, knowing this parameter set allows the calculation of all other thermodynamic properties at that point. In this work, a specific notation is used to indicate that the value of a state quantity is obtained from its relationship with other state quantities. The notation is illustrated in the following example for enthalpy h, temperature T and pressure p at the process point i:

$$h_i = \boldsymbol{f}\,[T_i, p_i] \xrightarrow{\text{used notation}} h_i[T_i, p_i] \quad . \tag{5.10}$$

Redefinition of the cryocooler stage-power

The temperature of the cryocooler stages are a function of the heat power applied to each stage (Chapter 4.2.3). However, in order to simplify the analysis in this chapter, the 1st stage temperature T_{1st} is fixed to 50 K, as a *new boundary condition*. This enables the redefinition of the stage power ($\dot{Q}_{1st}$; $\dot{Q}_{2nd}$) as a continuous function of the 2nd stage temperature T_{2nd}.

The stage power is estimated based on the supplier's data-sheets. The two stage-power functions are obtained by fitting 7 data points collected directly from the capacity maps in Figure 4.11 and Figure 4.12:

For $T_{1st} = 50$ K and 2.65 K $\leq T_{2nd} \leq 16.43$ K,

$$\left.\begin{array}{l} \dot{Q}_{2nd} \approx \dfrac{21.67 \cdot (T_{2nd})^{3.81}}{8.58^{3.81} + (T_{2nd})^{3.81}} \\[2mm] \dot{Q}_{1st} \approx 0.21 \cdot (T_{2nd})^2 - 5.38 \cdot T_{2nd} + 53.27 \end{array}\right\} \quad , \tag{5.11}$$

where the expressions T_{2nd} (K), $\dot{Q}_{1st}$ (W) and $\dot{Q}_{2nd}$ (W) are all in SI units, and the function domain corresponds to the temperature range of the fitted data. The stage-power functions, and the corresponding data points, are plotted in Figure 5.5. Error bars and error bands are according to the uncertainty analysis in chapter 8.3.2, and indicate the *95 % confidence interval* of the reported values. Further details concerning the data points and the fitted functions are available in Appendix A6.

The curves show that increasing the 2nd stage temperature T_{2nd} beyond 4.5 K results in a higher 2nd stage power $\dot{Q}_{2nd}$, but also decreases the available 1st stage power $\dot{Q}_{1st}$. The dominant source of uncertainty is the possible deviation between the data-sheet values and the actual values of the employed device. It is assumed that 95 % of the cryocoolers on the market are able to provide between 100 % and 120 % of the stage power specified by the supplier.

Cryocooler Stage Power :

Stage	1st	2nd
Data	▲	◆
Data Fit		
Curve	─··─	──
Function	Quadratic	Hill
	$y = c_0 + c_1\,x + c_2\,x^2$	$y = c_1\,x^n / (c_2^n + x^n)$
$c_0;\ c_1;\ c_2$	53.27; - 5.38; 0.21	- ; 21.68; 8.58
n	-	3.81
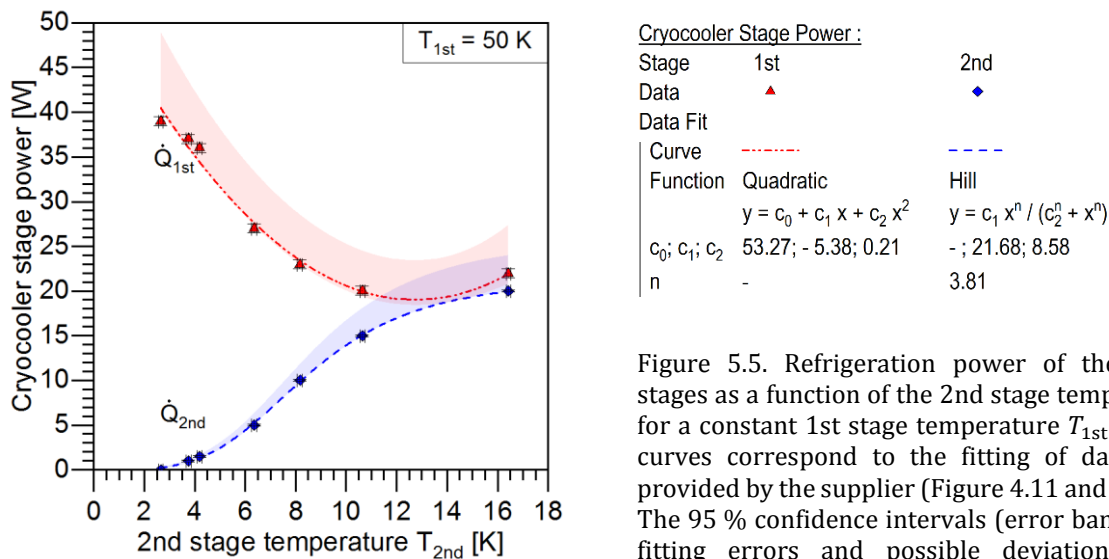
Figure 5.5. Refrigeration power of the cryocooler stages as a function of the 2nd stage temperature T_{2nd} for a constant 1st stage temperature T_{1st} of 50 K. The curves correspond to the fitting of data points as provided by the supplier (Figure 4.11 and Figure 4.12). The 95 % confidence intervals (error bands) consider fitting errors and possible deviations from the data-sheet values.

Since the 1st-stage temperature T_{1st} is fixed to a constant value, the outlet temperature of both 1st-stage thermalisators (HX1stA, HX1stB) can be considered to be constant as well (T_3 and T_5 in Figure 5.1); provided both thermalisators achieve a supply-line thermalisation close enough to the 1st-stage temperature T_{1st} ($\delta T \lesssim 0.1$ K). As a consequence, the inlet temperature of Region II (T_5) is considered to be constant, making Region II independent of Region I, but not vice versa.

Calculation uncertainty

Chapter 8 is concerned with the uncertainty analysis for the entirety of this work, providing the calculation uncertainty as the combined effect of numerical, input and model errors. The

calculation uncertainty is reported in terms of "*95 % confidence intervals*", which are intervals attributed with a 95 % probability of actually containing the (unknown) true value of the calculation result.

For this chapter, the dominant source of uncertainty is the capability of the calculation model to accurately describe the refrigeration process. The model is assumed to describe the transmission efficiency of the refrigeration process η_{TP} with a relative accuracy of ±15 %; the likelihood is assumed to be zero at the upper interval-bound and to increase steadily towards the lower bound. The uncertainties introduced by the stage-power functions (Eq. (5.11)) have a moderate impact on the calculation uncertainty, whereas the remaining sources of uncertainty are of little relevance.

5.2.2 Region I: Higher temperature section

This region is characterised for its relatively high temperature ($\gtrsim T_{1st} = 50$ K) and for defining, to a great extent, the non-isothermal refrigeration power $\dot{Q}_R^I$ that is provided to Circuit I. Since the temperature range is well above 20 K, helium can be assumed to behave as an ideal gas.

The flow of refrigeration power and exergy are illustrated in Figure 5.6. As defined in chapter 5.1.2, the transmission efficiency η_{CSS}^I derives from the performance of the refrigerator's insulation and quantifies the fraction of cooling power that is available for the thermodynamic process after compensating from external heat sources (i.e. heat conducted from the surroundings). In contrast, the transmission efficiency η_{TP}^I derives from the choice of the thermodynamic process itself and quantifies the fraction of cooling power that the refrigerator delivers to Circuit I. The exergetic efficiencies ζ_{CSS}^I and ζ_{TP}^I are defined in an analogous way. The non-isothermal refrigeration power $\dot{Q}_R^I$ provided by the refrigerator to Circuit I is

$$\dot{Q}_R^I = \eta_{CSS}^I \cdot \eta_{TP}^I \cdot \dot{Q}_{1st} \quad , \tag{5.12}$$

with the corresponding exergy flow being

$$\dot{E}_R^I = \zeta_{CSS}^I \cdot \zeta_{TP}^I \cdot \dot{E}_{1st} \quad . \tag{5.13}$$
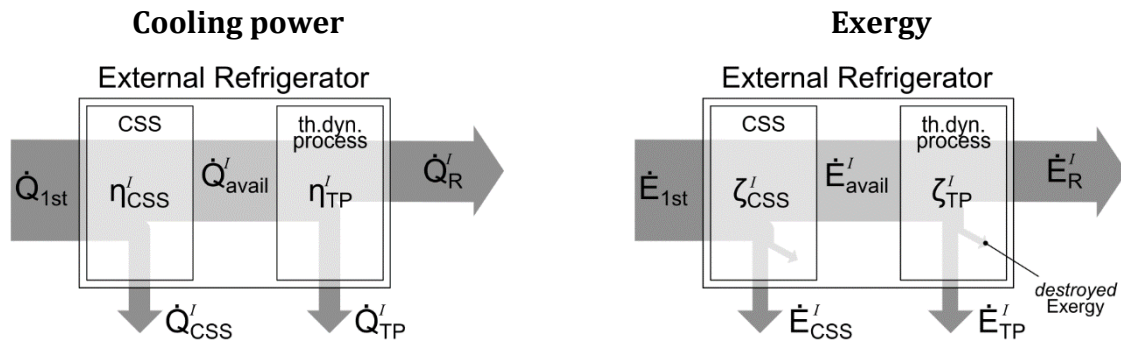
Figure 5.6. Flow of the cooling power and exergy provided by the cryocooler's 1st stage.

The flow diagram used for the thermodynamic analysis of Region I is illustrated in Figure 5.7 and it presents a total of three interfaces. It is connected at the warmer end to the circulation circuit (⑩→①), which generates the forced-flow of helium providing a supply stream at room

temperature. The supply line is then thermalised close to $T_{1st} = 50$ K by the combined effort of recuperator HX1 and thermalisator HX1stA (①→③). The next connection is used to provide the refrigeration power $\dot{Q}_R^I$ to Circuit I (③→④), collecting the heat with the cold supply stream and then rejecting it by using thermalisator HX1stB (④→⑤). Finally, the connection at the colder end (⑤→⑨) is used to provide Region II with a thermalised stream close to $T_{1st} = 50$ K.
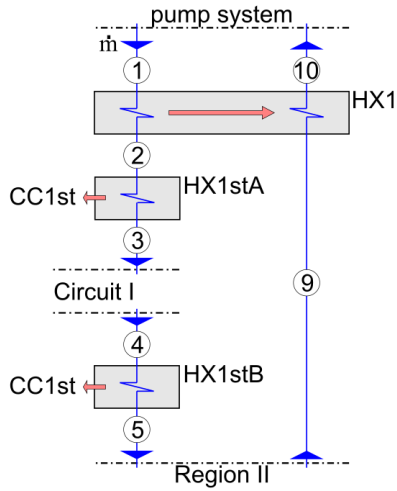
Figure 5.7. Flow diagram of Region I with interfaces to the pump system, Circuit I, and Region II.

The thermodynamic process in Region I is fully defined by the set of parameter values in Table 5.3 and the set of linear equations in Table 5.2. The Eqs. (5.14.1-5) give the temperature T_i or the enthalpy h_i of the fluid at a given process point i, and Eqs. (5.14.6-9) describe the heat power extracted by the thermalisators and the cryocooler. Each one of Eqs. (5.14.2-6) derives from the relationship between a process point i and an adjacent heat exchanger, with such a relationship being expressed in terms of either a local temperature difference δT or the change in specific enthalpy Δh. The local temperature difference δT_{HX1} at the cold end of recuperator HX1 is defined as the free design parameter and is therefore highlighted in orange font.

Table 5.2. System of linear equations describing Region I.

Description	Equation	Eq.
Initial incoming flow temperature	$T_1 = T_a$	(5.14.1)
Δh on HX1	$h_{10} = h_9 + (h_1 - h_2)$	(5.14.2)
δT on cold end of HX1stA	$T_3 = T_{1st} + \delta T_{HX1stA}$	(5.14.3)
δT on cold end of HX1stB	$T_5 = T_{1st} + \delta T_{HX1stB}$	(5.14.4)
δT on cold end of HX1	$T_2 = T_9 + \delta T_{HX1}$	(5.14.5)
δT on cold end of HX2	$T_9 = T_5 - \delta T_{HX2}$	(5.14.6)
Power extracted by HX1stA	$\dot{Q}_{HX1stA} = \dot{m} \cdot (h_2 - h_3)$	(5.14.7)
Power extracted by HX1stB	$\dot{Q}_{HX1stB} = \dot{m} \cdot (h_4 - h_5)$	(5.14.8)
Available cryocooler power	$\eta_{CSS}^I \cdot \dot{Q}_{1st} = \dot{Q}_{HX1stA} + \dot{Q}_{HX1stB}$	(5.14.9)

Table 5.3. Summary of process parameters for the analysis of Region I of the refrigeration cycle.

Type	Parameter		Value	Description
Boundary condition:	T_a	[K]	293.15	Ambient temperature.
	T_{1st}	[K]	50	Cryocooler's 1st stage temperature.
Model simplification:	Λ	[-]	$\ll 0.01$	Negligible longitudinal condition on heat exchangers.
	η_{CSS}^{II}	[%]	100	The entirety of the cryocooler's power $\dot{Q}_{1st}$ is available for the refrigeration cycle.
	$\dot{C}_{HX1}^*$	[-]	1	Recuperator HX1 has a balanced flow.
	Δp	[bar]	$\Delta p_{1\to5} \approx 0$	Isobaric consideration for feed line.
			$\Delta p_{9\to10} \approx 0$	Isobaric consideration for return line.
			$\Delta p_{5\to9} \leq 0$	Pressure reduction at Region II due to throttling.
	T_3	[K]	$\approx T_5$	Similar outlet temperatures for HX1stA and HX1stB, since both are thermalised to the 1st stage. (Postuated for $\delta T_{HX1stA} \approx \delta T_{HX1stB} \lesssim 0.1$ K $\ll T_{1st}$)
	$\overline{c}_p$	[J/g-K]	≈ 5.19	Heat capacity c_p of helium assumed for $T \gg 20$ K ($\overline{c}_p \neq \boldsymbol{f}[T]$).
Design value:	T_1	[K]	T_a	Temperature of the incoming flow from the circulation system.
	δT_{HX1stA}	[K]	0.1	Local temperature difference at the cold end of HX1stA ($T_3 - T_{1st}$).
	δT_{HX1stB}	[K]	0.1	Local temperature difference at the cold end of HX1stB ($T_5 - T_{1st}$).
	δT_{HX2}	[K]	0.5	Local temperature difference at the warm end of HX2. ($T_6 - T_8$).
Values defined by equations and parameters of Region II:	$\dot{m}$			Mass flow.
	T_{2nd}	[K]	4.5	Cryocooler's 2nd stage temperature.
	p_1	[bar]	$\geq p_{sat}$	Pressure of the flow to/from Region II is equal or higher/lower than the saturation pressure required in Circuit II ($p_{sat}[4.5$ K$] = 130.3$ kPa).
	p_9	[bar]	$\leq p_{sat}$	
Free design parameter (range):	δT_{HX1}	[K]	$\delta T_{HX2} \to \frac{\eta_{CSS}^I \cdot \dot{Q}_{1st}}{\dot{m} \cdot \overline{c}_p}$	Local temperature difference at the cold end of HX1 ($T_2 - T_9$).
Others:	$\dot{Q}_{1st}$	[W]	33.35	Cooling power of the cryocooler's 1st stage.
	$\dot{Q}_{2nd}$	[W]	1.71	Cooling power of the cryocooler's 2nd stage.

The heat-exchange duty of recuperator HX1 $\dot{Q}_{HX1}$ corresponds to the decrease in enthalpy rate of the incoming stream

$$\dot{Q}_{HX1} = \dot{H}_1 - \dot{H}_2 = \dot{m} \cdot (h_1 - h_2) \quad , \tag{5.15a}$$

which is then rewritten as follows

$$\dot{Q}_{HX1} = \dot{m} \cdot (h_1 - h_2[p_1, T_9 + \delta T_{HX1}]) \tag{5.15b}$$

to emphasize its dependency from the free design parameter δT_{HX1}. Under the assumption of an ideal-gas behaviour, the equation can be approximated as

$$\dot{Q}_{HX1} \approx \dot{m} \cdot \overline{c}_p \cdot (T_1 - T_2) = \dot{m} \cdot \overline{c}_p \cdot (T_1 - (T_9 + \delta T_{HX1})) \quad , \tag{5.15c}$$

where $\bar{c}_p \approx 5.19$ J/g-K is the temperature <u>independent</u> heat capacity of helium. The deviation to the real-gas scenario that is introduced by this approximation is considered marginal: the deviation increases almost linearly from -0.08 % to -0.45 % for a supply-pressure range from $p_1 = 1.3$ bar to 26 bar.

Eq. (5.15c) can be rewritten as

$$\dot{Q}_{HX1} \approx \underbrace{\dot{m} \cdot \bar{c}_p \cdot (T_1 - T_9)}_{\substack{\text{maximum possible} \\ \text{heat-exchange duty}}} - \underbrace{\dot{m} \cdot \bar{c}_p \cdot \delta T_{HX1}}_{\substack{\text{lost opportunity of} \\ \text{heat-power transfer}}} \quad , \tag{5.15d}$$

where the first term corresponds to the highest theoretical heat-power that can be exchanged by an idealised and *infinitely* large recuperator HX1 (chapter 3.3.1), and the second term corresponds to the amount of heat power that is not transferred due to the non-ideal thermal performance (resulting in a "lost opportunity" for heat transfer).

The equation shows that the heat-exchange duty $\dot{Q}_{HX1}$ is direct proportional to the mass flow $\dot{m}$ (Figure 5.8) and that it decreases linearly by increasing values of δT_{HX1}; however, it is shown later in Eq. (5.34) that the second term is greater than zero but not larger than $\eta_{CSS}^l \cdot \dot{Q}_{1st}$ ($\approx$ 33 W) and, therefore, is of secondary importance when compared to the magnitude of the first term.
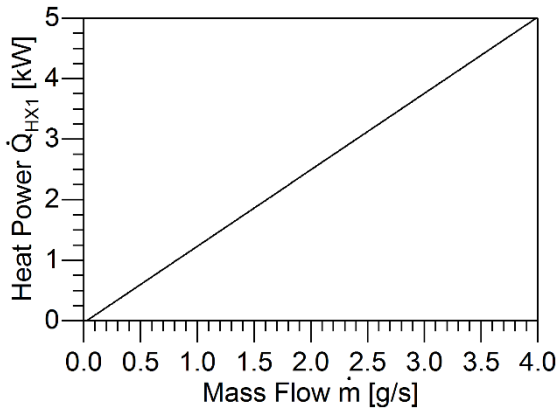
Figure 5.8. Linear relationship of the heat exchange duty $\dot{Q}_{HX1}$ with the mass flow $\dot{m}$. The lowering effect resulting from an increase in the free design parameter δT_{HX1} is considered negligible ($\leq \eta_{CSS}^l \cdot \dot{Q}_{1st} \approx$ 33 W). Valid for parameter values in Table 5.3 and assuming an ideal-gas behaviour with $\bar{c}_p \approx 5.19$ J/g-K.

According to the definitions of Eq. (3.37) and Eq. (3.43), the effectiveness and exergetic efficiency of recuperator HX1 are

$$\varepsilon_{HX1} = \frac{T_1 - T_2}{T_1 - T_9} = 1 - \frac{\delta T_{HX1}}{T_1 - T_9} = 1 - \frac{\delta T_{HX1}}{T_a - T_5 + \delta T_{HX2}} \quad , \tag{5.16}$$

and

$$\zeta_{HX1} = \frac{e_2 - e_1}{e_9 - e_{10}} = \frac{e_2[p_1, T_9 + \delta T_{HX1}] - e_1}{e_9 - e_{10}} \quad . \tag{5.17}$$

Since the recuperator HX1 is assumed to be balanced ($\dot{C}_{HX1}^* = 1$), its NTU value can be estimated using Eq. (3.42), yielding

$$\text{NTU}_{HX1} = \frac{\varepsilon_{HX1}}{1 - \varepsilon_{HX1}} = \frac{T_a - T_5 + \delta T_{HX2}}{\delta T_{HX1}} - 1 \quad . \tag{5.18}$$

The terms for the thermalisators HX1stA and HX1stB are obtained in analogy to Eqs. (5.15a) to (5.18), and all of them are summarised in Table 5.4.

Table 5.4. Terms describing the heat exchangers on Region I.

Recuperator HX1:

(5.15a-c) $\quad \dot{Q}_{HX1} = \dot{H}_1 - \dot{H}_2 = \dot{m} \cdot (h_1 - h_2) = \dot{m} \cdot (h_1 - h_2[p_1, T_9 + \delta T_{HX1}]) \approx \dot{m} \cdot \bar{c}_p \cdot (T_1 - (T_9 + \delta T_{HX1}))$

(5.16) $\quad \varepsilon_{HX1} = \dfrac{T_1 - T_2}{T_1 - T_9} = 1 - \dfrac{\delta T_{HX1}}{T_1 - T_9} = 1 - \dfrac{\delta T_{HX1}}{T_a - T_5 + \delta T_{HX2}}$

(5.17) $\quad \zeta_{HX1} = \dfrac{e_2 - e_1}{e_9 - e_{10}} = \dfrac{e_2[p_1, T_9 + \delta T_{HX1}] - e_1}{e_9 - e_{10}}$

(5.18) $\quad NTU_{HX1} = \dfrac{\varepsilon_{HX1}}{1 - \varepsilon_{HX1}} = \dfrac{T_a - T_5 + \delta T_{HX2}}{\delta T_{HX1}} - 1$

Thermalisator HX1stA:

(5.19) $\quad \dot{Q}_{HX1stA} = \dot{H}_2 - \dot{H}_3 = \dot{m} \cdot (h_2 - h_3) \approx \dot{m} \cdot \bar{c}_p \cdot ((T_9 + \delta T_{HX1}) - T_3)$

(5.20) $\quad \varepsilon_{HX1stA} = \dfrac{T_2 - T_3}{T_2 - T_{1st}} = \dfrac{T_2 - (T_{1st} + \delta T_{HX1stA})}{T_2 - T_{1st}} = 1 - \dfrac{\delta T_{HX1stA}}{T_9 + \delta T_{HX1} - T_{1st}}$

(5.21) $\quad NTU_{HX1stA} = \dfrac{T_9 + \delta T_{HX1} - T_{1st}}{\delta T_{HX1stA}} - 1$

(5.22) $\quad \zeta_{HX1stA} = \dfrac{\dot{m} \cdot (e_2 - e_3)}{\eta_C[T_{1st}] \cdot \dot{Q}_{HX1stA}} = \eta_C^{-1}[T_{1st}] \cdot \left(1 - \dfrac{T_a \cdot \Delta s_{2 \to 3}}{\Delta h_{2 \to 3}}\right) = \eta_C^{-1}[T_{1st}] \cdot \left(1 - \dfrac{T_a \cdot \ln \frac{T_3}{T_2}}{\Delta T_{2 \to 3}}\right)$

Thermalisator HX1stB:

(5.23) $\quad \dot{Q}_{HX1stB} = \dot{H}_4 - \dot{H}_5$

(5.24) $\quad \varepsilon_{HX1stB} = \dfrac{T_4 - T_5}{T_4 - T_{1st}} = 1 - \dfrac{\delta T_{HX1stB}}{T_4 - T_{1st}}$

(5.25) $\quad NTU_{HX1stB} = \dfrac{T_4 - T_{1st}}{\delta T_{HX1stB}} - 1$

(5.26) $\quad \zeta_{HX1stB} = \eta_C^{-1}[T_{1st}] \cdot \left(1 - \dfrac{T_a \cdot \ln \frac{T_5}{T_4}}{\Delta T_{4 \to 5}}\right)$

The joint purpose of recuperator HX1 and thermalisator HX1stA is to cool down the supply stream from ambient temperature $T_1 = T_a$ to the inlet temperature of Circuit I $T_3 = T_{1st} + \delta T_{HX1}$; this is part of the *supply-line thermalisation* (chapter 5.1.1), where the supply-stream leaving the recuperator HX1 is cooled down further (or *after-cooled*) by the thermalisator HX1stA. Therefore, and based on Eq. (5.5), the amount of extracted heat power by thermalisator HX1stA ($\dot{Q}_{HX1stA}$) is directly related to the effectiveness of recuperator HX1 (ε_{HX1}) and the temperature to be achieved (T_3):

$$\begin{aligned} \dot{Q}_{HX1stA} &= (1 - \varepsilon_{HX1}) \cdot \dot{Q}_{HX1MAX} - \dot{m} \cdot \bar{c}_p \cdot (T_3 - T_9) \\ &= (1 - \varepsilon_{HX1}) \cdot (\dot{H}_1 - \dot{H}_9) - \dot{m} \cdot \bar{c}_p \cdot (T_3 - T_9) \quad . \end{aligned} \tag{5.27}$$

Using Eq. (5.16) results in

$$\dot{Q}_{HX1stA} = \delta T_{HX1} \cdot \dot{m} \cdot \dfrac{h_1 - h_9}{T_1 - T_9} - \dot{m} \cdot \bar{c}_p \cdot \delta T_{HX2} \quad , \tag{5.28}$$

and substituting with Eq. (5.24), Eq. (5.14.6), and $T_5 \approx T_3$ yields

$$\underbrace{\dot{Q}_{\text{HX1stA}}}_{\substack{\text{after-cooling} \\ \text{by HX1stA}}} = \underbrace{\dot{m} \cdot \overline{c}_{\text{p}} \cdot \delta T_{\text{HX1}}}_{\substack{\text{lost opportunity of} \\ \text{heat-power transfer} \\ \text{for HX1}}} - \underbrace{\dot{m} \cdot \overline{c}_{\text{p}} \cdot \delta T_{\text{HX2}}}_{\substack{\text{lost opportunity of} \\ \text{heat-power transfer} \\ \text{for HX2}}} \quad , \tag{5.29}$$

where the first and second term correspond to the lost opportunity for heat transfer on recuperators HX1 and HX2. This indicates that the after-cooling required by thermalisator HX1stA ($\dot{Q}_{\text{HX1stA}}$) is dictated indirectly by the thermal performance of recuperators HX1 and HX2.

From this equation it is derived that $\delta T_{\text{HX1}} \geq \delta T_{\text{HX2}}$, due to the prerequisite that the heat-power extracted by thermalisator HX1stA is zero or positive ($\dot{Q}_{\text{HX1stA}} \geq 0$). Later, it is shown that the special case of $\delta T_{\text{HX1}} = \delta T_{\text{HX2}}$ corresponds to an atypical scenario for Region I, since no cooling power is spent by thermalisator HX1stA ($\dot{Q}_{\text{HX1stA}} = 0$).

It will be shown that the refrigeration power $\dot{Q}_{\text{R}}^{I}$ and the transmission efficiency η_{TP}^{I} are both affected by the thermal performance of recuperator HX1, which is defined through the free design parameter δT_{HX1}. First, the refrigeration power $\dot{Q}_{\text{R}}^{I}$ is expressed as the total change in enthalpy rate along Circuit I

$$\dot{Q}_{\text{R}}^{I} = \dot{H}_4 - \dot{H}_3 \quad . \tag{5.30}$$

Due to the relationships $\delta T_{\text{HX1A}} \approx \delta T_{\text{HX1B}} \lesssim 0.1 \, \text{K} \ll T_{1st}$, it can be safely assumed that $T_3 \approx T_5$, and therefore that $\dot{H}_3 \approx \dot{H}_5$. Consequently, the substitution of Eq. (5.14.8), and then of Eq. (5.14.9), into Eq. (5.30) yields

$$\dot{Q}_{\text{R}}^{I} \approx \dot{H}_4 - \dot{H}_5 = \underbrace{\dot{Q}_{\text{HX1stB}}}_{\substack{\text{extraction of} \\ \text{heat power} \\ \text{from Circuit I}}} = \underbrace{\eta_{\text{CSS}}^{I} \cdot \dot{Q}_{\text{1st}}}_{\substack{\text{available} \\ \text{1st stage} \\ \text{power}}} - \underbrace{\dot{Q}_{\text{HX1stA}}}_{\substack{\text{after-cooling} \\ \text{by HX1stA}}} \quad , \tag{5.31}$$

confirming that the only duty of the thermalisator HX1stB ($\dot{Q}_{\text{HX1stB}}$) is to extract the heat power previously absorbed from Circuit I ($\dot{Q}_{\text{R}}^{I}$), and that the refrigeration power available for Circuit I ($\eta_{\text{CSS}}^{I} \cdot \dot{Q}_{\text{1st}}$) is only diminished by the after-cooling in thermalisator HX1stA ($\dot{Q}_{\text{HXst1A}}$). Finally, the refrigeration power $\dot{Q}_{\text{R}}^{I}$ is expressed as a function of the free design parameter δT_{HX1} by substituting Eq. (5.31) with Eq. (5.30):

$$\dot{Q}_{\text{R}}^{I} \approx \eta_{\text{CSS}}^{I} \cdot \dot{Q}_{\text{1st}} - (\delta T_{\text{HX1}} - \delta T_{\text{HX2}}) \cdot \dot{m} \cdot \overline{c}_{\text{p}} \quad , \tag{5.32}$$

with the transmission efficiency η_{TP}^{I} being

$$\eta_{\text{TP}}^{I} = \frac{\dot{Q}_{\text{R}}^{I}}{\eta_{\text{CSS}}^{I} \cdot \dot{Q}_{\text{1st}}} \approx 1 - \frac{(\delta T_{\text{HX1}} - \delta T_{\text{HX2}}) \cdot \dot{m} \cdot \overline{c}_{\text{p}}}{\eta_{\text{CSS}}^{I} \cdot \dot{Q}_{\text{1st}}} \leq 1 \quad . \tag{5.33}$$

The equations indicate that both terms, $\dot{Q}_{\text{R}}^{I}$ and η_{TP}^{I}, have the following dependencies:

I. To the heat-power extracted by thermalisator HX1stA, the value of which is strongly driven by the design parameter δT_{HX1};
II. To the fraction of 1st stage power that remains available after compensating from external heat sources $\eta_{\text{CSS}}^{I} \cdot \dot{Q}_{\text{1st}}$;
III. To two parameters imposed by the system of linear equations and the parameter-values of Region II (chapter 5.2.3): the mass flow $\dot{m}$ explicitly, and the 2nd-stage temperature T_{2nd} implicitly through $\dot{Q}_{\text{1st}}[T_{\text{2nd}}]$.

A further analysis shows that the free design parameter δT_{HX1} is confined to the following range

$$\delta T_{HX2} \leq \delta T_{HX1} \leq \frac{\eta_{CSS}^{I} \cdot \dot{Q}_{1st}}{\dot{m} \cdot \bar{c}_{p}} + \delta T_{HX2} \quad , \tag{5.34}$$

where each boundary is the result of a different limiting condition. The lower boundary derives from the prerequisite in Eq. (5.29) that thermalisator HX1stA shall extract heat-power from the system ($\dot{Q}_{HX1stA} \geq 0$). The higher boundary is dictated by Eq. (5.32) from the consideration that the fluid in Circuit I shall absorb heat-power from the client system ($\dot{Q}_{R}^{I} \geq 0$).

Implementing the parameter values of Table 5.3 into Eq. (5.34) yields

$$0.5 \text{ K} \leq \delta T_{HX1} \leq \frac{6.43 \text{ g s}^{-1} \text{ K}}{\dot{m}} + 0.5 \text{ K} \quad , \tag{5.34b}$$

which corresponds to the range of permissible values for the mass flow $\dot{m}$ and the free design parameter δT_{HX1}. As it will be shown in the following figures, this range defines the valid function domain of the refrigeration power $\dot{Q}_{R}^{I}$.

Figure 5.9 shows a contour map of the refrigeration power $\dot{Q}_{R}^{I}$ as a function of mass flow $\dot{m}$ and local temperature difference δT_{HX1}. The contour map is based on Eq. (5.32), and the grey area indicates the valid graph domain based on Eq. (5.34b).

For $\delta T_{HX1} > 0.5$ K, the refrigeration power $\dot{Q}_{R}^{I}$ decreases as the product $\delta T_{HX1} \cdot \dot{m}$ increases. As shown in Eq. (5.29) and Eq. (5.32), this is because the available cooling-power for Circuit I is rapidly depleted by thermalisator HX1stA, the value of which depends on the lost opportunity for heat transfer in recuperator HX1 ($\sim \delta T_{HX1} \cdot \dot{m}$). For the special case of $\delta T_{HX1} = 0.5$ K, the refrigeration power $\dot{Q}_{R}^{I}$ is independent from the mass flow $\dot{m}$ attaining a constant maximal value of 33.35 W.
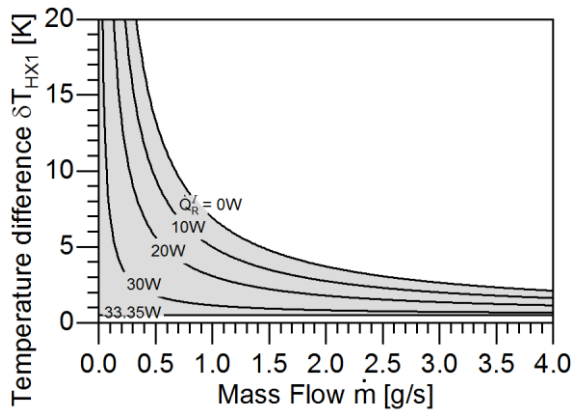
Figure 5.9. Contour map of the refrigeration power $\dot{Q}_{R}^{I}$ over the mass flow $\dot{m}$ and the local temperature difference δT_{HX1} (free design parameter). The relationship results from synergetic effects originating in recuperator HX1.
The valid graph domain (grey area) derives from Eq. (5.34).

Figure 5.10 shows three contour maps of the refrigeration power $\dot{Q}_{R}^{I}$ as a function of the mass flow $\dot{m}$ and the thermal performance of recuperator HX1; the latter expressed in terms of a) effectiveness ε_{HX1}, b) Number of Transfer Units NTU_{HX1}, and c) exergetic effiency ζ_{HX1}. As shown in Eqs. (5.16) to (5.18), the thermal performance of recuperator HX1 increases with lower values of δT_{HX1} (dashed lines) and is independent from the mass flow $\dot{m}$.

For a given refrigeration power $\dot{Q}_{R}^{I}$, decreasing the free design parameter δT_{HX1} or increasing the mass flow $\dot{m}$ results in more demanding thermal requirements for recuperator HX1. This is due to the role of recuperator HX1, and the rise of its heat exchange duty $\dot{Q}_{HX1}$ by increasing mass flow $\dot{m}$, so that the penalization of its inherent "inefficiency" rises as well.

a)

b)

c)
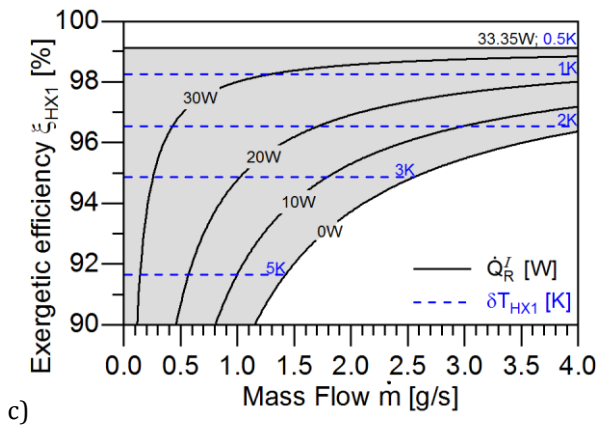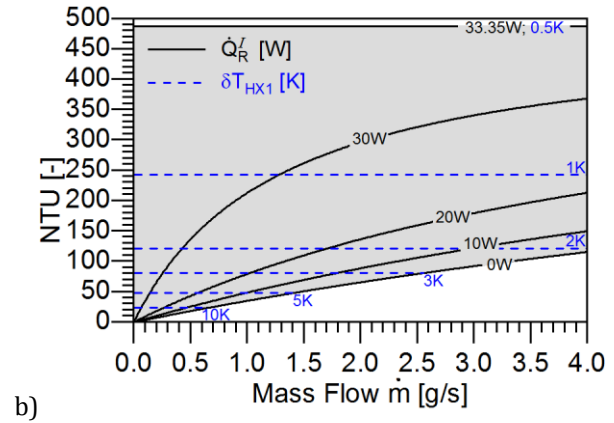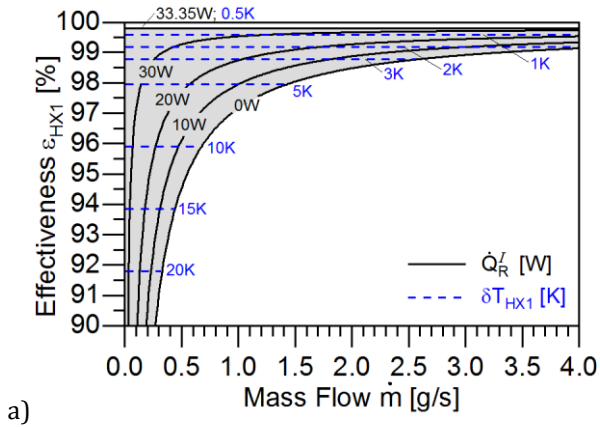
Figure 5.10. Requirements in thermal performance for recuperator HX1 (ε_{HX1}, NTU_{HX1}, ζ_{HX1}) are dictated by the local temperature difference δT_{HX1} (also free design parameter). The provided refrigeration power $\dot{Q}_R^I$ diminishes by increasing mass flow $\dot{m}$, the value of which is defined by Region II.
The valid graph domain (grey area) derives from Eq. (5.34).

Four parameters that describe the cooling capabilities of Region I are the refrigeration power $\dot{Q}_R^I$ and transmission efficiency η_{TP}^I in terms of energy, and the exergetic power $\dot{E}_R^I$ and exergetic efficiency ζ_{TP}^I in terms of exergy. Their respective equations are summarised in Table 5.5, and show that each "parameter-pair" is direct proportional to each other ($\dot{Q}_R^I \propto \eta_{TP}^I$; $\dot{E}_R^I \propto \zeta_{TP}^I$). Figure 5.11 shows the four parameters plotted as a function of mass flow $\dot{m}$ for different constant values of δT_{HX1} (solid lines) and $\dot{Q}_R^I$ (dashed lines); chart a) shows the energetic parameters ($\dot{Q}_R^I$, η_{TP}^I), and chart b) the exergetic parameters ($\dot{E}_R^I$, ζ_{TP}^I).

The refrigeration power $\dot{Q}_R^I$ decreases linearly for increasing mass flow $\dot{m}$ and constant values of $\delta T_{HX1} > 0.5$ K (chart a). However, for the special case of $\delta T_{HX1} = 0.5$ K, the refrigeration power $\dot{Q}_R^I$ remains at a maximal value of 33.35 W, independent of the mass flow $\dot{m}$; this corresponds to the maximal transmission efficiency η_{TP}^I of 100 %. The cause of this dependency derives from the effect described previously in Eq. (5.29), where both parameters (δT_{HX1}, $\dot{m}$) define the amount of 1st-stage cooling-power spent by thermalisator HX1stA.

For increasing mass flow $\dot{m}$ and constant values of $\dot{Q}_R^I$, the amount of exergetic power $\dot{E}_R^I$ provided to Circuit I increases sharply, stabilises quickly, and then grows asymptotically (dashed lines in chart b). The behaviour depends greatly on the temperature change experienced by the fluid during the heat-power transfer in Circuit I, the value of which is inverse proportional to the mass flow $\dot{m}$; (T_4-$T_3 \sim \dot{Q}_R^I/\dot{m}$). The sharp increase at low values of $\dot{m}$ comes from a very small stream experiencing a huge change in specific entropy, due to a significant increase in temperature ($\Delta s_{3 \to 4} \sim \ln(T_4/T_3)$). A further increase in mass flow $\dot{m}$ leads to a smaller temperature change ($\Delta T_{3 \to 4}$), and therefore, to a much lower entropy change ($\Delta s_{3 \to 4}$). The asymptotic growth at high values of $\dot{m}$ comes from a relative large stream experiencing a minor

change in specific entropy. For the theoretical case of $\dot{m} \to \infty$, the heat-power transfer becomes isothermal and reversible ($\Delta T_{3 \to 4} \to 0$; $\Delta s_{3 \to 4} \to 0$), and the exergetic power $\dot{E}_R^I$ approaches the limiting value of $\eta_C[T_3] \cdot \dot{Q}_R^I = 5.85 \cdot \dot{Q}_R^I$.

For an increasing mass flow $\dot{m}$ and constant values of $\delta T_{HX1} > 0.5$ K, the amount of exergetic power $\dot{E}_R^I$ provided to Circuit I increases sharply, attains a maximum value, and then decreases steadily towards zero (solid lines in chart b). This behaviour is a combination of the effects described previously: the sharp increase derives from a large change in specific entropy $\Delta s_{3 \to 4}$ (dashed lines in chart b), while the steady decrease originates from a constant depletion of refrigeration power $\dot{Q}_R^I$ (solid lines in chart a). Since the refrigeration power $\dot{Q}_R^I$ is constant for $\delta T_{HX1} = 0.5$ K, the exergetic power $\dot{E}_R^I$ grows monotonically, with the same behaviour as described previously.

a)

b)
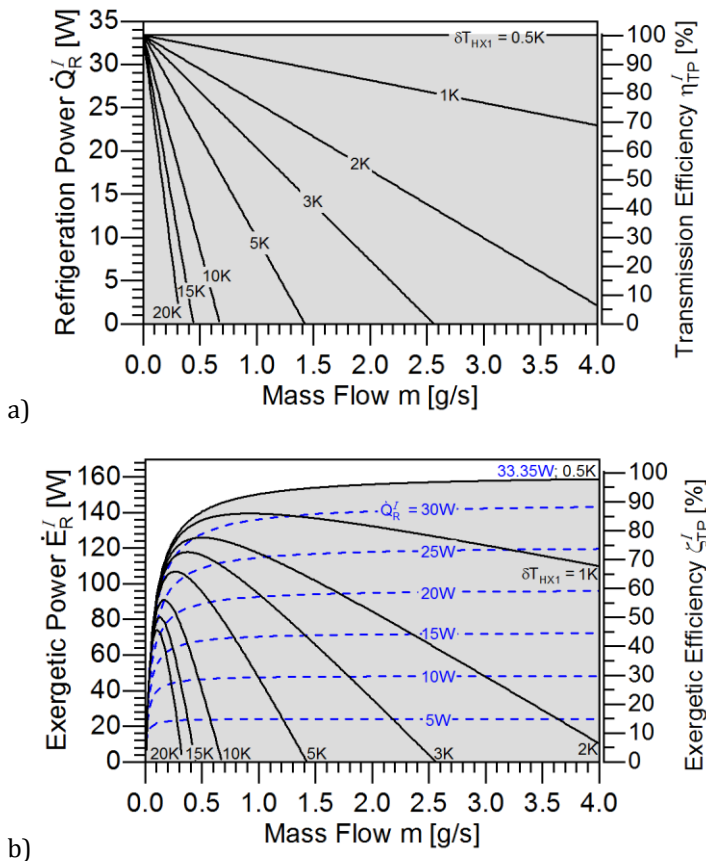
Figure 5.11. Cooling capabilities of Region I as a function of the mass flow $\dot{m}$ (defined by Region II) and the local temperature difference δT_{HX1} (also free design parameter).
The valid graph domain (grey area) derives from Eq. (5.34).

Table 5.5. Parameters describing the cooling capabilities of Region I.

In terms of thermal energy:

(5.32) $$\dot{Q}_R^I = \dot{H}_4 - \dot{H}_3 \approx \eta_{CSS}^I \cdot \dot{Q}_{1st} - (\delta T_{HX1} - \delta T_{HX2}) \cdot \dot{m} \cdot \overline{c_p}$$

(5.33) $$\eta_{TP}^I = \frac{\dot{Q}_R^I}{\eta_{CSS}^I \cdot \dot{Q}_{1st}} \approx 1 - \frac{(\delta T_{HX1} - \delta T_{HX2}) \cdot \dot{m} \cdot \overline{c_p}}{\eta_{CSS}^I \cdot \dot{Q}_{1st}} \leq 1$$

In terms of exergy:

(5.35) $$\dot{E}_R^I = \dot{m} \cdot (e_3 - e_4) = \dot{Q}_R^I + \dot{m} \cdot T_a \cdot \Delta s_{3 \to 4} = \dot{Q}_R^I + \dot{m} \cdot \overline{c_p} \cdot T_a \cdot \ln \frac{T_4}{T_3}$$

$$= \dot{Q}_R^I + \dot{m} \cdot \overline{c_p} \cdot T_a \cdot \ln \left(1 + \frac{\dot{Q}_R^I}{(T_{1st} + \delta T_{HX1stA}) \cdot \dot{m} \cdot \overline{c_p}} \right)$$

(5.36) $$\zeta_{TP}^I = \frac{\dot{E}_R^I}{\zeta_{CSS}^I \cdot \dot{E}_{1st}} = \frac{\dot{E}_R^I}{-\zeta_{CSS}^I \cdot \eta_C[T_{1st}] \cdot \dot{Q}_{1st}} \leq 1$$

It was shown with Eq. (5.32) that the refrigeration power $\dot{Q}_R^I$ depends, to a large extent, on the mass flow $\dot{m}$ and the 2nd-stage temperature T_{2nd}, the values of which are imposed by the equations and parameters of Region II. The relationship between the three parameters is illustrated in Figure 5.12 for various values of the free design parameter δT_{HX1}.

The increase of mass flow $\dot{m}$ or 2nd-stage temperature T_{2nd} results in the decrease of refrigeration power $\dot{Q}_R^I$; a higher mass flow $\dot{m}$ leads to higher thermal losses at the recuperator HX1, and a higher 2nd stage temperature lowers the cooling power provided by the 1st stage. These effects, if too high, can result in the total depletion of the refrigeration power $\dot{Q}_R^I$.
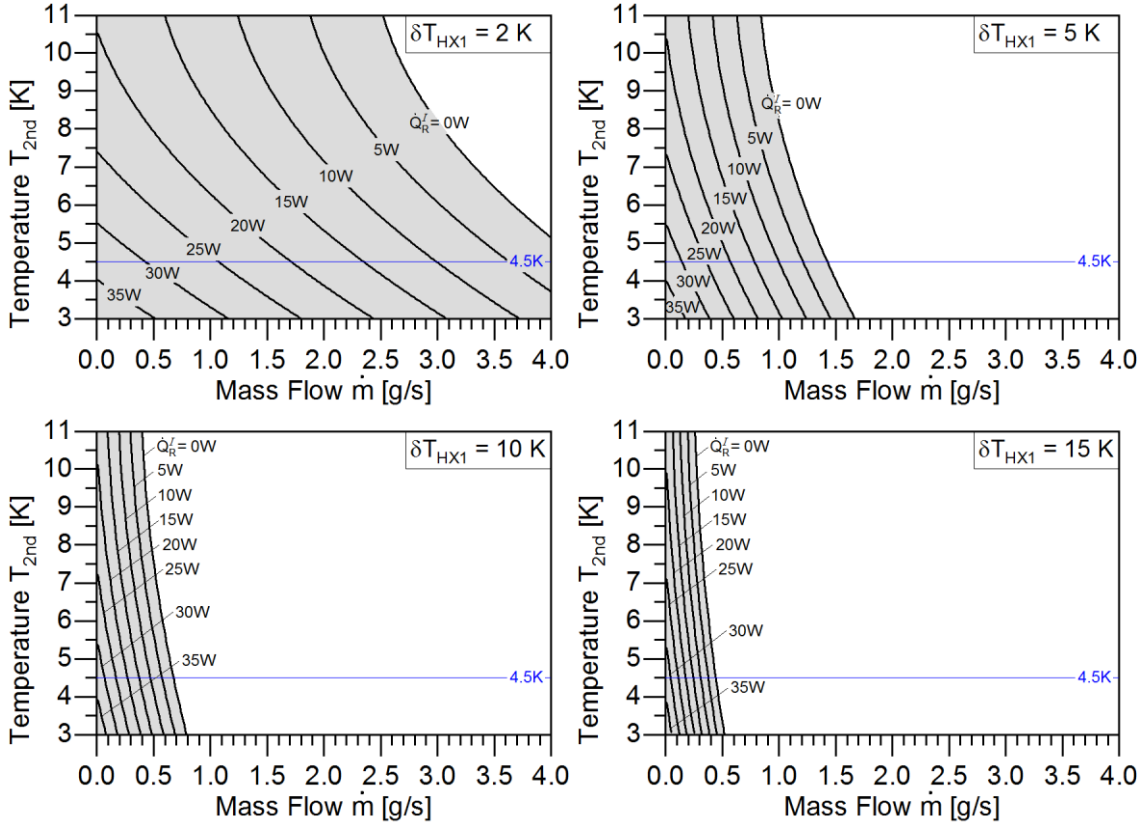
Figure 5.12. Refrigeration power delivered to Circuit I $\dot{Q}_R^I$ (solid lines) for a given pair of mass flow $\dot{m}$ and 2nd stage temperature T_{2nd}. Each plot corresponds to a different local temperature difference δT_{HX1} at the cold side of recuperator HX1, limiting the design parameter range at which $\dot{Q}_R^I$ is greater than zero. The valid graph domain (grey area) derives from Eq. (5.34).

5.2.3 Region II: Lower temperature section

Region II is characterised by its relatively low temperature ($\lesssim T_{1st} = 50$ K). It defines the isothermal refrigeration power $\dot{Q}_R^{II}$ that is provided to Circuit II. This region also defines the 2nd stage temperature T_{2nd}, and establishes the cooling power of both cryocooler stages ($\dot{Q}_{1st}$, $\dot{Q}_{2nd}$) as well. The flow of refrigeration power and exergy (Figure 5.6) is analogous to Region I, so that the transmission efficiencies η_{CSS}^{II} and η_{TP}^{II} also derive from the insulation performance and the process choice. The same is true for the exergetic efficiencies ζ_{CSS}^{II} and ζ_{TP}^{II}. Consequently, the amount of refrigeration power $\dot{Q}_R^{II}$ that the refrigerator provides to Circuit II is

$$\dot{Q}_R^{II} = \eta_{CSS}^{II} \cdot \eta_{TP}^{II} \cdot \dot{Q}_{2nd} \quad , \tag{5.37}$$

with the corresponding exergy flow being

$$\dot{E}_R^{II} = \zeta_{CSS}^{II} \cdot \zeta_{TP}^{II} \cdot \dot{E}_{2nd} \quad . \tag{5.38}$$
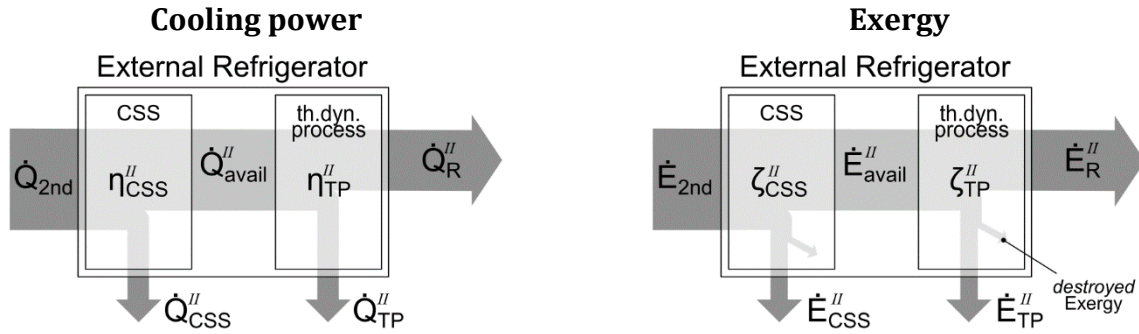
Figure 5.13. Flow of the cooling power and exergy provided by the cryocooler's 2nd stage.

Region II can present five different configurations (CFG0 to CFG4 in Table 5.6), where each configuration is a more complex variant of the previous one. This has the objective to increase the operational temperature of the 2nd stage (T_{2nd}), in order to increment the 2nd stage power $\dot{Q}_{2nd}[T_{2nd}]$, which can potentially result in a higher refrigeration power $\dot{Q}_R^{II}$. Each configuration is analysed individually in the following subchapters, showing that the resulting refrigeration power $\dot{Q}_R^{II}$ depends upon the choice of a particular configuration and its design parameters. The general features of each configuration are listed below.

CFG0: It is the basis of all other configurations and has two interfaces. The first one is connected to Region I, which provides a thermalised supply stream close to $T_{1st} = 50$ K. The supply line is then cooled down to close to the 2nd stage temperature T_{2nd} by the combined effort of recuperator HX2 and the heat exchanger HX2nd. The second interface is connected to Circuit II, and the isothermal refrigeration power $\dot{Q}_R^{II}$ is provided by the two-phase stream at the refrigeration temperature $T_R^{II} = 4.5$ K.
This particular configuration was introduced previously in chapter 5.1 and is the only one where the 2nd stage temperature T_{2nd} is below the refrigeration temperature T_R^{II}.

CFG1: Presents an additional JT expansion step (throttling process) to lower the stream temperature after it has been thermalised at the 2nd stage ($T_{2nd} > T_R^{II}$).

CFG2: Similar to CFG1, but with the addition of recuperator HX3 to further precool the supply stream before its JT expansion.

CFG3: Analogous to CFG2, but with the integration of a JT expansion step in the additional recuperator. This extra feature allows the supply stream to be cooled and expanded at the same time. Such a recuperator is, from now on, referred to as a "Joule-Thomson heat exchanger" (JTHX).

CFG4: Results from the combination of CFG2 and CFG3.

Note that Table 5.6 only includes permutations of the component set {JT; HX3; JTHX} that have been found to be thermodynamically and technically feasible.

Table 5.6. Possible Region-II configurations as obtained from the permutation of system components. Each configuration increases in complexity with respect to the previous one.

		Configuration of Region II				
		CFG0	CFG1	CFG2	CFG3	CFG4
Components	HX2	✓	✓	✓	✓	✓
	HX2nd	✓	✓	✓	✓	✓
	JT	-	✓	✓	✓	✓
	HX3	-	-	✓	-	✓
	JTHX	-	-	-	✓	✓

The four following tables summarize the values and equations used in the thermodynamic analysis of all Region II configurations. Each thermodynamic cycle is fully defined by the set of parameter values in Table 5.7 and the set of linear equations in Table 5.8. The equations to describe the heat exchangers and cooling capabilities of Region II are listed in Table 5.9 and Table 5.10 respectively.

Table 5.7. Summary of process parameters for the analysis of configurations CFG0 to CFG4.

Type	Parameter		CFG0	CFG1	CFG2	CFG3	CFG4	Description
Boundary condition:	T_R^{II}	[K]	4.5	4.5	4.5	4.5	4.5	Refrigeration temperature of Circuit II (at the returning stream).
	T_{1st}	[K]	50	50	50	50	50	Cryocooler's 1st stage temperature.
Model simplification:	Λ	[-]	≪0.01	≪0.01	≪0.01	≪0.01	≪0.01	Negligible longitudinal condition on the heat exchangers.
	η_{CSS}^{II}	[%]	100	100	100	100	100	The entirety of the cryocooler's power $\dot{Q}_{2nd}$ is available for the refrigeration cycle.
	Δp	[bar]	$\Delta p_{5\to9}\approx0$	$\Delta p_{5\to7}\approx0$	$\Delta p_{5\to8}\approx0$	$\Delta p_{5\to7}\approx0$	$\Delta p_{5\to8}\approx0$	Isobaric consideration for low-pressure circuit.
			-	$\Delta p_{8\to10}\approx0$	$\Delta p_{9\to12}\approx0$	$\Delta p_{9\to12}\approx0$	$\Delta p_{10\to14}\approx0$	Isobaric consideration for high-pressure circuit.
Design value:	δT_{HX1stB}	[K]	0.1	0.1	0.1	0.1	0.1	Local temperature difference at the cold end of HX1stB.
	δT_{HX2nd}	[K]	0.2	0.2	0.2	0.2	0.2	Local temperature difference at the cold end of HX2nd.
	δT_{HX2}	[K]	0.5 1)	0.5	0.5	0.5	0.5	Local temperature difference at the warmer end of HX2.
	δT_{HX3}	[K]	-	-	0.25	-	0.25	Local temperature difference at the warmer end of HX3.
	δT_{JTHX}	[K]	-	-	-	0.25	0.25	Local temperature difference at the warmer end of JTHX.
	x	[%]	0	2)	2)	2)	2)	Vapour quality of incoming flow to Circuit II.
			100	100	100	100	100	Vapour quality of returning flow from Circuit II.
	p_{MP}	[bar]	-	-	-	2.74	2.74	Medium-pressure is inversion pressure at the colder outlet of JTHX. (Value for δT=0.25 at the colder end of JTHX.)
	T_{INV}	[K]	-	$T_{7,INV}[p_{HP}]$	$T_{8,INV}[p_{HP}]$	$T_{8,INV}[p_{MP}]$	$T_{9,INV}[p_{MP}]$	Lower inversion temperature ($\mu_{JT}=0$) prior JT expansion.
			-	-	-	$T_{7,INV}[p_{HP}]$	$T_{8,INV}[p_{HP}]$	Lower inversion temperature ($\mu_{JT}=0$) prior JTHX.
Free design parameter (range):	δT_{HX2}	[K]	0 → 1	-	-	-	-	Local temperature difference at the warmer end of HX2.
	p_{HP}	[bar]	-	1.87 → 13.4	2.74 → 13.4	p_{MP} → 25.3	p_{MP} → 25.3	High-pressure is inversion pressure prior first isenthalpic expansion (at JTHX, otherwise at JT expansion step).
Others:	p_{sat}	[bar]	1.303	1.303	1.303	1.303	1.303	Saturation pressure at T_R^{II} = 4.5 K.
	h_{evap}	[J/g]	18.82	18.82	18.82	18.82	18.82	Evaporation enthalpy at T_R^{II} = 4.5 K.

1) Although a free design parameter, fix parameter value used in further analysis and design. 2) Not a design parameter.

Table 5.8. System of linear equations describing configurations CFG0 to CFG4.

Description	Eq.	CFG0 (5.39._)	CFG1 (5.40._)	CFG2 (5.41._)	CFG3 (5.42._)	CFG4 (5.43._)
Free design parameter	(_._.1)	$\delta T_{HX2} = T_9 - T_5$	$p_{HP} = p_7$	$p_{HP} = p_8$	$p_{HP} = p_7$	$p_{HP} = p_8$
Temp. from Region I	(_._.2)	$T_5 = T_{1st} + \delta T_{HX1stB}$	as CFG0	as CFG0	as CFG0	as CFG0
Δh on HX2	(_._.3)	$h_6 = h_5 - (h_9 - h_8)$	$h_6 = h_5 - (h_{10} - h_9)$	$h_6 = h_5 - (h_{12} - h_{11})$	as CFG2	$h_6 = h_5 - (h_{14} - h_{13})$
Δh on HX3	(_._.4)	-	-	$h_7 = h_8 + (h_{11} - h_{10})$	-	$h_7 = h_8 + (h_{13} - h_{12})$
Δh on JTHX	(_._.5)	-	-	-	$h_{11} = h_{10} + (h_7 - h_8)$	$h_{12} = h_{11} + (h_8 - h_9)$
δT on warm end of HX2	(_._.6)	$T_9 = T_5 - \delta T_{HX2}$ [1)]	$T_{10} = T_5 - \delta T_{HX2}$	$T_{12} = T_5 - \delta T_{HX2}$	as CFG2	$T_{14} = T_5 - \delta T_{HX2}$
δT on warm end of HX3	(_._.7)	-	-	$T_{11} = T_7 - \delta T_{HX3}$	-	$T_{13} = T_7 - \delta T_{HX3}$
δT on warm end of JTHX	(_._.8)	-	-	-	$T_{11} = T_7 - \delta T_{JTHX}$ [1)]	$T_{12} = T_7 - \delta T_{JTHX}$ [1)]
T_{INV} prior JTHX	(_._.9)	-	-	-	$T_7 = T[p_{HP}, \mu_{JT} = 0]$	$T_8 = T_{8,INV} = f(p_{HP})$
T_{INV} prior JT expansion	(_._.10)	-	$T_7 = T[p_{HP}, \mu_{JT} = 0]$	$T_8 = T[p_{HP}, \mu_{JT} = 0]$	$T_8 = T[p_{MP}, \mu_{JT} = 0]$	$T_9 = T_{9,INV} = f(p_{MP})$
Isenthalpic expansion	(_._.11)	-	$h_8 = h_7[p_{HP}, T_7]$	$h_9 = h_8[p_{HP}, T_8]$	$h_9 = h_8[p_{MP}, T_8]$	$h_{10} = h_9[p_{MP}, T_9]$
Isothermal evaporation	(_._.12)	$T_8 = T_7$	$T_8 = T_9$ [1)]	$T_9 = T_{10}$ [1)]	as CFG2	$T_{10} = T_9$ [1)]
Saturation pressure p_{sat}	(_._.13)	$p_8 = p[[T_8, x_8]$	$p_9 = p[T_9, x_9]$	$p_{10} = p[T_{10}, x_{10}]$	as CFG2	$p_{11} = p[T_{11}, x_{11}]$
2nd stage temperature T_{2nd}	(_._.14)	$T_{2nd} = T_7 - \delta T_{HX2nd}$	as CFG0	as CFG0	as CFG0	as CFG0
Mass flow $\dot m$	(_._.15)	$\dot m = \frac{\dot Q_{HX2nd}}{h_6 - h_7}$	as CFG0	as CFG0	as CFG0	as CFG0
Available cryocooler power	(_._.16)	$\eta_{CSS}^{II} \cdot \dot Q_{2nd} = \dot Q_{HX2nd}$	as CFG0	as CFG0	as CFG0	as CFG0
Low-pressure points p_{LP}	(_._.17)	$p_{i=5,6,7,8,9}$	$p_{i=8,9,10}$	$p_{i=9,10,11,12}$	as CFG2	$p_{i=10,11,12,13,14}$
Medium-pressure points p_{MP}	(_._.18)	-	-	-	p_8	p_9
High-pressure points p_{HP}	(_._.19)	-	$p_{i=5,6,7}$	$p_{i=5,6,7,8}$	$p_{i=5,6,7}$	$p_{i=5,6,7,8}$

1) For information only, since redundant to solve the system of linear equations.

Table 5.9. Terms describing the heat exchangers on configurations CFG0 to CFG4.

	General expression	CFG0	CFG1	CFG2	CFG3	CFG4
Eq.	(_._.1)	(_._.2)	(_._.3)	(_._.4)	(_._.5)	(_._.6)
	Recuperator HX2:					
(5.44._)	$\dot{Q}_{HX2} = \dot{H}_{h,IN} - \dot{H}_{h,OUT}$	$\dot{m} \cdot (h_5 - h_6)$	$\dot{m} \cdot \underbrace{(h_{10} - h_9)}_{\neq f(p_{HP})}$	$\dot{m} \cdot (h_{12} - h_{11})$	as CFG2	$\dot{m} \cdot (h_5 - h_6)$
(5.45._)	$\varepsilon_{HX2} = \dfrac{T_{c,OUT} - T_{c,IN}}{T_{h,IN} - T_{c,IN}}$	$1 - \dfrac{\delta T_{HX2}}{T_{1st} + \delta T_{HX1stB} - T_R^{II}}$	as CFG0 $\neq f(p_{HP})$	$1 - \dfrac{\delta T_{HX2}}{T_{1st} + \delta T_{HX1stB} - T_{11}}$	as CFG2	$1 - \dfrac{\delta T_{HX2}}{T_{1st} + \delta T_{HX1stB} - T_{13}}$
(5.46._)	$\zeta_{HX2} = \dfrac{e_{h,OUT} - e_{h,IN}}{e_{c,IN} - e_{c,OUT}}$	$\dfrac{e_6 - e_5}{e_8 - e_9}$	$\dfrac{e_6 - e_5}{e_9 - e_{10}}$	$\dfrac{e_6 - e_5}{e_{11} - e_{12}}$	as CFG2	$\dfrac{e_6 - e_5}{e_{13} - e_{14}}$
	Thermalisator HX2nd:					
(5.47._)	$\dot{Q}_{HX2nd} = \dot{H}_{IN} - \dot{H}_{OUT}$	$\dot{m} \cdot (h_6 - h_7)$	as CFG0	as CFG0	as CFG0	as CFG0
(5.48._)	$\varepsilon_{HX2nd} = \dfrac{T_{IN} - T_{OUT}}{T_{OUT} - T_{2nd}}$	$1 - \dfrac{\delta T_{HX2nd}}{T_6 - T_{2nd}}$	as CFG0	as CFG0	as CFG0	as CFG0
(5.49._)	$\zeta_{HX2nd} = \dfrac{\dot{m} \cdot (e_{IN} - e_{OUT})}{\eta_C[T_{2nd}] \cdot \dot{Q}_{HX2nd}}$	$\eta_C^{-1}[T_{1st}] \cdot \left(1 - \dfrac{T_a \cdot \Delta s_{7\to6}}{\eta_{CSS}^{II} \cdot \dot{Q}_{2nd}}\right)$	as CFG0	as CFG0	as CFG0	as CFG0
	Recuperator HX3:					
(5.50._)	$\dot{Q}_{HX3} = \dot{H}_{h,IN} - \dot{H}_{h,OUT}$	-	-	$\dot{m} \cdot (h_7 - h_{8,INV}[p_{HP}])$	-	as CFG2
(5.51._)	$\varepsilon_{HX3} = \dfrac{T_{c,OUT} - T_{c,IN}}{T_{h,IN} - T_{c,IN}}$	-	-	$1 - \dfrac{\delta T_{HX3}}{T_7 - T_{10}}$	-	$1 - \dfrac{\delta T_{HX3}}{T_7 - T_{12}}$
(5.52._)	$\zeta_{HX3} = \dfrac{e_{h,OUT} - e_{h,IN}}{e_{c,IN} - e_{c,OUT}}$	-	-	$\dfrac{e_8 - e_7}{e_{10} - e_{11}}$	-	$\dfrac{e_8 - e_7}{e_{12} - e_{13}}$
	Recuperator JTHX:					
(5.53._)	$\dot{Q}_{JTHX} = \dot{H}_{h,IN} - \dot{H}_{h,OUT}$	-	-	-	$\dot{m} \cdot (h_{7,INV}[p_{HP}] - h_{8,INV}[p_{HP}])$	$\dot{m} \cdot (h_{8,INV}[p_{HP}] - h_{9,INV}[p_{HP}])$
(5.54._)	$\varepsilon_{JTHX} = \dfrac{T_{c,OUT} - T_{c,IN}}{T_{h,IN} - T_{c,IN}}$	-	-	-	$1 - \dfrac{\delta T_{JTHX}}{T_7 - T_{10}}$	$1 - \dfrac{\delta T_{JTHX}}{T_8 - T_{11}}$
(5.55._)	$\zeta_{JTHX} = \dfrac{e_{h,OUT} - e_{h,IN}}{e_{c,IN} - e_{c,OUT}}$	-	-	-	$\dfrac{e_8 - e_7}{e_{10} - e_{11}}$	$\dfrac{e_9 - e_8}{e_{11} - e_{12}}$

Table 5.10. Terms describing the cooling capabilities of configurations CFG0 to CFG4.

	General expression	CFG0	CFG1	CFG2	CFG3	CFG4
Eq.	(_._.1)	(_._.2)	(_._.3)	(_._.4)	(_._.5)	(_._.6)
	In terms of thermal energy:					
(5.56._)	$\dot{Q}_R^{II} = \dot{m} \cdot h_{evap} \cdot \Delta x$	$\dot{m} \cdot h_{evap}[T_8] \cdot (x_8 - x_7)$	$\dot{m} \cdot h_{evap} \cdot (x_9 - x_8)$	$\dot{m} \cdot h_{evap} \cdot (x_{10} - x_9)$	as CFG2	$\dot{m} \cdot h_{evap} \cdot (x_{11} - x_{10})$
(5.57._)	$\eta_{TP}^{II} = \dfrac{\dot{Q}_R^{II}}{\eta_{CSS}^{II} \cdot \dot{Q}_{2nd}} \leq 1$ $\neq \boldsymbol{f}(\dot{Q}_{2nd}, \dot{Q}_{1st})$	$h_{evap} \cdot \dfrac{(x_8 - x_7)}{h_6 - h_7}$	$h_{evap} \cdot \dfrac{(x_9 - x_8)}{h_6 - h_7}$	$h_{evap} \cdot \dfrac{(x_{10} - x_9)}{h_6 - h_7}$	as CFG2	$h_{evap} \cdot \dfrac{(x_{11} - x_{10})}{h_6 - h_7}$
	In terms of exergy:					
(5.58._)	$\dot{E}_R^{II} = \dot{m} \cdot \Delta e$	$-\dot{Q}_R^{II} + \dot{m} \cdot T_a \cdot \Delta s_{7 \to 8}$	$-\dot{Q}_R^{II} + \dot{m} \cdot T_a \cdot \Delta s_{8 \to 9}$	$-\dot{Q}_R^{II} + \dot{m} \cdot T_a \cdot \Delta s_{9 \to 10}$	as CFG2	$-\dot{Q}_R^{II} + \dot{m} \cdot T_a \cdot \Delta s_{10 \to 11}$
(5.59._)	$\zeta_{TP}^{II} = \dfrac{\dot{E}_R^{II}}{\zeta_{CSS}^{II} \cdot \dot{E}_{2nd}} \leq 1$	$\dfrac{\dot{E}_R^{II}}{-\zeta_{CSS}^{II} \cdot \eta_C[T_{2nd}] \cdot \dot{Q}_{2nd}}$	$\dfrac{\dot{E}_R^{II}}{-\zeta_{CSS}^{II} \cdot \eta_C[T_{2nd}] \cdot \dot{Q}_{2nd}}$	$\dfrac{\dot{E}_R^{II}}{-\zeta_{CSS}^{II} \cdot \eta_C[T_{2nd}] \cdot \dot{Q}_{2nd}}$	as CFG2	$\dfrac{\dot{E}_R^{II}}{-\zeta_{CSS}^{II} \cdot \eta_C[T_{2nd}] \cdot \dot{Q}_{2nd}}$

5.2.3.1 CFG0: Basic configuration

Configuration CFG0 is the basis of all other configurations and comprises of recuperator HX2 and thermalisator HX2nd. Figure 5.14 illustrates the flow diagram and temperature profile used for the thermodynamic analysis of this configuration. The refrigeration cycle is fully described by the set of parameter values and the system of linear equations listed previously in Table 5.7 and Table 5.8, where the local temperature difference δT_{HX2} at the warm end of recuperator HX2 is defined as the free design parameter.
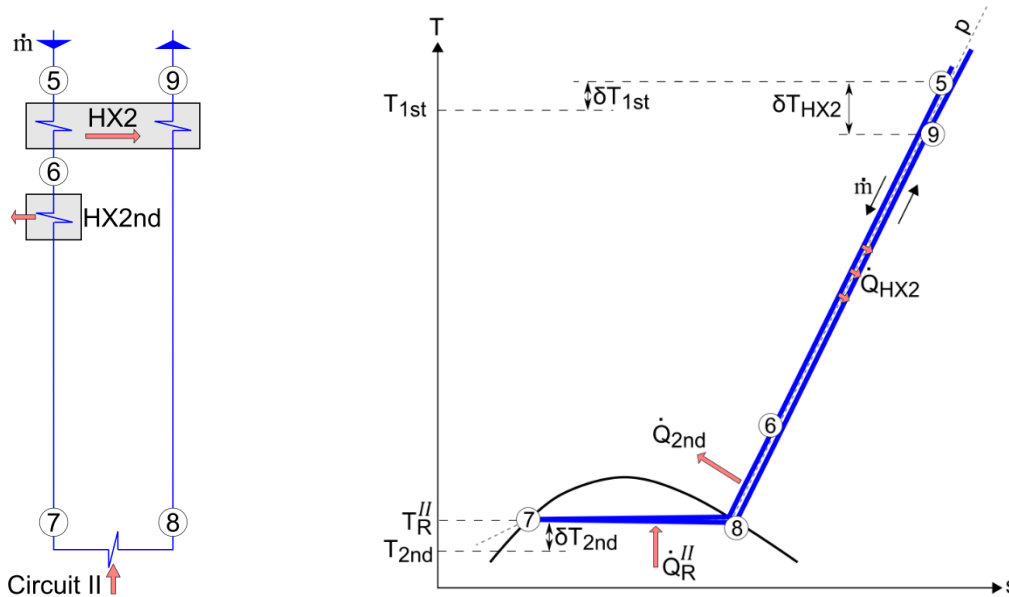
Figure 5.14. Segment of the flow chart (left) and T-s diagram (right) of configuration CFG0. This basic configuration does not comprise any additional component.

The fluid state expressions listed on Table 5.11 show that the enthalpies h_5, h_7 and h_8 are all fully defined by the parameter values on Table 5.7, while the enthalpies h_6 and h_9 are a function of the free design parameter δT_{HX2}.

Table 5.11. Non-extensive list of fluid state expressions used for the analysis of configuration CFG0. The expressions are either fully defined through the values in Table 5.7 or a function of the free design parameter δT_{HX2}.

Fully defined		Function of δT_{HX2}	
(5.60)	$h_5 = h_5[p_5, T_5] = h_5[p_8, T_{1st} + \delta T_{HX1stB}]$	(5.39.3)	$h_6 = h_5 - \left(h_9 - h_8[T_R^{II}, x_8]\right)$
(5.61)	$h_7 = h_7[T_R^{II}, x_7]$	(5.62)	$h_9 = h_9[p_8, T_{1st} + \delta T_{HX1stB} - \delta T_{HX2}]$
(5.63)	$h_8 = h_8[T_R^{II}, x_8]$		

The equations describing heat exchangers HX2 and HX2nd were listed in Table 5.9. The heat exchange duties $\dot{Q}_{HX2}$ and $\dot{Q}_{HX2nd}$ correspond to the respective decrease in entropy rate of the incoming stream. The effectiveness and exergetic efficiency are expressed according to the definitions of Eq. (3.37) and Eq. (3.43).

By design, the thermalisator HX2nd acts partially as a *condenser*, generating liquid helium at the refrigeration temperature $T_R^{II} = T_8$. In addition, and based on Eqs. (5.39.15-16), this heat exchanger is what relates the required mass flow $\dot{m}$ to the available 2nd stage power ($\eta_{CSS}^{II} \cdot \dot{Q}_{2nd}$). The mass flow $\dot{m}$ is a function from the enthalpy h_6, hence it is implicitly dependent on the free design parameter δT_{HX2}.

Since helium is assumed to behave as a real-gas within Region II, Table 5.9 does not show any specific equation for NTU because this would require the previous definition of the exchangers' geometry. The reason is that the NTU results from the integrated relationship between geometrical and temperature dependent terms ($U/\dot{C}$) along the heat exchanger (chapter 3.3.2).

The equations describing the cooling capabilities of configuration CFG0 were listed in Table 5.10. The supply of refrigeration power $\dot{Q}_R^{II}$ to Circuit II is accompanied by a flow of exergetic power $\dot{E}_R^{II}$ with the corresponding exergetic efficiency ζ_{TP}^{II}. The refrigeration power $\dot{Q}_R^{II}$ corresponds to the amount of evaporated liquid in Circuit II (⑦→⑧), where $h_{evap}[T_8]$ is the evaporation enthalpy of helium at the temperature T_8.

The substitution of Eq. (5.61) and Eq. (5.39.3) into Eq. (5.57.2) shows that the transmission efficiency η_{TP}^{II} is a function of the parameter set $\{T_R^{II}, p_8, T_{1st}, \delta T_{HX1stB}, \delta T_{HX2}, x_8, x_7\}$. All parameters in the set derive, directly or indirectly, from the definition of the thermodynamic cycle and are independent from the cryocooler's stage-power. This makes the transmission efficiency η_{TP}^{II} *cryocooler-independent*. The same is not true for the refrigeration power $\dot{Q}_R^{II}$ since it is a function of the cryocooler-dependent mass flow $\dot{m}$.

The calculated values of selected process parameters are presented in Figure 5.16a-f as a function of the free design parameter δT_{HX2}, with their corresponding relationships illustrated in Figure 5.15. The calculation uncertainty is shown in terms of *95 % confidence bands,* and applies to cryocooler-dependent parameters (d-f), as well as the transmission efficiency (c).

An increase in the local temperature difference δT_{HX2} reduces the HX2 effectiveness ε_{HX2} (a) and increases the enthalpy h_6. Consequently, as the recuperator HX2 extracts less specific energy from the incoming stream $|\Delta h_{5\to6}|$ (b), the amount of specific energy to be extracted by the 2nd stage $|\Delta h_{6\to7}|$ (b) becomes larger, which results in a reduction of mass flow $\dot{m}$ (d) since the 2nd stage power $\dot{Q}_{2nd}[T_{1st}, T_{2nd}]$ (f) remains constant at 1.45 W. Both, a decreasing mass flow $\dot{m}$ (d), and a decreasing enthalpy difference $|\Delta h_{5\to6}|$ (b), result in a strong decrease of heat power $\dot{Q}_{HX2}$ (e) to be transferred by the recuperator. The transmission efficiency η_{TP}^{II} (c) decreases because the amount of specific energy extracted by the 2nd stage $|\Delta h_{5\to6}|$ (b) increases while the evaporation enthalpy of the fluid $h_{evap}[T_R^{II}]$ remains constant at 18.82 J/g. This results in a decrease of the refrigeration power $\dot{Q}_R^{II}$ (f), since the transmission efficiency η_{TP}^{II} (c) decreases while the 2nd stage power $\dot{Q}_{2nd}$ (e) remains constant. In conclusion, the thermal design of recuperator HX2 has a significant impact on the final refrigeration power $\dot{Q}_R^{II}$ (f). For example, an effectiveness ε_{HX2} (a) of 98.9 % (δT_{HX2} = 0.5 K) is necessary to obtain an 87.9% of transmission efficiency η_{TP}^{II} (c), leading to a refrigeration power $\dot{Q}_R^{II}$ of 1.27 W (f).
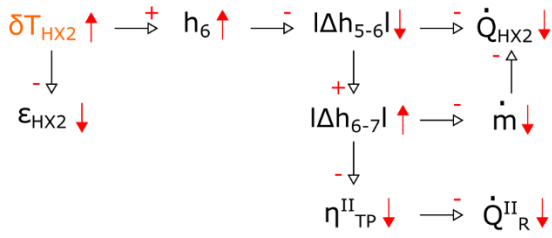
Figure 5.15. Relationship of process parameters as a function of the local temperature difference δT_{HX2} for configuration CFG0.
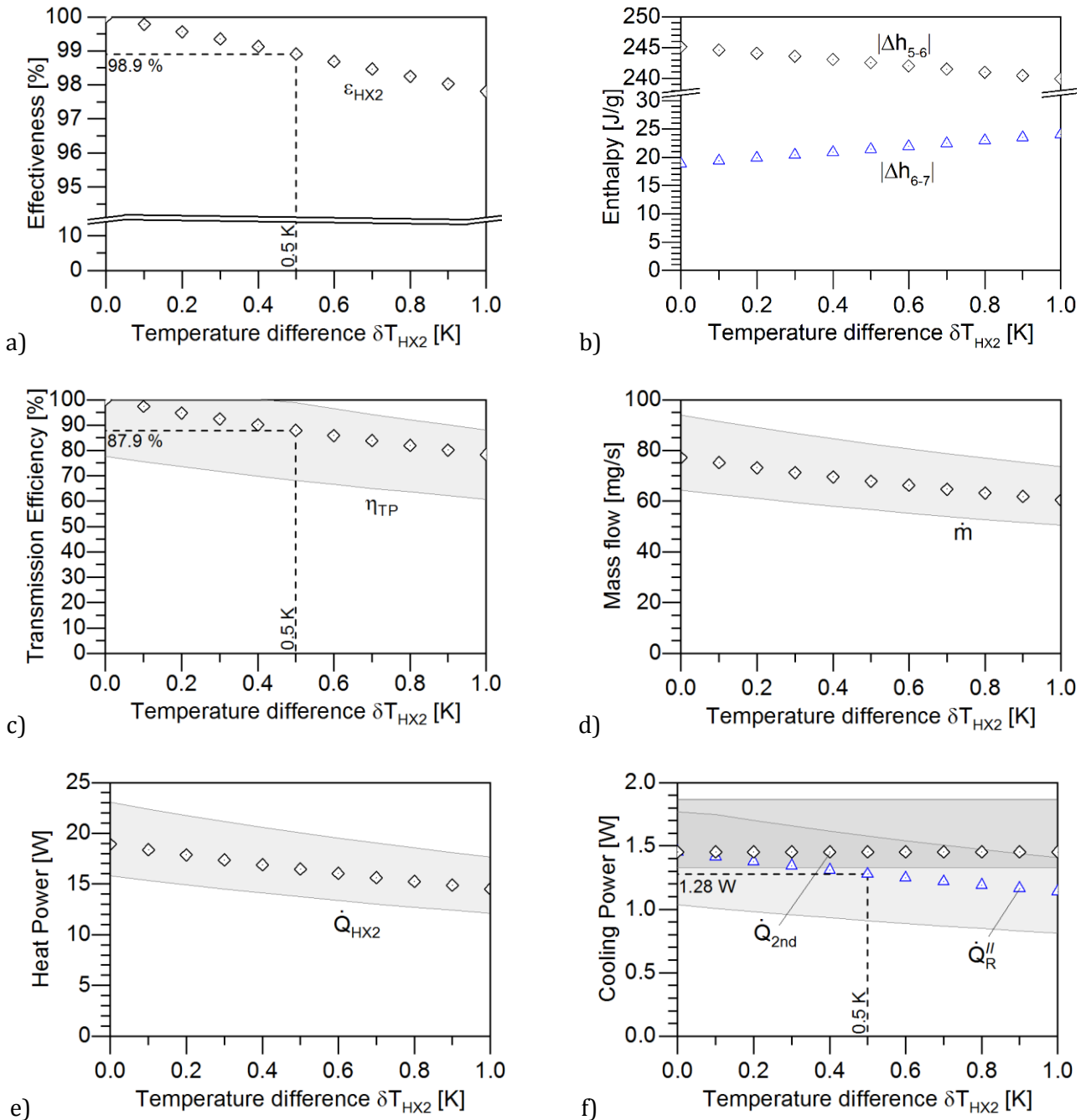
Figure 5.16. Calculated process parameters of configuration CFG0 as a function of the local temperature difference δT_{HX2} (free design parameter). Values are valid for the parameter set shown in Table 5.7. The 95 % confidence intervals (error bands in c-f) indicate the calculation uncertainty according to chapter 8.3.3.

5.2.3.2 CFG1: Added JT expansion step

The configuration CFG1 is based on the basic scheme CFG0 with the addition of a JT expansion step (⑦→⑧), in order to reduce the helium temperature after it has been thermalised to the 2nd stage temperature T_{2nd} (Figure 5.17). This throttling process results in a significant pressure reduction ($\Delta p_{7\to 8} < 0$), with the upstream helium at high-pressure p_{HP}, and the downstream helium at low-pressure p_{LP}. The refrigeration cycle is fully defined in Table 5.7 and Table 5.8; the high-pressure before the throttling process $p_7(=p_{HP})$ corresponds to the free design parameter.
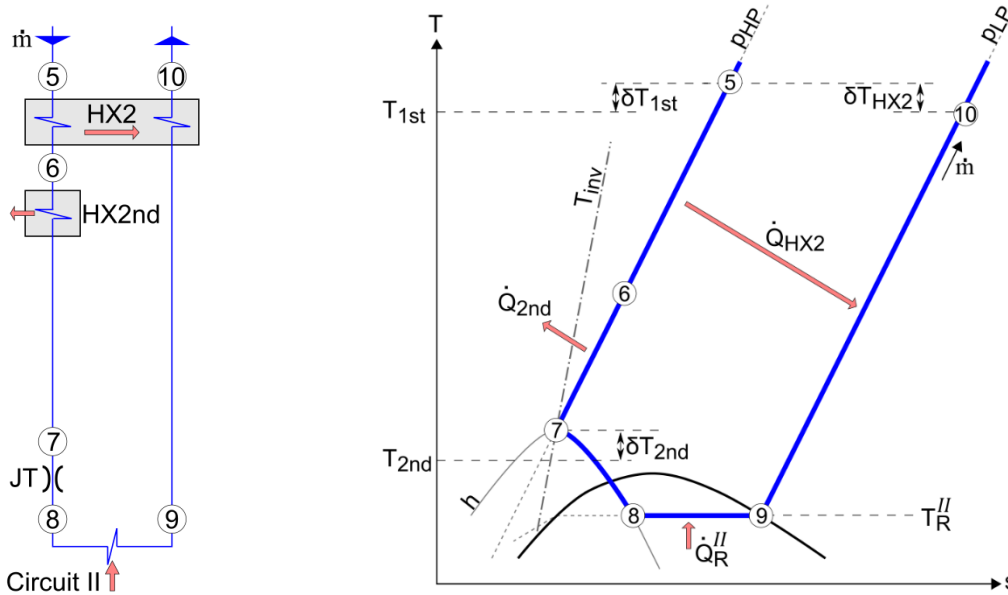
Figure 5.17. Segment of the flow chart (left) and T-s diagram (right) of configuration CFG1. This configuration uses a JT expansion step to lower the helium go stream temperature below the 2nd stage temperature T_{2nd}.

It will be shown that the definition of point ⑦ (state prior the throttling process) is best defined based on the following criteria

I.   11.7 J/g $\leq h_7 < 30.45$ J/g ($\to$ to generate a fluid with $0 \leq x_8 < 1$);
II. T_7 is inversion temperature ($\to$ maximizes $\Delta T_{7\to 8} \to$ increases $T_{2nd} \to$ increases $\dot{Q}_{2nd}$).

As illustrated in Figure 5.18, the value for the enthalpy h_7 is limited to a specific range, because the isenthalpic expansion shall produce a fluid with

$$0 \leq x_8 \leq 1 \quad . \tag{5.64}$$

The reason is that neither the production of overheated gas nor undercooled liquid is of interest; cooling with overheated gas is not an option because it does not fulfil the requirements of isothermal refrigeration, and providing undercooled liquid at a temperature lower than necessary is less efficient than providing saturated liquid at the desired temperature.

It is of interest to maximize the temperature at which the expansion step starts (T_7), because it defines the cryocooler's temperature T_{2nd}, and thus the stage power $\dot{Q}_{2nd}$. In contrast, the temperature T_8 cannot be modified freely, because it is linked to the refrigeration temperature T_R^{II} (a boundary condition). Based on these two criteria, the temperature difference $\Delta T_{7\to 8}$ that corresponds to the temperature decrease caused by the expansion step,

shall be maximised. For a given enthalpy h_7, this maximum occurs when the temperature T_7 corresponds to an inversion temperature T_{INV}

$$\Delta T_{7 \to 8} \text{ is maxima for } T_7 = T_{7,INV}[p_7, \mu_{JT} = 0] \quad , \tag{5.65}$$

where $T_{7,INV}$ denotes the inversion temperature at the pressure p_7. As illustrated in Figure 5.18, in order to produce a two-phase fluid by means of isenthalpic expansion, the free design parameter p_{HP} is constrained to the range

$$1.87 \text{ bar} \leq p_{HP} = p_7 \leq 13.4 \text{ bar} \quad . \tag{5.66}$$

In addition, for any given pressure p_7 within that range there is only one corresponding inversion temperature $T_{7,INV}$ (see chapter 2.2), which results in the pressure p_{HP} being the only parameter required to fully define point ⑦.
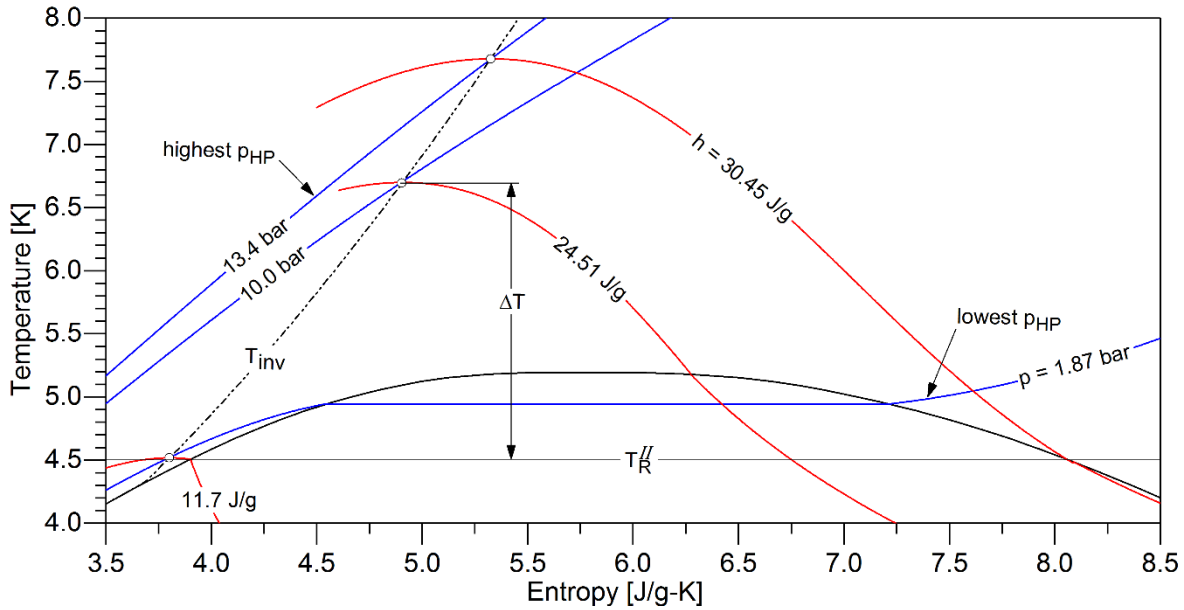
Figure 5.18. The production of two-phase helium by means of (ideal) isenthalpic expansion requires a starting pressure p_{HP} within the range of 1.87 to 13.4 bar. The decrease in temperature ΔT is maximum when the expanding fluid starts at its inversion state T_{INV}.

In analogy to configuration CFG0, Table 5.12 presents a list of relevant fluid state expressions. The terms describing the heat exchangers were listed in Table 5.9, with the additional remark that for recuperator HX2, the change in specific enthalpy $(h_5 - h_6) = (h_{10} - h_9)$ and the effectiveness ε_{HX2} are independent of the free design parameter p_{HP}. The equations describing the cooling capabilities of configuration CFG1 are similar to CFG0 (Table 5.10). However, the 2nd stage temperature T_{2nd} is now a function of the respective free design parameter, which leads to the expressions

$$T_{2nd} = T_{7,INV}[p_{HP}] - \delta T_{HX2nd} \quad , \tag{5.40.14b}$$

and

$$\dot{Q}_{2nd} = \dot{Q}_{2nd}[T_{1st}, T_{2nd}] = \dot{Q}_{2nd}\left[T_{1st}, T_{7,INV}[p_{HP}] - \delta T_{HX2nd}\right] \quad . \tag{5.67}$$

Table 5.12. Non-extensive list of fluid state expressions used for the analysis of configuration CFG1. The expressions are either fully defined through the values in Table 5.7 or a function of the free design parameter p_{HP}.

Fully defined		Function of p_{HP}	
(5.68)	$h_9 = h_9[p_{LP}, x_9]$	(5.69)	$h_5 = h_5[p_{HP}, T_5]$
(5.70)	$h_{10} = h_{10}[p_{LP}, T_5 - \delta T_{HX2}]$	(5.40.3)	$h_6 = h_5[p_{HP}, T_5] + h_9 - h_{10}$
(5.71)	$T_5 = T_{1st} + \delta T_{HX1stB}$	(5.40.12)	$h_8 = h_7 = h_{7,INV}[p_{HP}]$
		(5.72)	$x_8 = x_8[p_8, h_8] = x_8\left[p_{LP}, h_{7,INV}[p_{HP}]\right]$

The values calculated for selected process parameters are plotted in Figure 5.20a-h, with their corresponding relationship illustrated in Figure 5.19. An increase in pressure p_{HP} results in a nearly linear increase of the inversion temperature $T_{7,INV}$ (a) and the inversion enthalpy $h_{7,INV}$ at point ⑦ (b). In addition, it also results in a very small change of the enthalpy h_5, the value of which increases around 0.5% over the whole pressure range, and is therefore considered of secondary importance. The growing inversion temperature $T_{7,INV}$ (a) results in a growing stage temperature T_{2nd} (a), which leads to an increase of the stage power $\dot{Q}_{2nd}$ (h). Since the specific energy transferred by the recuperator HX2 $|\Delta h_{5\to6}|$ (c) is independent of the pressure p_{HP}, the amount of specific energy extracted by the 2nd stage $|\Delta h_{6\to7}|$ (c) decreases almost linearly due to the increase in inversion enthalpy $h_{7,INV}$ (b). Both an increasing stage power $\dot{Q}_{2nd}$ (h), and a decreasing enthalpy difference $|\Delta h_{6\to7}|$ (c), result in a rising mass flow $\dot{m}$ (f) that grows at an increasing rate. This growing rate is also true for the heat power $\dot{Q}_{HX2}$ (g), because it is direct proportional to the mass flow $\dot{m}$ (f). The growing inversion enthalpy $h_{7,INV}$ (b) leads to a vapour quality x_8 (d) that grows almost linearly, shrinking the condensate yield. Consequently, and despite the positive effect of the decreasing entropy difference $|\Delta h_{6\to7}|$ (c), the transmission efficiency η_{TP}^{II} (e) is diminished towards zero at an increasing rate. The refrigeration power $\dot{Q}_R^{II}$ (h) grows smoothly, reaches a local maximum, and then declines sharply towards zero, because it is direct proportional to both the increasing stage power $\dot{Q}_{2nd}$ (h) and the decreasing transmission efficiency η_{TP}^{II} (e). The maximum value of $\dot{Q}_R^{II} = 3.45$ W (h) is reached at a pressure p_{HP} of 10.02 bar.

Figure 5.19. Relationship of process parameters as a function of the high-pressure p_{HP} for configuration CFG1.

Figure 5.20. Calculated process parameters of configuration CFG1 as a function of the pressure p_{HP}. Values are valid for the parameter set shown in Table 5.7. The 95 % confidence intervals (error bands in e-h) indicate the calculation uncertainty according to chapter 8.3.3.

5.2.3.3 CFG2: Added recuperator and JT expansion step

The configuration CFG2 is based on CFG1, with the addition of recuperator HX3 (⑦→⑧) to further increase the operational temperature of the 2nd stage, increasing its cooling power (Figure 5.21). Once the supply stream has been thermalised close to the 2nd stage temperature T_{2nd} (⑥→⑦), its temperature is lowered by the combined effort of recuperator HX3 (⑦→⑧) and the subsequent JT expansion (⑧→⑨).

The refrigeration cycle is fully defined in Table 5.7 and Table 5.8; the high-pressure before the throttling process $p_8 (= p_{HP})$ corresponds to the free design parameter.

Figure 5.21. Segment of the flow chart (left) and T-s diagram (right) of configuration CFG2. It presents a recuperator HX3 between the cryocooler's 2nd stage and the JT expansion step.

The characterisation of the JT expansion step is similar to the one presented for the configuration CFG1. For example, the upstream helium at high-pressure p_{HP} and the downstream helium at low-pressure p_{LP}. In addition, the temperature at point ⑧ (prior to the JT expansion step) corresponds to the inversion temperature T_{INV}, and is defined by the pressure $p_8 = p_{HP}$ only

$$T_8[p_{HP}] = T_{8,INV}[p_{HP}, \mu_{JT} = 0] \quad . \tag{5.73}$$

However, the value for the pressure p_{HP} is limited to a smaller range than in the configuration CFG1:

$$2.27 \text{ bar} \leq p_{HP} = p_8 \leq 13.4 \text{ bar} \quad , \tag{5.74}$$

where the lower bound corresponds to the critical pressure of helium. The reason is that the high-pressure stream at the recuperator HX3 shall be supercritical in order to avoid any liquid condensation.

The fluid states at point ⑧ and ⑩, which correspond to the cold end of recuperator HX3, are fully defined by the parameters $T_{10} = T_R^{II}$, x_{10} and $p_8 = p_{HP}$. Consequently, the heat exchange at the recuperator HX3 is determined by these parameters as well. Figure 5.22 shows the temperature evolution of both streams at HX3 as specific energy is exchanged between them. Note that the abscissa corresponds to the specific energy that has been transferred to the

low-pressure stream since it entered the recuperator at its colder end. The values shown in the graph are valid for the parameter set shown in Table 5.7 and a high-pressure p_{HP} of 5 bar. The temperature of both streams increase steadily, but at different rates, which indicates that the recuperator is unbalanced ($\dot{C}_h \neq \dot{C}_c$). The recuperator transfers a total specific energy of 14.7 J/g, and the local temperature difference at its warm end has the design value of $\delta T_{\mathrm{HX3}} = 0.25$ K. This results in a temperature T_7 of 6.78 K, which based on Eq. (5.41.14) defines the 2nd stage temperature to be maximised. Point A indicates the theoretical case of a recuperator with infinite heat exchange area ($\delta T_{\mathrm{HX3}} \to 0$). It corresponds to the highest amount of specific energy that could be transferred, and the highest value of temperature T_7 that could be obtained.

Figure 5.22. Temperature evolution of the streams passing through the recuperator HX3 as specific energy is transferred from the high to the low-pressure stream. Values are valid for the parameter set shown in Table 5.7, a high-pressure $p_8 = p_{\mathrm{HP}}$ of 5 bar, and a local temperature difference δT_{HX3} of 0.25 K.

Based on the previous figure, the evolution of the local temperature difference δT between both streams is shown in Figure 5.23 for different values of p_{HP}. In all cases, the local temperature difference δT starts at a certain value, then increases to reach a local maximum, before finally decreasing to reach the design value $\delta T_{\mathrm{HX3}} = 0.25$ K. The starting temperature difference (at $\Delta h = 0$) is 0.25 K for $p_{\mathrm{HP}} = 2.74$ bar and becomes higher for increasing pressures. This shortens the pressure range defined in Eq. (5.74) to

$$2.74 \text{ bar} \leq p_{\mathrm{HP}} = p_8 \leq 13.4 \text{ bar} \quad , \text{ for } \delta T_{\mathrm{HX3}} = 0.25 \text{ K}. \tag{5.75}$$

The higher the pressure p_{HP}, the higher the total amount of specific energy Δh that is transferred by the recuperator. Therefore, the temperature T_7 increases with higher pressures p_{HP}. The same is true for the 2nd stage temperature T_{2nd}.
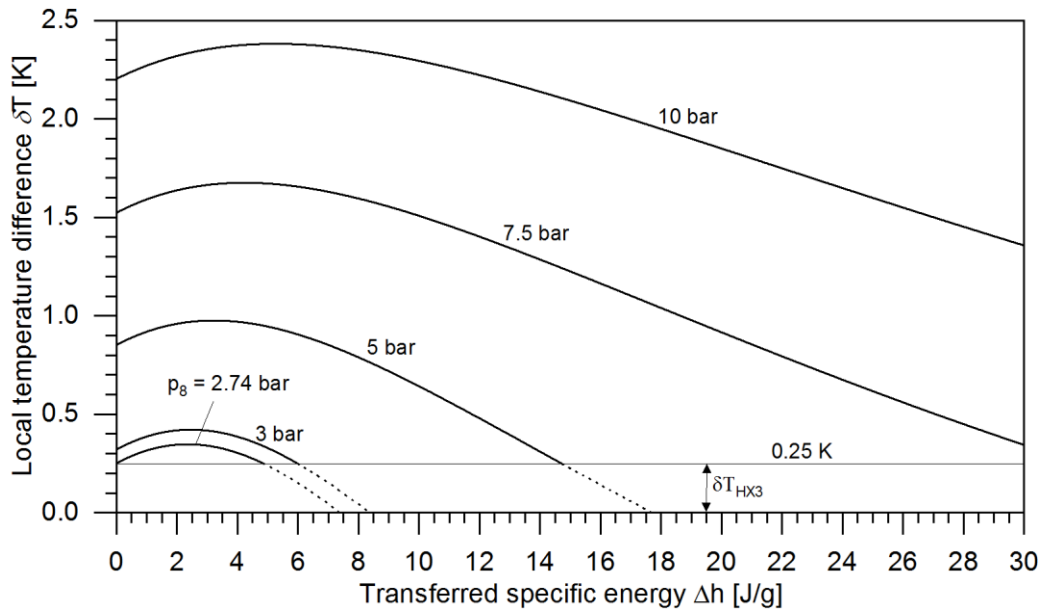
Figure 5.23. Evolution of the local temperature difference δT at the recuperator HX3 as specific energy is transferred from the high to the low-pressure stream. Values are valid for the parameter set shown in Table 5.7.

The temperature T_7 cannot be expressed explicitly. However, it is possible to determine its value by calculating the temperature evolution of the streams passing through the recuperator HX3 (Figure 5.22), showing that it is a function of the parameter set $\{p_{\text{LP}}, p_{\text{HP}}, \delta T_{\text{HX3}}, x_{10}\}$

$$T_7 = \boldsymbol{f}(p_{\text{LP}}, p_{\text{HP}}, \delta T_{\text{HX3}}, x_{10}) \quad . \tag{5.76}$$

Therefore, the 2$^{\text{nd}}$ stage temperature T_{2nd} can be expressed as

$$T_{\text{2nd}} = T_7[p_{\text{LP}}, p_{\text{HP}}, \delta T_{\text{HX3}}, x_{10}] - \delta T_{\text{HX2nd}} \quad , \tag{5.41.14b}$$

with the 2$^{\text{nd}}$ stage power $\dot{Q}_{\text{2nd}}$ as

$$\dot{Q}_{\text{2nd}}[T_{\text{1st}}, T_{\text{2nd}}] = \dot{Q}_{\text{2nd}}[T_{\text{1st}}, T_7[p_{\text{LP}}, p_{\text{HP}}, \delta T_{\text{HX3}}, x_{10}] - \delta T_{\text{HX2nd}}] \quad . \tag{5.77}$$

The terms describing the heat exchangers, and the equations describing the cooling capabilities of configuration CFG2 are analogous to previous configurations (Table 5.9, Table 5.10). Based on the list of fully defined expressions (Table 5.13), the total amount of specific energy that is transferred by the combined effort of both recuperators is not a function of the free design variable p_{HP}

$$\Delta h_{5\rightarrow6} + \Delta h_{7\rightarrow8} = h_{10}[p_{\text{LP}}, x_{10}] - h_{12}[p_{\text{LP}}, T_5 - \delta T_{\text{HX2}}] \neq \boldsymbol{f}(p_{\text{HP}}) \quad . \tag{5.78}$$

Table 5.13. List of fluid state expressions used for the analysis of configuration CFG2. The expressions are either fully defined through the values in Table 5.7 or a function of the free design parameter p_{HP}.

Fully defined		Function of p_{HP}	
(5.79)	$x_{10} = x_{10}[p_{LP}]$	(5.80)	$h_5 = h_5[p_{HP}, T_{1st} + \delta T_{HX1stB}]$
(5.81)	$h_{10} = h_{10}[p_{LP}]$	(5.41.3)	$h_6 = h_5[p_{HP}, T_{1st} + \delta T_{HX1stB}] + h_{11} - h_{12}$
(5.82)	$h_{12} = h_{12}[p_{LP}, T_{1st} + \delta T_{HX1stB} - \delta T_{HX2}]$	(5.76)	$T_7 = T_7[p_{LP}, p_{HP}, \delta T_{HX3}, x_{10}]$
		(5.83)	$h_7 = h_7[p_{LP}, T_7[p_{LP}, p_{HP}, \delta T_{HX3}, x_{10}]]$
		(5.84)	$x_9 = x_9[p_9, h_9] = x_9\left[p_{LP}, h_{8,INV}[p_{HP}]\right]$
		(5.41.7)	$T_{11} = T_7[p_{LP}, p_{HP}, \delta T_{HX3}, x_{10}] - \delta T_{HX3}$
		(5.85)	$h_{11} = h_{11}[p_{LP}, T_{11}]$

Equation (5.41.14b) shows that the 2nd stage temperature T_{2nd} derives from the definition of the thermodynamic cycle, and is therefore cryocooler-independent. The temperature values span the range

$$5.10 \text{ K} \geq T_{2nd} \geq 31.09 \text{ K} \quad , \tag{5.86}$$

which extends beyond the domain of the fitted stage-power functions defined in Eq. (5.11). As shown in Figure 5.24, the temperature range spanned in configuration CFG2 (A to C) goes over the upper domain-boundary (B) of the fitted function for $\dot{Q}_{2nd}$. The domain boundary lies at T_{2nd} = 16.43 K (B) and corresponds to a pressure p_{HP} of 10.42 bar. The function is extrapolated for temperature (or pressure) values beyond this region (B to C).

Further analysis in Figure 5.26e shows that the extrapolated region (p_{HP} > 10.42 bar, T_{2nd} > 16.43 K) is of little interest, because it exhibits a much lower transmission efficiency η_{TP}^{II} than the region before. Nonetheless, and for the sake of completeness, the function describing the 2nd stage power $\dot{Q}_{2nd}$ is extrapolated in order to allow the computation of cryocooler-dependent parameters. This is accomplished under the assumption of a constant increase of 2nd stage power $\dot{Q}_{2nd}$ towards 30 W at the end of the temperature range (point C, Figure 5.24).
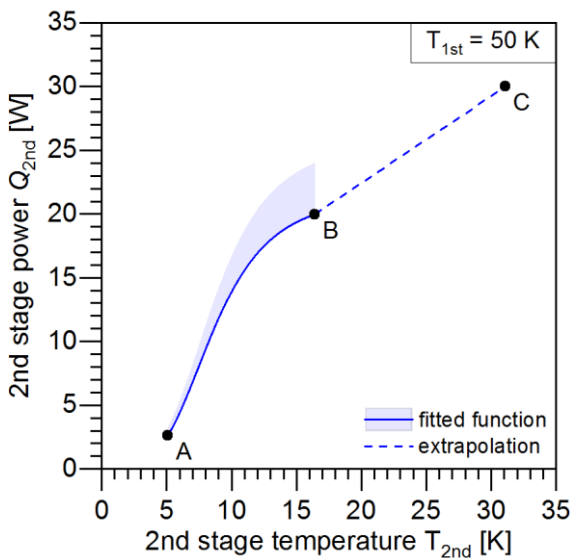
Point	T_{2nd} [K]	$\dot{Q}_{2nd}$ [W]	p_{HP} [bar]
A	5.10	2.62	2.74
B	16.43	19.99	10.42
C	31.09	30.00	13.40

Figure 5.24. *Extended* function for the 2nd stage power $\dot{Q}_{2nd}$ employed for configuration CFG2 (A to C). The fitted function for the 2nd stage power (A to B) was defined in Eq. (5.11) and has its upper domain-boundary at 16.43 K (point B). For configuration CFG2, the fitted function is extended by extrapolation assuming a linear increase in stage-power towards 30 W at 31.09 K (B to C); the slope of the extrapolated line is approximately 0.68 W/K.

The calculated value of selected process parameters are presented in Figure 5.26a-h, with their corresponding relationship illustrated in Figure 5.25. Cryocooler-dependent parameters (h-f) are extrapolated for pressure values larger than 10.42 bar (corresponds to T_{2nd} > 16.43 K in graph a).

The effects of an increasing pressure p_{HP} is analogous to configuration CFG1 for corresponding parameters (b, d-f). However, the specific energy deposited to the low-pressure stream ($\Delta h_{5\to6}$+$\Delta h_{7\to8}$ in c), which is independent of the pressure p_{HP}, is transferred by two recuperators instead of a single one (HX2 and HX3 in g). High pressures p_{HP} allow the recuperator HX3 to transfer large amounts of specific energy $\Delta h_{7\to8}$ (c), which considerably increases the difference between the 2nd stage temperature T_{2nd} (a) and the inversion temperature $T_{8,INV}$ (a). However, the transmission efficiency η_{TP}^{II} (e) diminishes towards zero at an increasing rate when the pressure p_{HP} increases. This is the reason why the refrigeration power $\dot{Q}_R^{II}$ (h) declines sharply towards zero after reaching a maximum value of 12.07 W at p_{HP} = 9.61 bar.
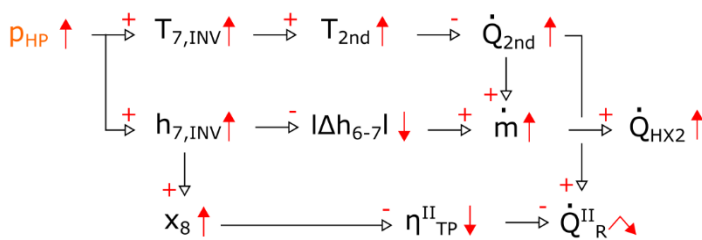

Figure 5.25. Relationship of process parameters as a function of the high-pressure p_{HP} for configuration CFG2.
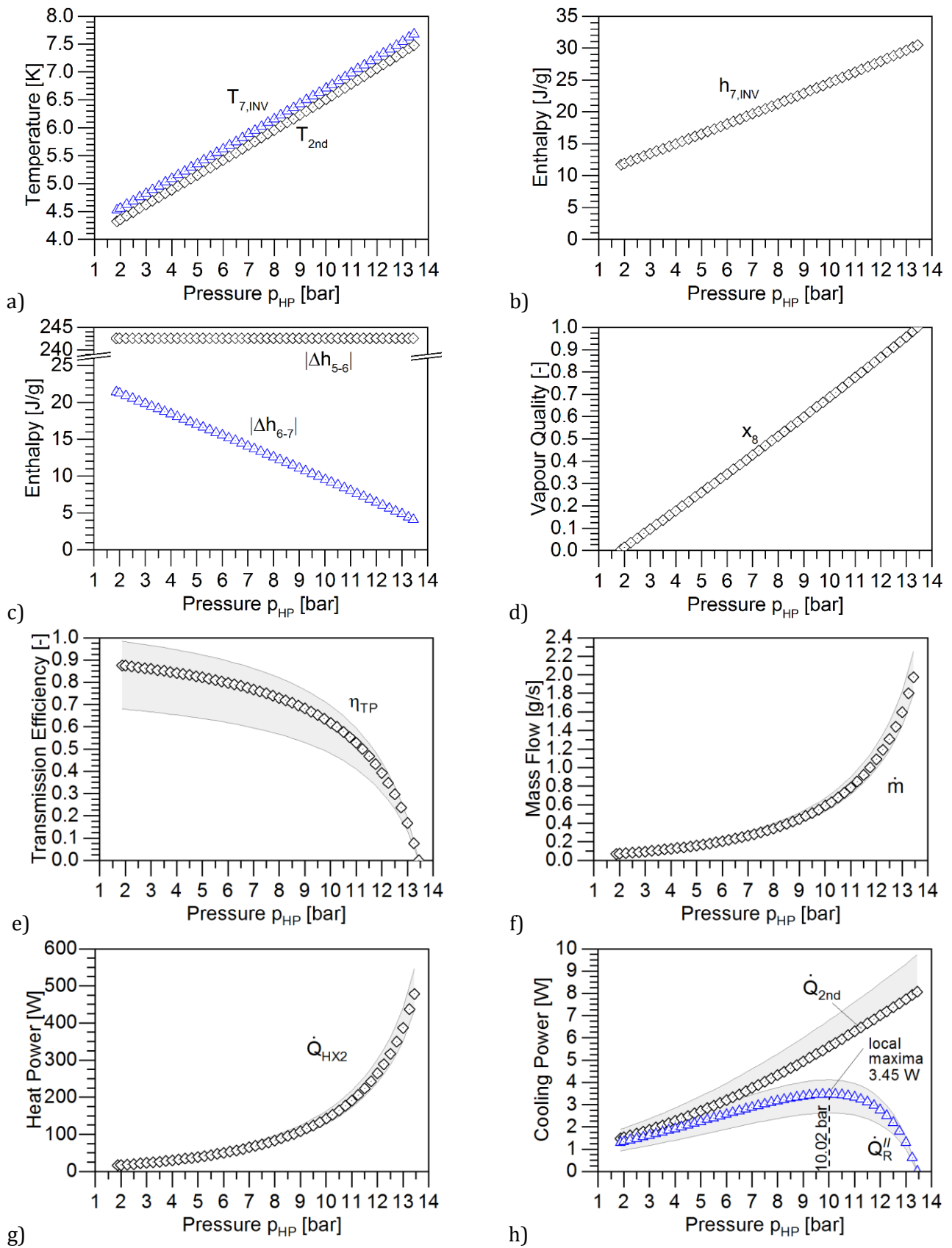
Figure 5.26. Calculated process parameters of configuration CFG2 as a function of the pressure p_{HP}. Values are valid for the parameter set shown in Table 5.7. The 95 % confidence intervals (error bands in e-h) indicate the calculation uncertainty according to chapter 8.3.3.

5.2.3.4 CFG3: Added JT-recuperator and JT expansion step

The configuration CFG3 is based on CFG2, with the difference that the additional recuperator, now denominated JTHX, is also used to perform a JT expansion on the high-pressure stream (⑦→⑧), allowing it to be both cooled and expanded at the same time (Figure 5.27). This additional throttling process leads to an intermediate pressure p_{MP} at point ⑧ before the stream is further expanded. The refrigeration cycle is fully defined in Table 5.7 and Table 5.8. The high-pressure $p_7 (= p_{HP})$, before the throttling process at the heat exchanger JTHX, is defined as the free design parameter.
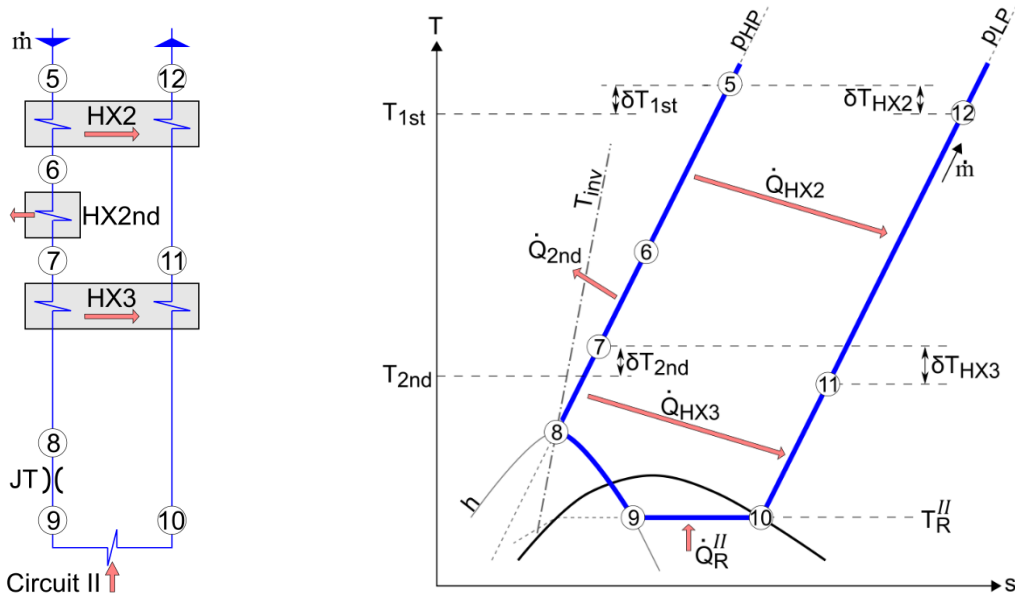

Figure 5.27. Segment of the flow chart (left) and T-s diagram (right) of configuration CFG3. It presents a Joule-Thomson recuperator JTHX before the JT expansion step.

The characterisation of both the JT expansion step and the recuperator JTHX, is analogous to the one presented for configuration CFG2. Consequently, the temperature prior to the JT expansion step T_8 corresponds to the inversion temperature T_{INV}. It is defined by the intermediate pressure p_{MP} as

$$T_8[p_{MP}] = T_{8,INV}[p_{MP}, \mu_{JT} = 0] \quad , \tag{5.87}$$

where

$$2.27 \text{ bar} \leq p_{MP} = p_8 \leq 13.4 \text{ bar} \quad . \tag{5.88}$$

In addition, the cold end of recuperator JTHX is fully defined by the parameters $T_{10} = T_R^{II}$, x_{10} and $p_8 = p_{MP}$. The expansion of the high-pressure stream (⑦→⑧) shall occur along the differential inversion curve, in order to maximize the local temperature difference δT, therefore maximising the total specific energy transmitted by the recuperator. Consequently, the temperature at point ⑦ corresponds to the inversion temperature T_{INV} defined by the high-pressure $p_7 = p_{HP}$

$$T_7[p_{HP}] = T_{7,INV}[p_{HP}, \mu_{JT} = 0] \quad . \tag{5.89}$$

Analogous to recuperator HX3 in CFG2 (Figure 5.22), the temperature evolution of both streams at the recuperator JTHX is shown in Figure 5.28. The values in the graph are valid for the parameter set shown in Table 5.7, a temperature difference δT_{JTHX} of 0.25 K and a high-pressure p_{HP} of 25.3 bar. The pressure evolution of the warmer stream is denoted along its temperature curve, and the unequal temperature evolution of both streams indicates an unbalanced recuperator ($\dot{C}_h \neq \dot{C}_c$). The recuperator transfers a total specific energy of 41.8 J/g, resulting in a temperature T_7 of 11.58 K.
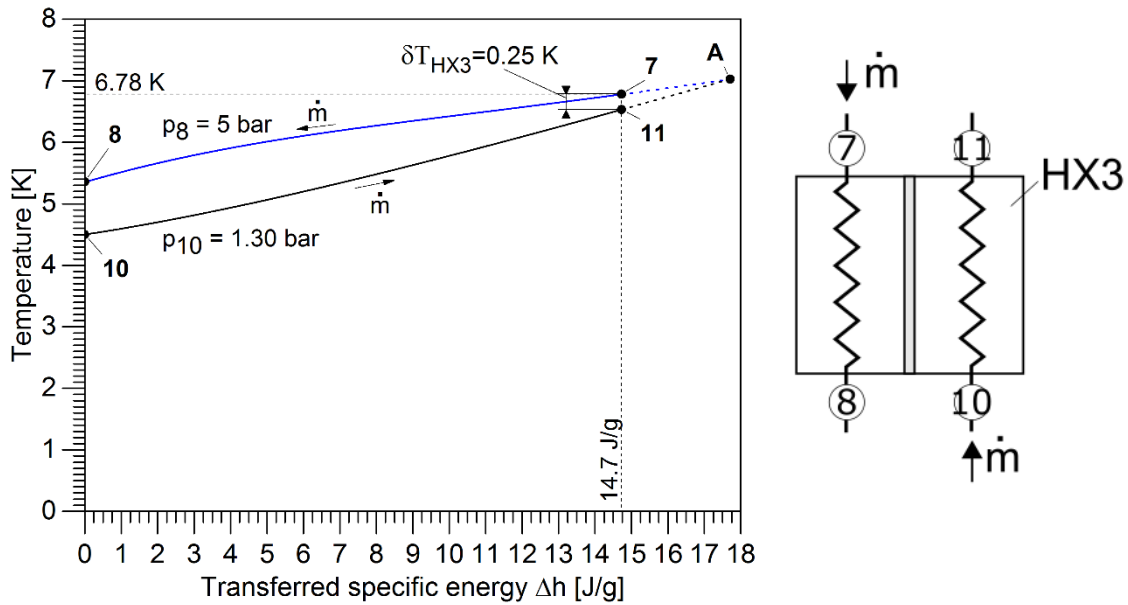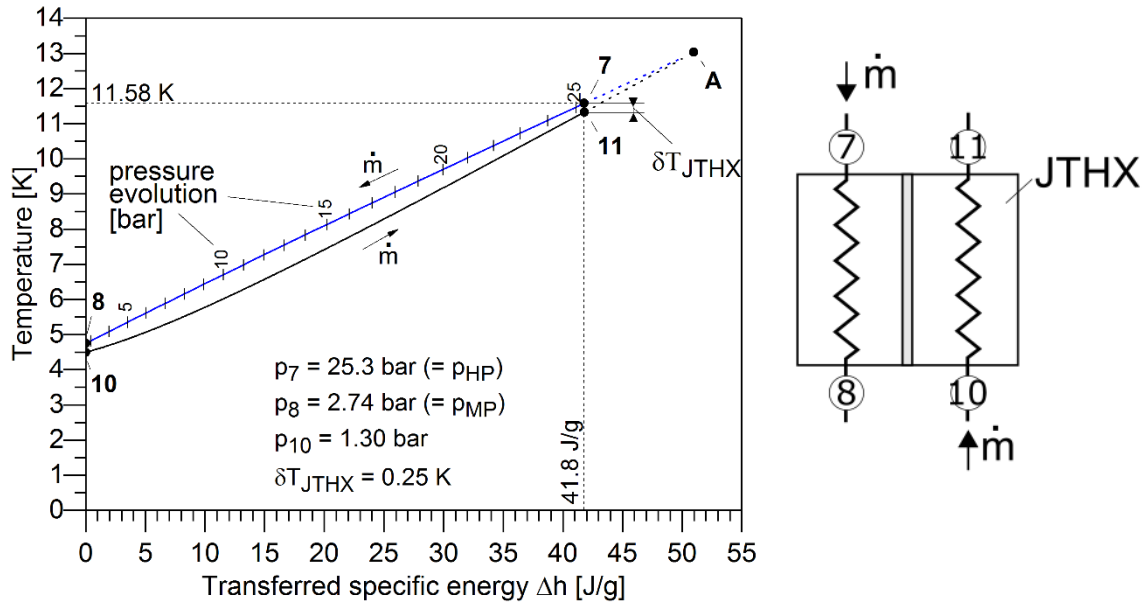

Figure 5.28. Temperature and pressure evolution of the streams passing through the recuperator JTHX as specific energy is transferred from the high-pressure to the low-pressure stream. Values are valid for the parameter set shown in Table 5.7, a high-pressure p_{HP} of 25.3 bar and a temperature difference δT_{JTHX} of 0.25 K. (c.f. Figure 5.22).

The evolution of the local temperature difference δT between both streams is shown in Figure 5.29 for different values of p_{MP}. For the warmer stream, the corresponding pressure evolution is shown in Figure 5.30. In all cases, the local temperature difference δT starts at a certain value, increases to reach a local maximum, and finally decreases to reach a value of $\delta T_{\text{JTHX}} = 0.25$ K. The starting temperature difference $(T_{8,\text{INV}} - T_{10})$ equals 0.25 K for $p_{\text{MP}} = 2.74$ bar and becomes higher for increasing pressures. Although this is the same behaviour as for HX3 in CFG2 (Figure 5.23), the specific energy transferred by JTHX is many times higher for the same fluid conditions at the recuperators cold end. The pressure of the warmer stream grows at a decreasing rate for all cases. A higher value for p_{MP} results in a higher transfer of specific energy Δh, but also in a higher pressure at the recuperators warm end ($p_7 = p_{\text{HP}}$). Moreover, for the same amount of transferred specific energy Δh, a higher warm stream pressure is required for increasing values of p_{MP}. For this reason, the intermediate pressure p_{MP} is to be minimised when possible.
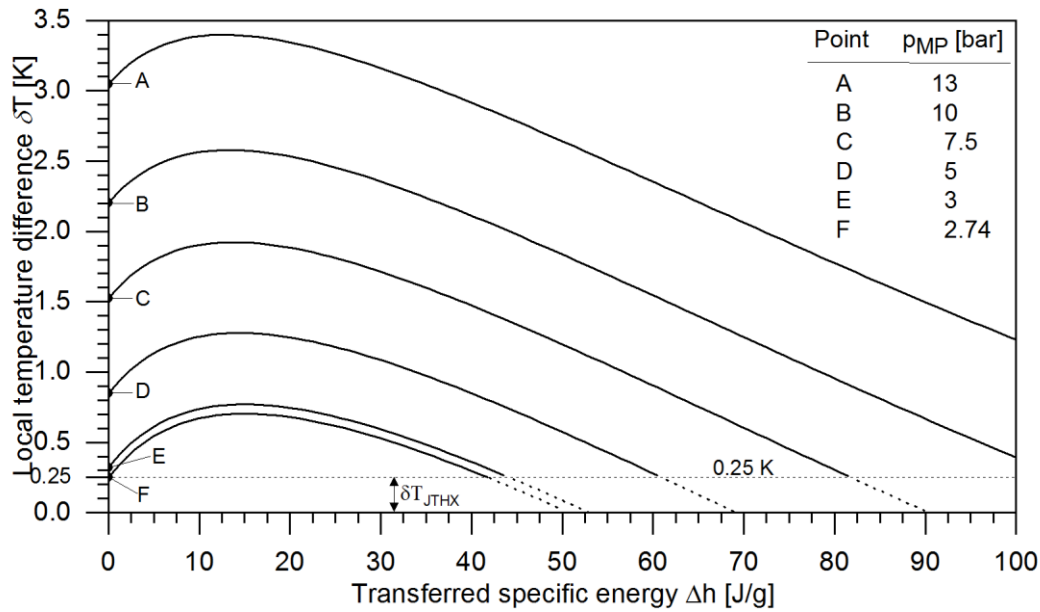
Figure 5.29. Evolution of the local temperature difference δT at the recuperator JTHX as specific energy is transferred from the high to the low-pressure stream. Values are valid for the parameter set in Table 5.7.
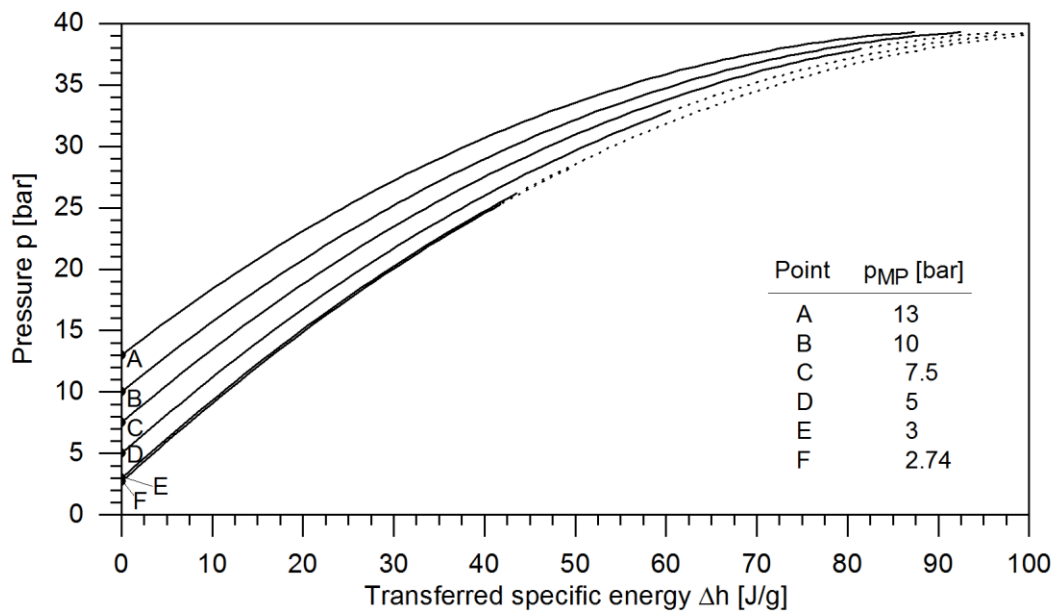
Figure 5.30. Pressure evolution of the warmer stream at the recuperator JTHX as specific energy is transferred from the high to the low-pressure stream. Values are valid for the parameter set in Table 5.7.

The equations defining configuration CFG3 were listed in Table 5.9 and Table 5.10. The expressions are the same as in CFG2, with the exception of the newly introduced parameter p_{MP}. Thus, δT_{HX3} in CFG2 corresponds here to δT_{JTHX}, where

$$\delta T_{JTHX} = T_7 - T_{11} = f(p_{LP}, p_{MP}, p_{HP}, x_{10}) \quad , \tag{5.90}$$

and

$$h_8 = h_{8,INV}[p_{MP}] \quad . \tag{5.91}$$

As previously stated, for the transfer of a given amount of enthalpy $\Delta h_{7\to8}$, the minimisation of the intermediate pressure p_{MP} allows the reduction of the required high-pressure p_{HP}. In addition, reducing p_{MP} also results in a decrease of the vapour quality x_9, and hence, an increase of the transmission efficiency η_{TP}^{II}. For this reason, a design value of 2.74 bar is set for the intermediate pressure p_{MP}, resulting in a vapour quality x_9 of 7.3 % and a local temperature difference at the <u>cold</u> end of recuperator JTHX of $\delta T = T_8 - T_{10} = 0.25$ K (Figure 5.28). Note that this collapses the pressure range defined in Eq. (5.88) to

$$p_{MP} = p_8 = 2.74 \text{ bar} \quad , \text{ for } \delta T = 0.25 \text{ K at the cold end of JTHX;} \tag{5.92}$$

and due to the design constraint $\delta T_{JTHX} \geq 0.25$ K at the <u>warm</u> end of recuperator JTHX, the high-pressure p_{HP} is limited to a maximal value of 25.3 bar, resulting in the pressure range

$$p_{MP} \leq p_{7,INV} (= p_{HP}) \leq 25.3 \text{ bar} \quad , \text{ for } \delta T_{JTHX} \geq 0.25 \text{ K} . \tag{5.93}$$

The calculated values of selected process parameters are presented in Figure 5.32a-h, with their corresponding relationship illustrated in Figure 5.31. The graphs and relationships are similar to the ones presented previously for configuration CFG2. However, the effects of an increasing pressure p_{HP} differ for certain parameters, and the local temperature difference δT_{JTHX} (d) is plotted instead of the (now constant) vapour quality x_9.

The inversion temperature $T_{7,INV}$ (a) increases nearly linearly, resulting in a growing stage temperature T_{2nd} (a), which leads to an increase of stage power $\dot{Q}_{2nd}$ (h). The amount of specific energy transferred by the recuperator JTHX $|\Delta h_{7\to8}|$ (c) increases steadily. This results in a local temperature difference δT_{JTHX} (d) that, starting at the minimal design value of 0.25 K, grows sharply to reach a local maximum around 0.7 K, and then declines smoother to its initial value. The amount of specific energy extracted by the 2nd stage $|\Delta h_{6\to7}|$ (c) increases by only 13% over the whole pressure range. Consequently, the increase in mass flow $\dot{m}$ (f) is driven mainly by the growing stage power $\dot{Q}_{2nd}$ (h). In addition, the decreasing transmission efficiency η_{TP}^{II} (e) is inverse proportional to the increasing enthalpy difference $|\Delta h_{6\to7}|$ (c). Finally, the refrigeration power $\dot{Q}_R^{II}$ (h) increases monotonically, because the stage power $\dot{Q}_{2nd}$ (h) grows at a higher rate than the transmission efficiency η_{TP}^{II} (e) decreases.
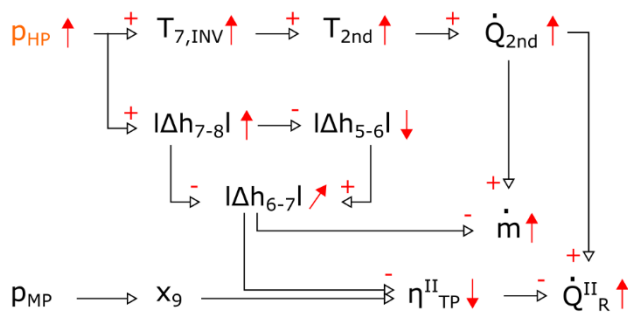
Figure 5.31. Relationship of process parameters as a function of the high-pressure p_{HP} for configuration CFG3.
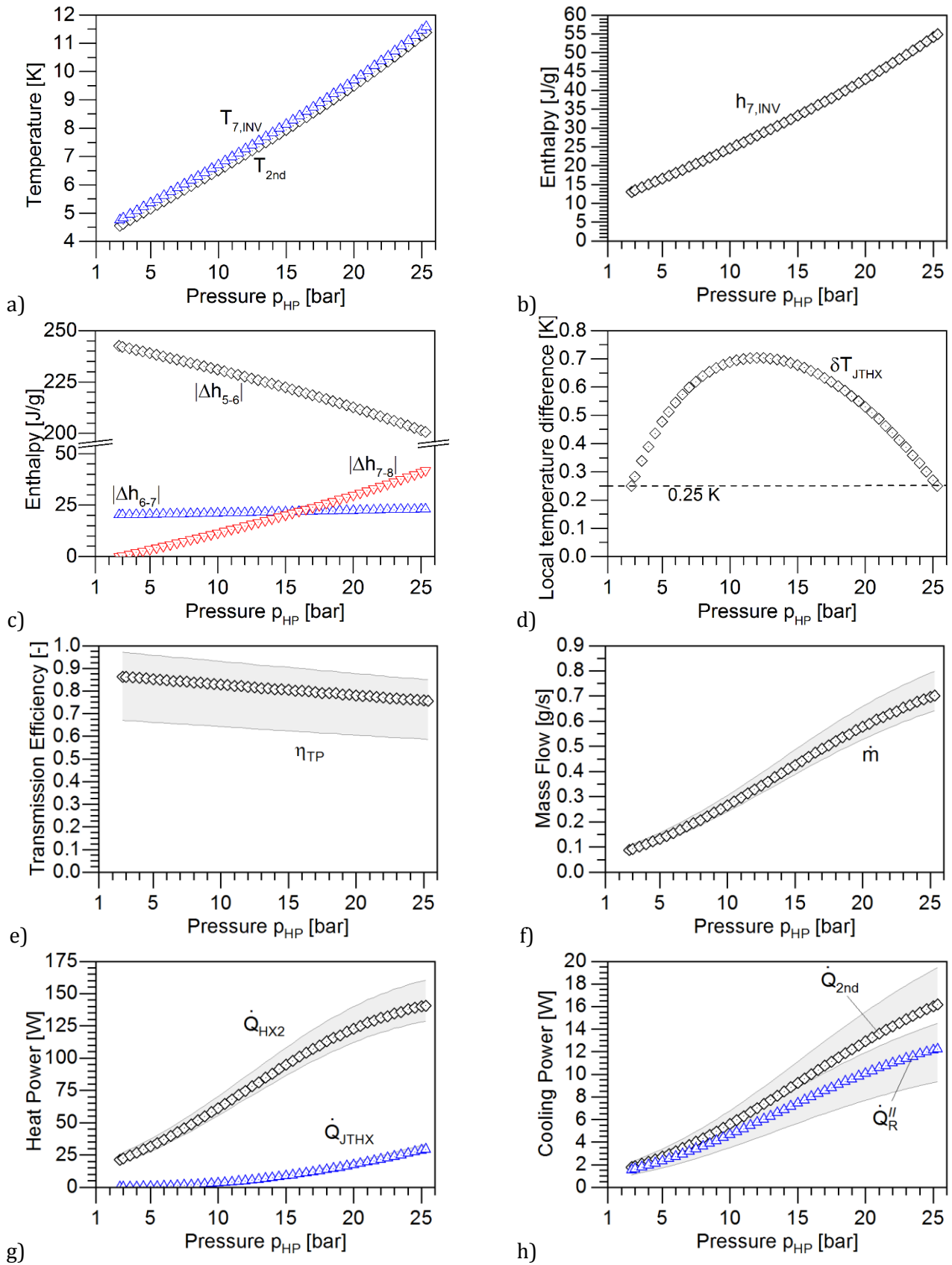
Figure 5.32. Calculated process parameters of configuration CFG3 as a function of the pressure p_{HP}. Values are valid for the parameter set shown in Table 5.7. The 95 % confidence intervals (error bands in e-h) indicate the calculation uncertainty according to chapter 8.3.3.

5.2.3.5 CFG4: Added recuperator, JT-recuperator and JT expansion step

The configuration CFG4 combines the components of all previous configurations (Figure 5.33). After the stream is thermalised at the 2nd stage (⑥→⑦), its temperature is lowered further by the recuperator HX3 (⑦→⑧), the recuperator JTHX (⑧→⑨) and the subsequent JT expansion step (⑨→⑩). The refrigeration cycle is fully defined in Table 5.7 and Table 5.8. The high-pressure $p_8(= p_{HP})$, before the throttling process at the heat exchanger JTHX, is defined as the free design parameter.
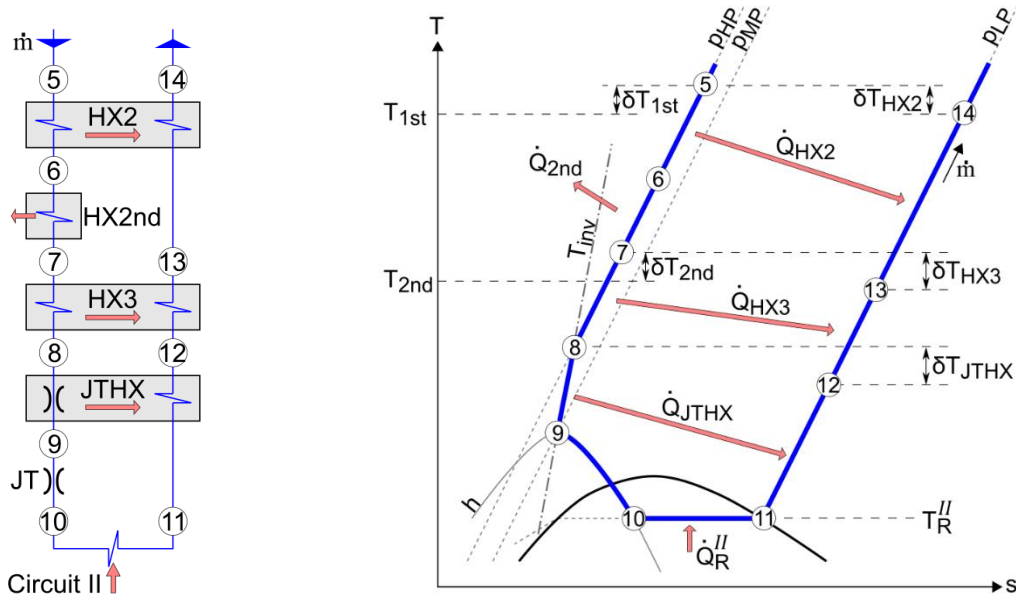
Figure 5.33. Segment of the flow chart (left) and T-s diagram (right) of configuration CFG4. It presents a recuperator HX3, a Joule-Thomson recuperator JTHX and a JT expansion step.

The characterisation of the JT expansion step, the recuperator HX3 and the recuperator JTHX is analogous to the one presented for the previous configurations (Table 5.9, Table 5.10). The intermediate pressure p_{MP} and the high-pressure p_{HP} are defined according to CFG3. The intermediate pressure p_{MP} is set to 2.27 bar, resulting in a vapour quality x_{10} of 7.3 % and a local temperature difference at the <u>cold</u> end of recuperator JTHX of $\delta T = T_9 - T_{11} = 0.25$ K. The high-pressure p_{HP} is limited to the range

$$p_{MP} \leq p_{HP} = p_8 \leq 25.31 \text{ bar} \quad , \tag{5.94}$$

due to the design constraint $\delta T_{JTHX} \geq 0.25$ K at the <u>warm</u> end of recuperator JTHX.

In analogy to Eq. (5.90) for JTHX and Eq. (5.76) for HX3, it applies

$$\delta T_{JTHX} = T_7 - T_{11} = \boldsymbol{f}(p_{LP}, p_{MP}, p_{HP}, x_{11}) \quad , \tag{5.95}$$

and

$$T_7 = \boldsymbol{f}(p_{LP}, p_{HP}, \delta T_{HX3}, h_{12}) \quad ; \tag{5.96}$$

where

$$h_{12} = h_{8,INV}[p_{MP}] - h_{9,INV}[p_{HP}] + h_{11}[p_{LP}, x_{11}] \quad . \tag{5.97}$$

The specific energy deposited to the low-pressure stream (⑪→⑭) is transferred by the combined effort of the three recuperators HX2, HX3 and JTHX

$$\Delta h_{5\to6} + \Delta h_{7\to8} + \Delta h_{8\to9} = h_{11}[p_{LP}, x_{11}] - h_{14}[p_{LP}, T_5 - \delta T_{HX2}] \neq \boldsymbol{f}(p_{HP}) \ , \qquad (5.98)$$

and is independent of the free design variable p_{HP}.

The calculated value of selected process parameters as a function of the free design variable p_{HP} are presented in Figure 5.35a-h, and their corresponding relationship is illustrated in Figure 5.34. Although the graphs and relationships are similar to the ones presented for the previous configurations, the effects of an increasing pressure p_{HP} differ for certain parameters.

The inversion temperature $T_{8,INV}$ (a) increases, resulting in a growing amount of specific energy transferred by the recuperator JTHX $|\Delta h_{8\to9}|$ (c). This results in a local temperature difference δT_{JTHX} (d) that grows from the minimal design value of 0.25 K to a local maximum close to 0.7 K, and then declines to its initial value. This temperature difference also corresponds to the local temperature difference at the cold end of the recuperator HX3. Consequently, the specific energy transferred by HX3 $|\Delta h_{7\to8}|$ (d) also grows, before later decreasing. The specific energy to be transferred by HX2 $|\Delta h_{5\to6}|$ (d) declines at a decreasing rate, reaching a minimum value at $p_{HP} = 24.9$ bar. This is because the sum of the specific energies $\Delta h_{5\to6}$, $\Delta h_{7\to8}$ and $\Delta h_{8\to9}$ remains constant, as stated by Eq. (5.98). As a result, the temperature T_7 (a), and thus also T_{2nd} (a), grows at a decreasing rate and reaches a maximum value at $p_{HP} = 24.9$ bar. Accordingly, the stage power $\dot{Q}_{2nd}$ (h), the massflow $\dot{m}$ (f) and the refrigeration power $\dot{Q}_R^{II}$ (h) all exhibit the same behaviour. As a further consequence, this is the only configuration where the mass flow $\dot{m}$ does not grow monotonically by increasing pressure p_{HP}. The maximal refrigeration power $\dot{Q}_R^{II}$ is 12.37 W at a pressure p_{HP} of 24.9 bar (h).
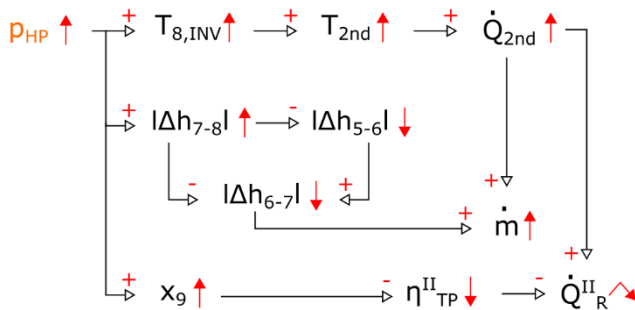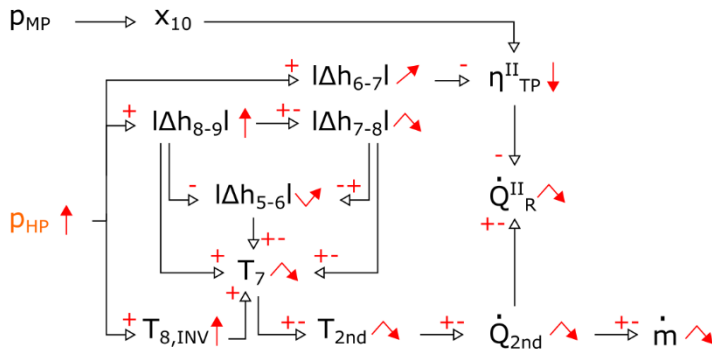

Figure 5.34. Relationship of process parameters as a function of the high-pressure p_{HP} for configuration CFG4.
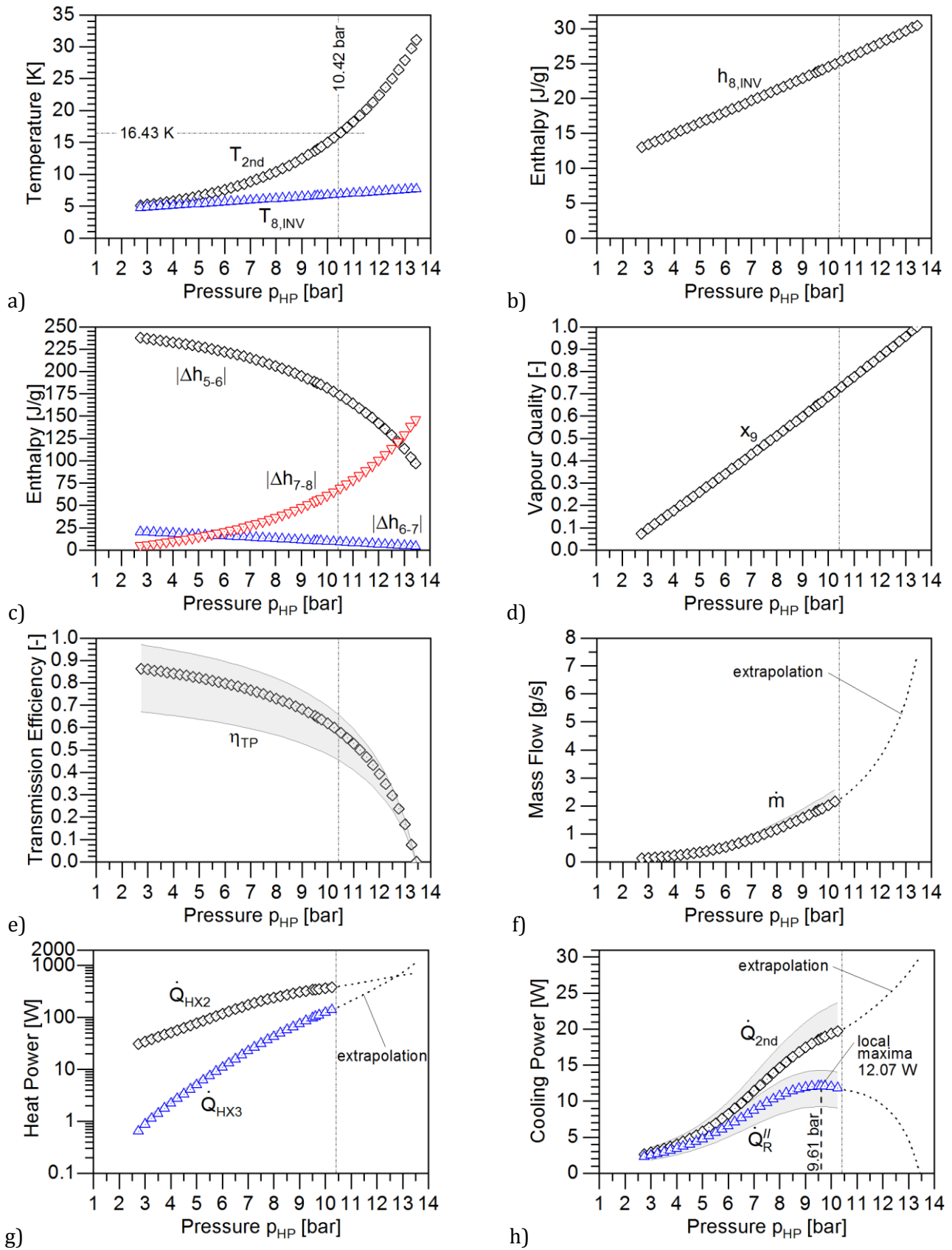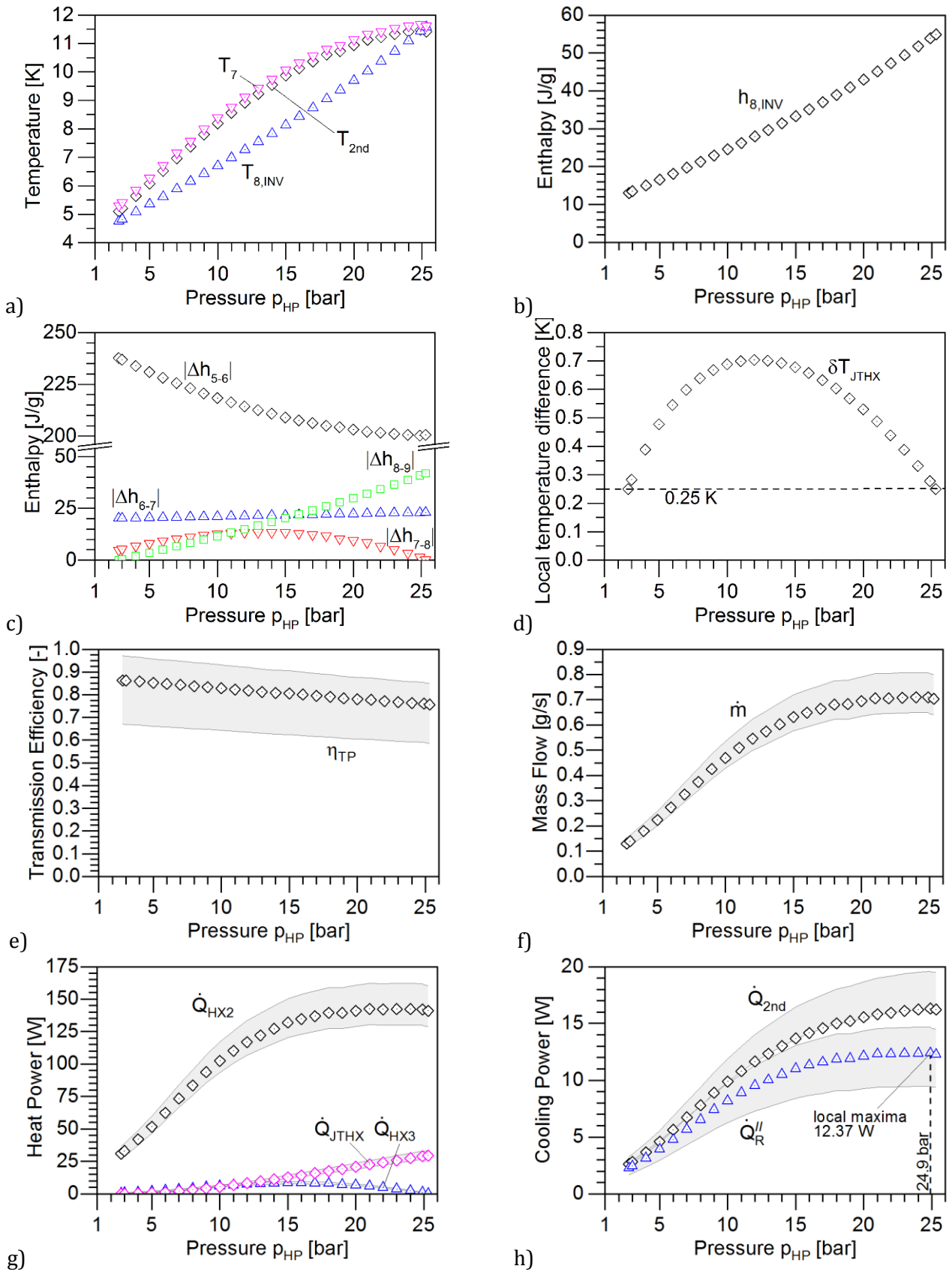
Figure 5.35. Calculated process parameters of configuration CFG4 as a function of the pressure p_{HP}. Values are valid for the parameter set shown in Table 5.7. The 95 % confidence intervals (error bands in e-h) indicate the calculation uncertainty according to chapter 8.3.3.

5.3 Process comparison

The comparison of the different configuration schemes allows the identification of their relative advantages. For this, selected process parameters are first listed together (Table 5.14), and then, their relationship to each other is plotted and analysed. Some parameters are *cryocooler-independent,* since their values are established through the definition of the thermodynamic cycle.

Table 5.14. Comparison of the minimal/maximal values of selected process parameters for the various configurations of Region II as calculated in chapter 5.2.3. The non-exhaustive list categorises parameters according to their dependency on the selected cryocooler device.

	Name	Parameter	CFG0	CFG1	CFG2	CFG3	CFG4
Cryocooler independent	High-pressure	p_{HP} [bar]	1.303	1.87 / 13.4	2.74 / 13.4	2.74 / 25.3	2.74 / 25.3
	Second stage temperature	T_{2nd} [K]	4.30	4.32 / 7.48	5.10 / 31.09	4.55 / 11.39	5.10 / 11.47
	Vapour quality prior Circuit II.	x [%]	0	0 / 100	7.32 / 100	7.3	7.3
	Transmission efficiency	η_{TP}^{II} [%]	87.9	0 / 87.5	0 / 86.3	75.56 / 86.29	75.55 / 86.29
Cryocooler dependent	Second stage power	$\dot{Q}_{2nd}$	1.45	1.48 / 8.07	2.63 / 30.03	1.77 / 16.17	2.63 / 16.29
	Refrigeration power of Circuit II.	$\dot{Q}_R^{II}$ [W]	1.276	0 / 3.45	0 / 12.07	1.53 / 12.22	2.27 / 12.37
	Mass flow	$\dot{m}$ [g/s]	0.067	0.069 / 1.97	0.13 / 7.34	0.088 / 0.70	0.13 / 0.70

Note: CFG0 for δT_{HX2} = 0.5 K.

The high-pressure p_{HP}, the 2nd stage temperature T_{2nd}, the vapour quality x, and the transmission efficiency η_{TP}^{II} are four cryocooler-independent parameters closely related to each other. The p_{HP}-T_{2nd} and the p_{HP}-x relationships are illustrated qualitatively in Figure 5.36 for a given pressure p_{HP} on the different configurations. The x-η_{TP}^{II} relationship was indicated previously in Table 5.10 Eqs. (5.57.2-6), showing that the transmission efficiency η_{TP}^{II} decreases in direct proportionality to an increase of x. The quantitative relationship between the four parameters ($p_{HP}, T_{2nd}, x, \eta_{TP}^{II}$) is presented in Figure 5.37 as a function of the high-pressure p_{HP}.

In general, low values for p_{HP} are desired in order to minimise the compression ratio p_{HP}/p_{LP} required from the circulation system. High values for T_{2nd} increase the 2nd stage power $\dot{Q}_{2nd}$ from the cryocooler. A low vapour quality x means a high yield of liquid helium, hence reducing the mass-flow requirements. Finally, maximizing the transmission efficiency η_{TP}^{II} increases the fraction of available 2nd stage power ($\eta_{CSS}^{II} \cdot \dot{Q}_{2nd}$) delivered as refrigeration power $\dot{Q}_R^{II}$.

Comparing the different configurations in Figure 5.36 and Figure 5.37 shows that:

- The base configuration CFG0 has the particularity of being completely independent of the pressure p_{HP}, because it does not have a JT expansion. It has the highest value for η_{TP}^{II}, and the lowest value for T_{2nd} and x among all configurations.

- The p_{HP}-T_{2nd} relationship is identical in CFG1 and CFG3 because it derives from the same inversion temperature $T_{INV}[p_{HP}]$ prior to the JT expansion. Each pressure range is different, because they are imposed by the respective components (JT on CFG1; JTHX on CFG3).
- For a given pressure p_{HP}, the temperature T_{2nd} in CFG2 and CFG4 is always higher than CFG1 and CFG3, as a result of the heat exchanged by the additional recuperator HX3. In addition, CFG2 can have considerably higher values of T_{2nd} than any other configuration due to a higher local temperature difference δT at the cold end of recuperator HX3.
- The p_{HP}-x relationship is identical for CFG1 and CFG2, because in both cases the inversion pressure prior to the JT expansion step corresponds to the high-pressure p_{HP}. For an increasing pressure p_{HP}, the values of vapour quality x and transmission efficiency η_{TP}^{II} worsen at a relatively high rate for CFG1 and CFG2.
  In contrast, CFG3 and CFG4 have the same value of vapour quality x independent of the pressure p_{HP}, because the inversion pressure prior to the JT expansion step is fixed to the medium-pressure p_{MD} (= 2.74 bar). In spite of this, their transmission efficiency η_{TP}^{II} does change for increasing pressure p_{HP}, decreasing at a very low rate as a result of the monotonically growing 2nd stage temperature T_{2nd}.
- For a given pressure value p_{HP}, CFG3 and CFG4 are considered to present the most favourable relationship between the three remaining parameters. This means, a high transmission efficiency η_{TP}^{II}, a low vapour quality x and yet, a moderately high 2nd stage temperature T_{2nd}.

These insights underline the two main interplays between the hardware configuration and the four parameters p_{HP}, T_{2nd}, x and η_{TP}^{II}:

- The implementation of a throttling process results in a higher temperature T_{2nd} with increasing values of p_{HP}. The effect is then largely magnified when additional heat is exchanged by recuperator HX3. Adding recuperator JTHX, however, does not increase the values of temperature T_{2nd}.
- The use of recuperator JTHX considerably improves the values of parameters x and η_{TP}^{II}, because it decouples the increase of high-pressure p_{HP} from the pressure prior to the final JT expansion step, thus allowing a relatively low and fixed value of 2.74 bar (= p_{MD}). The use of recuperator HX3, however, has no impact on the values of x or η_{TP}^{II}.
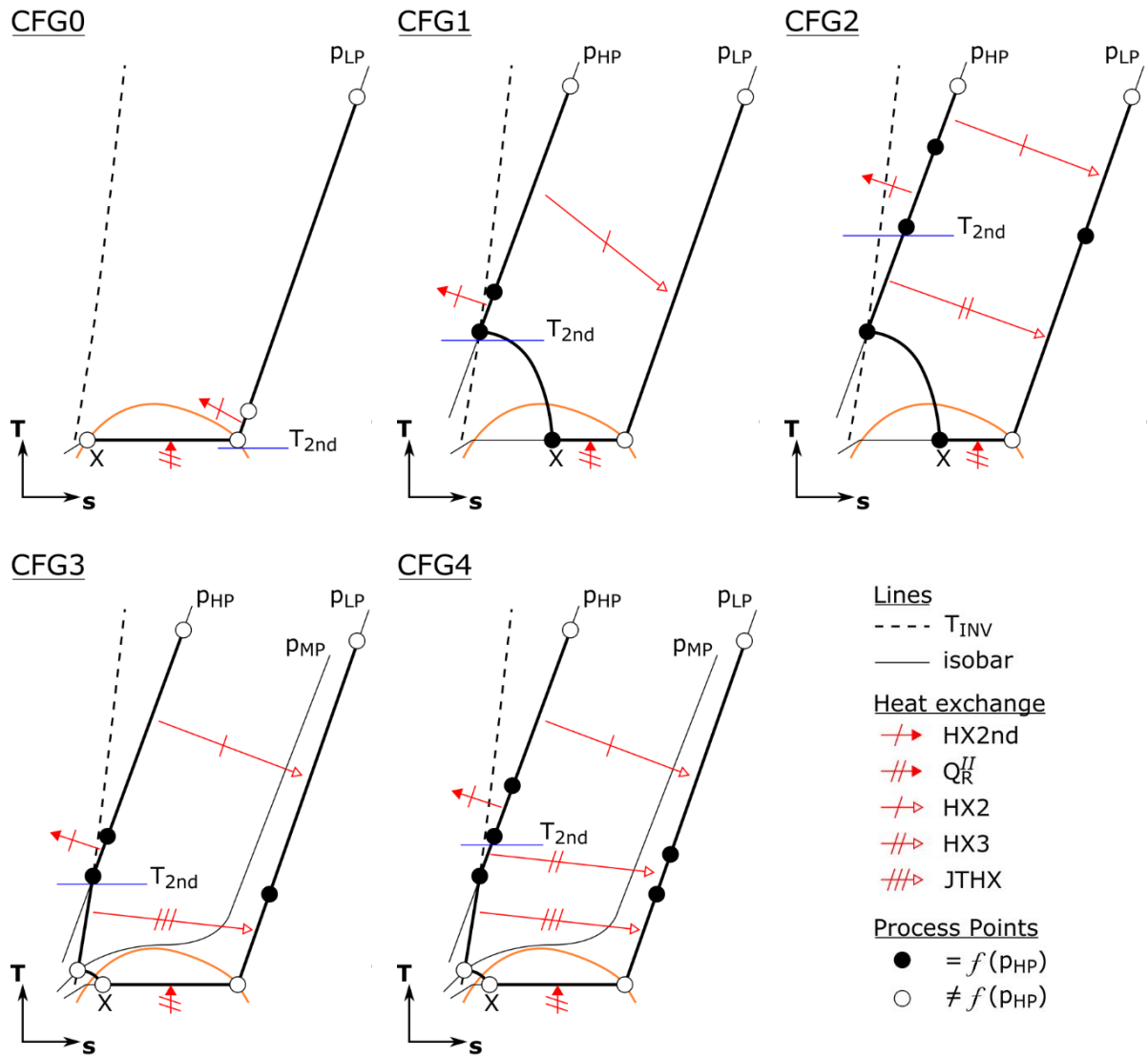
Figure 5.36. Simplified T-s diagrams of Region II showing the qualitative relationship of a given high-pressure p_{HP} to the 2nd stage temperature T_{2nd} and the vapour quality x.
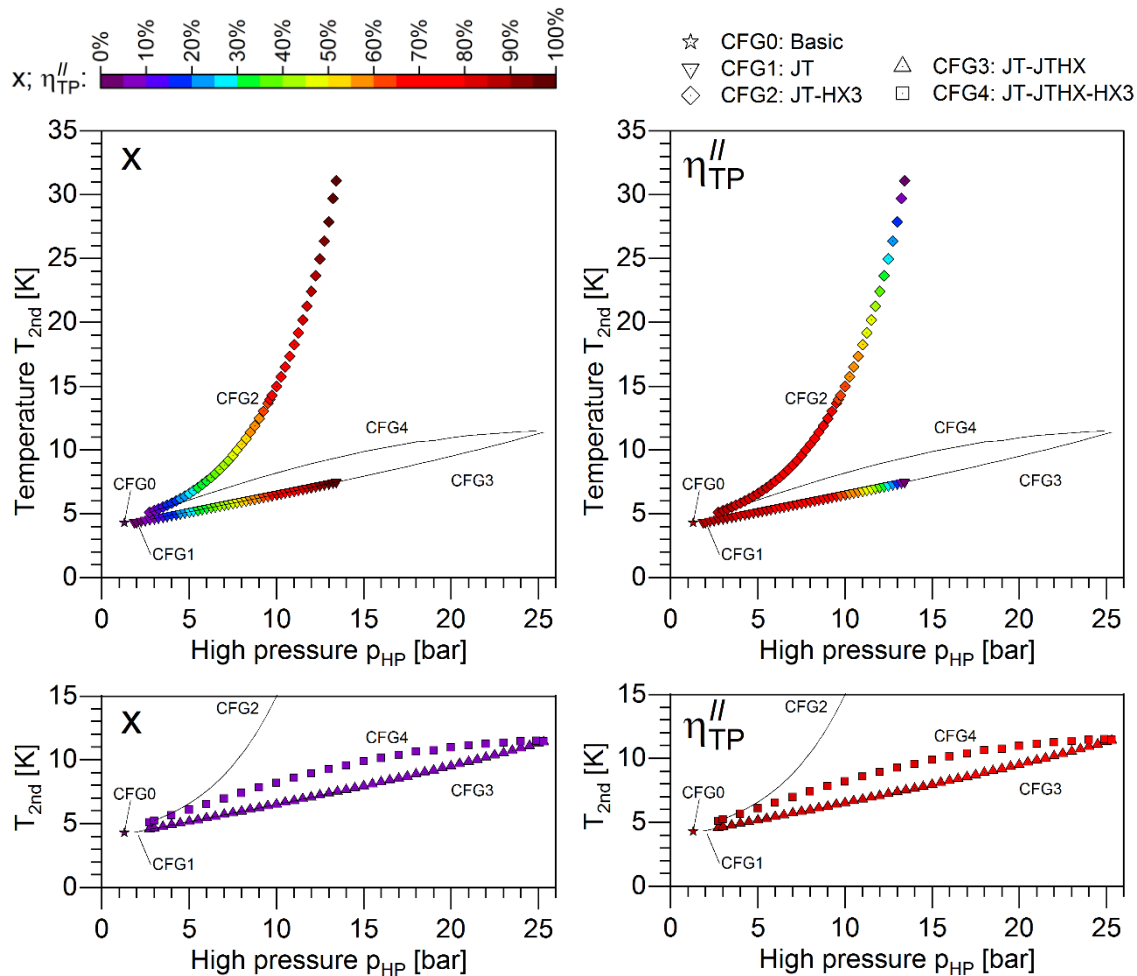
Figure 5.37. Coloured scatter-plots illustrating the vapour quality x (left plots) and transmission efficiency η_{TP}^{II} (right plots) for a given pair of high-pressure p_{HP} and 2nd stage temperature T_{2nd} on different Region II configurations. The upper plots only show data points for configurations CFG0, CFG1, and CFG2; the lower plots for CFG0, CFG3 and CFG4. Maximizing the transmission efficiency η_{TP}^{II} exploits the available cooling power $\eta_{CSS}^{II} \cdot \dot{Q}_{2nd}$. Minimizing the vapour quality x reduces the required mass flow $\dot{m}$.

Two of the most relevant cryocooler-dependent parameters are the refrigeration power $\dot{Q}_R^{II}$ and the mass flow $\dot{m}$. The relationship to each other, and with respect to the high-pressure p_{HP}, is illustrated in Figure 5.38 and Figure 5.39. On the one hand, it is of high interest to maximise the refrigeration power $\dot{Q}_R^{II}$. On the other hand, low values in pressure p_{HP} and mass flow $\dot{m}$ are desired from a design point of view, since they potentially lead to less demanding design requirements on several components (i.e. heat exchange duty and thermal size of heat exchangers; throughput and compression power of the circulation pump). The comparison of both Figures shows that:

- Although CFG0 provides the least refrigeration power $\dot{Q}_R^{II}$, it also requires the least mass flow $\dot{m}$ and pressure p_{HP}.
- The highest values in refrigeration power $\dot{Q}_R^{II}$ are reached by CFG2, CFG3 and CFG4 (around 12 W), with CFG0 and CFG1 providing a small fraction of it.
- With increasing mass flow $\dot{m}$, the refrigeration power $\dot{Q}_R^{II}$ in CFG1 and CFG2 grows at a decreasing rate, reaching a local maximum before declining smoothly towards zero. The region before the local maximum is considered superior to the region afterwards, because it

exhibits lower values in mass flow $\dot{m}$ and pressure p_{HP} for the same refrigeration power $\dot{Q}_R^{II}$. In contrast, the refrigeration power $\dot{Q}_R^{II}$ in CFG3 and CFG4 grows at a higher rate and is almost direct proportional to the mass flow $\dot{m}$.

- For the same refrigeration power $\dot{Q}_R^{II}$, CFG3 and CFG4 need equal amounts of mass flow $\dot{m}$, which is always lower than for CFG2. However, from those three configurations, CFG2 needs by far the lowest pressure p_{HP}, followed by CFG4 and then by CFG3.

    By comparison, CFG1 exhibits the highest, and therefore worst, values for mass flow $\dot{m}$ and pressure p_{HP}.

- For the sake of simplicity, the region of interest (ROI) for the parameter $\dot{m}$ is constrained to the range of 0 to 2 g/s, in order to exclude most non-relevant values for CFG2; it also removes all extrapolated values from the evaluation. Indirectly, the ROI constrains the range of the 2nd stage temperature to 4.3 K≤ T_{2nd} ≤ 15 K.

- In each configuration, a value of p_{HP} defines a single value of $\dot{m}$, which in turn defines a single value of $\dot{Q}_R^{II}$. Therefore, the refrigeration power $\dot{Q}_R^{II}$ can be expressed as a function of the mass flow $\dot{m}$, and then as a function of the pressure p_{HP}.

    With the exception of CFG4, the pressure p_{HP} can also be expressed as a function of the mass flow $\dot{m}$.
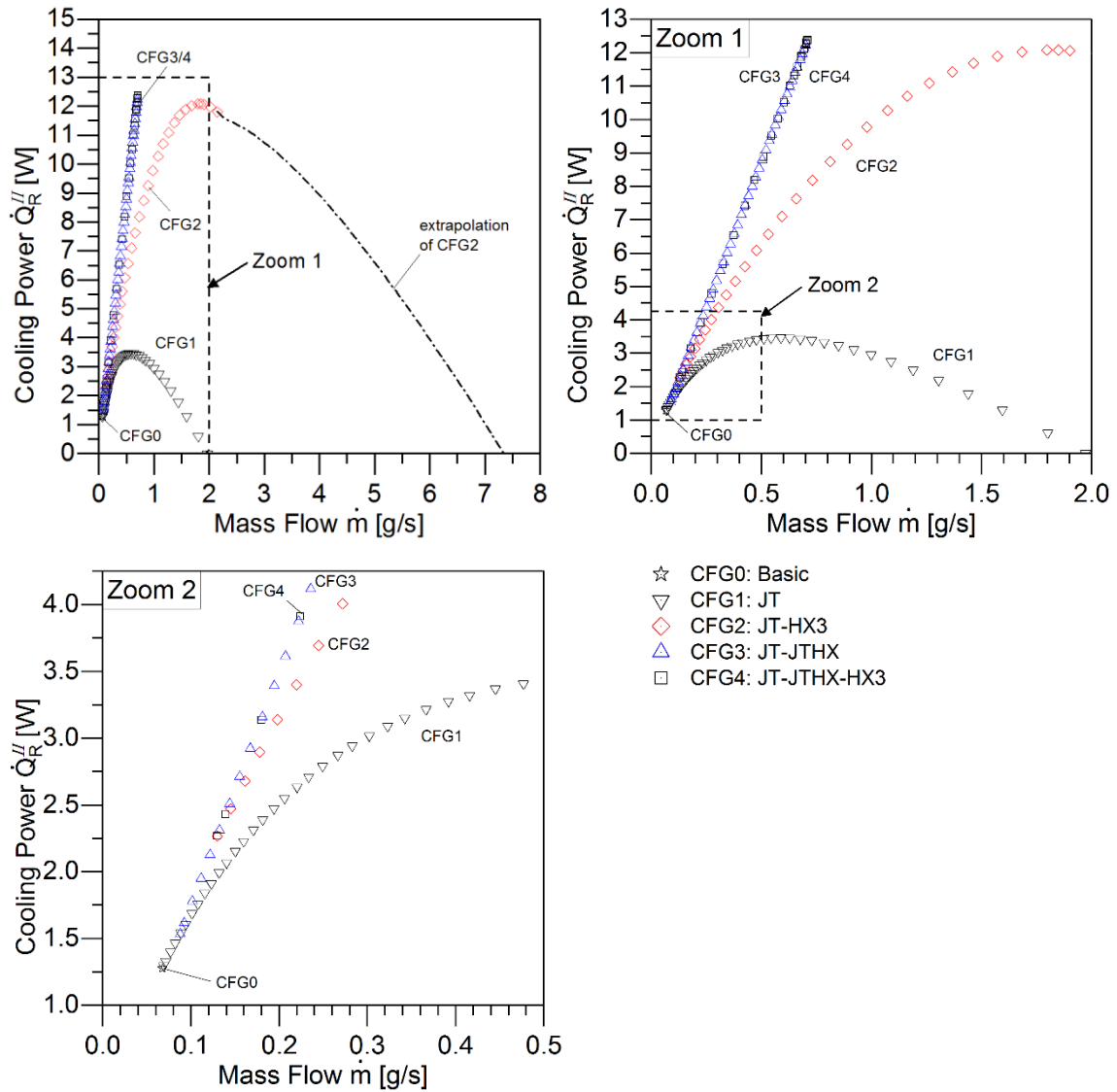
Figure 5.38. Cooling power $\dot{Q}_R^{II}$ over mass flow $\dot{m}$ for the different Region II configurations. Both terms are dependent on the selected cryocooler device.
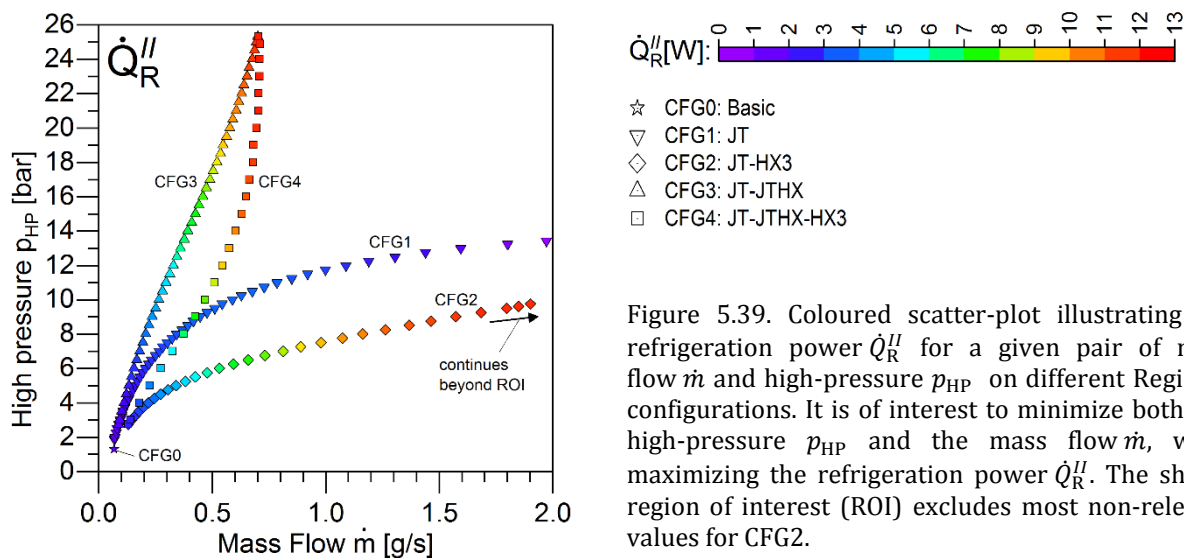
Figure 5.39. Coloured scatter-plot illustrating the refrigeration power $\dot{Q}_R^{II}$ for a given pair of mass flow $\dot{m}$ and high-pressure p_{HP} on different Region II configurations. It is of interest to minimize both, the high-pressure p_{HP} and the mass flow $\dot{m}$, while maximizing the refrigeration power $\dot{Q}_R^{II}$. The shown region of interest (ROI) excludes most non-relevant values for CFG2.

Figure 5.40 shows the amount of heat exchange duty $\dot{Q}$ that is required by each recuperator (HX1, HX2, HX3 and JTHX) in relation to the delivered refrigeration power $\dot{Q}_R^{II}$. In general, low values of heat exchange duty $\dot{Q}$ are desired in order to lower the thermal requirements for a given recuperator. However, the comparison of heat exchange duties $\dot{Q}$ between the presented data points does not necessarily correspond to the comparison of thermal sizes $(U_m \cdot A)$, despite their correlation through $\dot{Q} = U_m A \cdot \delta T_m$. This is because each data point corresponds to a particular set of process parameters. The heat transfer coefficient U_m might vary considerably between data points as a result of distinct working conditions due to differences in terms of mass flow, pressure or temperature. Moreover, a comparison based on a $\dot{Q}_R^{II}$-$U_m A$ relationship is not performed, since this would require the previous definition of the recuperators geometry on all data points.

The comparison in terms of heat exchange duty $\dot{Q}$ shows that:

- For recuperators HX1 and HX2, the $\dot{Q}_R^{II}$-$\dot{Q}$ relationship is very similar to the $\dot{Q}_R^{II}$-$\dot{m}$ relationship previously shown in Figure 5.39, which confirms the strong dependency on the mass flow $\dot{m}$. As shown before (i.e. page 84, Figure 5.20), with increasing values of $\dot{Q}_R^{II}$ the change in the amount of specific energy that is transferred by the two recuperators is lower than the resulting change in mass flow $\dot{m}$.

  Therefore, for the same refrigeration power $\dot{Q}_R^{II}$, CFG3 and CFG4 require the same heat exchange duty for recuperators HX1 and HX2 (Figure 5.40a, b), which is always lower than for CFG2 and then for CFG1. By comparison, CFG0 requires the least heat exchange duty, although it also provides the lowest refrigeration power $\dot{Q}_R^{II}$.

- For recuperators HX3 and JTHX (Figure 5.40c, d), the configuration CFG4 requires less heat exchange duty for the same refrigeration power $\dot{Q}_R^{II}$ than the respective configurations CFG2 and CFG3. However, CFG4 is the only configuration requiring both recuperators.
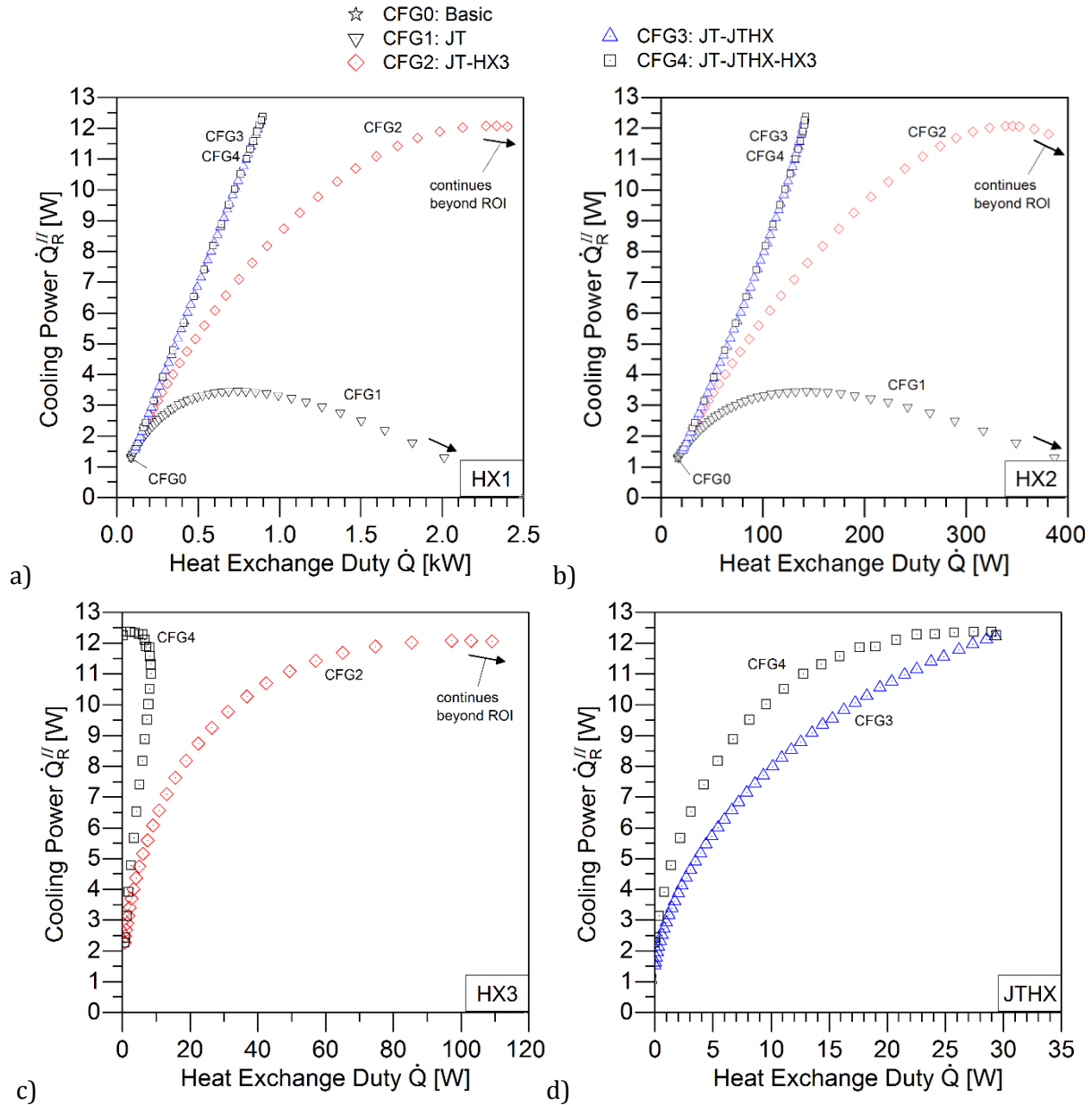
Figure 5.40. Comparison of the requirements in heat exchange duty $\dot{Q}$ for the recuperators HX1, HX2, HX3 and JTHX in order to deliver a given cooling power $\dot{Q}_R^{II}$. The shown region of interest (ROI) excludes some non-relevant values for CFG1 and CFG2.

Finally, the relationship between the cooling power provided to Circuit I $\dot{Q}_R^I$ and to Circuit II $\dot{Q}_R^{II}$ is presented in Figure 5.41, which results from their shown dependency as a function of the mass flow $\dot{m}$ (Figure 5.11, Figure 5.38). Thus, the data points in a given configuration have unique values of $\dot{m}$. The local temperature difference δT_{HX1} (at the cold end) is given to fully define the thermal performance of recuperator HX1, establishing the cooling power to Circuit I $\dot{Q}_R^I$. By comparing the four charts in Figure 5.41, it can be shown that:

- For a given mass flow $\dot{m}$, an increase in δT_{HX1} results in a reduction of $\dot{Q}_R^I$ without affecting $\dot{Q}_R^{II}$ (i.e. data point within red circle). According to Eq. (5.32), this decrease is proportional to the increase of $\dot{m} \cdot \delta T_{HX1}$, penalizing a high mass flow $\dot{m}$ and eventually leading to the total depletion of $\dot{Q}_R^I$. A further decrease into $\dot{Q}_R^I < 0$ is discarded as a practical

option, because it would imply the refrigerator system heating Circuit I.

The effect is illustrated in the four graphs (a-d) as the horizontal translation of each data point (i.e. red circle) towards lower values of $\dot{Q}_R^I$, transmuting the non-linear $\dot{Q}_R^{II}$-$\dot{Q}_R^I$ relationship into a linear one with reduced slope.

- Configuration CFG0 always provides the highest cooling power $\dot{Q}_R^I$ thanks to its inherent low requirements in mass flow $\dot{m}$.
- For a given value of $\dot{Q}_R^I$, CFG3 and CFG4 provide equal amounts of cooling power $\dot{Q}_R^{II}$. This amount is also the highest among all configurations, followed by CFG2 and then by CFG1.
- The $\dot{Q}_R^{II}$-$\dot{Q}_R^I$ relationship results in a trade-off between both parameters, with the highest possible value of $\dot{Q}_R^{II}$ being strongly dictated by the achieved thermal performance of recuperator HX1 (which in its turn is a function of δT_{HX1}).
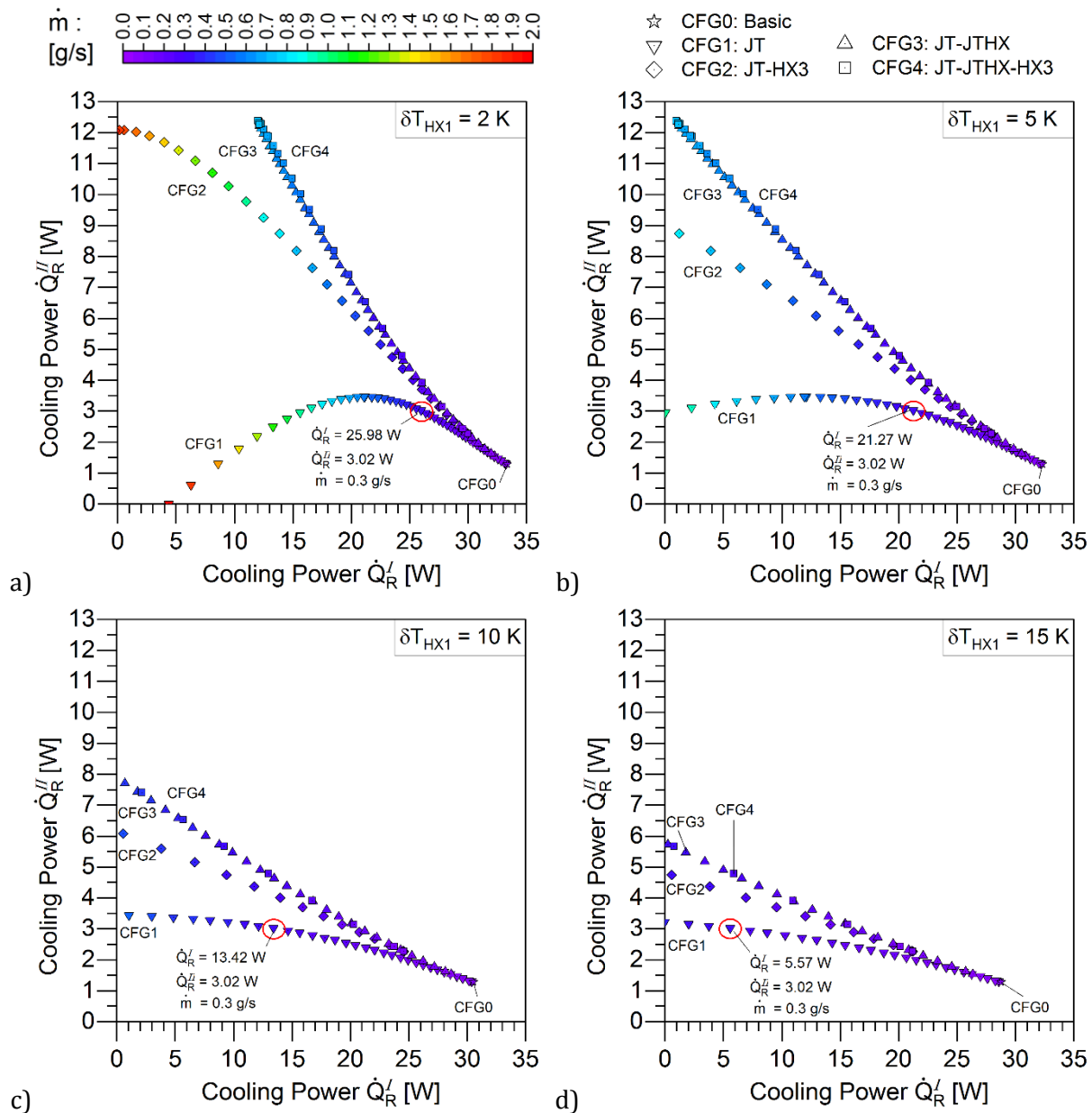
Figure 5.41. Relationship between the cooling power provided to Circuits I and II ($\dot{Q}_R^I$, $\dot{Q}_R^{II}$). Each plot corresponds to a given local temperature difference δT_{HX1}, which increasing value results in the horizontal translation of all data points (i.e. red circle) towards lower values of $\dot{Q}_R^I$, while preserving the values for $\dot{Q}_R^{II}$ and $\dot{m}$. The translation is proportional to the increasing value of $\bar{c}_p \cdot \dot{m} \cdot \delta T_{HX1}$, where $\bar{c}_p = 5.19$ J/g-K. The shown region of interest excludes discarded data with $\dot{Q}_R^I < 0$.

In conclusion, the comparison of process parameters allowed the identification of the relative advantages of the five configuration schemes. These insights are summarised in Table 5.15, which compares the parameter values qualitatively. It shows that no configuration is ideal, and that all configurations are superior for some parameters but inferior for others. In this work, however, the selection of a suitable configuration is primarily defined by the requirements in cooling power $\dot{Q}_R^{II}$ for Circuit II, whereas the cooling power $\dot{Q}_R^I$ for Circuit I is of subordinate importance. Figure 5.42 indicates the relative superiority of a configuration in providing such cooling power, and is based on the following statements:

CFG0.   Unrivalled in its ability to refrigerate systems with relatively low cooling requirements up to 1.3 W, because it is the simplest and most efficient of all five configurations. It does not need any additional components, requires the lowest pressure p_{HP}, and has the lowest demands in terms of mass flow $\dot{m}$ due to its excellent condensation rate. As a consequence, it also needs the lowest heat exchange duty for each of its two recuperators ($\dot{Q}_{HX1}$, $\dot{Q}_{HX2}$). In addition, this configuration can deliver the highest refrigeration power to Circuit I $\dot{Q}_R^I$, although it is also the most limited in terms of refrigeration power to Circuit II $\dot{Q}_R^{II}$;

CFG1.   Most competitive in the region around 1.3 to 3 W, which is a region above the cooling capabilities of CFG0, but low enough to content, with other configurations that would require additional recuperators. However, the advantages diminish rapidly with growing cooling power, due to increasing requirements in mass flow $\dot{m}$ and pressure p_{HP};

CFG2.   Of interest in the region around 2.3 to 7 W because it requires the lowest pressure p_{HP}. In the higher part of this region, this is the only major advantage of CFG2 with respect to CFG3 or CFG4. However, in the lower part of this region, CFG2 is superior to both of them due to the minor difference in mass flow requirements;

CFG3.   Relatively unattractive configuration because it requires a higher pressure p_{HP} than the closest alternatives CFG2 and CFG4;

CFG4.   Best suited in the region around 4 to 11 W due to its low mass-flow requirements. It is most advantageous for high amounts of cooling power $\dot{Q}_R^{II}$ because it has the best compromise in terms of mass flow $\dot{m}$ and pressure p_{HP}.

Table 5.15. Qualitative comparison of parameter values for all configuration schemes.

Parameter dependency	Cryocooler Independent				Cryocooler Dependent						
Parameter	p_{HP}	T_{2nd}	x	η_{TP}^{II}	$\dot{Q}_{HX1}$	$\dot{Q}_{HX2}$	$\dot{Q}_{HX3}$	$\dot{Q}_{JTHX}$	$\dot{m}$	$\dot{Q}_R^I$	$\dot{Q}_R^{II}$
Compared at a given value of	$\dot{Q}_R^{II}$	p_{HP}			$\dot{Q}_R^{II}$						$\dot{Q}_R^I$
ideal direction	↓↓	↑↑	↓↓	↑↑	↓↓	↓↓	↓↓	↓↓	↓↓	↑↑	↑↑
CFG0	↓↓	↓↓	↓↓	↑↑	↓↓	↓↓	-	-	↓↓	↑↑	↓↓
CFG1	↓	↑	↑↑	↓↓	↑↑	↑↑	-	-	↑↑	↓↓	↓
CFG2	↓↓	↑↑	↑↑	↓↓	↑	↑	↑	-	↑	↓	↑↑
CFG3	↑↑	↑	↓↓	↑↑	↓	↓	-	↑	↓	↑	↑↑
CFG4	↑	↑	↓↓	↑↑	↓	↓	↓↓	↓	↓	↑	↑↑

↑ / ↓: high / low value; arrows in red colour highlight the undesired direction
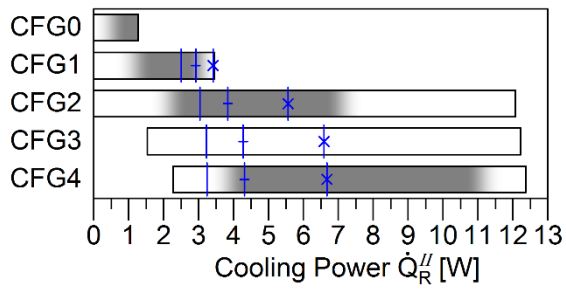
Figure 5.42. Range of cooling power $\dot{Q}_R^{II}$ that a configuration can provide to Circuit II. The *region of interest* indicates the relative superiority of a configuration in providing such cooling power.

6 Design of the Cryo Supply System

A demonstrator of the Cryo Supply System (CSS) is built to prove the viability of the overall refrigeration concept by cooling the superconducting cyclotron. This chapter presents the design of such a demonstrator system, and focuses on the thermo-hydraulic and thermo-mechanical design of its internal components. First, the CSS design is introduced using technical models and flow schemes. Then, after defining the working point of the system, the refrigeration power is estimated and compared to the cooling requirements. Next, the design process of each heat-exchanger type is described in detail and the corresponding results are presented. The sensitivity of the system to possible deviations from design values is described at the end. The complete list of calculated process and performance values is available in Appendix A2.

The design of the Cryo Supply System (CSS) is, to a large extent, determined by the selection of the configuration scheme. The analysis performed in the last chapter shows that all evaluated configuration schemes (CFG0 to CFG4) are capable of providing the required refrigeration power. However, it also shows that refrigeration power and technical complexity are two competing factors, so that a compromise in the selection process becomes unavoidable. On the one hand, a higher refrigeration power is desirable because it results in a larger refrigeration margin, and therefore, in more operational freedom. On the other hand, a low technical complexity entails not only economic advantages but also a lower risk of system failure due to technical difficulties. For the design of this first-generation demonstrator system, a lower technical complexity is considered of higher importance than a larger refrigeration margin. This results in the selection of the basic configuration scheme CFG0, because it can provide the required refrigeration power whilst also being the technically simplest and thermodynamically most transmission-efficient (η_{TP}^{II} = 0.88) of all evaluated schemes.

The design process attempts to determine the set of conditions in which the CSS is capable of providing the required refrigeration power, whilst also accounting for possible deviations from the design values. Consequently, at its *design working point*, the CSS shall present sufficient refrigeration margin to accommodate the design uncertainty with a reasonable degree of confidence; in this case, the confidence threshold is set to 95 %. In addition, the design shall consider the cryocooler stage-power as specified on the supplier's data-sheet (chapter 4.2.3) to ensure the design validity when employing any cryocooler of the same type.

The technical model of the CSS is introduced in Figure 6.1, showing the cryocooler stages (a) and the various heat exchangers (b) inside a vacuum vessel (c). The colder components are enclosed by a thermal shield (d) for better thermal performance. The vacuum vessel (c) consist of a cylindrical body with a top and a bottom flange. The top flange (e) provides mechanical support to all components and is equipped with four small vacuum flanges

for electrical feedthroughs and with the connection to the room-temperature circulation system (h). The bottom flange (f) provides the interface to the transfer line.

Figure 6.1. Simplified cross-sectional view of the Cryo Supply System (CSS) connected to the transfer line. Dimensions are in millimetres.
a) cryocooler stages; b) heat exchangers; c) vacuum vessels; d) thermal shield; e) top flange; f) bottom flange; g) feedthrough; h) connection to pump system.

The schematics of the CSS are introduced in Figure 6.2 and show relevant process values. The refrigeration cycle is fully described by the system of linear equations and the set of parameter values listed in Table 6.1 and Table 6.2. The parameter set defines the design working point of the CSS, and corresponds to a *first version* of parameter values deriving from preliminary requirements, which differs from a *second version* used in chapter 7 corresponding to the nominal working conditions of the overall cryogenic system.

The CSS has a total of six heat exchangers in three types (Figure 6.2). The first type consists of the three recuperators HX1A, HX1B and HX2. The recuperators HX1A and HX1B are connected in series to act as a single unit corresponding to the recuperator previously referred to as HX1; this *segmentation* distributes the working temperature range between both recuperators allowing the colder one (HX1B) to be placed inside the thermal shield for better thermal performance. The second heat-exchanger type consists of the two thermalisators HX1stA and HX1stB, which are thermally anchored to the cryocooler's 1st stage. The third heat-exchanger type is the condenser HX2nd, which is thermally anchored to the cryocooler's 2nd stage to generate liquid helium.

Figure 6.2. Flow schematics of the Cryo Supply System (CSS) showing relevant components and process values corresponding to the design working point.

Table 6.1. System of linear equations used for the design of the Cryo Supply System (CSS).

Description	Equation	Eq.
Initial incoming flow temperature	$T_1 = T_a$	(6.1.1)
Δh on HX1A	$h_{12} = h_{11} - (h_2 - h_1)$	(6.1.2)
Δh on HX1B	$h_{11} = h_{10} - (h_3 - h_2)$	(6.1.3)
Δh on HX2	$h_7 = h_6 - (h_{10} - h_9)$	(6.1.4)
δT on cold end of HX1stB	$T_6 = T_{1st} + \delta T_{HX1stB}$	(6.1.5)
δT on cold end of HX2	$T_{10} = T_6 - \delta T_{HX2}$	(6.1.6)
1st stage temperature	$T_{1st} = T_4 - \delta T_{HX1stA}$	(6.1.7)
2nd stage temperature	$T_{2nd} = T_8 - \delta T_{HX2nd}$	(6.1.8)
Power extracted by HX1stA	$\dot{Q}_{HX1stA} = \dot{m} \cdot (h_4 - h_3)$	(6.1.9)
Power extracted by HX1stB	$\dot{Q}_{HX1stB} = \dot{m} \cdot (h_6 - h_5)$	(6.1.10)
Power extracted by 1st stage	$\dot{Q}_{avail}^I = \dot{Q}_{HX1stA} + \dot{Q}_{HX1stB}$	(6.1.11)
Mass flow	$\dot{m} = \dot{Q}_{avail}^{II}/(h_8 - h_7)$	(6.1.12)
Available 1st stage power	$\dot{Q}_{avail}^I = \eta_{CSS}^I \cdot \dot{Q}_{1st}$	(6.1.13)
Available 2nd stage power	$\dot{Q}_{avail}^{II} = \eta_{CSS}^{II} \cdot \dot{Q}_{2nd}$	(6.1.14)

Table 6.2. Summary of process parameters used for the design of the Cryo Supply System (CSS). The list defines the design working point of the CSS and differs from Table 7.2 for the nominal working conditions of the overall cryogenic system.

Type	Parameter		Value	Description
Thermal budget requirement:	$\dot{Q}_R^I$	[W]	≥ 15	Required refrigeration power on Circuit I and II, as specified for the CSS design.
	$\dot{Q}_R^{II}$	[W]	≥ 0.7	
Boundary condition:	T_a	[K]	293.15	Ambient temperature.
	T_R^{II}	[K]	4.5	Refrigeration temperature of Circuit II (at the returning stream; point ⑨).
	T_4	[K]	40	Temperature of incoming flow to Circuit I.
Model simplification:	η_{CSS}^I	[%]	100	The entirety of the cryocooler power on each stage ($\dot{Q}_{1st}$, $\dot{Q}_{2nd}$) is available for the refrigeration cycle.
	η_{CSS}^{II}	[%]	100	
	Δp	[bar]	$\Delta p_{1\to12} \approx 0$	Isobaric consideration for the entire circuit.
Design value:	T_1	[K]	T_a	Temperature of the incoming flow from the circulation system.
	T_2	[K]	150	Temperature defining the "segmentation" of recuperator HX1 into two parts: HX1A and HX1B.
	δT_{HX2}	[K]	0.5	Local temperature difference at the warm end of HX2 ($T_6 - T_{10}$).
	δT_{HX1stA}	[K]	0.1	Local temperature difference at the cold end of HX1stA and HX1stB ($T_4 - T_{1st}$; $T_6 - T_{1st}$).
	δT_{HX1stB}	[K]	0.1	
	δT_{HX2nd}	[K]	0.2	Local temperature difference at the cold end of HX2nd ($T_8 - T_{2nd}$).
	$\dot{Q}_{HX1stA}$	[W]	5	Heat power extracted by thermalisator HX1stA (indirectly defining effectiveness ε_{HX1A} and ε_{HX1B})
	x_8	[-]	0.1	Vapour quality of incoming flow to Circuit II.
	x_9	[-]	1	Vapour quality of returning flow from Circuit II.
	Λ	[-]	$\ll 0.01$	Negligible longitudinal condition on the heat exchangers.
Others relevant parameters:	T_{1st}	[K]	39.9	Temperature of the cryocooler stages.
	T_{2nd}	[K]	4.3	
	$\dot{Q}_{1st}$	[W]	24.91	Cooling power of the cryocooler stages. (values extracted from Figure 4.12)
	$\dot{Q}_{2nd}$	[W]	1.51	
	η_{TP}^I	[%]	79.9	Transmission efficiency of the thermodynamic process for Circuit I and II.
	η_{TP}^{II}	[%]	86.7	
	y_{LHe}	[%]	86.7	Condensate yield.
	$\dot{m}$	[g/s]	0.0770	Total mass flow.
	$\dot{Q}_R^I$	[W]	19.91	Refrigeration power for Circuit I and II.
	$\dot{Q}_R^{II}$	[W]	1.30	
	p_{sat}	[bar]	1.3026	Saturation pressure at T_R^{II}.
	h_{evap}	[J/g]	18.82	Evaporation enthalpy at T_R^{II}.
	ε_{HX2}	[%]	99.2	Effectiveness of recuperator HX2 $(T_{10} - T_9)/(T_6 - T_9)$.

Figure 6.3 depicts the CSS insert, which is the assembly comprising all components that are, directly or indirectly, supported by the top flange. A suspension system attached to the top flange is used to support the recuperators (HX1A, HX1B, HX2), whereas the remaining heat exchangers (HX1stA, HX1stB, HX2nd) are attached to the cryocooler stages. The thermal shield is supported and thermalised by a flange attached to the cryocooler's 1st stage.

The images also show the *validation unit*, which is a sub-system specifically designed to emulate the thermo-hydraulic conditions of Circuits I and II, and which allows the experimental testing of the CSS insert. Haug et al. [55] used this particular setup to prove the viability of the design principle, showing that the demonstrator system is capable of providing a refrigeration power of 25 W to Circuit I (non-isothermal, 40-100 K) and 1.4 W to Circuit II (isothermal, 4.5 K). The design and manufacturing of the validation unit, including the test campaigns, are beyond the scope of this work.

Computer design	**Before interconnecting the main components**	**With full insulation and instrumentation**
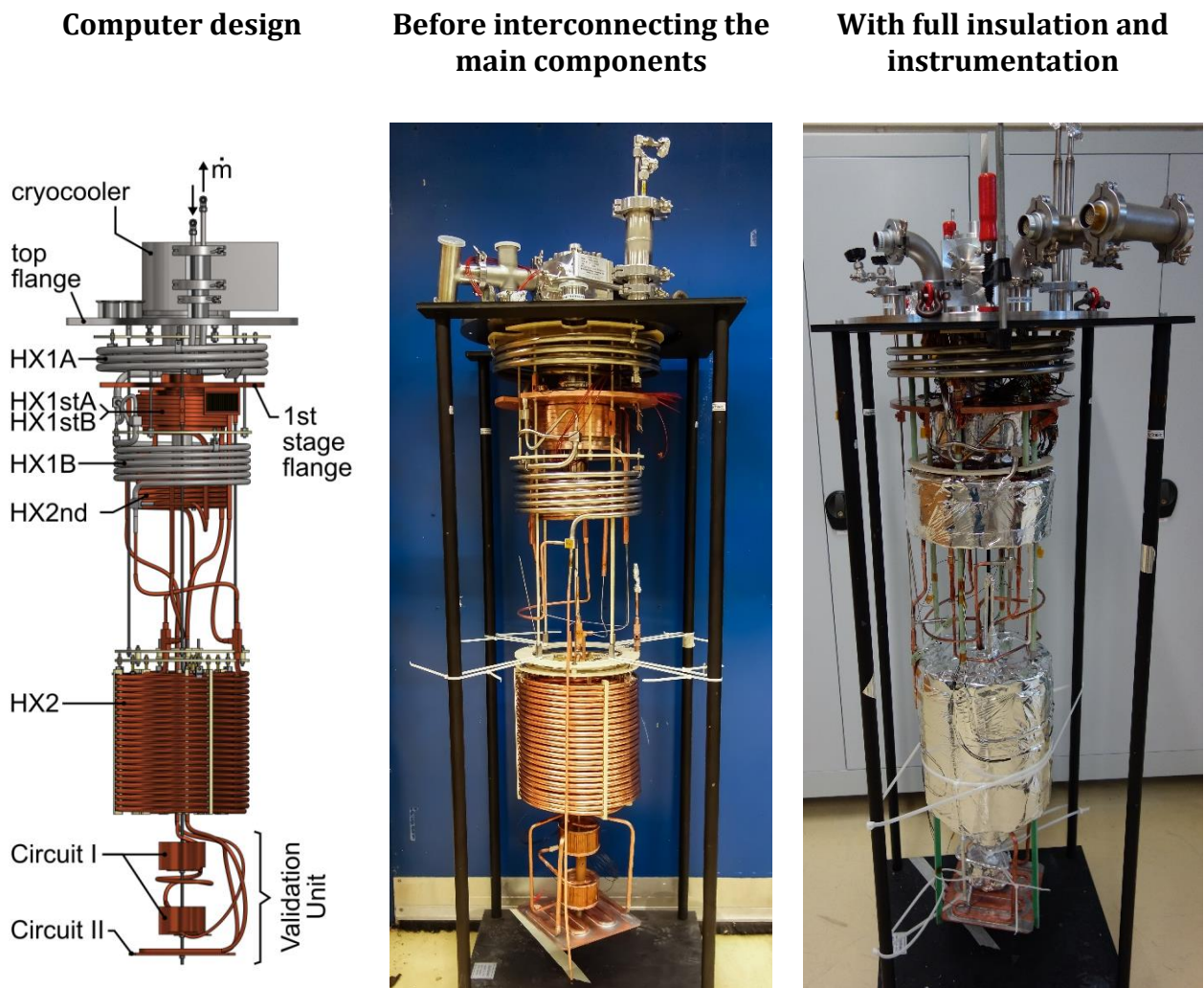
Figure 6.3. Built demonstrator of the Cryo Supply System (CSS). The assemblies show the CSS insert without thermal shield, including the validation unit for experimental testing.

Figure 6.4 shows the estimate of the refrigeration power $\dot{Q}_R$ provided by the CSS under design conditions, and compares it with the design requirements ($\dot{Q}_R^I$ / $\dot{Q}_R^{II}$ = 15 / 0.7 W; Table 4.2). The refrigeration power measured by Haug et al. [55] is shown for reference.

The calculated values are based exclusively on the thermo-hydraulic design of the CSS; deviations from the actual manufacturing values are accounted for in terms of uncertainty. As shown later in chapter 8.3.3, the calculation uncertainty is strongly dominated by the accuracy of the model describing the thermodynamic process; the heat-exchanger models are of much lower relevance. The uncertainty introduced by considering the cooling-power specifications of a *generic* cryocooler has, by comparison, a moderate contribution. Unfortunately, the uncertainty analysis for the experimental data reported in [55] is not yet available. Nonetheless, considering the description of the used experimental setup (an industrial-grade data acquisition architecture measuring specifically calibrated temperature sensors with state-of-the-art thermalisation strips), this work deems it reasonable to estimate a confidence interval in the order of ±10 %.

At its design working point (dot markers), the CSS is sized to supply a non-isothermal refrigeration power $\dot{Q}_R^I$ of 19.91 W and an isothermal refrigeration power $\dot{Q}_R^{II}$ of 1.30 W, which corresponds to process efficiencies of $\eta_{TP}^I = 79.9\,\%$ and $\eta_{TP}^{II} = 86.7\,\%$. This refrigeration power is higher than the design requirements (grey columns), resulting in a power reserve (dashed columns) of 33 % and 86 %, respectively. However, when considering the design uncertainty (solid error bars), the refrigeration power estimated for each circuit varies within a range of $-24\,\%$ and $+17\,\%$. In spite of this variation, the refrigeration power is still expected to exceed the design requirements, with the power surplus varying accordingly.

The refrigeration power measured at the demonstrator system (triangle markers, including error bars) is considerably higher than the design requirements and overlaps with the higher region of the estimated design range. The agreement between the measured and calculated values is statistically significant ($\gtrsim 5\,\%$), since chapter 8.3.3 estimates that the probability of both confidence intervals referring to the *same* true-value is 5 % for $\dot{Q}_R^I$ and 18 % for $\dot{Q}_R^{II}$.

In conclusion, the CSS is sized to provide the required refrigeration power, whilst having enough power reserve to accommodate for design uncertainties. Measurements of the built demonstrator system [55] indicate that the design approach is rather conservative. As it will be shown in chapter 7, this is likely due to the underestimation of the employed cryocooler device, the power of which surpasses the supplier's specifications by over 20 %.
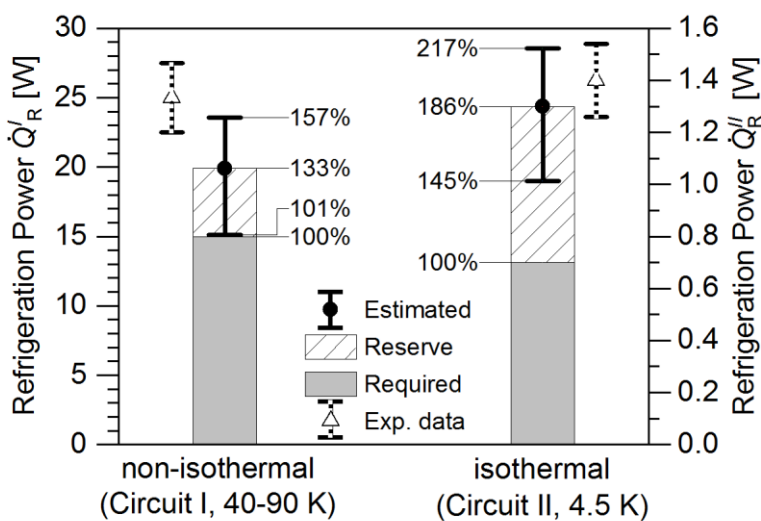
Figure 6.4. Estimated refrigeration power $\dot{Q}_R$ on Circuits I and II for the design working point (Table 6.2). It is distinguished between cooling requirements and reserve, where the cooling requirements correspond to the preliminary values used in the CSS design (Table 4.2). The error bars correspond to 95 % confidence intervals, and the experimental data to measurements reported by Haug et al. [55].

6.1 Heat exchanger design

The thermal design of the heat exchangers, and in particular their final effectiveness, determines to a large extent the overall performance of the CSS. However, ultimate design decisions also depend on a number of external factors such as physical size, technical complexity, final cost, etc. The evaluation of thermal, mechanical, and economic considerations reveals that certain factors compete with each other and that a compromise is unavoidable. An example of competing factors are effectiveness and cost, because the realisation of a heat exchanger with a very high thermal performance habitually requires complex technical solutions, entailing costly manufacturing procedures and efforts. Dominant factors for the CSS design are the stringent dimensional limitations at the final installation site and economic constraints.

The factors taken into consideration for the heat exchanger design are summarised in Table 6.3. First, the thermal considerations derive from the requirement of high effectiveness ε. Therefore, pressure drop Δp and local temperature difference δT are to be minimised. Consequently, the heat-exchanger channels shall present, within limitations, the largest possible hydraulic diameter D_h and the highest possible thermal conductance $(U \cdot A)$. In addition, the longitudinal heat conduction $\dot{Q}_{\text{long}}$ shall be minimised for recuperators, requiring the smallest possible cross-sectional wall area A_{wall} with the lowest possible heat conduction coefficient λ_{wall}. Second, the mechanical considerations derive from the technological solution to be chosen. The component size shall be small and compact enough to fit within the limited space inside the existing vacuum vessel [59]. In addition, the number of joints (welded, brazed or screwed) shall be kept to a minimum in order to reduce the risk of leakages during operation. Third, the economic consideration to be minimised is the total manufacturing cost, which is assessed on a case-by-case basis. In general, commercially available components are preferred over specific design solutions of new developments.

Table 6.3. Factors considered during the heat exchanger design.

Type of Consideration	Contemplated factor	Description
Thermal	• $\varepsilon \uparrow$	Heat exchangers effectiveness.
	○ $\Delta p \downarrow$	Pressure drop
	▪ $D_h \uparrow$	Hydraulic diameter
	○ $\delta T \downarrow$	Local temperature difference.
	▪ $(U \cdot A) \uparrow$	Thermal conductance.
	○ $\dot{Q}_{\text{long}} \downarrow *$	Longitudinal heat conduction.
	▪ $\lambda_{\text{wall}} \downarrow *$	Heat conduction coefficient of the wall material.
	▪ $A_{\text{wall}} \downarrow *$	Cross-sectional area of the wall.
Mechanical	• Size $\downarrow$	Physical size of the heat exchanger.
	○ Shape	Component fits inside limited space of the CSS.
	• Leakages $\downarrow$	Risk of leakages.
	○ Joints $\downarrow$	Number of joints.
Economic	• Cost $\downarrow$	"Affordable" cost (decided on a case-to-case basis). Commercially available components are preferred.

↑ / ↓: Factor should be maximised / minimised.
* Only applied for recuperator design.

Recuperative thin-plate heat exchangers are widely used in cryogenic applications and have the advantage of presenting a relatively large heat transfer area A in compact form [25].

However, the use of many thin-plates also leads to a larger cross-sectional area A_wall, and therefore, to an increase in longitudinal heat conduction $\dot{Q}_\text{long}$. For this reason, more sophisticated thin-plate designs use composite plates with anisotropic thermal properties in order to reduce the longitudinal heat conduction $\dot{Q}_\text{long}$ without affecting the thermal conductance $U \cdot A$. However, the use of thin-plate heat exchangers is discarded because manufacturing composite plates is considered too costly, and each of the numerous joints between conventional plates represent an intrinsic risk of leakage. In contrast, tubular heat exchangers made exclusively of single seamless pipes have the major advantage of requiring a considerably lower number of joints, decreasing the total risk of leakage. In addition, the use of industrial available pipes for the bulk of the component reduces cost, and the pipes can be bent in a helical shape, allowing a relatively compact arrangement inside the vacuum vessel. Therefore, the use of tubular heat exchangers is chosen for this work due to their thermal and mechanical simplicity.

6.1.1 Recuperator design

Each one of the three recuperators (HX1A, HX1B, and HX2) is made of two seamless pipes in coaxial arrangement. Each one of the three recuperators (HX1A, HX1B, and HX2) is made of two seamless pipes in coaxial arrangement. Their thermo-hydraulic model (Figure 6.5) considers the energy balance of both fluids and the local heat transfer resistance R_UA. The model assumes uniform fluid properties within a given control volume k, flow channels resulting from two perfectly concentric and straight round pipes, and no external heat-in-leaks. For simplification purposes, longitudinal heat conduction and pressure drop are not considered* in the model because, by design, their contribution is of secondary importance. Nonetheless, both values are estimated separately in order to verify this design criterion.
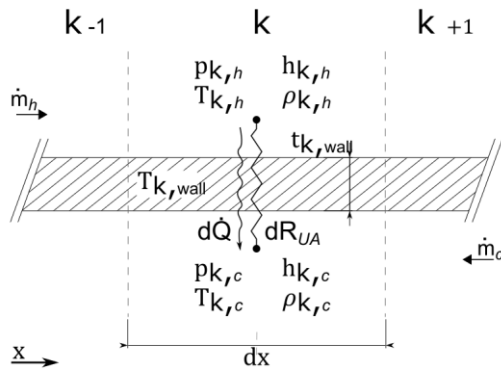
Figure 6.5. Thermo-hydraulic model of the recuperators HX1A, HX1B and HX2.

The pressure drop Δp is calculated based on chapter 3.4.3 and is a function of the channel geometry and fluid properties. Since the fluid temperature varies considerably along the flow channels, the pressure drop Δp between two points ($i \rightarrow i + 1$ in Figure 6.2) is approximated

---

* For a future optimization of the heat exchangers, it is referred to [25], [42], [41] and [60] for examples of thermo-hydraulic models considering longitudinal heat conduction, pressure drop and external heat-in leaks.

as the arithmetical mean of two pressure drop values: one that considers the fluid properties at the pipe inlet (i) and one that considers the fluid properties at the pipe outlet ($i + 1$)

$$\Delta p_{i \to i+1} \approx (\ \Delta p_{i \to i+1}\Big|_{T_i} + \Delta p_{i \to i+1}\Big|_{T_{i+1}} \ )/2 \quad . \tag{6.2}$$

Based on the previous considerations, Table 6.4 lists the thermal design values of the three recuperators, Figure 6.6 shows their temperature profile over the dimensionless length $\xi = x/L$, and Figure 6.7 compares their exergy exchange. The recuperator HX2 has the highest thermal performance among all heat exchangers (ε_{HX2} = 99.2 %, ζ_{HX2} = 95.8 %). For this reason, it requires a pipe ten-times longer than the other recuperators, despite having 25-35 % of their heat exchange duty ($\dot{Q}_{HX2} \approx$ 15 W, $L_{HX2} \approx$ 46 m).
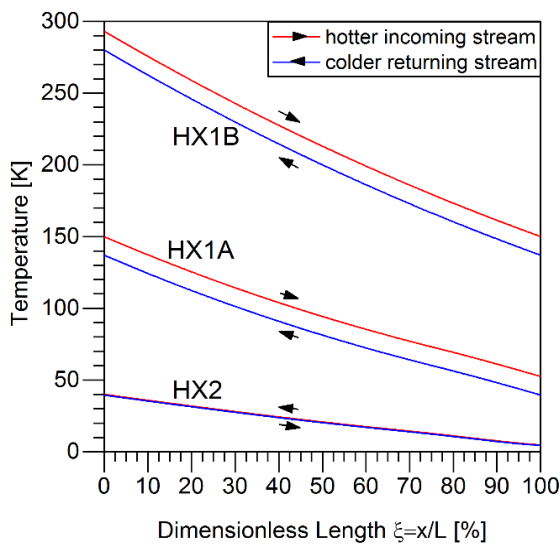
Figure 6.6. Temperature profile of the recuperative coaxial heat exchangers HX1A, HX1B and HX2 over the dimensionless length $\xi = x/L$.
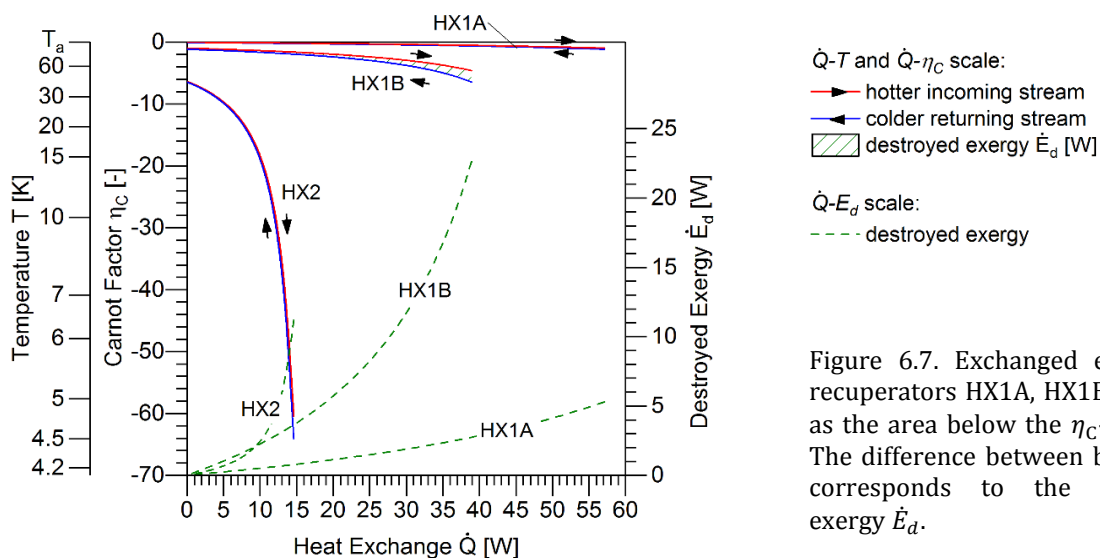
Figure 6.7. Exchanged exergy on recuperators HX1A, HX1B and HX2 as the area below the η_C-$\dot{Q}$ curves. The difference between both areas corresponds to the destroyed exergy $\dot{E}_d$.

Table 6.4. Thermal design values for recuperators HX1A, HX1B and HX2.

	HX1A		HX1B		HX2	
	OP	IP	OP	IP	OP	IP
Pipe diameter * [mm]	13	8	10	6	8	4
Channel cross-section A_h [mm²]	54.19	50.27	28.27	28.27	21.99	12.57
Temperature range [K]	293.15-150.00	280.15-137.00	150.00-52.47	137.00-39.50	40.00-4.77	39.50-4.50
Reynolds number Re [-]	217-341	644-1040	436-821	1387-2968	1262-4967	4452-8133
Pressure drop Δp [mbar]	12.84	1.77	18.42	1.88	24.58	28.09
Heat exchange duty $\dot{Q}$ [W]	57.26		39.03		14.63	
Pipe Length L [m]	4.17		4.77		46.51	
Mean overall thermal conductance $U_m \cdot A$ [W/K]	4.40		3.00		30.63	
Mean temperature difference δT_m [K]	13.00		12.99		0.48	
Effectiveness ε [%]	91.7		88.3		99.2	
NTU [-]	11.01		7.51		73.29	
Transferred exergy $\Delta \dot{E}_h$ [W]	21.31		84.22		255.50	
Destroyed exergy $\dot{E}_d$ [W]	5.31		22.75		11.23	
Exergetic efficiency ζ [%]	80.0		78.7		95.8	

OP: Outer pipe with hotter stream; IP: Inner pipe with colder stream.
* Corresponds to pipe inner-diameter with a wall thickness of 1 mm.

Table 6.5 presents the values resulting from the manufacturing design of the three heat exchangers. The recuperators are made of single seamless pipes bent helically in up to four concentric layers, thereby achieving a compact design. The manufacturing length L_M of the pipes is maximised by exploiting the available space. This increases the heat exchange area with respect to the thermal design leading to the safety factor S_A. The relative position between inner and outer pipes is undefined since various manufacturing constraints impeded the use of centring spacers. Stainless steel is the preferred pipe material due to its good weldability and relatively low thermal conductivity. The latter has the advantage of reducing longitudinal heat conduction with negligible impact on the heat transfer coefficient U. Consequently, the recuperators HX1A and HX1B are made of stainless steel AISI316L. However, the recuperator HX2 is made of copper C12200 (DHP Cu) due to the commercial availability of single seamless pipes at lengths exceeding 10 m. Despite the higher thermal conductivity of copper, the longitudinal heat conduction $\dot{Q}_{long}$ on HX2 remains acceptable due to the relatively low thermal gradient (dT/dx).

Table 6.5. Manufacturing design values for recuperators HX1A, HX1B and HX2.

	HX1A	HX1B	HX2
Pipe material	Stainless Steel AISI 316L	Stainless Steel AISI 316L	Copper (DHP) C12200
Pipe diameter (OP/IP) [mm] * †	13/8	10/6	8/4
Pipe Length L_M (design L †) [m]	5.62 (4.17)	5.43 (4.77)	55.8 (46.51)
Long. heat $\dot{Q}_{long}$ (OP/IP) [mW] ‖	21.41/13.76	6.90/4.39	2.59 §/1.44 §
Long. conduction parameter Λ [10^6] ‖	0.05	0.03	0.02 §
Safety factor S_A [-] ‡	1.35	1.14	1.20
D [mm]	150/342	272	90/150/210/270
H [mm]	≈90	≈105	≈305
Windings [-]	1.7/3.3	6	23/23/23/23
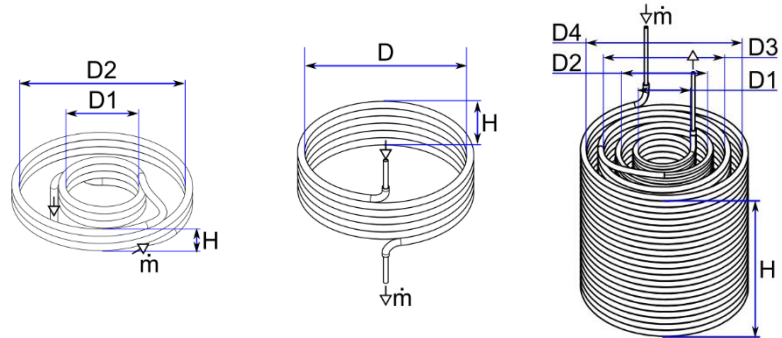
OP: Outer pipe (hotter stream); IP: Inner pipe (colder stream).

* Corresponds to pipe innerdiameter with a wall thickness of 1 mm.

§ The thermal conductivity $\lambda_{wall}(T)$ for Cu DHP (C12200) was obtained from [62].
A constant value of $\lambda_{wall}(T = 77 \text{ K}) = 120 \frac{W}{m \cdot K}$ was used in the calculation.

† Value as defined in **Table 6.4**.

‖ As a conservative approach, the value is calculated in relation to the shorter design length L.

‡ With respect to total heat exchange area A ($\sim L_M / L$)

Each recuperator is supported from the top flange by a customised suspension system, which consists of a set of rods and disks specifically designed to minimise the heat flux between components (Figure 6.8). The recuperators are supported from the top by a set of clamps (d) attached to a disk (c) made of glass-fiber reinforced polymer sheets (GFRP-CR). The disk is then supported by a set of four GFRP-CR rods (b) screwed to the top flange (a). The support system of recuperator HX2 has an additional support disk and the rods are thermalised to the 1st stage (e) in order to reduce heat conduction. The recuperator HX2 is self-supported by a set of GFRP-CR bars to reduce geometrical deformations due to its own weight.

Side view   **Perspective view**
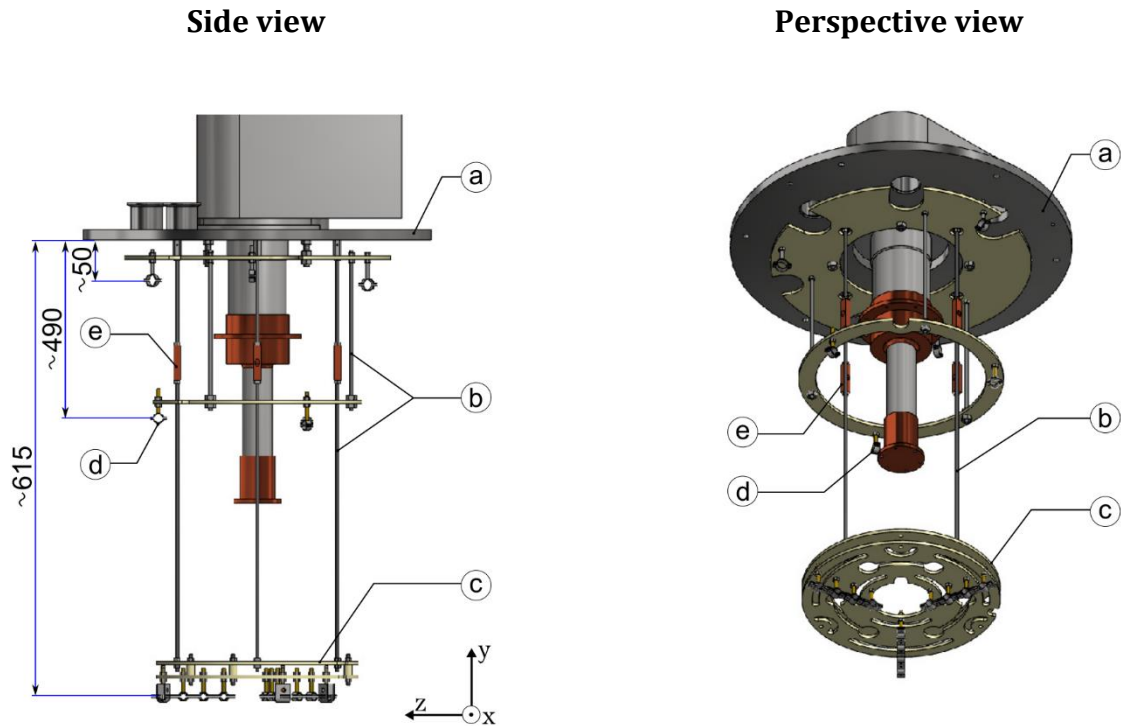
Figure 6.8. Customised suspension system of recuperators HX1A, HX1B, and HX2. Dimensions are in millimetres.

a) top flange; b) support rods; c) support disks; d) support clamps; e) piece for thermalisation to the cryocooler's 1st stage.

6.1.2 Thermalisator design

The design approach of the thermalisators HX1stA and HX1sB is analogous to the one presented for the recuperators. However, each thermalisator consists of a single pipe that is thermally anchored to the 1st stage. The corresponding thermo-hydraulic model is introduced in Figure 6.9 and assumes a homogeneous temperature at the cryocooler stage. The thermal design values are listed in Table 6.6, the temperature profiles are shown in Figure 6.10, and their exergy exchange is compared in Figure 6.11.
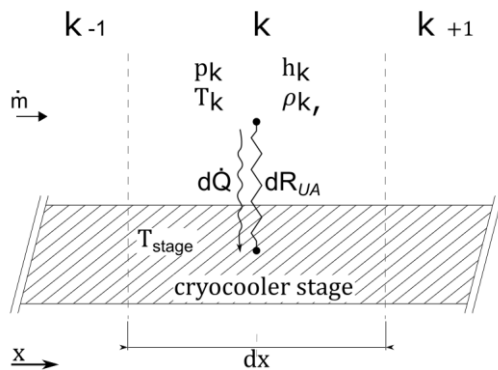
Figure 6.9. Thermo-hydraulic model of the thermalisators HX1stA and HX1stB.

Table 6.6. Thermal design values for thermalisators HX1stA and HX1stB.

	HX1stA	HX1stB
Pipe diameter * [mm]	6	6
Channel cross-section [mm²]	28.27	28.27
Temperature range [K]	52.47 - 40.00	89.71 - 40.00
Reynolds Re [-]	2492 - 2945	1788 - 2945
Pressure drop [mbar]	0.42	0.81
Heat exchange duty $\dot{Q}$ [W]	5.00	19.91
Pipe Length L [m]	2.54	3.35
Mean overall thermal conductance $U_m \cdot A$ [W/K]	1.92	2.46
Mean temperature difference δT_m [K]	2.61	8.10
Effectiveness ε [%]	99.2	99.8
NTU [-]	4.78	6.13
Transferred exergy $\Delta \dot{E}_h$ [W]	26.89	74.94
Destroyed exergy $\dot{E}_d$ [W]	4.84	51.42
Exergetic efficiency ζ [%]	84.8	59.3

* Corresponds to pipe innerdiameter with a wall thickness of 1.5 mm.
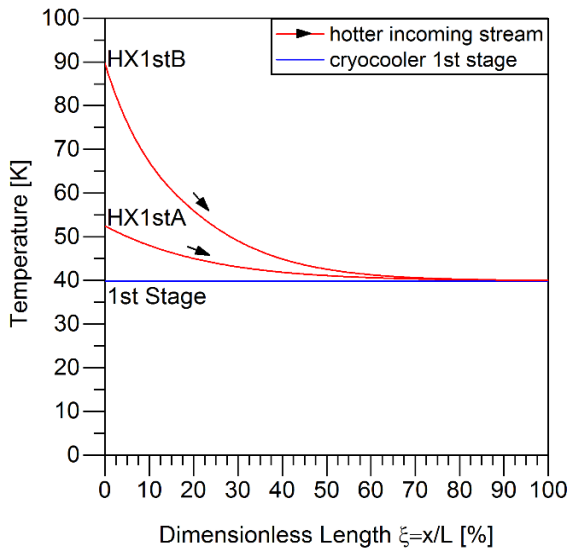
Figure 6.10. Temperature profile of the thermalisators HX1stA and HX1stB over the dimensionless length $\xi = x/L$.
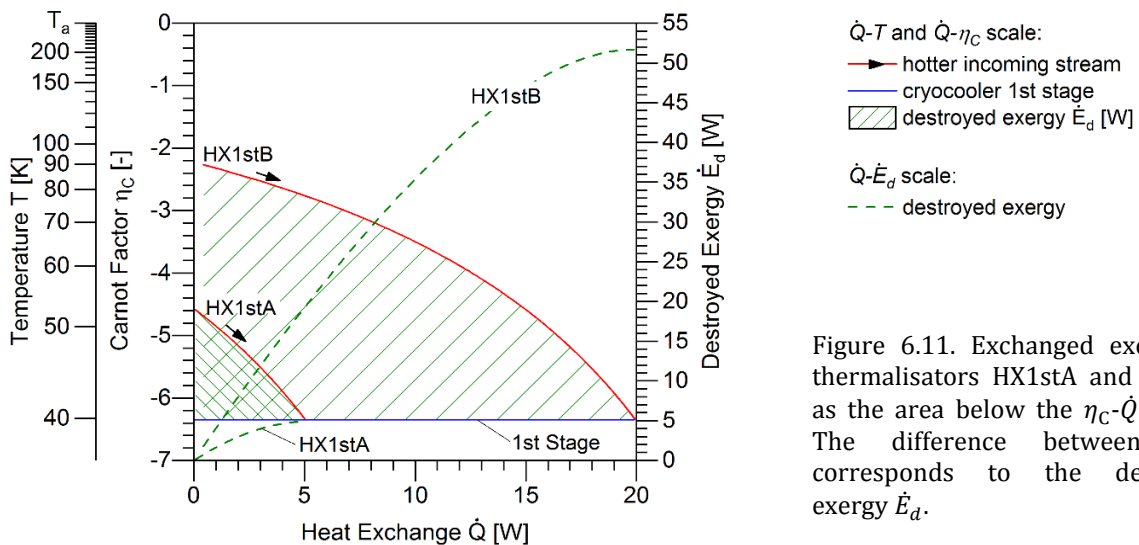
Figure 6.11. Exchanged exergy on thermalisators HX1stA and HX1stB as the area below the η_C-$\dot{Q}$ curves. The difference between both corresponds to the destroyed exergy $\dot{E}_d$.

Table 6.7 presents the manufacturing design values for the two thermalisators, which are made of single seamless square pipes bent helically in a common layer. In analogy to the recuperators design, the manufacturing length L_M exploits the available space and is longer than the thermal design length L, leading to the safety factor S_A. Both pipes are brazed directly to a cylindrical body, which acts as a thermal coupler to the 1st stage (Figure 6.12). The pipes are made of copper C12200 (Cu DHP) and the thermal coupler is made of a single piece of oxygen-free high thermal conductivity copper C10300. The flow direction on both recuperators goes from bottom to top, opposite to the temperature gradient of the thermal coupler, resulting in an arrangement that is analogous to a counter-flow heat exchanger.

Table 6.7. Manufacturing design values for thermalisators HX1stA and HX1stB.

	HX1stA	HX1stB
Pipe material	Copper C12200 (Cu DHP)	
Pipe dimensions [mm] (innerdiameter/edge length)	Ø6/9	
Pipe Length L_M (design L †) [m]	4.83 (2.54)	4.16 (3.35)
Safety factor ‡ S_A [-]	1.90	1.24
D [mm]	152	180
H [mm]	≈81	≈63
Windings [-]	9	7
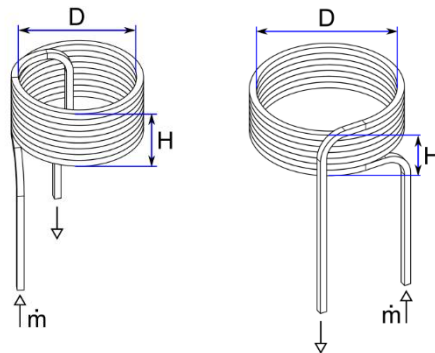
‡ With respect to total heat exchange area A ($\sim L_M / L$)
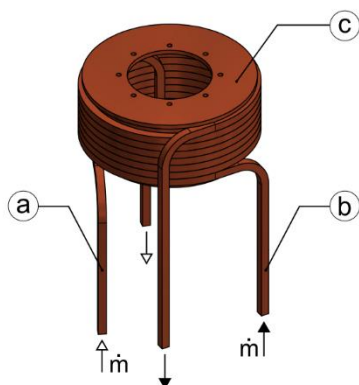
Figure 6.12. Assembly of thermalisators HX1stA (a), HX1stB (b) attached to the thermal coupler (c) to the 1st stage.

6.1.3 Condenser design

The condenser HX2nd is made of a single seamless pipe thermally attached to the 2nd stage, which is similar to the design of thermalisators HX1stA and HX1stB. However, since this particular heat exchanger is used to condensate helium, a pipe specifically designed for industrial condensers is used instead. The pipe available for this work is of type "TECTUBE©_fin CVS" from the company KME (Table 6.8). This pipe has an inner profile with grooves that enhance the heat transfer by increasing the inner surface area by a factor F_A of 1.96 with respect to a smooth reference pipe with the same inner diameter d. This type of pipe supports dropwise condensation and is designed mainly for industrial condensers using hydrofluorocarbon (HFS) refrigerants. [63]

Table 6.8. Seamless pipe used for the condenser HX2nd. The inner-grooved pipe from type TECTUBE©_fin CVS from the company KME is specially conceived for industrial condensers. [63]

TECTUBE©_fin CVS		
Profile Designation	95240CVS20/74B	
Material	Copper	
Pipe diameter [mm] (D/d†)	9.52/8.32	
Bottom wall thickness t_b [mm]	0.4	
Number of grooves	66	
Groove depth h [mm]	0.2	
Lead angle φ	20°	
Top angle γ	20°	
Enhancement Factor F_A ‡	1.96	
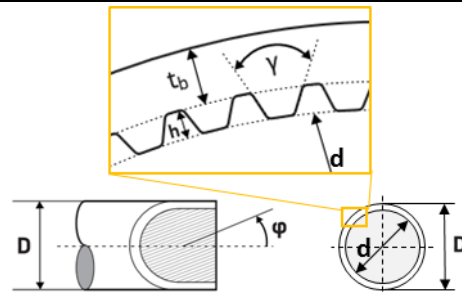
† Innerdiameter is used as reference dimension when comparing to a smooth pipe.
‡ Enhancement factor in terms of inner surface area A with respect to a smooth reference.

Commonly used flow-pattern maps (i.e. *Baker´s Chart*) are not applicable for two-phase helium ([59], [64], [65], [66]), as demonstrated by experimental data ([67], [68]). Filippov [66] attributes this discrepancy to the fact that certain physical properties of helium differ greatly from the properties of traditional mixtures. Publications concerning helium flow-patterns are scarce.

The experimental setup of Filippov [66] is considered fairly representative for the flow conditions of condenser HX2nd; this assumption is based on the similarity in pipe diameter and static pressure (Table 6.10). Consequently, Figure 6.13 includes an overlay of the flow-pattern boundaries as published in [66] (line a). Although the impact of the inner grooves remains unclear, the mass velocity ϑ inside the condenser HX2nd (line b) is low enough to assume a stratified flow-pattern. Therefore, each phase is treated separately assuming no entrainment between them; the subscripts g and l are used to denote the gaseous and liquid phases. This is in contrast to the *homogeneous flow model*, also known as *friction factor* or *fog flow model*, which considers the two phases flowing as a single fluid with average fluid properties ([65], [66], [40]).

Table 6.9. Comparison of flow conditions between the condenser HX2nd and the experimental setup from Filippov [66].

		HX2nd	Filippov 's
Channel properties	Hydraulic diameter D_h [mm]	8.32 *	7.90
	Cross-section [mm²]	54.37	40.02
	Geometry	Circular *	Circular
	Inclination (to horizon) [°]	0-5	0
Flow properties	Saturation pressure [kPa]	130.26 †	140.00
	Phase density ratio ρ_l/ρ_g [-]	5.39	4.85
	Mass flow [g/s]	0.0770	0.9-14.7
	Mass velocity ϑ [kg/m²/s]	1.42	20-300

* The inner-grooved pipe of condenser HX2nd is simplified as a smooth round pipe with its inner-diameter corresponding to the hydraulic diameter.
† Corresponds to helium at 4.5 K.
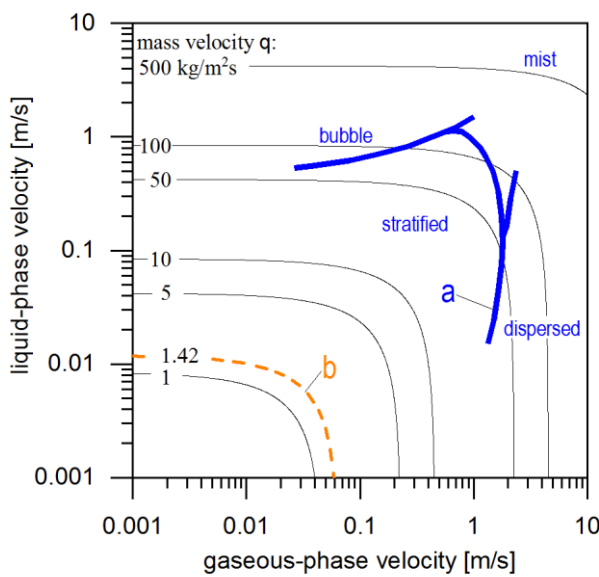
Phase velocity
liquid: $\vartheta \cdot (1-x)/\rho_l$
gas: $\vartheta \cdot x/\rho_g$

Figure 6.13. Flow pattern map of two-phase helium at a temperature of 4.5 K ($p = 130.26$ kPa, $\rho_l/\rho_g = 5.39$) for different mass velocities ϑ.
a) Overlay of flow-pattern boundaries by Filippov [66] assuming the representativeness of his experimental setup ($p = 140$ kPa, $\rho_l/\rho_g = 4.85$).
b) Curve for the mass velocity expected in condenser HX2nd.

The major constraint for the condenser design is the stringent space limitation, which leads to an unavoidable compromise between thermal performance and size. In addition, the total weight attached to the 2nd stage is required to remain well below a guidance value of 15 kg. For these reasons, and in order to decrease the thermal-size requirements ($U_m \cdot A$), a temperature difference of 0.2 K is accepted between the 2nd stage and the saturated fluid. For comparison, it is estimated that halving this temperature difference to 0.1 K would result in an increase of 2nd-stage power by 120 mW (+8 %).

Since the inner-grooved pipe is specifically designed to support the dropwise condensation of industrial refrigerants, it is assumed that this is also true for helium. Therefore, the liquid helium is considered to condense in the form of droplets, which grow in size, coalesce with neighbouring droplets and eventually roll off the surface. Moreover, the entire surface is considered to be dry and available for condensation, which is a best-case scenario that considerably simplifies the thermal design process.

These considerations lead to the same thermo-hydraulic model used for both thermalisators (Figure 6.9), but with a heat exchange area that is increased by the enhancement factor $F_A = 1.96$. The thermal design values are listed in Table 6.10, the temperature profile is shown in Figure 6.14, and the exergy exchange is illustrated in Figure 6.15. The first 9.6 % of

the heat exchanger is used to cool down the gaseous helium to its saturation temperature of 4.5 K. The remaining length is then used to isothermally condense the fluid on the walls.
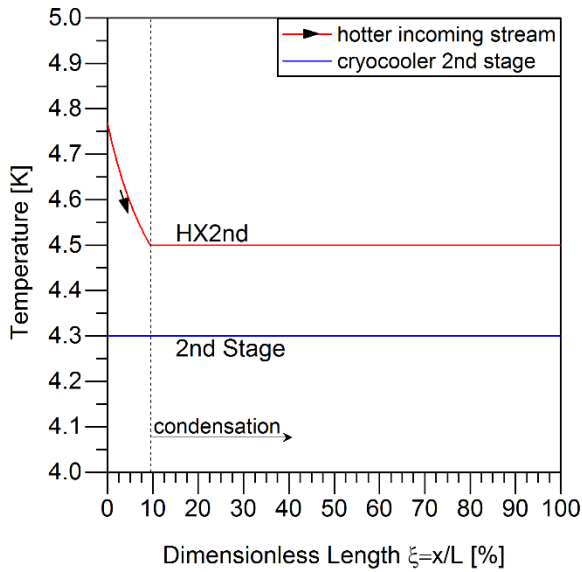
Figure 6.14. Temperature profile of the condensation heat exchanger HX2nd over the dimensionless length ξ. The idealised heat exchangers have a finite length.
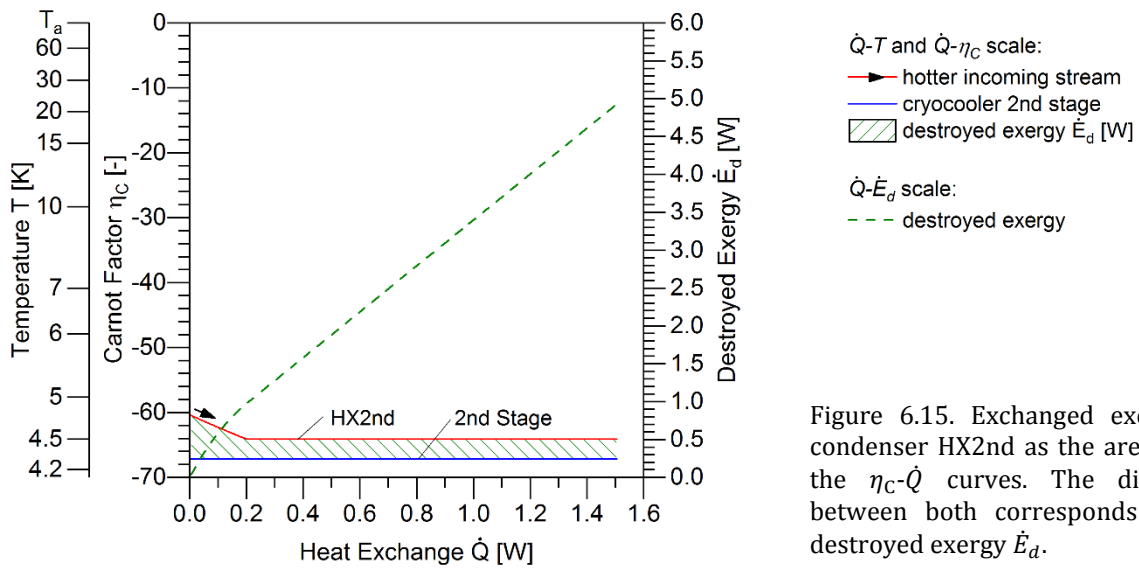
Figure 6.15. Exchanged exergy on condenser HX2nd as the area below the η_C-$\dot{Q}$ curves. The difference between both corresponds to the destroyed exergy $\dot{E}_d$.

Table 6.10. Thermal design values for condenser HX2nd.

	HX2nd
Pipe diameter [mm] *	8.32
Channel cross-section [mm²]	54.37
Temperature range [K]	4.77 - 4.50
Reynolds Re [-]	8358 – 3810
Pressure drop [mbar]	-
Heat exchange duty $\dot{Q}$ [W]	1.51
Pipe Length L [m]	2.94
Mean overall thermal conductance $U_m \cdot A$ [W/K] *	7.17
Mean temperature difference δT_m [K]	0.21
Effectiveness ε [%]	57.3
NTU [-]	13.4
Transferred exergy $\Delta \dot{E}_h$ [W]	96.0
Destroyed exergy $\dot{E}_d$ [W]	5.10
Exergetic efficiency ζ [%]	95.0

* The inner-grooved pipe is modelled as a smooth copper pipe with inner diameter 8.32mm, a wall thickness of 0.6mm and an enhanced heat exchange area by a factor of 1.96.

Table 6.11 presents the manufacturing design values for the condenser HX2nd, which is made of a single seamless pipe bent helically in a single layer. In analogy to the previous heat exchangers, the safety factor S_A results from the manufacturing length L_M being longer than the thermal design length L. The pipe is brazed directly to the thermal coupler attached to the 2nd stage, which is made of a single piece of oxygen-free high thermal conductivity copper C10300 (Figure 6.16). The whole assembly weighs approx. 8.5 kg. The coupler foresees a helical groove to fit the circular pipe, in order to enhance the thermal contact between them. The flow direction on the condenser goes from top to bottom so that forming droplets can roll off by gravity. The flow direction is opposite to the temperature gradient of the thermal coupler, resulting in an arrangement analogous to a counter-flow heat exchanger.

Table 6.11. Manufacturing design values for condenser HX2nd.

	HX2nd
Pipe material	Copper
Pipe dimensions [mm] * (inner diameter/wall thickness)	Ø8.32/0.6
Pipe Length L_M (design L †) [m]	4.48 (2.94)
Safety factor‡ S_A [-]	1.53
D [mm]	185.2
H [mm]	≈79
Windings [-]	7.5
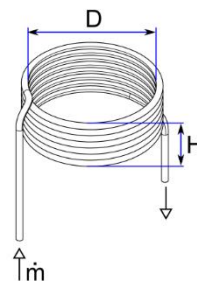
‡ With respect to total heat exchange area A ($\sim L_M / L$).
* Inner-grooved pipe from type "TECTUBE©_fin CVS" from the company KME [63].
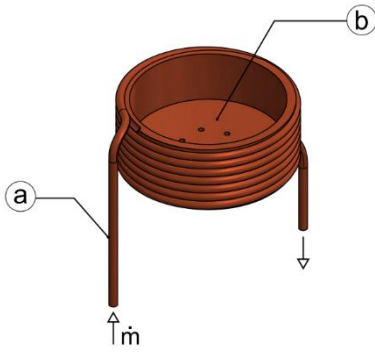
Figure 6.16. Assembly of condenser HX2nd (a) attached to the thermal coupler (b) to the 2nd stage. The total weight is approx. 8.5 kg.

6.2 System sensitivity to deviations from design values

The following evaluation determines the influence of design parameters on the refrigeration power ($\dot{Q}_R^I$, $\dot{Q}_R^{II}$), the process efficiency (η_{TP}^I, η_{TP}^{II}), and the mass flow ($\dot{m}$). The evaluation focuses on two types of design parameters: those establishing the net cooling power that is available for the thermodynamic process ($\dot{Q}_{avail}^I$, $\dot{Q}_{avail}^{II}$) and those dictating the thermal size of the heat exchangers ($U_m \cdot A$). Parameters belonging to the first group are the cryocooler stage-power ($\dot{Q}_{1st}$, $\dot{Q}_{2nd}$) and the parasitic heat losses on the CSS hardware ($\dot{Q}_{CSS}^I$, $\dot{Q}_{CSS}^{II}$). Those belonging to the second group are the exchangers pipe-length L and the cross-sectional fluid-domain area A_{cross}.

The *absolute sensitivity coefficient* $\theta_{Y,X}$ describes the influence of an input parameter X to an output parameter Y, and corresponds to the partial derivative

$$\theta_{Y,X} = \frac{\partial Y}{\partial X} \ . \tag{6.3}$$

The relative impact can be expressed in terms of the dimensionless *magnification factor* MF, which is defined as

$$\text{MF}_{Y,X} \equiv \theta_{Y,X} \cdot \frac{X_0}{Y_0}, \tag{6.4}$$

where X_0 and Y_0 correspond to the reference conditions. A positive magnification value ($\text{MF}_{Y,X} > 0$) indicates that input and output variations have the same sign (positive linear relationship), whereas a negative value ($\text{MF}_{Y,X} < 0$) indicates the opposite. An absolute value of $|\text{MF}_{Y,X}| > 1$ indicates that the input variation is magnified, and $|\text{MF}_{Y,X}| < 1$ indicates that it diminishes.

The sensitivity is evaluated at the design working point of the CSS (X_0) for a domain of $\pm 20\ \%$ ($\Delta X / X_0$). The sensitivity coefficients $\theta_{Y,X}$ are determined numerically, and if possible, also analytically; the latter is accomplished by partial differentiation and is used to verify the numerical solution.

The numerical method varies one design parameter at a time in four steps of 5 % in either direction, while quantifying the system response. The results show a strong linear relationship between parameter pairs ($Y \sim X$), so that the sensitivity coefficient is approximated as the slope

obtained from simple linear regression ($\theta_{Y,X} \approx \Delta Y / \Delta X$). The detailed list of input/output values is available in Appendix A2.

   Table 6.12 shows the magnification factors MF for the considered parameter pairs. The results confirm the insights obtained for the basis configuration CFG0 (chapters 5.2.2 and 5.2.3.1), since it can be shown that:

- The parameters that derive from the definition of the thermodynamic cycle (i.e. η_{TP}^{II}) are cryocooler-independent, and for this reason, are also independent from the available cooling power ($\dot{Q}_{avail}^{I}$, $\dot{Q}_{avail}^{II}$).
- The parameters defined exclusively by Region II (i.e. $\dot{Q}_{R}^{II}$, $\dot{m}$) are not influenced by the available cooling power in Region I ($\dot{Q}_{avail}^{I}$).
- A variation in the available cooling power for the Region II $\dot{Q}_{avail}^{II}$ corresponds to a variation in refrigeration power to Circuit II $\dot{Q}_{R}^{II}$ (MF = 1); the mass flow $\dot{m}$ varies accordingly since it "transports" the refrigeration power in the form of latent heat (MF = 1 since $\dot{m} \sim \dot{Q}_{R}^{II}$).

   Moreover, a variation in the available cooling power $\dot{Q}_{avail}^{II}$ also leads to an opposite variation in refrigeration power to Circuit I $\dot{Q}_{R}^{I}$ (MF = −0.43). The cause of this effect is rooted in the mass-flow variation described above: an increase in mass flow $\dot{m}$ is penalised by the inefficiency of the recuperators, therefore increasing the amount of 1st-stage power spent on the supply-line thermalisation.

- An increase in the local thermal conductance of the heat exchangers $d(U \cdot A)$ leads to a lower mean temperature difference δT_m, and therefore, to an improvement in the supply-line thermalisation. This results in a higher process efficiency (η_{TP}^{I}, η_{TP}^{II}), which in turn increases the refrigeration power ($\dot{Q}_{R}^{I}$, $\dot{Q}_{R}^{II}$) as well. The impact of the thermal conductance $d(U \cdot A)$ is comparatively low (MF $\approx$ 0.15) because the decline in temperature difference δT_m is asymptotic for heat exchangers with a high effectiveness ε.

   In conclusion, the evaluation shows that reducing parasitic heat losses on the CSS hardware ($\dot{Q}_{CSS}^{I}$, $\dot{Q}_{CSS}^{II}$) has, in general, a much greater impact than improving the thermal conductance of the heat exchangers ($U_m \cdot A$). Therefore, attaining a high insulation performance is more critical than manufacturing heat exchangers with stringent geometrical tolerances.

Table 6.12. Sensitivity of process parameters to variations in available cooling power ($\dot{Q}_{avail}^{I}$, $\dot{Q}_{avail}^{II}$) and local thermal conductance $d(U \cdot A)$. The influence of input to output variations is expressed in terms of the dimensionless magnification factor MF.

Input parameters		Magnification factor MF [-]				
		Refrigeration power		Process efficiency		Mass flow
		$\dot{Q}_{R}^{I}$	$\dot{Q}_{R}^{II}$	η_{TP}^{I}	η_{TP}^{II}	$\dot{m}$
$\dot{Q}_{avail}^{I}$	$(= \dot{Q}_{1st} - \dot{Q}_{CSS},)$	1.25	-	0.25	-	-
$\dot{Q}_{avail}^{II}$	$(= \dot{Q}_{2nd} - \dot{Q}_{CSS},)$	−0.43	1.00	−0.43	-	1.00
$d(U \cdot A)$	$(\sim L/A_{cross})$	0.17	0.15	0.17	0.15	0.15

7 Assessment of the overall cryogenic system

The refrigeration process of the overall cryogenic system is assessed considering the conceptual design introduced in chapter 4.2 and the CSS manufacturing values defined in chapter 6. First, the flow scheme of the overall system is introduced and the nominal working point of the refrigeration cycle is defined. Based on this, the refrigeration power is estimated at steady conditions and compared to the cooling requirements. Selected results are presented at the end, including the allocation of the cryocooler power across the system, the quantification of exergetic losses at the various heat exchangers and the estimation of the helium inventory. The complete list of calculated process and performance values is available in Appendix A3.

The schematics of the overall cryogenic system are introduced in Figure 7.1. All sub-systems at cryogenic temperatures (CSS, transfer line, connector box and cyclotron) share the same insulation vacuum, with vacuum ports and electrical feedthroughs only at the CSS and connector box. Pressure-relief valves and rupture disks protect the helium circuit against overpressure; one valve at the pump system, one disk at the CSS and one of each at the connector box. A buffer tank increases the total volume of helium, reducing pressure variations due to changing temperatures in the system. The CSS contains two normally-closed cryogenic valves in order to bypass the recuperator HX2 during the cooldown phase of the system. Electrical heaters at the cryocooler stages are foreseen for warming up the system and for the simulation of heat loads [69].

The refrigeration cycle is fully described by the system of linear equations and the set of parameter values listed in Table 7.1 and Table 7.2. The parameter set defines the nominal working point of the overall system and differs from the previous version of parameter values used in chapter 6 for the CSS design. Consequently, the CSS will be operating off-design when the overall cryogenic system is at nominal conditions.

Most notably, the parameter set in Table 7.2 considers the cooling power of the employed cryocooler device as determined by preliminary hardware tests performed beyond the scope of this work. As stated in chapter 4.2.1, the thermal budget of the entire system was re-assessed to take advantage of the employed cryocooler, the power of which showed to be significantly higher than anticipated by the supplier's specifications [55][56]: $\dot{Q}_{1st} \approx 32$ W at 39.9 K for the 1st stage (+22 %), and $\dot{Q}_{2nd} \approx 1.90$ W at 4.37 K for the 2nd stage (+29 %). Since the uncertainty estimate of this data is not available, this work assumes a 95 % confidence interval of ±10 % for the power of each stage.
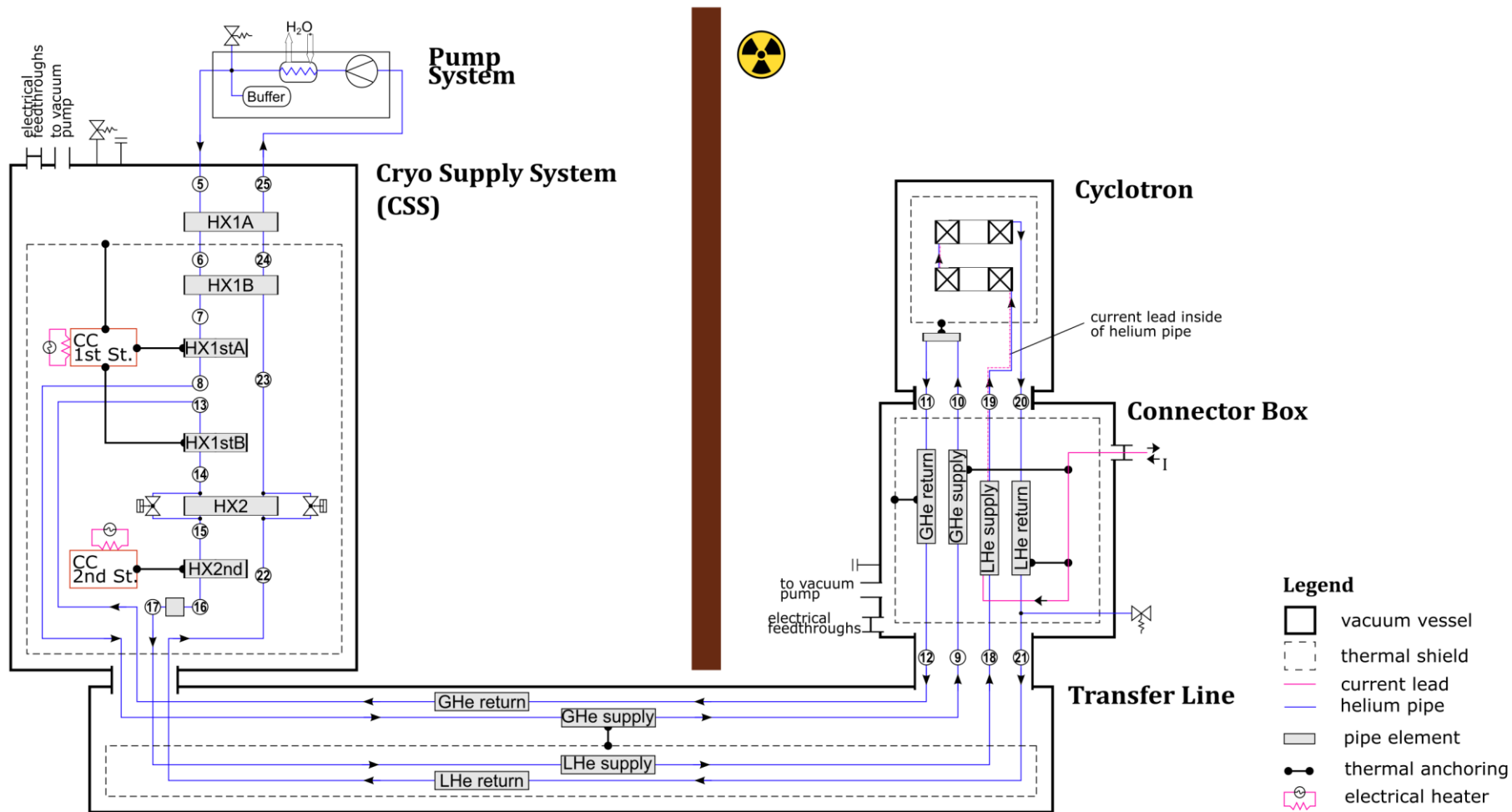
Figure 7.1. Simplified flow schematics of the overall cryogenic system showing relevant components and process values at nominal working conditions.

Table 7.1. System of linear equations for the estimation of the nominal working conditions of the overall cryogenic system.

	Description	Equation	Eq.
CSS	Initial incoming flow temperature	$T_5 = T_a$	(7.1.1)
	Δh on HX1A	$h_{25} = h_{24} - (h_6 - h_5)$	(7.1.2)
	Δh on HX1B	$h_{24} = h_{23} - (h_7 - h_6)$	(7.1.3)
	Δh on HX2	$h_{15} = h_{14} - (h_{23} - h_{22})$	(7.1.4)
	δT on cold end of HX1stB	$T_{14} = T_{1st} + \delta T_{HX1stB}$	(7.1.5)
	δT on cold end of HX2	$T_{23} = T_{14} - \delta T_{HX2}$	(7.1.6)
	1st stage temperature	$T_{1st} = T_8 - \delta T_{HX1stA}$	(7.1.7)
	2nd stage temperature	$T_{2nd} = T_{16} - \delta T_{HX2nd}$	(7.1.8)
	Power extracted by HX1stA	$\dot{Q}_{HX1stA} = \dot{m} \cdot (h_8 - h_7)$	(7.1.9)
	Power extracted by HX1stB	$\dot{Q}_{HX1stB} = \dot{m} \cdot (h_{13} - h_{14})$	(7.1.10)
	Power extracted by 1st stage	$\dot{Q}^I_{avail} = \dot{Q}_{HX1stA} + \dot{Q}_{HX1stB}$	(7.1.11)
	Mass flow	$\dot{m} = \dot{Q}^{II}_{avail}/(h_{16} - h_{15})$	(7.1.12)
	Available 1st stage power	$\dot{Q}^I_{avail} = \dot{Q}_{1st} - \dot{Q}^I_{CSS}$	(7.1.13)
	Available 2nd stage power	$\dot{Q}^{II}_{avail} = \dot{Q}_{2nd} - \dot{Q}^{II}_{CSS}$	(7.1.14)
Circuit I	Δh on supply line of TFL	$h_9 = h_8 + \dot{Q}^I_{TFL,supply}/\dot{m}$	(7.1.15)
	Δh on supply line of Connector Box	$h_{10} = h_9 + \dot{Q}^I_{CB,supply}/\dot{m}$	(7.1.16)
	Δh on return line of Connector Box	$h_{11} = h_{12} - \dot{Q}^I_{CB,return}/\dot{m}$	(7.1.17)
	Δh on return line of TFL	$h_{12} = h_{13} - \dot{Q}^I_{TFL,return}/\dot{m}$	(7.1.18)
Circuit II	Δh on supply line of TFL	$h_{18} = h_{17} + \dot{Q}^{II}_{TFL,supply}/\dot{m}$	(7.1.19)
	Δh on supply line of Connector Box	$h_{19} = h_{18} + \dot{Q}^{II}_{CB,supply}/\dot{m}$	(7.1.20)
	Δh on return line of Connector Box	$h_{20} = h_{21} - \dot{Q}^{II}_{CB,return}/\dot{m}$	(7.1.21)
	Δh on return line of TFL	$h_{21} = h_{22} - \dot{Q}^{II}_{TFL,return}/\dot{m}$	(7.1.22)

Table 7.2. Summary of process parameters used for the calculation of the overall cryogenic system at nominal working condition. The list differs from Table 6.2 as used to define the design working point of the CSS.

Type	Parameter		Value	Description
Thermal budget requirement:	$\dot{Q}_R^I$	[W]	≥ 21.84	Required refrigeration power on Circuit I and II, as specified for the nominal working point of the overall system.
	$\dot{Q}_R^{II}$	[W]	≥ 0.878	
Boundary condition:	T_a	[K]	293.15	Ambient temperature.
	T_R^{II}	[K]	4.5	Refrigeration temperature of Circuit II (at the returning stream; point 22).
	T_8	[K]	40	Temperature of incoming flow to Circuit I.
	T_{10}	[K]	≤70	Flow temperature after HTS current-lead thermalisation.
	x_{20}	[-]	<0.9	Flow vapour-quality after SC coils.
	x_{21}	[-]	<1	Flow vapour-quality after LTS current-lead thermalisation.
Model simplification:	Δp	[bar]	$\Delta p_{5\to25} \approx 0$	Isobaric consideration for the entire circuit.
Design value:	T_5	[K]	T_a	Temperature of the incoming flow from the circulation system.
	T_6	[K]	147.86	Temperature defining the "segmentation" of recuperator HX1 into two parts: HX1A and HX1B.
	δT_{HX2}	[K]	0.43	Local temperature difference at the warm end of HX2.
	δT_{HX1stA}	[K]	0.1	Local temperature difference at the cold end of HX1stA and HX1stB.
	δT_{HX1stB}	[K]	0.1	
	δT_{HX2nd}	[K]	0.13	Local temperature difference at the cold end of HX2nd.
	x_{16}	[-]	0.10	Vapour quality of flow leaving the condenser HX2nd.
	x_{22}	[-]	1.00	Vapour quality of returning flow from Circuit II.
	$\dot{Q}_{CSS}^I$	[W]	1.55	Thermal loads on the CSS hardware.
	$\dot{Q}_{CSS}^{II}$	[W]	0.023	
	Λ	[-]	≪ 0.01	Negligible longitudinal conduction on the heat exchangers.
⋮	⋮	⋮	⋮	⋮

Type	Parameter		Value	Description
⋮	⋮	⋮	⋮	⋮
Others relevant parameters:	T_{1st}	[K]	39.9	Temperature of the cryocooler stages.
	T_{2nd}	[K]	4.37	
	$\dot{Q}_{1st}$	[W]	32	Cooling power of the cryocooler stages.
	$\dot{Q}_{2nd}$	[W]	1.90	(Preliminary values from hardware tests [55][56]; assumes confidence interval of ±10 %)
	$\dot{Q}_R^I$	[W]	24.32	Refrigeration power for Circuit I and II.
	$\dot{Q}_R^{II}$	[W]	1.66	
	η_{CSS}^I	[%]	95.2	Transmission efficiency of the CSS hardware for Circuit I and II.
	η_{CSS}^{II}	[%]	98.8	
	η_{TP}^I	[%]	79.9	Transmission efficiency of the thermodynamic process for Circuit I and II.
	η_{TP}^{II}	[%]	88.3	
	y_{LHe}	[%]	88.3	Condensate yield.
	$\dot{m}$	[g/s]	0.0979	Total mass flow.
	$\dot{Q}_{HX1stA}$	[W]	6.13	Heat power extracted by thermalisator HX1stA.
	p_{sat}	[bar]	1.3026	Saturation pressure at T_R^{II}.
	h_{evap}	[J/g]	18.82	Evaporation enthalpy at T_R^{II}.

Figure 7.2 shows the estimate of the refrigeration power $\dot{Q}_R$ provided by the CSS under nominal conditions, and compares it with the design requirements ($\dot{Q}_R^I$ / $\dot{Q}_R^{II}$ = 21.84 / 0.878 W; Table 4.2). The refrigeration power measured by Haug et al. [55] is shown again for reference. The 95 % confidence intervals (error bars) are in accordance with the uncertainty analysis in chapter 8.3.3 and are based on the same considerations employed for Figure 6.4.

At its nominal working point (dot markers), the CSS is foreseen to supply a non-isothermal refrigeration power $\dot{Q}_R^I$ of 24.32 W and an isothermal refrigeration power $\dot{Q}_R^{II}$ of 1.66 W, corresponding to a compounded transmission efficiency ($\eta_{CSS} \cdot \eta_{TP}$) of 76.0 % for Circuit I and 87.3 % for Circuit II. This corresponds to a reserve in refrigeration power (dashed columns) of 11 % and 89 % with respect to the design requirements (grey columns).

When the uncertainty in the design is considered (solid error bars), the refrigeration power can vary between −26 % and +17 % for Circuit I, and between −28 % and +7 % for Circuit II. However, this power is not always sufficient to cover the design requirements. The refrigeration power provided to Circuit I is estimated between 82 % and 129 % of the design requirements, which corresponds to a 69 % probability estimate that Circuit I will receive at least the specified refrigeration power of 21.84 W. Even though this confidence level may be considered acceptable at the design stage, it also indicates a noteworthy risk (31 %) of insufficient cooling for Circuit I. In contrast, Circuit II, which is the circuit with the highest priority, is estimated to receive a relatively large surplus in refrigeration power between 37 % and 103 %.

The refrigeration power measured at the demonstrator system (triangle markers, including error bars) exceeds the design requirements, and lies entirely within the predicted range. The agreement between the measured and calculated values is statistically significant ($\gtrsim$ 5 %); chapter 8.3.3 estimates that the probability of both confidence intervals referring to

the *same* true-value is 24 % for $\dot{Q}_R^I$ and 35 % for $\dot{Q}_R^{II}$, which is considerably higher than for the design working point in Figure 6.4.

In conclusion, the CSS at nominal conditions is still capable of providing the required refrigeration power, while also providing a reasonable power reserve to accommodate for deviations due to calculation uncertainty. The measurements of the built demonstrator system [55] are in good statistical agreement with the estimated power, which is strong evidence supporting the validity of the calculation results.
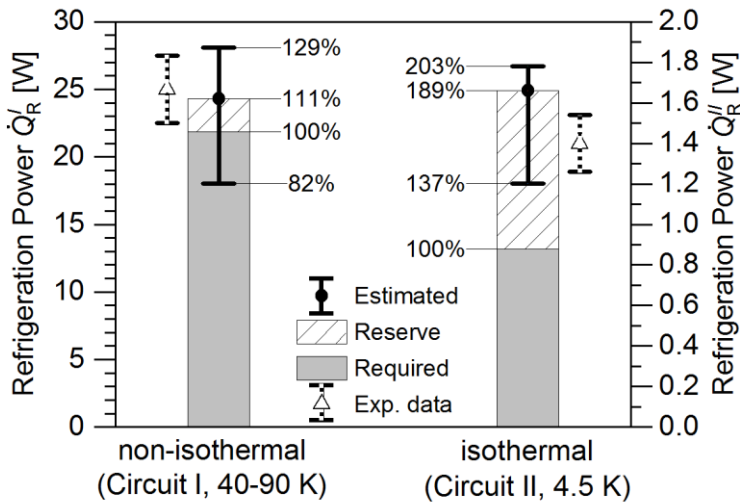
Figure 7.2. Estimated refrigeration power $\dot{Q}_R$ on Circuits I and II for the overall cryogenic system at nominal conditions (Table 7.2). It is distinguished between required and reserve power. Error bars correspond to 95 % confidence intervals, and experimental data-points to measurements reported by Haug et al. [55].

The two flow diagrams in Figure 7.3, also known as Sankey Diagrams, illustrate the allocation of cooling power that is delivered by the cryocooler stages at the nominal working point of the CSS. The values corresponding to the thermodynamic process and the cooling-power reserve are the result of the refrigerator assessment in this chapter. The remaining values correspond to input data obtained from the specification of the client system (chapter 4.2.1) and the CSS design (chapter 6.1). A breakdown of all values is provided in Appendix A3 (Tables A3.5-6).

Most of the cooling power generated by the cryocooler stages is provided to the client system: 23.49 W from the 1st-stage power (73.4 % of 32 W) and 1616 mW from the 2nd-stage power (85.1 % of 1900 mW). In both cases, the cyclotron exhibits one of the highest allocations of cooling power. It is a close second for the 1st-stage power (10.13 W, 31.7 %) and by far the dominant sub-system for the 2nd-stage power (1172 mW, 61.7 %). In contrast, the current leads have the highest cooling-power consumption from the 1st stage, but the lowest from the 2nd stage; 10.60 W (33.1 %) for the thermalisation of the first material transition (copper to HT-SC), whereas 32 mW (1.7 %) for the thermalisation of the second material transition (HT-SC to LT-SC). For the connector box, the required amount of cooling power can be considered moderate for the 1st stage (2.76 W, 8.6 %), but significant for the 2nd stage (412 mW, 21.7 %). The thermodynamic process exhibits, in both cases the third largest allocation of cooling power: 19 % for the 1st stage and 12 % for the 2nd stage. The ratio of cooling power used to compensate the static heat loads at the CSS and transfer line is among the lowest of the entire system (7.4 % for 1st stage; 3.5 % for 2nd stage).
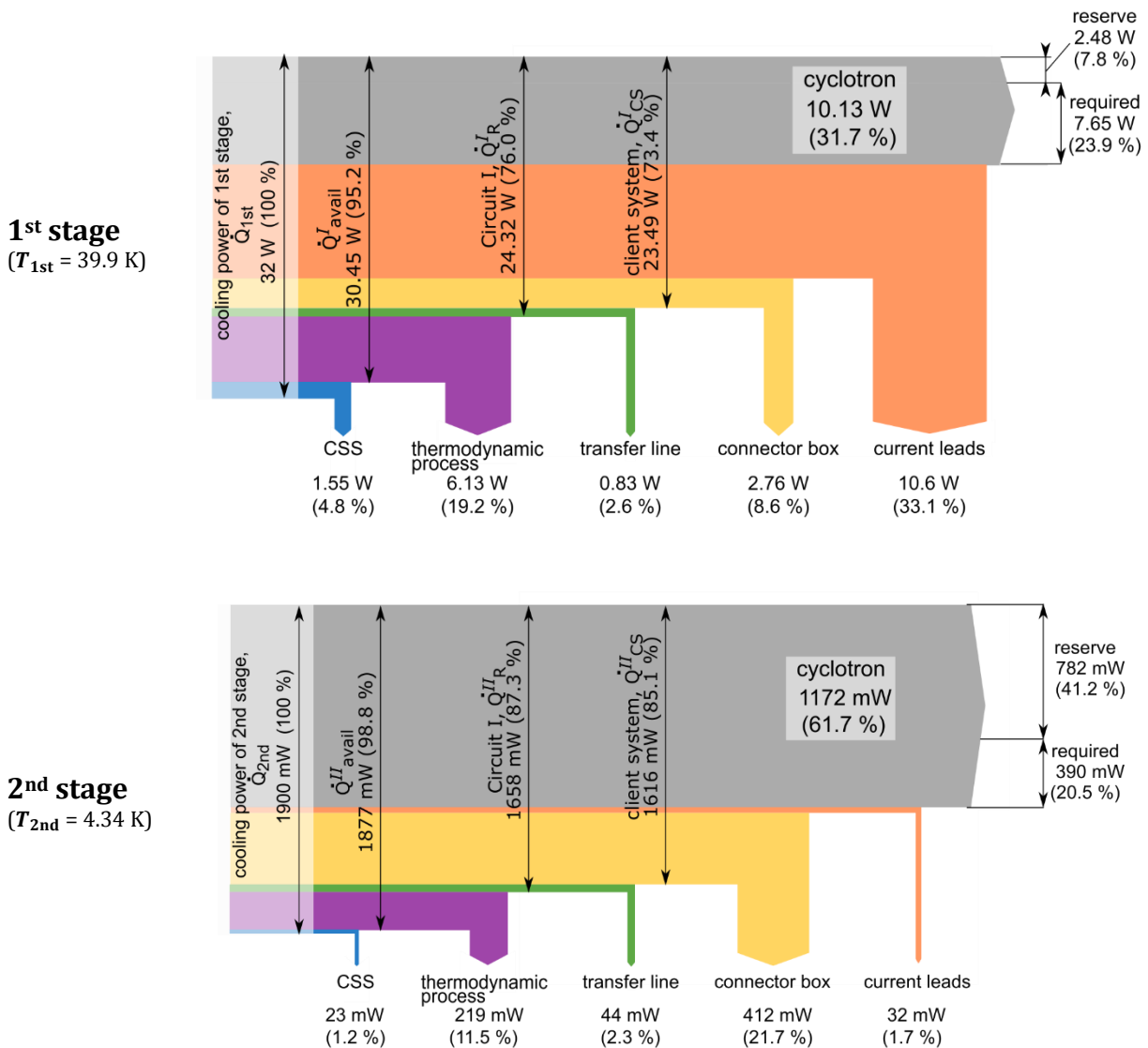
Figure 7.3. Flow diagram (Sankey Diagram) showing the allocation of cooling power that is provided by the cryocooler stages at nominal conditions.

Figure 7.4 compares the amount of exergetic power that is destroyed in the refrigeration cycle of the overall system, and it differentiates between three destruction causes: the non-zero temperature difference of the heat exchange processes, the frictional pressure loss of the flowing fluid, and the heat conduction along the pipes of the heat exchangers. The destroyed exergy is estimated to amount to a total of 324.56 W, with 98 % being attributed to the heat exchange processes alone. The relatively low contribution of pressure drop and longitudinal heat conduction confirm the fulfilment of the design requirements.
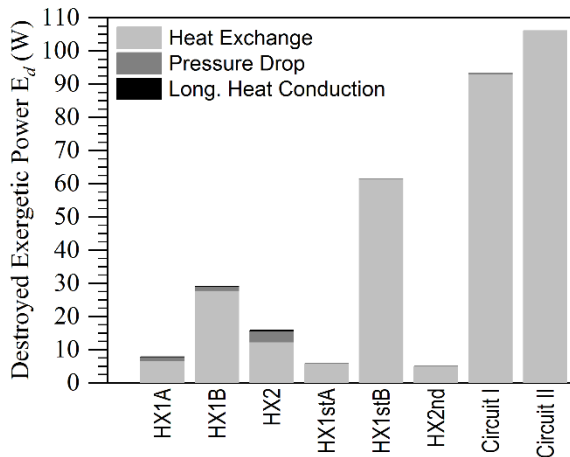
Figure 7.4. Destroyed exergetic power $\dot{E}_\mathrm{d}$ in the refrigeration cycle of the overall cryogenic system during nominal conditions. The heat exchange process is by far the dominant cause of exergy destruction, followed by the pressure drop and the longitudinal heat conduction.

The helium inventory in Table 7.3 is estimated from the pipes inner-volume and the fluid density. For each component, the average fluid density is obtained from the arithmetical mean of the density values at the inlet (i) and the outlet ($i + 1$) of each pipe segment, which is a method analogous to Eq. (6.2) for the pressure drop estimation. Excluding the buffer tank, the helium inventory is 56.95 g for a total volume of 3050 cm³; most of it is allocated at the CSS (74 %) and transfer line (18 %). The buffer tank at ambient temperature contains 21.38 g of helium and has a volume of 100 litres.

The pressure of the system at ambient temperature can be estimated by assuming isochore heating from nominal conditions, which has an average helium density of 0.76 kg/m³. This results in a pressure of 4.6 bar.

Table 7.3. Estimated helium inventory in the overall cryogenic system.

System	Sub-system	Component	Volume [cm³]	Mass of Helium [g]
Remote Refrigerator	Circulation pump	Buffer	100000	21.38
		Sub-Total	*100000*	*21.38*
	Cryo Supply System	HX1A *	282; 305	0.10; 0.10
		HX1B *	154; 154	0.16; 0.12
		HX2 *	701; 1227	8.31; 12.68
		HX1stA	137	0.19
		HX1stB	118	0.13
		HX2nd	244	12.40
		Pipes 17→18	99	8.04
		Sub-Total	*3421*	*42.23*
Transfer Line	Transfer Line	GHe supply	99	0.15
		GHe return	99	0.07
		LHe supple	99	8.04
		LHe return	99	2.20
		Sub-Total	*396*	*10.46*
Client System	Connector Box	GHe supply	6	0.01
		GHe return	6	< 0.01
		LHe supple	3	0.18
		LHe return	6	0.15
		Sub-Total	*21*	*0.34*
	Cyclotron	Thermal shield	20	0.02
		Superconducting magnets	92	3.90
		Sub-Total	*112*	*3.92*
		TOTAL	103050	78.33

* Coaxial heat exchanger with values for inner / outer pipe.

8 Evaluation of the calculation uncertainties

This chapter contains the uncertainty analysis of the results reported in chapters 5 to 7. The analysis is concerned with the identification of error sources and the quantification of their effect on the final results; an approach based on the statistical study of errors and their propagation. The objective is to estimate the unknown *true-value* of the calculation results.

Since the content of this work precedes the commissioning and testing of the refrigerator system, all uncertainties are quantified using an information pool based on data-sheets, specifications, physical relationships, experience, and expectations. This is a known practice employed at early development stages [70] and is rooted in the field of *subjective statistics* [71].

The scope of this chapter is divided in three parts. The first part defines the fundamental concepts of *error* and *uncertainty*, and provides the equations to calculate their value and propagation. The second part establishes the framework of the analysis by introducing the types of error that constitute the calculation uncertainty. The third part contains the evaluation itself; it estimates the uncertainties that are introduced throughout the calculation process and quantifies their effect on the calculation results.

8.1 Employed nomenclature and equations

The concepts of error ϵ and uncertainty u are defined based on the "*Guide to the Expression of Uncertainty in Measurement*" (GUM) [71] and extended according to the "*Standard for Verification and Validation in Computational Fluid Dynamics and Heat Transfer*" (V&V standard) [72] to apply to values resulting from simulations as well as from experiments.

An *error ϵ_X*, applicable to a variable X, is defined as the difference between the observed quantity X_{obs} (simulated or measured) and its true value X_{true}:

$$\epsilon_X \equiv X_{\mathrm{obs}} - X_{\mathrm{true}} \quad , \tag{8.1}$$

where the error ϵ_X is introduced through the combined effect of all systematic and random errors (Figure 8.1a). An error ϵ is always of unknown sign and magnitude, since known error elements are to be removed by correction.

The *standard uncertainty u* is intrinsically defined as an error estimate from the idealised perspective of the unknown true value: it characterises the estimation interval $\pm u_X$ containing the unknown error ϵ_X of an observed quantity X_{obs} (Figure 8.1b). The standard uncertainty u_X corresponds conceptually to an estimate of the standard deviation σ_X of the error's parent distribution (from which ϵ_X is a single realisation), but makes no assumption about the

distribution form. From the perspective of the observed quantity X_{obs}, the "error estimate" mutates into a more practical "true-value estimate": the interval $X_{obs} \pm u_X$ is an estimate of the unknown true-value X_{true}.

The *expanded uncertainty U* characterises the expanded interval $\pm U_X$ and assumes a distribution form (Figure 8.1c). Therefore, the probability that a particular error ϵ_i lies within the interval can be estimated; this corresponds to the *confidence level* of such an estimate. From the perspective of the observed quantity X_{obs}, the interval $X_{obs} \pm U_X$ estimates with a certain level of confidence the unknown true-value X_{true}. [72], [71], [73]

In this work, the confidence level of the expanded uncertainty interval is always set to 95 %; this will be shown in Table 8.2 for Eq. (8.26). Unless otherwise explicitly stated, the uncertainty of values are always reported in terms of 95 % confidence intervals (i.e. "10 ± 1 W", or "10 W ± 10 %" denotes X_{obs}=10 W and $\pm U_X = \pm 1$ W). The same is true for graphs depicting error bars or bands.

a)
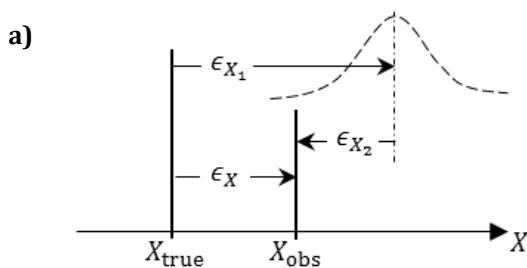
The unknown error ϵ_X results from the combination of systematic (ϵ_{X_1}) and random (ϵ_{X_2}) errors.

b)
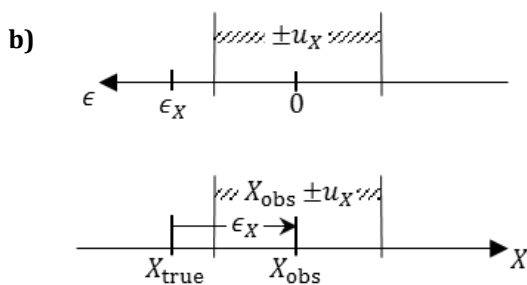
The standard uncertainty interval $\pm u_X$ is an error estimate for the actual value of the error ϵ_X; though the error's parent distribution is not necessarily determined.

Accordingly, the true-value estimate is given by the interval $X_{obs} \pm u_X$.

c)
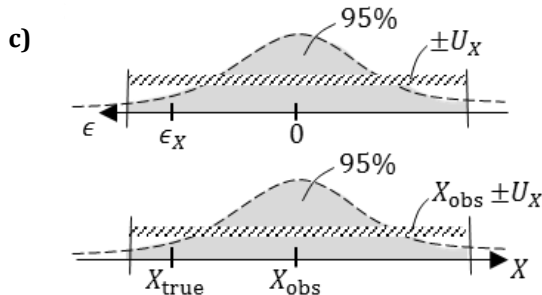
The expanded uncertainty interval $\pm U_X$ is an error estimate with a certain level of confidence for the actual value of the error ϵ_X. In the example, the confidence level is 95 % and assumes a Gaussian parent distribution for the error's population.
Accordingly, the true-value estimate with a certain level of confidence is given by the interval $X_{obs} \pm U_X$.

Figure 8.1. Concepts of error ϵ_X, standard uncertainty u_X, and expanded uncertainty U_X applied to the deviation between an observed quantity X_{obs} and its unknown true value X_{true}.

It is differentiated between *symmetric* and *asymmetric* error estimates. A symmetric estimate considers that the magnitude of an error ϵ is equally likely to be positive or negative; as was the case in Figure 8.1. In some cases, however, there is enough information to expect that the likelihood is shifted towards a particular direction; the estimate is asymmetric. As suggested by the V&V Standard, this work handles asymmetric estimates according to Coleman and Steele [73].

The introduced concepts of uncertainty intervals are generalised to apply to both, symmetric and asymmetric error estimates. The actual value of an error ϵ_i is now estimated to lie within the range

$$\hat{\epsilon} - u_i \leq \epsilon_i \leq \hat{\epsilon} + u_i \quad , \tag{8.2}$$

where u_i is the standard uncertainty as defined previously and $\hat{\epsilon}$ is the *mean* of the error's parent distribution. This re-defines the viewpoint of the error estimate from a "true-value perspective" into a "distribution-mean perspective", which will have implications when estimating the combination and propagation of errors. The true-value estimate (Figure 8.2a) is then defined as

$$\hat{X} - u_X \leq X_{true} \leq \hat{X} + u_X \quad , \tag{8.3}$$

or from the perspective of the observed quantity X_{obs}

$$X_{obs} - u_X + c_X \leq X_{true} \leq X_{obs} + u_X + c_X \quad , \tag{8.4}$$

where c_X is the *asymmetric expression* corresponding to the difference between the distribution mean $\hat{X}$ and the observed quantity X_{obs}. Similar to the standard uncertainty u_X, the asymmetric expression c_X makes no assumptions concerning the form of the parent distribution.

The expanded uncertainty interval of the true-value estimate (Figure 8.2b) is still defined as

$$X_{obs} - {}^-U_X \leq X_{true} \leq X_{obs} + {}^+U_X \quad , \tag{8.5}$$

where ${}^-U_X$ and ${}^+U_X$ are the expanded uncertainties for the lower and upper interval-bounds. The interval-limits, ${}^-X_{obs}$ and ${}^+X_{obs}$, are equidistant from the distribution mean $\hat{X}$. The *asymmetry factor* $F_X = \hat{X} - X_{obs}$ is conceptually equivalent to the asymmetric expression c_X, but assumes a distribution form.
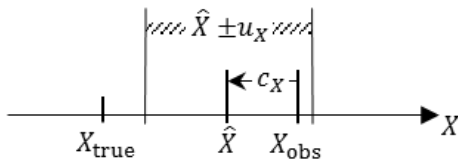
a) Standard uncertainty interval   **b) Expanded uncertainty interval**
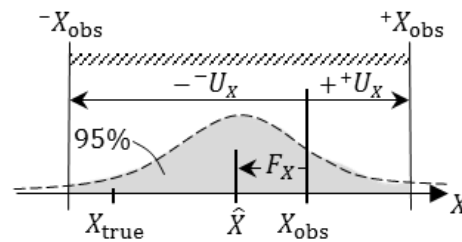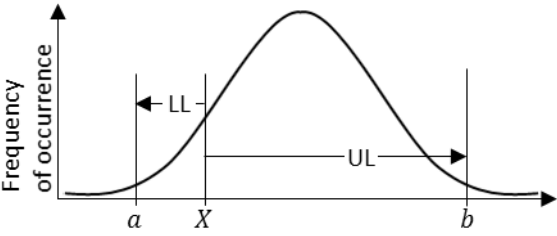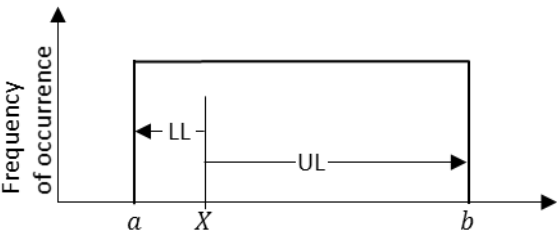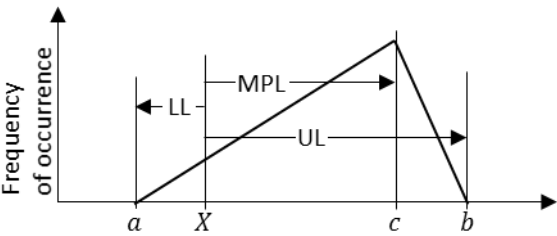
Figure 8.2. *Asymmetric* true-value estimate for an observed quantity X_{obs} and its unknown true value X_{true}.

For convenience of discussion, the GUM [71] categorises standard uncertainties u into two types, "A" and "B", to distinguish between their methods of determination: Type-A uncertainties are derived from experimental observations (frequency distributions), whereas Type-B uncertainties are assumed on the basis of an information pool (subjective probability). Apart from this distinction, both uncertainty types are evaluated in the same way. The uncertainties in this work are all from Type-B.

Table 8.1 introduces the equations to calculate the standard uncertainty u and asymmetric expression c_X from three types of parent distributions: Gaussian, rectangular, and triangular. The distributions are described in relation to a quantity X by their *lower limit* LL

$(a - X)$, their *upper limit* UL $(b - X)$, and their *most probable point* MPL $(c - X)$. Following the convention within this work, the lower and upper limits of the Gaussian distribution are set to cover an integrated probability of 95 %; more precisely, the limits correspond to the distribution mean ± 2 standard deviations.

Table 8.1. Standard uncertainty u_X and asymmetric expression c_X for Gaussian, rectangular, and triangular distributions relative to a quantity X. (cf. [73])

Distribution form (asymmetric)	Equation	Eq.
Gaussian		
	$u_X = \dfrac{(\text{UL} - \text{LL})}{4}$	(8.6)
	$c_X = \dfrac{\text{UL} + \text{LL}}{2}$	(8.7)
Rectangular		
	$u_X = \dfrac{(\text{UL} - \text{LL})}{\sqrt{12}}$	(8.8)
	$c_X = \dfrac{\text{UL} + \text{LL}}{2}$	(8.9)
Triangular		
	$u_X = \sqrt{\dfrac{\boldsymbol{A} - \text{LL} \cdot \text{UL} - \text{LL} \cdot \text{MPL} - \text{UL} \cdot \text{MPL}}{18}}$; $\boldsymbol{A} = \text{UL}^2 + \text{LL}^2 + \text{MPL}^2$	(8.10)
	$c_X = \dfrac{\text{UL} + \text{LL} + \text{MPL}}{3}$	(8.11)

Lower limit LL = $a - X$; Upper limit UL = $b - X$; Most probable point MPL = $c - X$.

The standard uncertainty u of a result is often introduced by the combined effect of multiple error sources, which is the case for values that are obtained through a data reduction equation as a function of variables containing their own set of errors. This is illustrated in Figure 8.3 for a parameter of interest $P[X, Y]$ with two independent variables (X, Y).

For example, a variable X containing n error sources exhibits n *elemental* uncertainties u_{X_i}; one for each error source. Therefore, the standard uncertainty u_X of a variable X corresponds to the combination of all elemental uncertainties u_{X_i}. The sensitivity coefficient $\theta_{P,X}$ describes the influence of variable X on the estimate of parameter P. The coefficient is used to obtain $u_{P,X}$, which corresponds to the *partial contribution* of the standard uncertainty u_X to the *compounded* standard uncertainty u_P of parameter $P[X, Y]$.

$\epsilon_{X_1}, \epsilon_{X_2}, \dots, \epsilon_{X_n}$ $\epsilon_{Y_1}, \epsilon_{Y_2}, \dots, \epsilon_{Y_m}$	Elemental error source.
$u_{X_1}, u_{X_2}, \dots, u_{X_n}$ $u_{Y_1}, u_{Y_2}, \dots, u_{Y_m}$	Elemental standard uncertainty of a variable.
u_X u_Y	Standard uncertainty of a variable (X, Y).
$(\theta_{P,X})$ $(\theta_{P,Y})$	(Absolute sensitivity coefficient)
$u_{P,X}$ $u_{P,Y}$	Partial contribution of the standard uncertainty of a variable to the standard uncertainty of a parameter $P = \boldsymbol{f}(X, Y)$.
u_P	Compounded standard uncertainty of a parameter $P = \boldsymbol{f}(X, Y)$.

Figure 8.3. Propagation of multiple elemental errors introducing a compounded standard uncertainty u_P.

Table 8.2 summarises the equations employed for the uncertainty analysis throughout this work in accordance with [71] and [73]. The equations are arranged thematically into seven groups (I-VII), with their main features described as follows:

I)   The results obtained from a simulation or experiment correspond to a specified set of conditions known as the *evaluation set-point*. For a variable X, the evaluation set-point is defined at X_0 and corresponds to the value at which the results are obtained. Eq. (8.2) centred error estimates at the distribution-mean, and therefore, error propagation is to be calculated at the *evaluation mean* $\hat{X}_0 = X_0 + c_X$. Similarly, a parameter of interest $P[X, Y]$ has an evaluation set-point $P_0 = P[X_0, Y_0]$ and an evaluation mean $\hat{P}_0 = P[\hat{X}_0, \hat{Y}_0]$.

II)   The standard uncertainty u_X of a variable X results from the root sum square of all elemental uncertainties u_{X_i}.

III)   This work employs the method of Taylor series expansion (TSE) to propagate the uncertainty of input variables u_j into the compounded standard uncertainty u_P of an output parameter P. The method is based on the first-order Taylor series approximation of a multivariable parameter $P[X, Y, \dots]$ at the evaluation mean $\hat{P}_0$. As shown in Eq. (8.22), the compounded standard uncertainty u_P combines the uncertainty associated with each variable (terms A; u_j) and the covariance between the variable-pairs (terms B; $u_{j,j+1}$). The sensitivity coefficient $\theta_{P,j}$ of a variable j corresponds to the partial derivative $\partial P / \partial j$. When all variables are independent from each other, the covariance terms in Eq. (8.22) are equal to zero and the compounded standard uncertainty u_P corresponds to the root sum square of the uncertainty contribution of each variable ($u_{P,j}$).

IV)   The partial derivative of a complex or unknown function can be obtained numerically using a finite-difference method. This work employs the Richardson extrapolation

method [75], which is based on two central-differencing finite-differences of a parameter P at the evaluation mean $\hat{P}_0$. For a variable X, the value of the finite difference ΔX is chosen at 5 % of X_0. The truncation error of this particular method behaves as ΔX^4.

V) The expanded uncertainty interval $(^-P_0, {}^+P_0)$ derives from the standard uncertainty u and the asymmetry factor F. The factor "2" in Eq. (8.26) corresponds to the *coverage factor* for a 95 % confidence interval on a Gaussian distribution, as recommended by the literature ([71], [73]). The assumption of the distribution form is based on the *central limit theorem*, which establishes that the combination of independent parent distributions of any form always tends towards a Gaussian distribution. The value of the coverage factor results from the "large-sample assumption" [73], which considers the effective number of degrees of freedom to be large enough to justify this constant coverage value (instead of computing the actual t-value in Student`s distribution).

VI) Three dimensionless expressions are particularly useful in the evaluation of uncertainties: the *percentage standard uncertainty* %u, the *uncertainty magnification factor* UMF, and the *uncertainty percentage contribution* UPC. The expressions correspond to normalised versions of the standard uncertainty u, the absolute sensitivity coefficient $\theta_{P,X}$, and the partial contribution of the uncertainty of a variable to the uncertainty of the result $u_{P,X}$. Note that the dimensionless definitions are normalised against the evaluation set-points X_0 and P_0, and not the evaluation means $\hat{X}_0$ or $\hat{P}_0$.

   This work also uses the prefix "%" to denote other dimensionless expressions that are normalised in analogy to Eq. (8.29). Some of those expressions are %$\hat{X}_0$, %U_P, %c_X, %F_P, %LL, ,%UL, ,%MPL, etc.

   The uncertainty magnification factor UMF indicates the influence of the uncertainty of a variable on the compounded uncertainty of the result; the expression is analogous to the *magnification factor* MF defined previously in Eq. (6.4). For example, an absolute value of $|\text{UMF}_{P,X}| > 1$ indicates that the uncertainty u_X is magnified as it propagates into the uncertainty u_P; a value of $|\text{UMF}_{P,X}| < 1$ indicates that it diminishes.

   The uncertainty percentage contribution UPC is used to assess the relative dominance of multiple uncertainty sources into a compounded result. For example, the value of $\text{UPC}_{P,X}$ gives the contribution of the squared standard uncertainty $u_X{}^2$ to the squared value of the compounded uncertainty $u_P{}^2$.

   It can be shown that two normalised versions of Eq. (8.22) for independent variables are

$$\%u_P{}^2 = \sum_{j=X,Y}^{n} \left(\text{UMF}_{P,j} \cdot \%u_j \right)^2 \quad , \qquad (8.12)$$

and

$$100\% = \sum_{j=X,Y}^{n} \left(\text{UPC}_{P,j} \right)^2 \quad . \qquad (8.13)$$

Table 8.2. Summary of definitions and equations for the uncertainty analysis. The equations are an example for a parameter of interest $P[X,Y]$ as a function of the variables X and Y.

	Description	Equation	Eq.
I)	Definition of the evaluation set-points and evaluation means.		
	Evaluation set-point of a variable X.	X_0	-
	Evaluation mean of a variable X.	$\hat{X}_0 = X_0 + c_X$	(8.14)
	Evaluation set-point of a parameter P.	$P_0 = P[X_0, Y_0]$	(8.15)
	Evaluation mean of a parameter P.	$\hat{P}_0 = P[\hat{X}_0, \hat{Y}_0]$	(8.16)
	Asymmetry factor of a parameter P.	$F_P = \hat{P}_0 - P_0$	(8.17)
II)	Standard uncertainty of a variable u_X		
	Standard uncertainty of variable X for i elemental error sources.	$u_X{}^2 = \sum\limits_{i=1,2,3\ldots}^{n} \left(u_{X_i}\right)^2$	(8.18)
III)	Uncertainty propagation into parameter P (TSE method).		
	Partial contribution of standard uncertainty associated to variable X.	$u_{P,X} = \theta_{P,X} \cdot u_X$	(8.19)
	Sensitivity coefficient as partial derivative.	$\theta_{P,X} = \dfrac{\partial P}{\partial X}$	(8.20)
	Covariance factor of two *correlated* variables with i elemental error sources that are *shared* by both variables; here for X and Y.	$u_{XY} = \sum\limits_{i=1,2,3\ldots}^{n} u_{X_i} \cdot u_{Y_i}$	(8.21)
	Uncertainty of parameter $P[X,Y]$ considering *all* its variables combined. Term **A** relates to the uncertainty associated with each variable, and term **B** to the *correlation effects* between variables.	$u_P{}^2 = \boldsymbol{A} + \boldsymbol{B}$; $$\boldsymbol{A} = \sum\limits_{j=X,Y}^{n} \left(\theta_{P,j} \cdot u_j\right)^2 \;\; ;$$ $$\boldsymbol{B} = 2 \sum\limits_{j=X,Y}^{n-1} \sum\limits_{k=j+1}^{n} \theta_{P,j} \cdot \theta_{P,k} \cdot u_{j,k} \; .$$	(8.22)
IV)	Approximation of partial derivatives of Parameter P (RE method).		
	Finite-difference used for variable X.	ΔX	-
	Parameter P at evaluation mean *extended* by a finite-difference.	$\hat{P}_{\pm \Delta X} = P[\hat{X}_0 \pm \Delta X, \hat{Y}_0]$	(8.23)
	Central difference of parameter P at evaluation mean.	$\widehat{D}_0[\Delta X] = \dfrac{\hat{P}_{+\Delta X} - \hat{P}_{-\Delta X}}{2\,\Delta X}$	(8.24)
	Partial derivative of parameter P at evaluation mean approximated using the RE method.	$\dfrac{\partial P}{\partial X} \approx \dfrac{4\,\widehat{D}_0[\Delta X] - \widehat{D}_0[2\,\Delta X]}{3}$	(8.25)
V)	Expanded uncertainty U.		
	Expanded uncertainty limits (lower, upper).	$^{-}P_0, \, ^{+}P_0$	(8.26)
	Expanded uncertainty interval (from, to).	$P_0 - {}^{-}U_P, \;\; P_0 + {}^{+}U_P$	(8.27)
	Expanded uncertainty (for 95 % confidence level).	$^{\pm}U_P = \pm 2\,u_p + F_P$	(8.28)
VI)	Dimensionless expressions		
	Percentage standard uncertainty (analogous definition for $\%U_X$, $\%c_X$, etc…)	$\%u_X \equiv \dfrac{u_X}{X_0} \cdot 100\%$	(8.29)
	Uncertainty magnification factor (UMF)	$\mathrm{UMF}_{P,X} \equiv \theta_{P,X} \cdot \dfrac{X_0}{P_0}$	(8.30)
	Uncertainty percentage contribution (UPC)	$\mathrm{UPC}_{P,X} \equiv \left(\theta_{P,X} \cdot \dfrac{u_X}{u_P}\right)^2 \cdot 100\%$	(8.31)

TSE = Taylor series expansion; RE = Richardson extrapolation.

Cause-effect diagrams, also known as Ikishawa diagrams, are used systematically to identify nested error sources and to illustrate the propagation of multiple errors towards a compounded result. Figure 8.4 shows a generic example of this type of diagram for a parameter of interest $P[X,Y,Z]$.

All branches in the diagram are numbered in order to create a unique identification number (ID) for each element throughout this work. The *error ID* is obtained by the concatenation of the respective branch numbers, starting always at the main branch. The first two numbers are the *root* of the error ID and are of categorical nature: the first number indicates the chapter where the specific error applies and the second number groups similar parameters together. For example, the error $\epsilon^{(0.1.2.3.4)}$ is one of the errors on the hypothetical chapter "0" (0), is attributed to a parameter of interest $P[X,Y,Z]$ (1), applies specifically to Circuit II (2), and is introduced to variable Z (3) through the element Z_4 (4). Similarly, the standard uncertainty $u^{(0.1.2.3.4)}$ and the extended uncertainty $U^{(0.1.2.3.4)}$ are related to the error $\epsilon^{(0.1.2.3.4)}$.

Dashed paths between two elements are used to indicate a common error source, since errors that are not independent from each other lead to correlated uncertainties between variables. In this particular example, the common error source for $\epsilon^{(0.1.2.2.2)}$ and $\epsilon^{(0.1.2.3.2)}$ leads to correlated uncertainties for variables Y and Z ($u^{(0.1.2.2)}$, $u^{(0.1.2.3)}$).
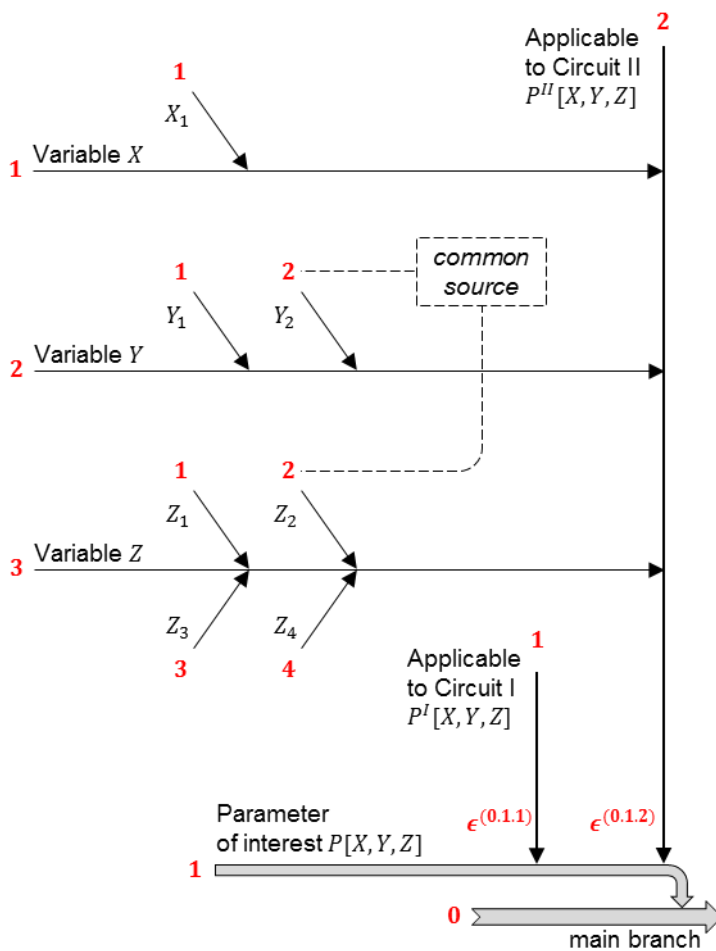
Figure 8.4. Generic example of a cause-effect diagram showing the error sources that contribute to the compounded uncertainty of a parameter of interest P. The errors are introduced through the elements (branch ends) and propagate towards the result of parameter P. The numeration of branches serves the unique identification of elements (i.e. "0.1.2.3.4" indicates element Z_4).

8.2   Sources of calculation error

According to the introduced concepts of uncertainty, there is always an intrinsic difference (error) between a calculation's "prediction" and the "truth". This deviation corresponds to the *calculation error* ϵ_{calc}, which is the difference between the calculation result P_{calc} and its unknown true-value P_{true}. It is the objective of the uncertainty evaluation in this work to estimate this *true* value from the perspective of the calculation results ($P_{calc} \pm U_{calc}$).

Figure 8.5 illustrates the type of errors considered in the evaluation. The accuracy of the calculation results derives from three aspects [74]: (1) the accuracy of the input data, (2) the physical accuracy of the calculation model, and (3) the numerical accuracy of the calculation method. Consequently, the calculation error ϵ_{calc} results from the combination of three types of errors [73]:

$$\epsilon_{calc} = \underbrace{\epsilon_{input}}_{(1)} + \underbrace{\epsilon_{model}}_{(2)} + \underbrace{\epsilon_{num}}_{(3)} \quad , \tag{8.32}$$

where

(1)   *input errors* are introduced by the error in the value of input-parameters,

(2)   *model errors* are originated by assumptions and approximations in the mathematical representation of physical processes, and

(3)   *numerical errors* are generated by solving equations through computation.
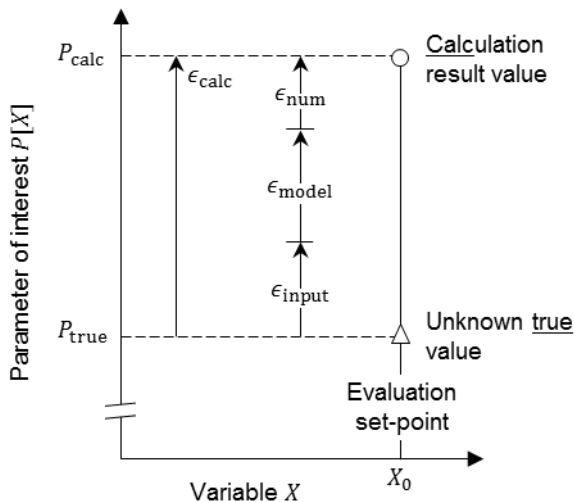
Figure 8.5. Schematic showing of the calculation error ϵ_{calc} as the difference between the unknown true-value P_{true} of a parameter $P[X]$ at the evaluation set-point X_0 and the calculation's prediction P_{calc}. The calculation error ϵ_{calc} corresponds to the combination of input, model, and numerical errors ($\epsilon_{input}, \epsilon_{model}, \epsilon_{num}$).

Input errors

The value of input parameters are either defined or gathered from multiple sources. For example, the pipe-length of a heat exchanger is established based on the design criteria, whereas the physical properties of helium are obtained from a specialised library. As a consequence, the magnitude of the input errors ϵ_{input} depends on the accuracy of the available information. This can be interpreted as the incorporation of "foreign" errors into the calculation.

Model errors

Solution validation is concerned with the physical accuracy of the calculation results and focuses on the estimation of the model error $\epsilon_{\mathrm{model}}$. Detailed experimental data is essential to estimate this error within an uncertainty range. As specified in the V&V standard [72], the model uncertainty u_{model} is best obtained indirectly from the difference between the value of calculation results and experiments. An outline of this validation procedure is provided in Appendix A7, and shows that it is critical to obtain the calculation results by using the same set of conditions at which the experiments are run.

Due to the absence of experimental data during the design phase, this work employs a rough estimate of the model uncertainty u_{model} (chapter 8.3.1). A sensitivity evaluation is then performed to assess the impact of this estimate on the compounded calculation uncertainty u_{calc} (chapter 8.3.3).

Numerical errors

Code and solution verification ensure the mathematical correctness and numerical accuracy of the calculation results [72]; as is shown below, *correctness* is evaluated, whereas *accuracy* is estimated.

Code verification is concerned with the mathematical correctness and comprises the evaluation of calculation results to identify possible errors in the source code. This work employs two approaches for code verification: the comparison of redundant results, and the convergence towards a "known" solution. In the first approach, the same quantity is computed through alternative calculation steps, which by definition, are expected to yield identical values. In the second approach, special cases with "known" analytical solutions are calculated explicitly and the obtained results are evaluated.

Solution verification is concerned with the numerical accuracy of the calculation results, focusing on the estimation of the numerical error ϵ_{num}. Whereas code verification precedes the uncertainty analysis, solution verification is part of the evaluation in chapter 8.3.1.

8.3   Uncertainty estimates

This section contains the evaluation of the uncertainty estimates. First, chapter 8.3.1 introduces the method employed to obtain the calculation-results, and clarifies the differences between chapters 5 to 7. The uncertainty sources are identified, the parameters that introduce them are established, and their magnitude is estimated. After that, the determination of confidence intervals is performed in two parts: in chapter 8.3.2 for the cryocooler stage-power ($\dot{Q}_{\mathrm{1st}}$, $\dot{Q}_{\mathrm{2nd}}$), and in chapter 8.3.3 for the refrigeration power ($\dot{Q}_{\mathrm{R}}^{I}$, $\dot{Q}_{\mathrm{R}}^{II}$). The evaluation also compares across the uncertainty sources with respect to their magnification factor (UMFs), and relative dominance (UPCs).

8.3.1 Input, model, and numerical uncertainties

The process to obtain the calculation results comprises three general steps (Figure 8.6). First, input parameters such as physical properties, design values and boundary conditions are either defined or gathered from multiple sources. Second, the parameters are implemented into the

overall calculation model comprising of a series of equations that are based on a set of assumptions and simplifications. The model equations are solved analytically, with few intermediate results being obtained through algorithms. Finally, the calculation output is used to obtain parameters of interest, such as the refrigeration power $\dot{Q}_R$.

More specifically, the results are obtained from the calculation of two models that are interconnected and solved iteratively. The process calculation (model 1) estimates the transmission efficiency η_{TP} and gives the required heat-exchange duty $\dot{Q}_{HX}$ for the process to work. The heat-exchanger calculation (model 2) estimates the heat exchange duty $\dot{Q}_{HX}$ that is provided by the employed heat exchangers under the flow conditions dictated by the process.

The exact implementation of the two models, however, varies from chapter to chapter. The thermodynamic analysis in chapter 5 is constrained to the process calculation, because it precedes the definition of the heat-exchangers design. In contrast, the CSS design in chapter 6 and the assessment of the overall cryogenic system in chapter 7 implement both models, in order to verify that the thermal design of the heat exchangers can satisfy the requirements of the refrigeration process. This is accomplished iteratively by comparing the heat-exchange duties of both models and adjusting their input parameters accordingly; the heat-exchanger design (L, D_h, A_{cross}) is adjusted in chapter 6, and the process temperatures (δT_{HX}) in chapter 7.

The "re-insertion" of errors when exchanging intermediate results between models is not explicitly considered. Instead, the effect of their "re-propagation" is understood to be covered by the respective model errors.
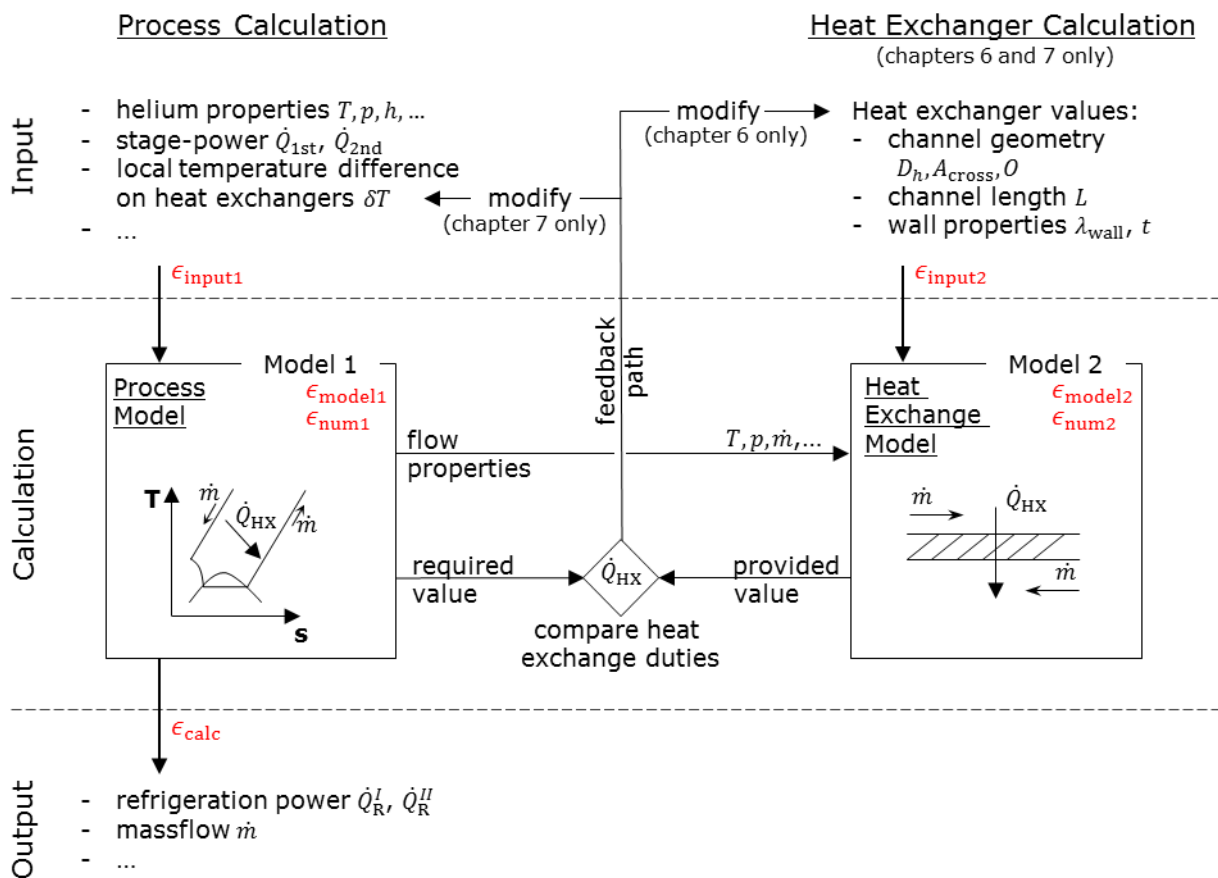
Figure 8.6. Diagram of the calculation method comprising of process and heat-exchanger calculations. The error at the calculation output (ϵ_{calc}) combines the errors introduced by the input parameters (ϵ_{input1}, ϵ_{input2}), the model definition (ϵ_{model1}, ϵ_{model2}), and the numerical calculation (ϵ_{num1}, ϵ_{num2}).

Figure 8.7 illustrates the introduction of parameter errors into the calculation of the refrigeration power $\dot{Q}_R$. The errors are introduced at various stages of the calculation process: at the estimation of the available cooling-power, at the calculation of the process and heat-exchanger models, and at the calculation output.

Input errors are introduced by parameters that establish the available cooling power for the thermodynamic process ($\dot{Q}_{avail}^I$, $\dot{Q}_{avail}^{II}$), determine the heat-power transfer of the heat exchangers ($\dot{Q}_{HX}$), or specify the physical properties of helium and solids. Input parameters belonging to the first group are the cryocooler stage-power ($\dot{Q}_{1st}$, $\dot{Q}_{2nd}$) and the transmission efficiency of the CSS hardware (η_{CSS}^I, η_{CSS}^{II}). Those belonging to the second group are the Nusselt number Nu, the exchangers pipe-length L, and the cross sectional fluid domain area A_{cross}. The third group corresponds to the many physical values that are employed throughout the calculation (T, p, h, etc.). Since it is impractical to assess each error from the last group, their combined effect is evaluated as a single error introduced directly to the refrigeration power $\dot{Q}_R$.

Model errors are assigned to specific parameters considered to "synthesise" the outcome of the respective models. These parameters are the transmission efficiency of the thermodynamic process (η_{TP}^I, η_{TP}^{II}) and the local heat-power transfer of the heat exchangers ($d\dot{Q}_{HX}$).

Numerical errors are introduced by the many computations throughout the calculation process. This includes rounding errors due to finite computational precision, and truncation errors introduced by solvers or algorithms. Similarly to the error of physical properties, the combined effect of all numerical errors is evaluated at the final result ($\dot{Q}_R$).
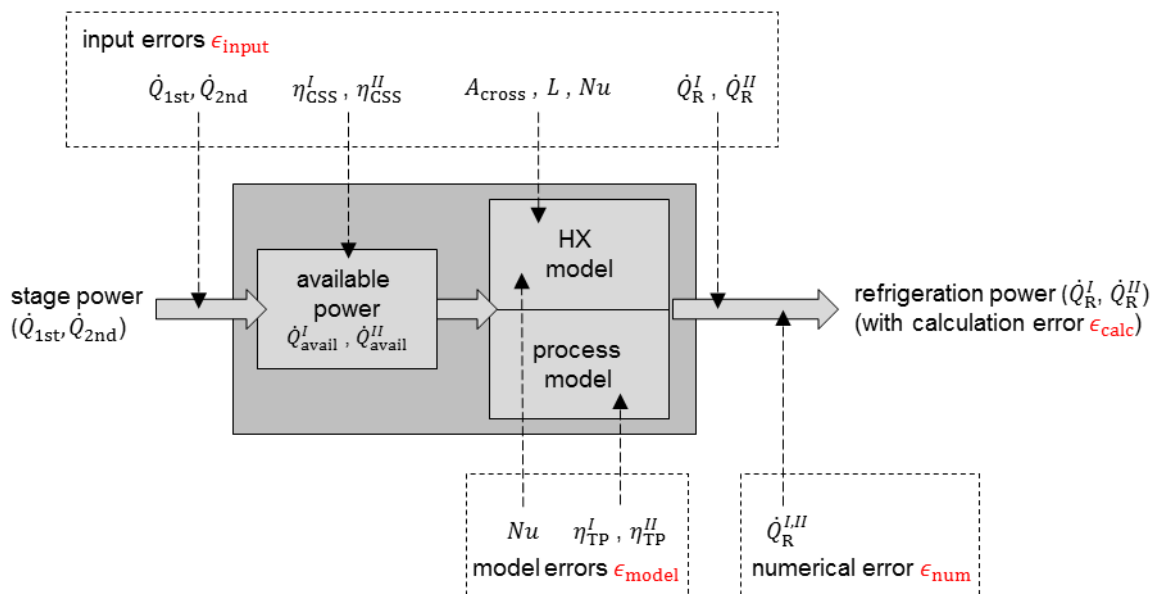
Figure 8.7. Introduction of parameter errors into the calculation process of the refrigeration power $\dot{Q}_R$. Input, model and numerical errors are introduced at different stages

Table 8.3 introduces the uncertainty estimates for the parameter errors presented above. The reasoning behind the values is described next.

$\dot{Q}_{1st/2nd}$: Due to their relevance, the uncertainty estimation for the cryocooler power is detailed in chapter 8.3.2. The determination of the stage power varies between chapters, and so does their standard uncertainty $\%u$: it is between 5 and 10 % in

chapter 5, between 5 and 6 % in chapter 6, and equal to 5 % in chapter 7. The confidence intervals in chapters 5 and 6 are asymmetric by +10 %.

η_{CSS}: It is considered reasonable to constrain the thermal budget allocated to the CSS hardware to a maximum of 10 % of the cryocooler stage-power; in chapter 7, this budget is 4.8 % for the 1st stage and 1.2 % for the 2nd stage. The consideration confines the transmission efficiency to the following interval: 90 % ≤ η_{CSS} ≤ 100 %. As a conservative approach, the lowest allowable efficiency (90 %) is chosen as the most probable scenario, with the likelihood decreasing steadily to finally reach zero at the ideal efficiency value of 100 %. This corresponds to a triangular distribution with limits at 90 % and 100 %, and with its most-probable point at the lower interval-limit (MPL = LL).

Nu: The empirical correlations employed to calculate the Nusselt number Nu have an estimated standard uncertainty of %u = 10 % (chapter 3.1, Table 3.1).

L, A_{cross}: The manufacturing tolerances of the heat exchangers are the main source of uncertainty %u for the pipe length L and the cross-sectional fluid-domain area A_{cross}. Based on the geometry requirements implemented during the manufacturing process, it is assumed a conservative uncertainty value of 5 % for the pipe length L and 10 % for the fluid-domain area A_{cross}.

$\eta_{\text{TP}}, \mathrm{d}\dot{Q}_{\text{HX}}$: The accuracy of the calculation models is estimated within a confidence interval of ±15 %. Since this is a rough estimate, its influence on the overall calculation uncertainty is assessed in a sensitivity evaluation in chapter 8.3.3.

For the process model, a pessimistic scenario is assumed in which the transmission efficiency η_{TP} is more likely to be overestimated. No assumptions are made concerning the local heat-power transfer $\mathrm{d}\dot{Q}_{\text{HX}}$. This leads to an error estimate with a negative-skewed triangular distribution (MPL = LL) for the process model, and with a symmetric rectangular distribution ($-$LL = UL) for the heat exchanger model.

$\dot{Q}_{\text{R}}$: Two uncertainty values are applied directly to the calculation results: %u = 1 % due to numerical errors, and %u = 1.5 % due to deviations in the values of physical properties. The first value is based on the precision of the computation method which considers 15 significant digits. According to De Levie [77], this level of precision is more than sufficient for a data analysis that is set to produce results with an accuracy of 1 %. The second value is based on the accuracy of the helium library (HePak©), which is driven by the uncertainty of the experimental data used to create the digital database, rather than by its internal computation method. Some physical properties are more accurately measured than others, with enthalpy differences being less accurate than density values (%u of 1.5 % vs 0.25 %), and with significant inherent inaccuracies in the vicinity of the critical point [20].

Table 8.3. Parameter uncertainties that contribute to the compounded uncertainty of the refrigeration power $\dot{Q}_R$.

Type	Chapters	Error ID [1]	Variable X	Standard uncertainty %u_X	Asymmetric expression %c_X	Assumed parent distribution [2] (Form | %LL | %UL | %MPL)
Num.	5, 6, 7	x.2.y.1	$\dot{Q}_R$	1.0 %	-	-
Input	5	x.1.1	$\dot{Q}_{1st}$ [3]	5.3-6.9 %	+10.0 %	-
	6			5.1 %	+10.0 %	-
	7			5.0 %	-	-
	5	x.1.2	$\dot{Q}_{2nd}$ [3]	5.1-9.4 %	+10.0 %	-
	6			6.0 %	+10.0 %	-
	7			5.0 %	-	-
	5, 6	x.2.y.2.1.2	η_{CSS}^{I} [4]	2.4 %	−6.7 %	(Triangular | −10 % | 0 % | −10 %)
	7			2.5 %	−1.9 %	(Triangular | −5.4 % | 5.1 % | −5.4 %)
	5, 6	x.2.y.2.2.2	η_{CSS}^{II} [4]	2.4 %	−6.7 %	(Triangular | −10 % | 0 % | −10 %)
	7			2.4 %	−5.5 %	(Triangular | −8.9 % | 1.2 % | −8.9 %)
	5, 6, 7	x.2.y.2.3	$\dot{Q}_R$	1.5 %	-	-
	6, 7	x.2.y.2.4.3	Nu	10.0 %	-	-
	6, 7	x.2.y.2.4.2.1	A_{cross}	10.0 %	-	-
	6, 7	x.2.y.2.4.1.1	L	5.0 %	-	-
Model	5, 6, 7	x.2.y.3.1.1	η_{TP}^{I}	7.1 %	−5.0 %	(Triangular | −15 % | 15 % | −15 %)
	5, 6, 7	x.2.y.3.1.2	η_{TP}^{II}			
	6, 7	x.2.y.3.2.1	$d\dot{Q}_{HX}$	8.7 %	-	(Rectangular | −15 % | 15 % | -)

1) Indicates the evaluated parameter of interest: "x" specifies the chapter, "y" specifies the circuit ("1" for Circuit I, "2" for Circuit II).
2) Parent distributions defined according to Table 8.1.
3) Values result from the combination of other elemental errors and vary between chapters. Details in chapter 8.3.2 (Table 8.5).
4) Relative values result from identical triangular distributions (defined in absolute terms): LL = 0.9, UL = 1, and MPL = LL.

8.3.2 Uncertainty of the cryocooler power

The uncertainty of the cryocooler stage-power ($\dot{Q}_{1st}$, $\dot{Q}_{2nd}$) is estimated for each chapter individually; $u^{(5.1)}$, $u^{(6.1)}$, and $u^{(7.1)}$ for chapters 5 to 7 respectively. The reason is the changing nature of the cryocooler values (Table 8.4). The thermodynamic analysis (chapter 5) employs the continuous stage-power functions in Eq. (5.11), which are obtained by fitting 7 data points collected from the supplier's data-sheet. The CSS design (chapter 6) uses the same data source, but employs discrete values of a single data point. In contrast, the assessment of the overall cryogenic system (chapter 7) employs discrete values from preliminary measurements on the actual device.

Four type of error sources are considered in the uncertainty analysis. *Data-sheet errors* correspond to the deviation between the data-sheet values and the actual values of the manufactured device. *Read-out errors* originate when data-points are collected from a source in graphical form (i.e. capacity maps). *Intrinsic fitting errors* are introduced by fitting data-points to a function and are inherent to the fitting approach itself. *Measurement errors* correspond to the deviation between hardware measurements and their true value.

Table 8.4. Attributes of the cryocooler values employed in chapters 5, 6, and 7.

	Chapter 5 (Thermodynamic analysis)	Chapter 6 (CSS Design)	Chapter 7 (Overall cryogenic system)
Employed values:	Defined in Eq. (5.11)	Listed in Table 6.2	Listed in Table 7.2
T_{1st} [K]	50	39.90	39.90
T_{2nd} [K]	2.65 – 16.43	4.30	4.37
$\dot{Q}_{1st}$ [W]	19.04 – 40.51	24.91	32
$\dot{Q}_{2nd}$ [W]	0.24 – 19.99	1.51	1.9
Expression type:	Continuous function fitted from 7 data points.	Discrete values from a single data point.	Discrete values from a single data point.
Data source:	Supplier's data-sheet for a generic device.	Supplier's data-sheet for a generic device.	Hardware measurements on the employed device.
Uncertainty ID:	root $u^{(5.1.\_)}$	root $u^{(6.1.\_)}$	root $u^{(7.1.\_)}$
for $\dot{Q}_{1st}$, $\dot{Q}_{2nd}$	$u^{(5.1.1)}$, $u^{(5.1.2)}$	$u^{(6.1.1)}$, $u^{(6.1.2)}$	$u^{(7.1.1)}$, $u^{(7.1.2)}$
Identified error sources:	Data-sheet deviation; Read-out accuracy; Intrinsic fitting error.	Data-sheet deviation; Read-out accuracy.	Measurement accuracy.

The determination of error sources and confidence intervals is performed in two parts: first for the continuous functions of chapter 5, and then for the discrete values of chapters 6 and 7. The estimated uncertainties are introduced beforehand in Table 8.5.

Table 8.5. Estimated uncertainties $u^{(x.1.y.z)}$ that contribute to the compounded uncertainty $u^{(x.1.y)}$ of the cryocooler stage-power.

	Error		Variable [Units]	Set-point	Standard uncertainty	Asymmetric expression	Assumed parent distribution [1]
	ID	Type	X	X_0	$\%u_X$	$\%c_X$	(Form | %LL | %UL)
Chapter 5	5.1.1.1	FF	$\dot{Q}_{1st}$ [W]	Eq. (5.11)	1.8-5.4 % [2]	-	-
	5.1.1.2	DS			5.0 %	+10 %	(Gaussian | 0 % | 20 %)
	5.1.1	SP			5.3-6.9 % [2]	+10 %	-
	5.1.2.1	FF	$\dot{Q}_{2nd}$ [W]	Eq. (5.11)	0.9-7.9 % [2]	-	-
	5.1.2.2	DS			5.0 %	+10 %	(Gaussian | 0 % | 20 %)
	5.1.2	SP			5.1-9.4 % [2]	+10 %	-
Chapter 6	6.1.1.1	RO	$\dot{Q}_{1st}$ [W]	24.91	1.0 %	-	-
	6.1.1.2	DS			5.0 %	+10 %	(Gaussian | 0 % | 20 %)
	6.1.1	SP			5.1 %	+10 %	-
	6.1.2.1	RO	$\dot{Q}_{2nd}$ [W]	1.51	3.3 %	-	-
	6.1.2.2	DS			5.0 %	+10 %	(Gaussian | 0 % | 20 %)
	6.1.2	SP			6.0 %	+10 %	-
Chapter 7	7.1.1.1	M	$\dot{Q}_{1st}$ [W]	32	5.0 %	-	(Gaussian | −10 % | 10 %)
	7.1.1	SP			5.0 %	-	-
	7.1.2.1	M	$\dot{Q}_{2nd}$ [W]	1.90	5.0 %	-	(Gaussian | −10 % | 10 %)
	7.1.2	SP			5.0 %	-	-

Error types: FF = fitted function; DS = data-sheet deviation; RO = read-out accuracy; SP = stage-power error; M = measurement error.
1) based on Table 8.1.
2) The standard uncertainty u is a function of the 2nd stage temperature T_{2nd}: Eq. (8.34) for ID (5.1.1.1), Eq. (8.36) for ID (5.1.1), Eq. (8.35) for ID (5.1.2.1), and Eq. (8.37) for ID (5.1.2).

Uncertainty $u^{(5.1.x)}$ (stage power in chapter 5)

Figure 8.8 shows the error sources that contribute to the stage-power uncertainty $u^{(5.1.x)}$ of the thermodynamic analysis in chapter 5. The uncertainty of both cryocooler stages ($u^{(5.1.1)}$, $u^{(5.1.2)}$) result from the propagation of intrinsic fitting errors $\epsilon^{(5.1.x.1.y.1)}$, read-out errors $\epsilon^{(5.1.x.1.y.2)}$, and data-sheet errors $\epsilon^{(1.x.2)}$. For each stage, the uncertainties of the fitting parameters $u^{(5.1.x.1.y)}$ are correlated to each other due to common sources of read-out and intrinsic fitting errors, and their combination corresponds to the uncertainty of the fitted functions $u^{(5.1.x.1)}$.
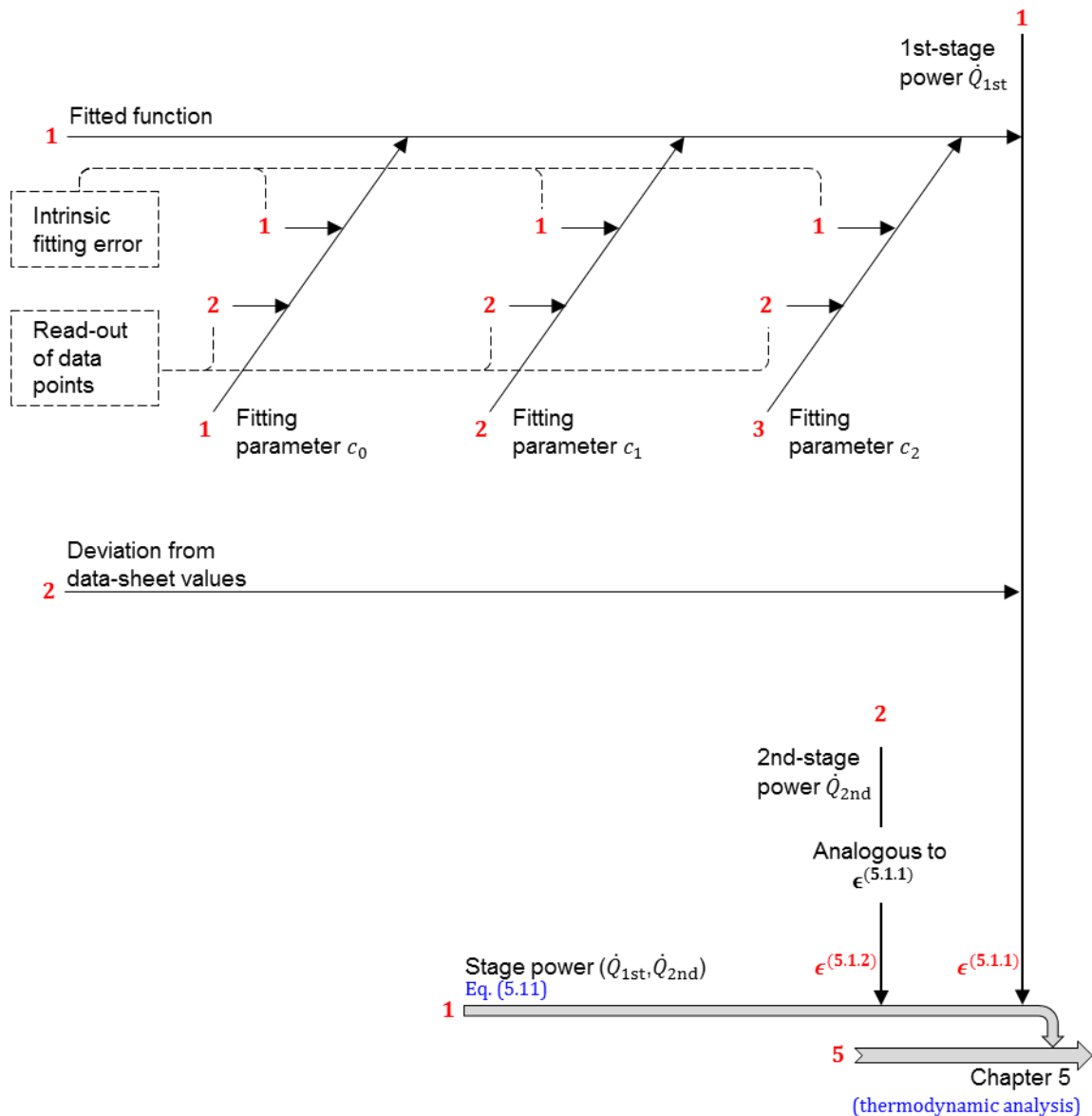
Figure 8.8. Error sources that contribute to the uncertainty of the cryocooler stage-power in chapter 5. The error $\epsilon^{(5.1.x)}$ applies to the fitted stage-power functions employed in the thermodynamic analysis.

Each stage-power function in Eq. (5.11) is obtained by fitting data points with the specialised data-analysis software "OriginPro" [76]. The read-out errors $\epsilon^{(5.1.x.1.y.2)}$ introduced to the collected data is estimated to lay within a confidence interval of ± 0.5 W for $\dot{Q}_{1st}$, and ± 0.1 W for $\dot{Q}_{2nd}$. Table 8.6 contains an extract of the fitting results, including uncertainties, covariances, and partial differentials. Further details concerning the collected data-points and the fitted functions are available in Appendix A6.

Table 8.6. Fitting results of the stage-power functions employed in chapter 5. The parameter uncertainties consider read-out and intrinsic fitting errors.

	$\dot{Q}_{1st}$ [W] as a function of T_{2nd} [K]	$\dot{Q}_{2nd}$[W] as a function of T_{2nd} [K]
Fitting function:	Quadratic equation	Hill equation
General form:	$y = c_2 \cdot x^2 + c_1 \cdot x + c_0$	$y = c_1 \cdot x^n \, (c_2{}^n + x^n)^{-1}$
Fitting parameters:	$c_0 = 53.27$; $c_1 = -5.38$; $c_2 = 0.21$	$n = 3.81$; $c_1 = 21.68$; $c_2 = 8.58$
Parameter uncertainties:	$u_{c_0} = 1.88$; $u_{c_1} = 0.49$; $u_{c_2} = 0.025$	$u_n = 0.15$; $u_{c_1} = 0.40$; $u_{c_2} = 0.12$
Covariance between parameters:	$u_{c_0 c_1} = -0.87$; $u_{c_0 c_2} = 0.042$; $u_{c_1 c_2} = -0.012$	$u_{n c_1} = -0.0435$; $u_{n c_2} = -0.0126$; $u_{c_1 c_2} = 0.043$
Partial differentials:	$\theta_{y,c_0} = 1$; $\theta_{y,c_1} = x$; $\theta_{y,c_2} = x^2$	$\theta_{y,n} = c_1 \, (c_2 \cdot x)^n \ln\left(\frac{x}{c_2}\right) (c_2{}^n + x^n)^{-2}$; $\theta_{y,c_1} = x^n \, (c_2{}^n + x^n)^{-1}$; $\theta_{y,c_2} = -n \cdot c_1 \cdot c_2{}^{n-1} \cdot x^n \, (c_2{}^n + x^n)^{-2}$

The fitting uncertainty of the stage-power functions $\epsilon^{(5.1.x.1)}$ combines the correlated uncertainties of the fitting parameters $\epsilon^{(5.1.x.1.y)}$, and is obtained with Eq. (8.22) and the expressions listed in Table 8.6. For example, the function of the 1st-stage power $\dot{Q}_{1st}$ has the form

$$\dot{Q}_{1st} = c_2 \cdot T_{2nd}{}^2 + c_1 \cdot T_{2nd} + c_0 \quad, \tag{8.33}$$

where c_0, c_1, and c_2 are the fitting parameters. Based on this, the fitting uncertainty $u^{(5.1.1.1)}$ is calculated according to Eq. (8.22):

$$\begin{aligned}
\left(u^{(5.1.1.1)}\right)^2 &= \left(\theta_{\dot{Q}_{1st},c_0} \cdot u_{c_0}\right)^2 + \left(\theta_{\dot{Q}_{1st},c_1} \cdot u_{c_1}\right)^2 + \left(\theta_{\dot{Q}_{1st},c_2} \cdot u_{c_2}\right)^2 \\
&+ 2 \cdot \theta_{\dot{Q}_{1st},c_0} \cdot \theta_{\dot{Q}_{1st},c_1} \cdot u_{c_0 c_1} + 2 \cdot \theta_{\dot{Q}_{1st},c_0} \cdot \theta_{\dot{Q}_{1st},c_2} \cdot u_{c_0 c_2} \\
&+ 2 \cdot \theta_{\dot{Q}_{1st},c_1} \cdot \theta_{\dot{Q}_{1st},c_2} \cdot u_{c_1 c_2} \quad,
\end{aligned} \tag{8.34}$$

where $\theta_{\dot{Q}_{1st},c_0} = 1$, $\theta_{\dot{Q}_{1st},c_1} = T_{2nd}$, and $\theta_{\dot{Q}_{1st},c_2} = T_{2nd}{}^2$. In a similar way, the fitting uncertainty of the 2nd-stage power $u^{(5.1.2.1)}$ is obtained with Table 8.6 and the following equation:

$$\begin{aligned}
\left(u^{(5.1.2.1)}\right)^2 &= \left(\theta_{\dot{Q}_{2nd},n} \cdot u_n\right)^2 + \left(\theta_{\dot{Q}_{2nd},c_1} \cdot u_{c_1}\right)^2 + \left(\theta_{\dot{Q}_{2nd},c_2} \cdot u_{c_2}\right)^2 \\
&+ 2 \cdot \theta_{\dot{Q}_{2nd},n} \cdot \theta_{\dot{Q}_{2nd},c_1} \cdot u_{n c_1} + 2 \cdot \theta_{\dot{Q}_{2nd},n} \cdot \theta_{\dot{Q}_{2nd},c_2} \cdot u_{n c_2} \\
&+ 2 \cdot \theta_{\dot{Q}_{2nd},c_1} \cdot \theta_{\dot{Q}_{2nd},c_2} \cdot u_{c_1 c_2} \quad.
\end{aligned} \tag{8.35}$$

For the region of interest in chapter 5 (4.3 K ≤ T_{2nd} ≤ 15.0 K), this results in a percentage uncertainty $\%u^{(5.1.x.1)}$ between 1.8 % and 5.4 % for the 1st stage, and 0.9 % and 7.9 % for the 2nd stage.

The data-sheet uncertainty $u^{(5.1.x.2)}$ is estimated under the assumption that the cryocooler manufacturer employs procedures to reduce and control the spread in performance of their final devices. It is assumed a 95 % confidence that purchased cryocoolers will at least provide the cooling power specified by their capacity maps, and will not exceed this nominal value by more than 20 %. This corresponds to an asymmetric Gaussian distribution with a percentage

confidence interval from 100 to 120 %, resulting in a standard uncertainty $\%u$ of 5 % and an asymmetry of +10 %.

The stage-power uncertainty $u^{(5.1.x)}$ combines the fitting and the data-sheet uncertainties, and is obtained from the root of the sum of squares:

$$u^{(5.1.1)} = \sqrt{(u^{(5.1.1.1)})^2 + (u^{(5.1.1.2)})^2} \quad , \tag{8.36}$$

and

$$u^{(5.1.2)} = \sqrt{(u^{(5.1.2.1)})^2 + (u^{(5.1.2.2)})^2} \quad . \tag{8.37}$$

Their percentage uncertainties $\%u$ range between 5.3 and 6.9 % for the 1st stage, and 5.1 and 9.4 % for the 2nd stage.

The UPCs of the fitting and data-sheet uncertainties to the compounded stage-power uncertainty $u^{(5.1.x)}$ are plotted in Figure 8.9 as a function of the 2nd stage temperature T_{2nd} within the region of interest (4.3 K $\leq T_{2nd} \leq$ 15.0 K). It shows that the data-sheet uncertainty $u^{(5.1.x.2)}$ is the dominant source of uncertainty over most of the range.

a) for the 1st stage   b) for the 2nd stage
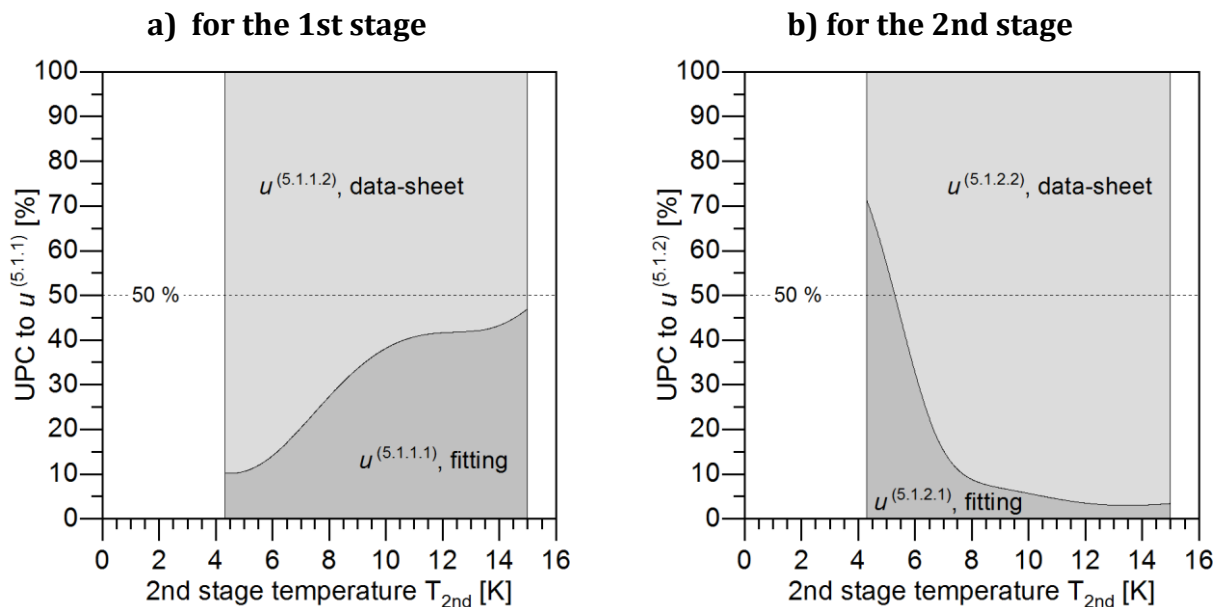
Figure 8.9. Uncertainty percentage contribution UPC of the fitting and data-sheet uncertainties to the stage-power uncertainty $u^{(5.1.x)}$ in chapter 5. The contribution of the data-sheet uncertainty is dominant across most of the temperature range.

The percentage confidence interval $\pm\%U^{(5.1.x)}$ is plotted as a function of the 2nd stage temperature T_{2nd} in Figure 8.10, with the corresponding expressions summarised in Table 8.7; the absolute confidence interval $\pm U$ was shown earlier in chapter 5.2.1 (Figure 5.5, page 60). The confidence intervals are strongly asymmetric towards higher values, ranging from 96 % to 124 % for the 1st stage, and from 91 % to 129 % for the 2nd stage; the asymmetry factor is kept constant at $\%F = +10$ %.

Table 8.7. Confidence interval applicable to the cooling power of the cryocooler stages in chapter 5.

Error ID	Parameter [Units]	Set-point	Standard uncertainty	Asymmetric Factor	95 % Confidence Interval
#	P	P_0	$\%u_P$	$\%F_P$	$\%P_0 \pm \%U_P$
5.1.1	$\dot{Q}_{1st}$ [W]	Eq. (5.11)	Eq. (8.36)*	+10 %	110 % $\pm$ 2 %u_P
5.1.2	$\dot{Q}_{2nd}$ [W]	Eq. (5.11)	Eq. (8.37)*	+10 %	110 % $\pm$ 2 %u_P

* the values are to be normalised by P_0 according to the definition in Eq. (8.29).

a) for the 1st stage   b) for the 2nd stage
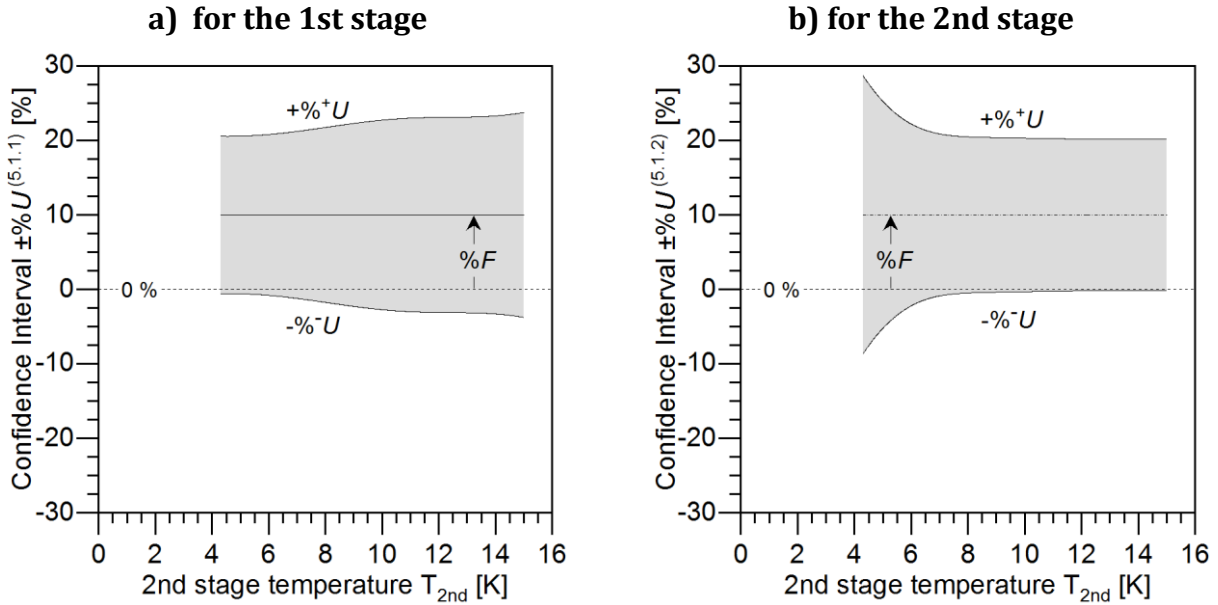
Figure 8.10. Confidence interval $\pm\%U^{(5.1,x)}$ for the stage-power in chapter 5.

Uncertainties $u^{(6.1.x)}$ and $u^{(7.1.x)}$ (stage power in chapters 6 and 7)

Figure 8.11 shows the error sources that contribute to the stage-power uncertainties of the CSS design in chapter 6 ($u^{(6.1.x)}$, left) and of the assessment of the overall cryogenic system in chapter 7 ($u^{(7.1.x)}$, right). The uncertainty $u^{(6.1.x)}$ results from the combination of read-out errors $\epsilon^{(6.1.x.1)}$ and data-sheet errors $\epsilon^{(6.1.x.2)}$, whereas the uncertainty $u^{(7.1.x)}$ is introduced by measurement errors $\epsilon^{(7.1.x.1)}$ only.

The estimates of read-out and data-sheet errors are the same as for chapter 5. A confidence interval of ±10 % is assumed for measurement data, since a detailed uncertainty analysis is not yet available.

Error sources of uncertainty $u^{(6.1.x)}$
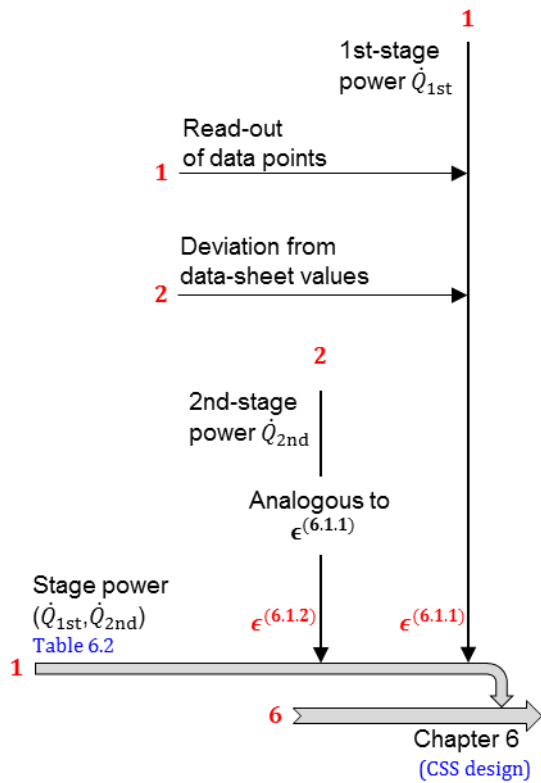
Error sources of uncertainty $u^{(7.1.x)}$
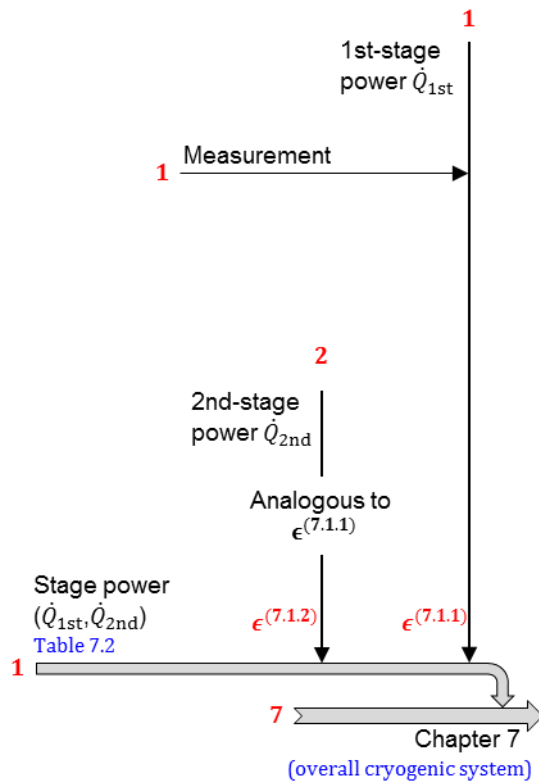
Figure 8.11. Error sources that contribute to the uncertainty of the cryocooler stage-power in chapter 6 (left) and chapter 7 (right). The error $\epsilon^{(6.1.x)}$ and $\epsilon^{(7.1.x)}$ apply to the discrete stage-power values employed in the CSS design and in the assessment of the overall cryogenic system, respectively.

The UPCs to the compounded stage-power uncertainty $u^{(6.1.x)}$ are plotted in Figure 8.12, and show the very strong dominance of the data-sheet uncertainty; as was the case for $u^{(5.1.x)}$ in Figure 8.9.
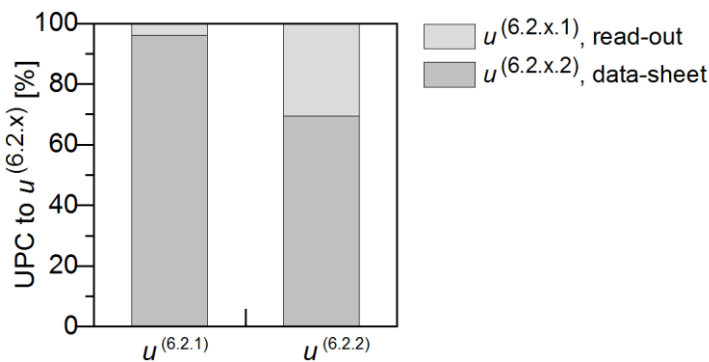
Figure 8.12. Uncertainty percentage contribution UPC of the read-out and data-sheet uncertainties to the stage-power uncertainty $u^{(6.2.x)}$ in chapter 6 ($u^{(6.2,1)}$ for 1st stage, $u^{(6.2,2)}$ for 2nd stage). The contribution of the data-sheet uncertainty $u^{(6.2,x.2)}$ strongly dominates in both stages.

The percentage confidence intervals $\pm\%U$ are listed in Table 8.8, and their absolute values are plotted in Figure 8.13 in a power-vs-power graph. This graph is also used to compare between the cryocooler stage-power in chapters 6 and 7, since in both cases the cryocooler is set to operate at virtually the same temperature ($T_{1st}^{(7)}/T_{1st}^{(6)} = 1$, $T_{2nd}^{(7)}/T_{2nd}^{(6)} = 1.02$). The

confidence intervals overlap slightly, hinting at the possibility that both intervals are estimating the *same* true-value. The probability of this actually happening is evaluated next.

Table 8.8. Confidence interval applicable to the cooling power of the cryocooler stages in chapters 6 and 7.

Error ID	Parameter [Units]	Set-point	Standard uncertainty	Asymmetric Factor	95 % Confidence Interval
#	P	P_0	$\%u_P$	$\%F_P$	$\%P_0 \pm \%U_P$
6.1.1	$\dot{Q}_{1st}$ [W]	24.91	5.1 %	+10.0 %	99.8 to 120.2 %
6.1.2	$\dot{Q}_{2nd}$ [W]	1.51	6.0 %	+10.0 %	98 to 122 %
7.1.1	$\dot{Q}_{1st}$ [W]	32.00	5.0 %	-	90 to 110 %
7.1.2	$\dot{Q}_{2nd}$ [W]	1.90	5.0 %	-	90 to 110 %
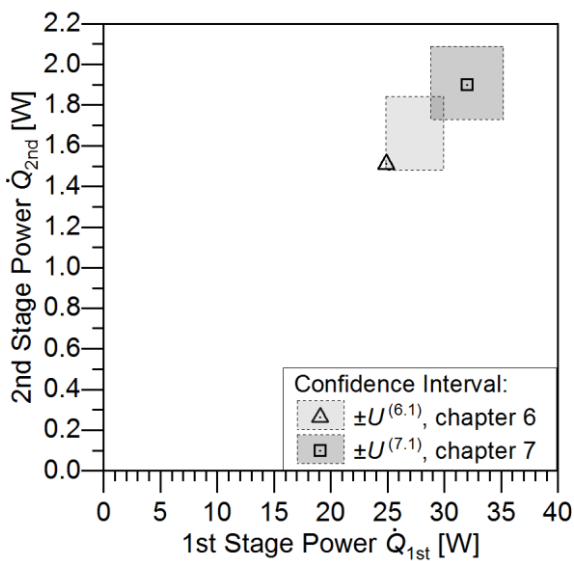
Figure 8.13. Confidence intervals $\pm\%U$ for the stage-power in chapters 6 and 7.

First, the dimensionless parameter β is introduced to express the relative difference between the evaluation set-points of two intervals:

$$\beta \equiv \frac{\text{"set-point value of interval 2"}}{\text{"set-point value of interval 1"}} - 1 \quad , \tag{8.38}$$

where an absolute difference of $|\beta| \leq 5\,\%$ is considered sufficient to assume that both intervals are indeed estimating the same true-value; the $\pm5\,\%$ deviation is assumed to be caused by random errors.

Then, the relative stage-power difference between the estimated value in chapter 6 and the experimental value in chapter 7 is obtained using Eq. (8.38):

$$\beta_j = \frac{\dot{Q}_j^{(7.1.x)}}{\dot{Q}_j^{(6.1.x)}} - 1 \quad , \tag{8.39}$$

where the subscript j denotes the correspondence to the 1st or the 2nd stage.

Finally, the confidence interval of the stage-power differences β_{1st} and β_{2nd} is obtained based on the uncertainties estimated previously and the assumption of a normal parent distribution. Figure 8.14 illustrates the confidence that the absolute stage-power difference $|\beta_j|$

is below a critical value β_j^{crit}, giving the probability that the stage-power estimates in chapters 6 and 7 agree with the true value within $\pm\beta_j^{\text{crit}}$. For $\beta_j^{\text{crit}} = 5\%$, the probability of an agreement is 7 % for the 1st stage and 12 % for the 2nd stage. The two values are considered statistically significant ($\gtrsim 5\%$) to contemplate the possibility, but still insufficient to confidently confirm the hypothesis; more data is needed to bring clarity by reducing the uncertainty involved in the estimation.
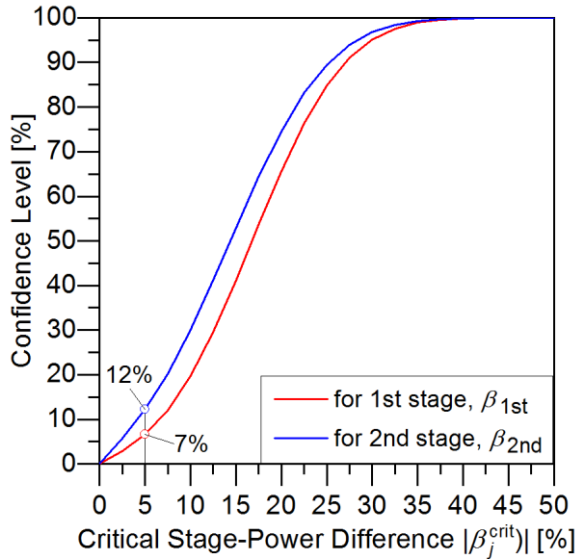
Figure 8.14. Confidence level that the stage-power estimates in chapters 6 and 7 agree in the true value within $\pm\beta_j^{\text{crit}}$. For a critical stage-power difference of $\beta_j^{\text{crit}} = 5\%$, the level of confidence is statistically significant ($\gtrsim 5\%$), but still insufficient to confidently assume an agreement.

8.3.3 Uncertainty of the refrigeration power

The uncertainty of the refrigeration power ($\dot{Q}_R^I$, $\dot{Q}_R^{II}$) is estimated for each chapter individually; $u^{(5.2)}$, $u^{(6.2)}$, and $u^{(7.2)}$ for chapters 5 to 7 respectively. As described before, the reason is the changing nature of the calculation method (Table 8.9) and the different stage-power uncertainties.

Table 8.9. Attributes of the calculation method employed in chapters 5, 6, and 7.

	Chapter 5 (Thermodynamic analysis)	Chapter 6 (CSS Design)	Chapter 7 (Overall cryogenic system)
Calculation model:	Process model.	Process model; Heat exchanger model.	Process model; Heat exchanger model.
Uncertainty ID: for $\dot{Q}_R^I$, $\dot{Q}_R^{II}$	root $u^{(5.2.\_)}$ $u^{(5.2.1)}$, $u^{(5.2.2)}$	root $u^{(6.2.\_)}$ $u^{(6.2.1)}$, $u^{(6.2.2)}$	root $u^{(7.2.\_)}$ $u^{(7.2.1)}$, $u^{(7.2.2)}$
Applied error sources:	Numerical computation; Available cooling power; Physical properties; Process model.	Numerical computation; Available cooling power; Physical properties; Heat exchange process; Process model; Heat exchanger model.	(Same as for chapter 6)
Applied stage-power uncertainty ($\dot{Q}_{1st}$, $\dot{Q}_{2nd}$):	$u^{(5.1.1)}$, $u^{(5.1.2)}$	$u^{(6.1.1)}$, $u^{(6.1.2)}$	$u^{(7.1.1)}$, $u^{(7.1.2)}$

The propagation of parameter errors towards the refrigeration power is illustrated in Figure 8.15; the corresponding uncertainty values were defined in Table 8.3. The determination of confidence intervals is first performed for chapter 5, and then for chapters 6 and 7.
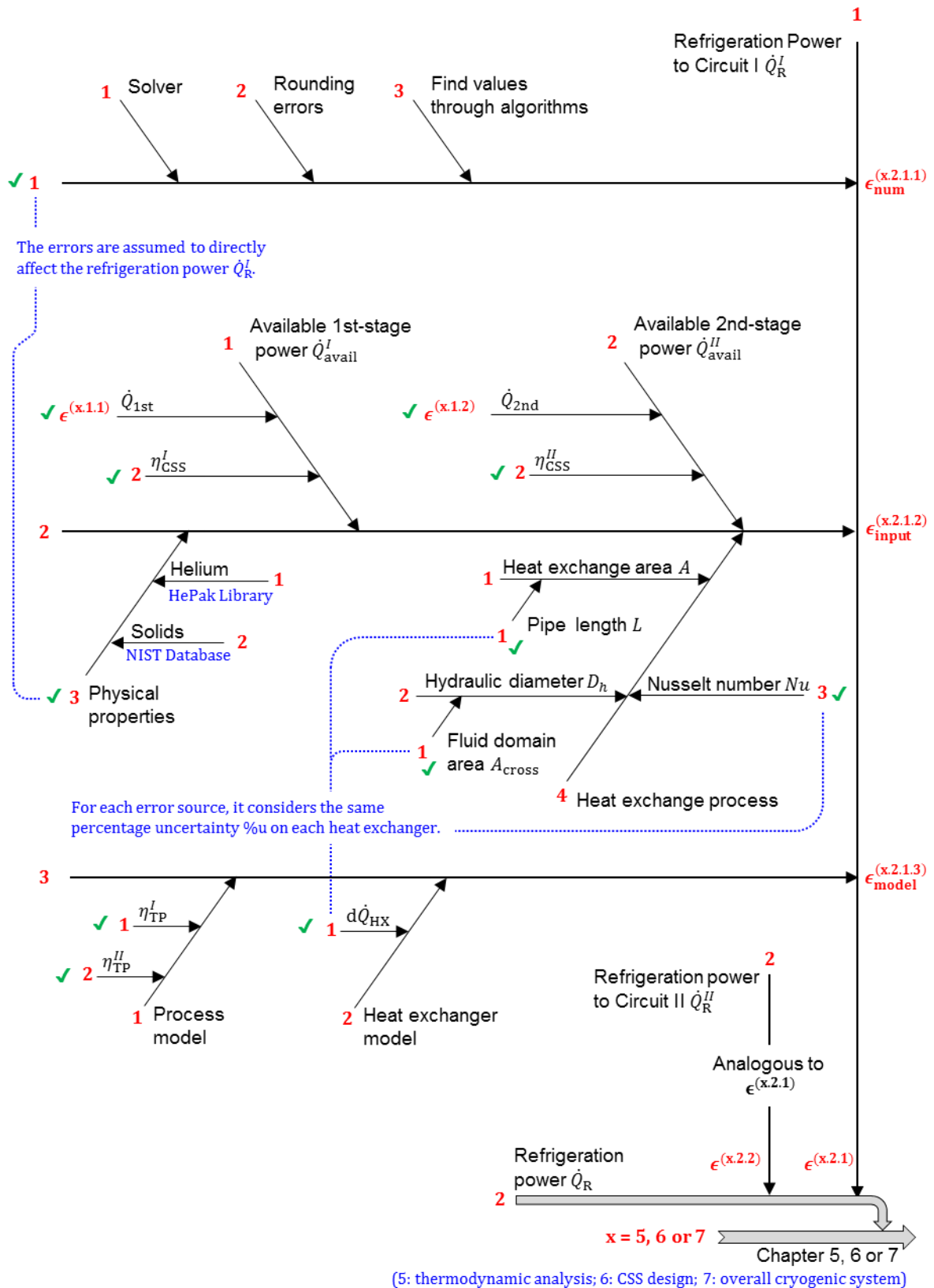
Figure 8.15. Error sources that contribute to the uncertainty of the refrigeration power. Check marks ("✓") indicate the elements defined in Table 8.3.

Uncertainty $u^{(5.2.x)}$ (refrigeration power in chapter 5)

The UPCs to the compounded refrigeration uncertainty $u^{(5.2.x)}$ are shown in Figure 8.16. The compounded uncertainty $\%u^{(5.2.x)}$ is a function of the 2nd-stage temperature T_{2nd}, due to the stage-power uncertainty $\%u^{(5.1.x)}$; all remaining uncertainties $\%u$ in chapter 5 have a constant value. The uncertainty of the process efficiency (η_{TP}^I, η_{TP}^{II}) and the stage-power ($\dot{Q}_{1st}$, $\dot{Q}_{2nd}$) are the major contributors, accounting together to over 85 %.
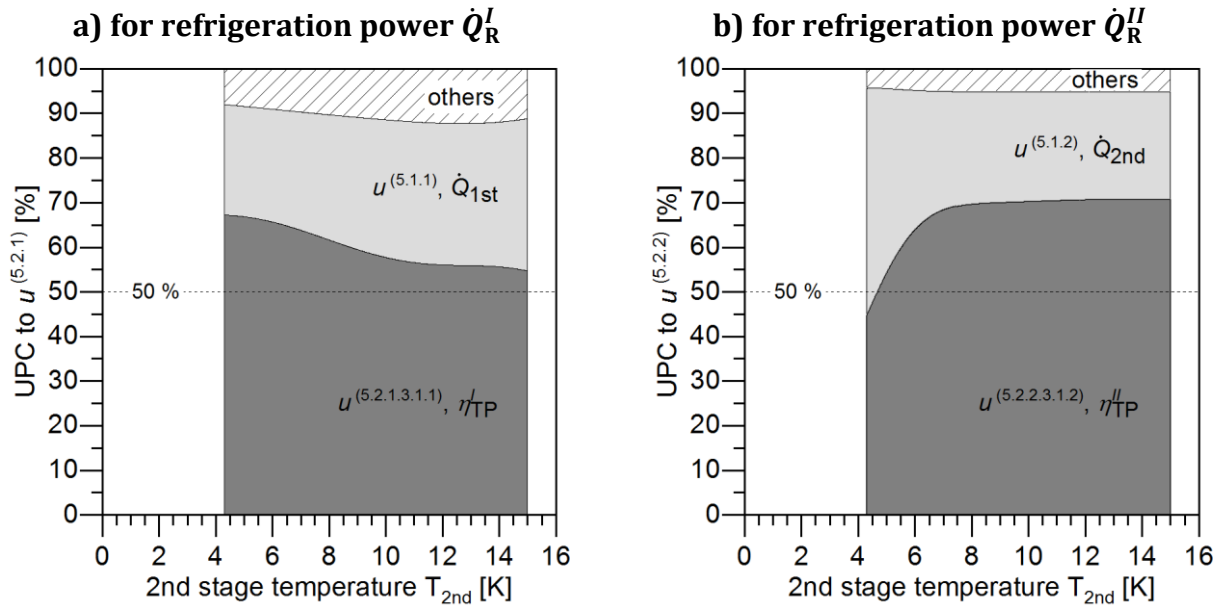
Figure 8.16. Uncertainty percentage contribution UPC to the refrigeration-power uncertainty $u^{(5.2.x)}$ in chapter 5. The main contributors correspond to the process efficiency (η_{TP}^I, η_{TP}^{II}) and the stage-power ($\dot{Q}_{1st}$, $\dot{Q}_{2nd}$).

The percentage confidence interval $\pm\%U^{(5.2.x)}$ is plotted in Figure 8.17, and ranges well within ±30 % for both Circuits. The intervals are nearly symmetric ($\%F = -2.5$ %), since the strong asymmetry of the stage-power interval ($+10$ %, Figure 8.10) counteracts the asymmetric uncertainties of hardware and process efficiencies (-6.7 % and -5.0 %, Table 8.3).
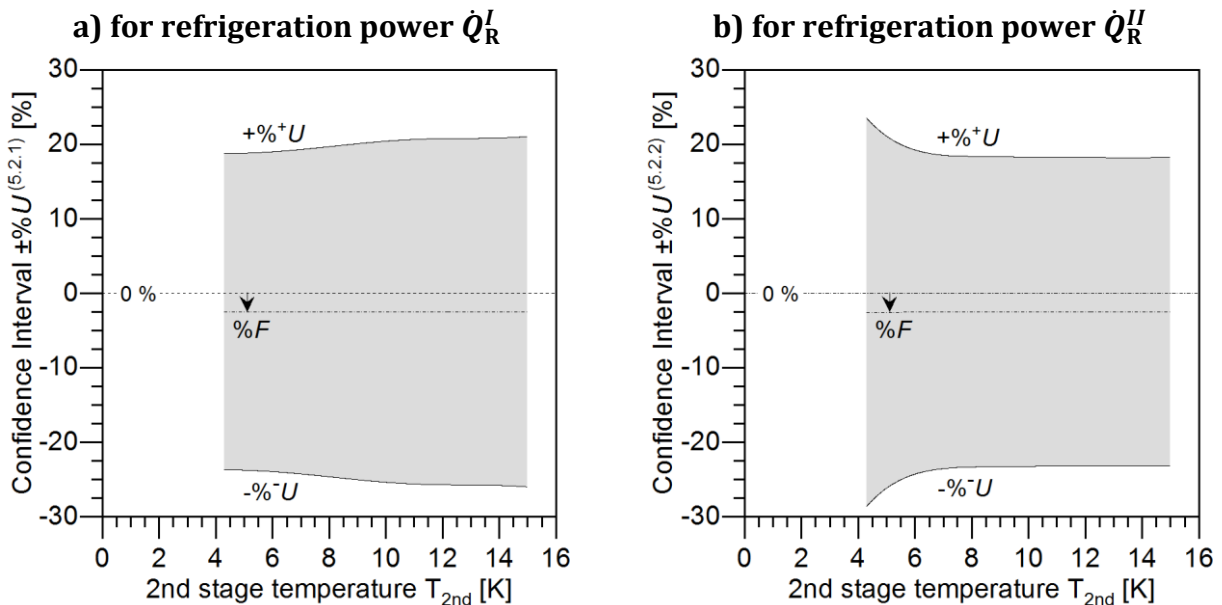
Figure 8.17. Confidence interval $\pm\%U^{(5.2,x)}$ for the refrigeration-power in chapter 5.

Uncertainties $u^{(6.2.x)}$ and $u^{(7.2.x)}$ (refrigeration power in chapters 6 and 7)

Figure 8.18 shows the uncertainty magnification factors (UMFs) of the elemental uncertainties when propagated to the compounded uncertainty of the refrigeration power. The UMF values are very similar between chapters 6 and 7, indicating that the parameter sensitivity of the CSS varies little between its design working-point (chapter 6) and nominal conditions (chapter 7).

The results are in agreement with the sensitivity evaluation performed in chapter 6.2. The uncertainty of parameters determining the power transfer of the heat exchangers are strongly diminished; $|\text{UMF}| \approx 0.15$ for $\text{d}\dot{Q}_{\text{HX}}$, Nu, L, and A_{cross}. This is also true for the uncertainty of parameters that refer to a particular Circuit (either Circuit I or II) but propagates to the uncertainty of the other Circuit. One example is the Circuit-II parameters $\dot{Q}_{\text{2nd}}$ and η_{CSS}^{II} to the Circuit-I power $\dot{Q}_{\text{R}}^{I}$ ($|\text{UMF}| \approx 0.4$). The other, more extreme, example is the parameters η_{TP}^{I}, η_{TP}^{II}, η_{CSS}^{I}, and $\dot{Q}_{\text{1st}}$; their UMFs equal zero.
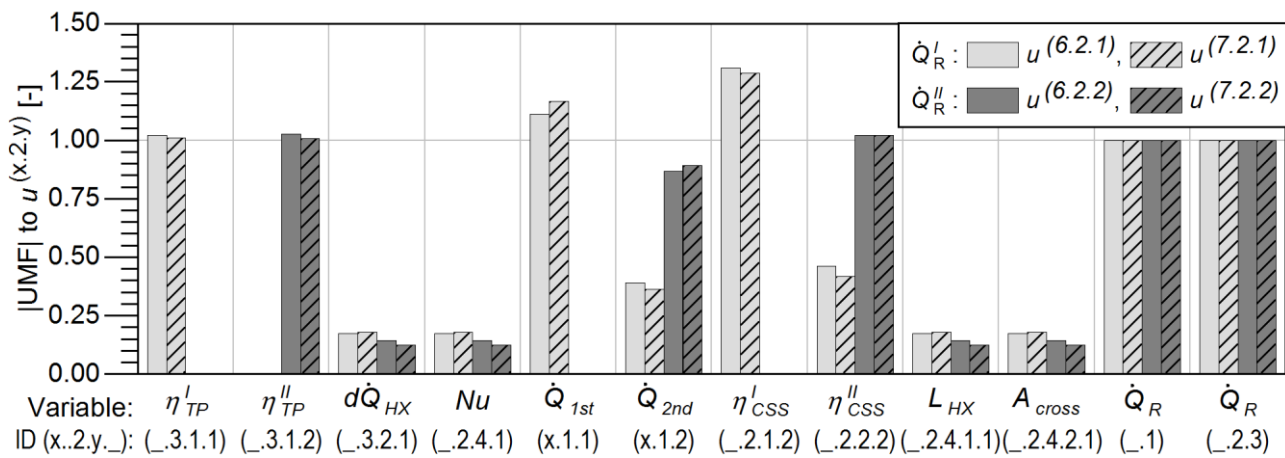
Figure 8.18. Uncertainty magnification factor UMF of parameter uncertainties to the refrigeration-power uncertainties $u^{(x.2.y)}$ in chapters 6 and 7. The uncertainty of parameters determining the heat-power transfer of the heat exchangers are strongly diminished ($\text{d}\dot{Q}_{\text{HX}}$, Nu, L, and A_{cross}).

The UPCs to the compounded refrigeration uncertainty $u^{(x.2.y)}$ are shown in Figure 8.19. The process efficiencies (η_{TP}^{I}, η_{TP}^{II}) are by far the dominant contributors. The stage power ($\dot{Q}_{\text{1st}}$, $\dot{Q}_{\text{2nd}}$) and the hardware efficiency (η_{CSS}^{I}, η_{CSS}^{II}) have a modest impact, while the remaining parameters are of little relevance.
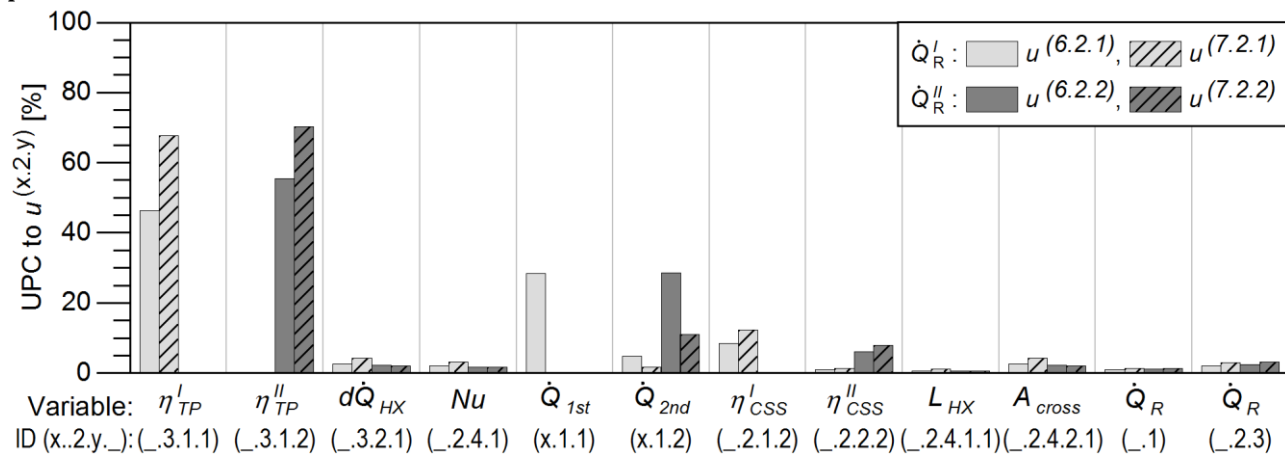
Figure 8.19. Uncertainty percentage contribution UPC to the refrigeration-power uncertainties $u^{(x.2.y)}$ in chapters 6 and 7. The process efficiency (η_{TP}^{I}, η_{TP}^{II}) is by far the dominant contributor, followed by the stage power ($\dot{Q}_{\text{1st}}$, $\dot{Q}_{\text{2nd}}$) and the hardware efficiency (η_{CSS}^{I}, η_{CSS}^{II}).

Table 8.10 lists the percentage confidence intervals $\pm\%U$ of the refrigeration power in chapters 6 and 7, as well as the refrigeration power measured by Haug et al. [55]. The absolute intervals are plotted in Figure 8.21 in two power-vs-power graphs; one for each chapter. The graphs also show the minimum power requirements specified in Table 4.2 (chapter 4.2.1).

The confidence intervals are within the range of $-28\,\%$ to $+18\,\%$, and are asymmetric towards lower values; the asymmetry factor $\%F$ is minor for chapter 6 ($-2.5\,\%$; $-2.9\,\%$), and more substantial for chapter 7 ($-5.2\,\%$; $-10.2\,\%$).

There is an agreement between the estimated refrigeration power and the experimental data, as the respective confidence intervals for $\dot{Q}_R^I$ and $\dot{Q}_R^{II}$ intersect. The probability that two overlapping intervals are referring to the *same* true-value is quantified analogous to Figure 8.13, and shows that the agreement is statistically significant ($\gtrsim 5\,\%$): for chapter 6 the probabilities are 5 % and 18 %, and for chapter 7 are 24 % and 35 %.

Only the interval for the refrigeration to Circuit I in chapter 7 extends below the power requirements; the lower interval-limit is 18.02 W, but 21.84 W is required. Assuming a Gaussian distribution for the true-value estimate, there is a 69 % confidence that $\dot{Q}_R^I \geq 21.84$ W. As stated in chapter 7 (Figure 7.2), this level of confidence is still considered acceptable. However, as it is shown next, the confidence value is strongly driven by the model accuracy, the uncertainty of which was roughly estimated due to the absence of experimental data.

Table 8.10. Confidence interval applicable to the refrigeration power in chapters 6 and 7.

Source	Error ID	Parameter [Units]	Evaluation set-point	Standard uncertainty	Asymmetric factor	95 % Confidence interval	
	#	P	P_0	$\%u_P$	$\%F_P$	$\%P_0 \pm \%U_P$	$P_0 \pm U_P$
Estimated within this work	6.2.1	$\dot{Q}_R^I$ [W]	19.91 W	10.6 %	−2.9 %	76 to 118 %	15.1 to 23.5 W
	6.2.2	$\dot{Q}_R^{II}$ [W]	1.30 W	9.7 %	−2.5 %	78 to 117 %	1.0 to 1.5 W
	7.2.1	$\dot{Q}_R^I$ [W]	24.32 W	10.4 %	−5.2 %	74 to 116 %	18.0 to 28.1 W
	7.2.2	$\dot{Q}_R^{II}$ [W]	1.66 W	8.8 %	−10.2 %	72 to 107 %	1.2 to 1.8 W
Measured by Haug et al. [55]	-	$\dot{Q}_R^I$ [W]	25.00 W	5.0 %	-	90 to 110 %	22.5 to 27.5 W
	-	$\dot{Q}_R^{II}$ [W]	1.44 W	5.0 %	-	90 to 110 %	1.3 to 1.6 W

a) At design conditions of the CSS (chapter 6)
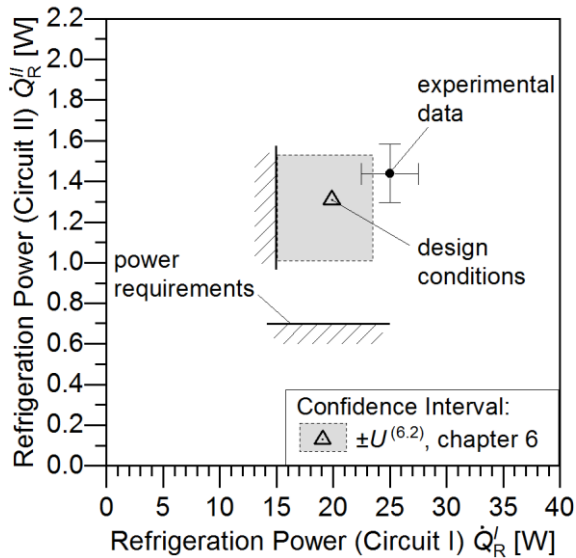
b) At nominal conditions of the overall system (chapter 7)
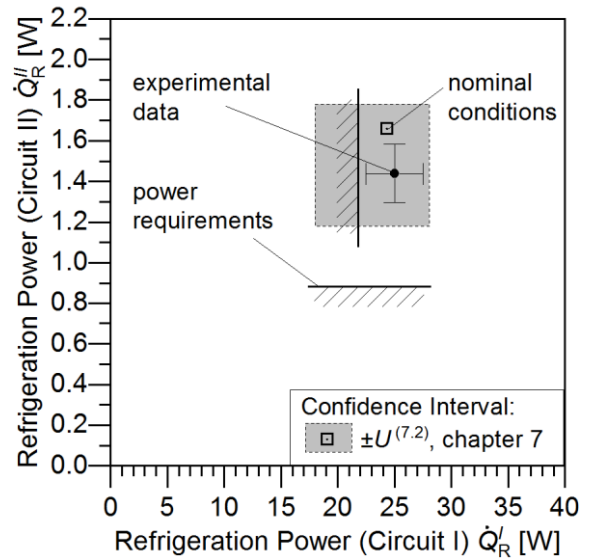
Figure 8.20. Confidence intervals $\pm\%U$ for the refrigeration power in chapters 6 and 7. The estimates are applicable to the CSS design (a) and to the assessment of the overall cryogenic system (b). The power requirements vary between chapters and the experimental data corresponds to the measurements reported by Haug et al. [55].

Figure 8.21 shows the impact of the model-error estimate on the confidence interval of the refrigeration power (error bars), and therefore, on the confidence of fulfilling the cooling-power requirements (solid line). The sensitivity to the model-error estimate is evaluated by varying the lower-limit of the model-uncertainty interval (%LL); the lower the value of %LL $\leq$ 0, the more the model could be overestimating the calculation results.

A low model accuracy (%LL $\ll$ 0) results in a wider and lower confidence interval for the refrigeration-power, and therefore, in a reduced confidence of supplying enough cooling power. The decline in confidence is significant for Circuit I, falling to 31 % for %LL $= -30$ %. In contrast, the confidence for Circuit II decreases marginally to a value of 99 %. As stated before, this work assumes a value of %LL $= -15$ %, resulting in a 69 % confidence of sufficient refrigeration for Circuit I.
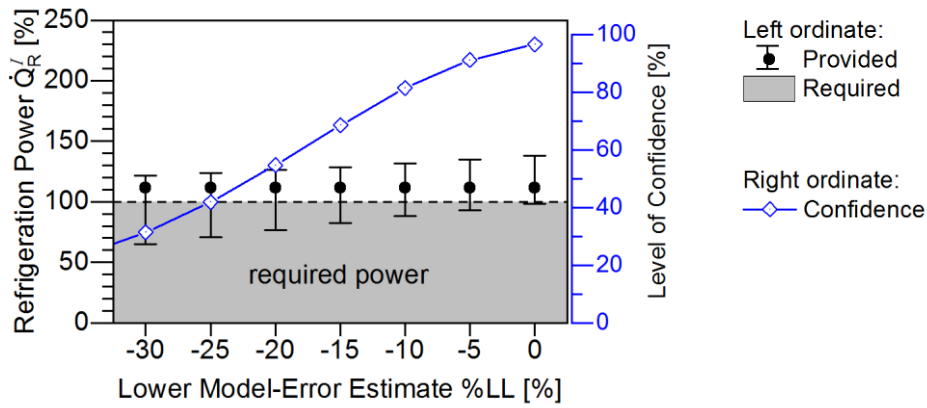
a)
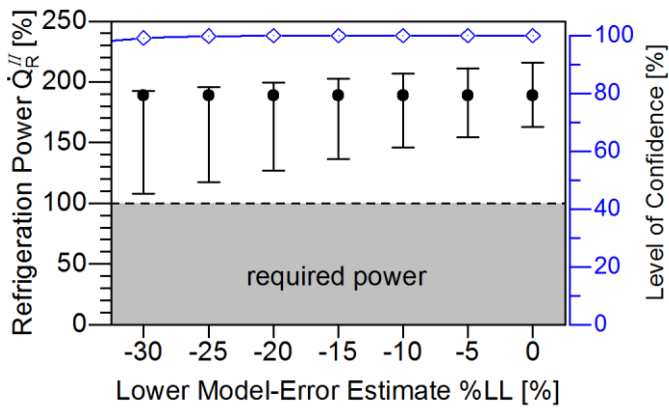
b)

Figure 8.21. Influence of the lower limit (%LL) of the model-error estimate on the refrigeration power for Circuit I (a) and Circuit II (b). A low model accuracy (%LL $\ll$ 0) widens the confidence interval of the refrigeration power (error bars) and reduces the confidence of providing the required cooling power (solid line). This work assumes a lower-limit value of %LL = −15 %.

9   Summary and outlook

This work presents a thermodynamic study for the cryogenic refrigeration of AMIT's cyclotron; a highly compact superconducting cyclotron for the single-dose production of radiopharmaceutical substances in a hospital environment. The study reviews design principles and thermodynamic fundamentals of cryocooler-based refrigeration at 4.5 K in the Watt-range, and describes the specific requirements and constraints on the cyclotron design. The study proposes five variants of a closed refrigeration-cycle for isothermal cooling, and provides the design of a novel cryocooler-based system for helium forced-flow refrigeration.

The configuration scheme of each variant is analysed in detail, focussing on the refrigeration cycle and the interplay between hardware configuration and process parameters. A parametric study explores the cooling performance of each scheme, and identifies their specific advantages and limitations under the given boundary conditions. The five configurations are first evaluated individually, and then compared to each other. The comparison reveals that there is no optimal solution. Each configuration is superior in some aspects, but inferior in others, so that compromises are unavoidable when choosing from the configurations. In particular, the analysis indicates that the isothermal cooling-power and technical complexity are two strongly competing factors: the simplest configuration can provide up to 1.3 W of isothermal refrigeration, whereas the most complex can reach up to 11 W.

The acquired insights are used to build a novel refrigerator, which is conceived as a first-generation demonstrator system to prove the viability of the cooling concept. The refrigerator design is based on the simplest configuration, whereas the more powerful variations are withheld for future design iterations. The process of designing the heat exchangers is described in detail, and considers a number of thermal, mechanical, and economic factors. The sensitivity of the system to deviations on the design parameters is also evaluated. The outcome is a refrigerator design that accounts for uncertainties in the design input, with a cooling power that is expected to satisfy the design requirements.

The suitability of the built refrigerator is verified by the thermodynamic assessment of the overall cryogenic system at nominal conditions. The assessment forecasts the cooling power provided by the refrigerator, shows the allocation of such power at the cyclotron system, quantifies the overall exergetic losses, and estimates the helium inventory. At nominal conditions, the built refrigerator is foreseen to provide 1.66 W of isothermal cooling at 4.5 K, and 24.32 W of non-isothermal cooling from 40 K to 70 K. A detailed uncertainty analysis estimates the 95 % confidence interval of these values to span between -26 % and $+17$ %, and between -28 % and $+7$ %, respectively. The validity of the calculation results is assessed by comparing the expected cooling power with third-party measurements on the refrigerator. The comparison shows a significant statistical agreement for the isothermal (35 %) and non-isothermal (24 %) cooling power, providing confidence in the calculations.

The working refrigerator is ready for experimental testing and final use cooling the cyclotron's magnet. The refrigeration concept can be applied beyond the specific use-case of AMIT's cyclotron, and could be implemented on diverse cryogenic systems requiring remote isothermal cooling from a small-scale closed system. This study contributes to the knowledge-base needed for the development of such types of refrigerators, establishing the theoretical foundation, exemplifying the design process, and outlining potential upgrades.

9.1   Future prospects

Testing the built refrigerator

After its successful design and manufacturing, the next development phase consists in the experimental validation of the built refrigerator. Two types of experimental setup are foreseen: first, a *stand-alone setup* using the validation unit to emulate the refrigeration loads (as in Figure 6.1), and later on, a *full-system setup* where the refrigerator is finally connected to the cyclotron system (as in Figure 7.1). So far, the stand-alone setup has been employed by Haug et al. [55] to prove the viability of the design principle.

Extensive test campaigns will be needed to characterise the system and gain operational experience. Of particular interest are transient operation-modes, such as cool-down, warm-up, and quench recovery.

Controlled experiments are also essential for determining the accuracy of the calculation model (chapter 8.2). The model uncertainty has been roughly estimated during the design phase ($U=\pm15\,\%$) and needs to be validated. Appendix A7 outlines a suitable validation approach, where the model uncertainty is determined indirectly by comparing the values of calculation results and experiments.

Differentiating between the individual sources of model-uncertainty may require additional test campaigns. The validation of the refrigerator system will provide an estimate of the *compounded* model-uncertainty, the value of which is strongly dominated by the model accuracy of the thermodynamic process (as indicated in Figure 8.19). Even though the models describing the heat exchangers are a noteworthy source of uncertainty, their contribution is likely to be overshadowed by the contribution of the process model. For this reason, an accurate differentiation between uncertainty sources may require individual validation campaigns at a component level; first for each heat-exchanger, and then for the entire process. This, however, is a time- and cost-intensive endeavour that demands a thorough evaluation to determine its added value.

Investigating the remaining configurations

The viability of the refrigeration concept still needs to be proven for the four more complex and powerful configurations (CFG1 to CFG4). As shown in chapter 5, those systems require a higher compression ratio and mass flow, leading to more demanding design requirements on the heat exchangers and pumping system. For this reason, further investigation will be needed to assess potential hardware limitations and overcome technological challenges.

In particular, the use of tubular heat exchangers may become impractical due to their low heat-exchange area per unit of length. Changing to thin-plate heat exchangers could be a viable solution, especially if a more compact design is desired. In any case, it is crucial to maintain the

longitudinal heat conduction to a minimum because it has a direct impact on the available cooling power.

Exploring other use-cases

It is of interest to explore other use-cases for the Cryo-Supply System (CSS), since it possesses four key-features that makes it an attractive cooling solution for a variety of applications:

    (1) it provides isothermal refrigeration power (helium evaporation),
    (2) it cools at a distance (helium forced-flow),
    (3) it operates continuously and uninterrupted (closed refrigeration-cycle), and
    (4) it requires low quantities of cryogenic fluid (~60 g of "cold" helium).

The first two features are important to attain temperature stability and to reduce space requirements next to the load. The last two features are essential to minimise the presence of technical personnel needed on site and to mitigate potential safety hazards; two aspects critical for the operation in non-technical environments such as hospitals.

These key-features derive from the design requirements and constraints imposed by AMIT's cyclotron (chapter 4, Table 4.1), and are what set the refrigerator apart from conventional cooling solutions. As shown in Table 9.1, regular Dewar-flasks only possess features (1) and (2), and cryocooler devices only (3) and (4). *Zero-boil-off cryostats* are state-of-the-art cooling solutions, where the load is submerged in a helium bath (1) and a cryocooler is used to re-condense the evaporated liquid (3) [80]. Even though the helium inventory could be kept low (4), the cryocooler still needs to be placed in the proximity of the load (2) because the helium re-circulation relies on natural convection or thermosiphon-effect.

Table 9.1. Comparison of conventional cooling solutions (Dewar, cryocoolers, and zero-boil-off cryostats) with respect to four key-features of the Cryo-Supply System.

#	Feature	Cryo-Supply System	Dewar-flasks	Cryocooler devices	Zero-boil-off cryostats
1.	Isothermal refrigeration	✓	✓	-	✓
2.	Distance cooling	✓	✓	-	-
3.	Closed cycle	✓	-	✓	✓
4.	Low helium inventory	✓	-	✓	(✓)

Like for AMIT's cyclotron, the CSS is particularly suited for cooling superconducting components in a hospital environment. One example are the superconducting magnets employed in medical-imaging techniques such as magnetic resonance imaging (MRI) [78]. Another example are superconducting quantum interference devices (SQUIDs), which are highly sensitive magnetometers used in functional neuroimaging techniques like magnetoencephalography (MEG) [79]. Modern versions of these devices are cooled using zero-boil-off cryostats [81]. The implementation of a remote refrigeration concept using the Cryo-Supply System would enable the relocation of cooling equipment to an adjacent service room, thereby allowing a more compact system at the patient's side.

References

[1] Timmerhaus, K. D. and Flynn, T. M. 2013. "Cryogenic process engineering". Springer Science & Business Media, New York, United States of America.
ISBN 978-1-4684-8756-5.

[2] Radebaugh, R. 2004. "Refrigeration for superconductors". *Proc. of the IEEE*, vol. 92, no. 10, pp. 1719–34.
doi: 10.1109/JPROC.2004.833678.

[3] Radebaugh, R. 2009. "Cryocoolers: the state of the art and recent developments". *Journal of Physics: Condensed Matter*, vol. 21, no. 16, p. 164219.
doi: 10.1088/0953-8984/21/16/164219.

[4] Barron, R.F. 1985. "Cryogenics Systems". Oxford University Press, Oxford, England.
ISBN 978-0-1950-3567-4.

[5] Hamm, R. W. and Hamm, M. E. 2012. "Industrial Accelerators and Their Applications". World Scientific Publishing, Singapore.
ISBN 978-9-8143-0704-8.

[6] Witman, S. 2014. "Ten things you might not know about particle accelerators". Online article in *Symmetry Magazine*, 15 Apr 2014. Fermi National Accelerator Laboratory / SLAC National Accelerator Laboratory, Batavia (IL) / Menlo Park (CA), United States of America.
https://www.symmetrymagazine.org/article/april-2014/ten-things-you-might-not-know-about-particle-accelerators. Last accessed 23 Aug 2019.

[7] Sessler, A. M. and Wilson. E. J. N. 2014. "Engines of Discovery: A Century of Particle Accelerators". Revised and expanded edition. World Scientific Publishing, Singapore.
ISBN 978-9-8144-1733-4.

[8] Granov, A. M., Tiutin, L. A. and Schwarz, T. 2013. "Positron Emission Tomography". *Springer Science & Business Media*, New York, United States of America.
ISBN 978-3-6422-1120-1.

[9] Valk, P. E. 2006. "Positron Emission Tomography: Clinical Practice". *Springer Science & Business Media*, New York, United States of America.
ISBN 978-1-8462-8187-7.

[10] PMB Alcen. "ISOTRACE Cyclotron". Official product website. Paris, France.
https://www.alcen.com/en/medical-healthcare/medical-machines/isotrace-cyclotron. Last accessed 23 Aug 2019.

[11] Advanced Molecular Vision, Inc. 2010. "Preclinical Products - Advanced Biomarker Technology (ABT)". Official product website. London, England.
http://www.amv-europe.com/preclinical/products/advanced-biomarker-technologys. Last accessed 23 Aug 2019.

[12] Schmor, P. 2010. "Review of Cyclotrons Used in the Production of Radioisotopes for Biomedical Applications". *Proc. of Cyclotrons 2010,* the 19th International Conference on Cyclotrons and their Applications, p. 419. Lanzhou, China.
http://accelconf.web.cern.ch/AccelConf/Cyclotrons2010/html/auth0353.htm. Last accessed 23 Aug 2019.

[13] Lewis, D. M., and Zetterberg, U. 2012. „Medical-Isotope Cyclotron Designs Go Full Circle". Magazine article in *CERN Courier,* vol. 52, no. 3, pp. 21-23. IOP Publishing, Geneva, Switzerland.
https://cds.cern.ch/record/1734778. Last accessed 23 Aug 2019.

[14] Lewis, D. M. 2011. "Accelerator Driven Production of Medical Isotopes - World Market Usage and Industrial Production". Presentation at *Accelerator-driven Production of Medical Isotopes*. The Cockcroft Institute of Accelerator Science and Technology, Warrington, England.

[15] Zetterberg, U. 2015. "A Change in Usage of Cyclotrons for Medical Isotope Production?" Presentation at the *Compact Accelerators for Isotope Production*. The Cockcroft Institute of Accelerator Science and Technology, Warrington, England.
https://indi.to/D45Sg. Last accessed 23 Aug 2019.

[16] Webster, W., Parks, G. T., Titov, D., Beasley, P. and Heid, O. 2015. "A Compact, Low-Energy Accelerator for Medical Radioisotope Production — Yields and Isotopic Purity". Presentation at the *Compact Accelerators for Isotope Production*. The Cockcroft Institute of Accelerator Science and Technology, Warrington, England.
https://indi.to/h9z2S. Last accessed 23 Aug 2019.

[17] Vretenar, M. 2015. "A Compact RFQ for Radio Isotope Production in Hospitals". Presentation at the *Compact Accelerators for Isotope Production*. The Cockcroft Institute of Accelerator Science and Technology, Warrington, England.
https://indi.to/FWSC8. Last accessed 23 Aug 2019.

[18] Jensen, M. 2015. "Radioisotope Yields and Operating Experience with a New 7.8 MeV Cyclotron for Point of Demand Isotope Production". Presentation at the *Compact Accelerators for Isotope Production*. The Cockcroft Institute of Accelerator Science and Technology, Warrington, England.
https://indi.to/WknQk. Last accessed 23 Aug 2019.

[19] Walker, G. and Bingham, E. R. 1994. "Low-capacity cryogenic refrigeration". Oxford University Press, Oxford, England.
ISBN 978-0-1985-1760-3.

[20] Cryodata, Inc. 1999. "HePak". Database software, version 3.4. Horizon Technologies, Littleton (Colorado), United States of America.
http://www.htess.com/hepak.htm. Last accessed 23 Aug 2019.

[21] National Institute of Standards and Technology. 2014. "Cryogenics Material Properties". Online Reference Content. Gaithersburg (Maryland), United States of America.
https://trc.nist.gov/cryogenics/materials/materialproperties.htm. Last accessed 23 Aug 2019.

[22] SHI Cryogenics Group. 2014. "Cryocooler Product Catalogue". Sumitomo Heavy Industries, Ltd. Shinagawa, Tokio, Japan.
http://www.shicryogenics.com/wp-content/uploads/2019/08/Cryocooler_Product_Catalogue.pdf. Last accessed 23 Aug 2019.

[23] Claudet, S., Gayet, P. and Wagner, U. 2000. "Specification of Four New Large 4.5 K Helium Refrigerators for the LHC". *Adv. in Cryogenic Eng.* vol. 45B. pp. 1285-92. Kluwer Academic / Plenum Publishers, New York, United States of America.
https://doi.org/10.1007/978-1-4615-4215-5_40.

[24] National Institute of Standards and Technology. 2018. "CODATA Value: Boltzmann constant". Online Reference Database. Gaithersburg (Maryland), United States of America.
https://physics.nist.gov/cgi-bin/cuu/Value?k. Last accessed 23 Aug 2019.

[25] Shah, R. K. and Sekulic, D. P. 2003. "Fundamentals of heat exchanger design". John Wiley & Sons, Hoboken (NJ), United States of America.
ISBN 978-0-4701-7260-5.

[26] Walker, G. 1983. "Cryocoolers". Plenum Press, New York, United States of America.
ISBN 978-1-4899-5286-8.

[27] Weisend, J. G. 1998. "Handbook of Cryogenic Engineering". Taylor & Francis Press, Oxfordshire, England.
ISBN 978-1-5603-2332-7.

[28] SHI Cryogenics Group. 2018. "RDE-418D4 4K Cryocooler Series". Official product website. Sumitomo Heavy Industries, Ltd. Shinagawa, Tokio, Japan.
http://www.shicryogenics.com/products/4k-cryocoolers/rde-418d4-4k-cryocooler-series/. Last accessed 23 Aug 2019.

[29] Cryomech, Inc. 2018. "PT420 Cryocooler". Official product website. Syracuse (NY), United States of America.
www.cryomech.com/products/pt420. Last accessed 23 Aug 2019.

[30] Tahara, K. 2011. "SHI Cryocooler Specification – Model: CG310SLCR". Data Sheet/Product Specification. Cryogenics Division, Precision Equipment Group, Sumitomo Heavy Industries, Ltd. Shinagawa, Tokio, Japan.

[31] Sumitomo Heavy Industries, ltd. 2016. "Cryocoolers. Features: GM-JT Cryocoolers". Official product website. Shinagawa, Tokio, Japan.
http://www.shi.co.jp/english/products/precision/cold/. Last accessed 23 Aug 2019.

[32] Van Sciver, S. W. 2012. "Helium cryogenics". *Springer Science & Business Media*, New York, United States of America.
ISBN 978-1-4419-9978-8.

[33] Maytal, B.-Z. 2012. "Miniature Joule-Thomson Cryocooling: Principles and Practice". *Springer Science & Business Media*, New York, United States of America.
ISBN 978-1-4419-8285-8.

[34] Baehr, H. D. and Kabelac, S. 2012. „Thermodynamik Grundlagen und technische Anwendungen". *Springer Science & Business Media*, New York, United States of America.
ISBN 978-3-5403-6855-7.

[35] Fakheri, A. 2007. "Heat Exchanger Efficiency". *Journal of Heat Transfer*. vol. 129, no. 9. p. 1268.
doi: 10.1115/1.2739620.

[36] Verein Deutscher Ingenieure. 2006. „VDI-Wärmeatlas". Springer Vieweg Verlag, Wiesbaden, Germany.
ISBN 978-3-5403-2218-4.

[37] Sekulić, D. P. 2000. "A Unified Approach to the Analysis of Unidirectional and Bi-Directional Parallel Flow Heat Exchangers". *Int. Journal of Mechanical Eng. Education.* vol. 28, no. 4, p. 307–20.
doi: 10.7227/IJMEE.28.4.3.

[38] Fakheri, A. 2010. "Second Law Analysis of Heat Exchangers". *Journal of Heat Transfer*. vol. 132, no. 11, p. 111802.
doi: 10.1115/1.4002097.

[39] Lerou, P.-P. 2007. "Micromachined Joule-Thomson Cryocooler". Dissertation. Faculty of Science and Technology, University of Twente. Enschede, Netherlands.
https://research.utwente.nl/en/publications/micromachined-joule-thomson-cryocooler. Last accessed 23 Aug 2019.

[40] Barron, R. F. 1999. "Cryogenic heat transfer". CRC Press, Taylor & Francis Group, Boca Raton (FL), United States of America.
ISBN 978-1-5603-2551-2.

[41] Pacio, J.C., Dorao, C.A. 2011. "A review on heat exchanger thermal hydraulic models for cryogenic applications". *Cryogenics.* vol. 51, p. 366–79.
doi: 10.1016/j.cryogenics.2011.04.005.

[42] Gupta, P.K., Kush, P.K., Tiwari, A. 2007. "Second law analysis of counter flow cryogenic heat exchangers in presence of ambient heat-in-leak and longitudinal conduction through wall". *International Journal of Heat and Mass Transfer.* vol. 50, p. 4754–66.
doi: 10.1016/j.ijheatmasstransfer.2007.03.035.

[43] Fredrich, O. 2003. "Untersuchungen an einer Kolbenexpansionsmaschine mit integrierten Wärmeübertragerflächen (Wärmeübertrager-Expander) zur Realisierung eines neuartigen Neon-Tieftemperatur-Prozesses". Dissertation. Faculty of Mechanical Science and Engineering, Technische Universität Dresden. Dresden, Germany.
https://katalogbeta.slub-dresden.de//id/0-1187283681/. Last accessed 23 Aug 2019.

[44] Kroeger, P.G. 1967. "Performance Deterioration in High Effectiveness Heat Exchangers Due to Axial Conduction Effects". *Adv. in Cryogenic Eng.* vol. 12, pp. 363-72.

[45] Brown, G. O. 2002. "The history of the Darcy-Weisbach equation for pipe flow resistance". *150th Civil Eng. Conf. and Exposition* of the American Society of Civil Engineers (ASCE). *p.* 34-43.
doi: 10.1061/40650(2003)4.

[46] Böswirth, L. and Bschorer, S. 2012. "Technische Strömungslehre Lehr- und Ubungsbuch". Springer Vieweg Verlag, Wiesbaden, Germany.
ISBN 978-3-8348-1718-1.

[47] Brkić, D. 2011. "Review of Explicit Approximations to the Colebrook Relation for Flow Friction". *Journal of Petroleum Science and Engineering.* vol. 77, no. 1, p. 34–48. doi: 10.1016/j.petrol.2011.02.006.

[48] Buzzelli, D. 2008. "Calculating Friction in One Step". Magazine article in *Machine Design*, vol. 80, no. 12, p. 54-55. Informa USA, New York, United States of America.

[49] Extreme Rigs. 2015. "Phobya HPC 360mm Radiator Review". Webpage content. San Diego, United States of America. https://www.xtremerigs.net/2015/05/30/phobya-hpc-360mm-radiator-review/2/. Last accessed 23 Aug 2019.

[50] AEE Intec. 2017. "Distillation with heat integration". Webpage content. Gleisdorf, Austria. http://wiki.zero-emissions.at/index.php?title=Distillation_with_heat_integration. Last accessed 23 Aug 2019.

[51] Toral, F. 2016. „Testing the superconducting coils of AMIT cyclotron at MagNet". Presentation at *3rd EuCARD-2 Annual Meeting*. Malta. https://indi.to/K5h8d. Last accessed 23 Aug 2019.

[52] Lee, S.-Y. 2004. "Accelerator Physics". 2nd edition. World Scientific Publishing, Singapore. ISBN 978-9-8131-0203-3.

[53] García-Tabarés, L. 2013. "Superconducting Compact Cyclotrons for Isotope Production," Presentation at *Academia-Industry matching event on superconductivity.* Madrid, Spain. https://indi.to/wHrVq. Last accessed 23 Aug 2019.

[54] García-Tabarés, L., Abramian, P., Calero, J., Gutierrez, J. L., Munilla, J., Obradors, D., Perez, J. M., et al. 2016. "Development of a Superconducting Magnet for a Compact Cyclotron for Radioisotope Production". *IEEE Transactions on Applied Superconductivity*. vol. 26, no. 4, p. 1–4. doi: 10.1109/TASC.2016.2548429.

[55] Haug, F., Berkowitz Zamora, D., et al. 2017. „A small scale remote cooling system for a superconducting cyclotron magnet". *IOP Conf. Ser.: Mater. Sci. Eng.* vol. 171, no. 1, Art. no. 012038. doi: 10.1088/1757-899X/171/1/012038.

[56] Haug, F. 2012. "The AMIT magnet cryosystem". *Proc. Panel Review Meeting*, pp. 10-2. Cryogenics Group, Technology Department, European Organization for Nuclear Research (CERN), Geneva, Switzerland.

[57] Michels, M. 2014. "Entwicklung eines thermisch optimierten Helium Transfer Systems für einen supraleitenden Zyklotron bei 4 K". Diplomarbeit. Institute of Fusion and Reactor Technology (IFRT), Department of Mechanical Engineering. Karlsruhe Institute of Technology (KIT). Karlsruhe, Germany.

[58] Österle, D. 2016. „Studie zur Leistungssteigerung eines kompakten 4.5 K-Helium-Refrigeratorsystems mittels Joule-Thomson-Entspannung". Bachelor thesis. Faculty of Mechanical Engineering, Esslingen University of Applied Sciences. Esslingen, Germany.

[59] Striebel, A. 2012. "Konstruktion und Aufbau Cryocooler-Teststand". Master thesis. Department of Mechanical and Process Engineering, Offenburg University of Applied Sciences. Offenburg, Germany.

[60] Nellis, G.F. 2003. "A heat exchanger model that includes axial conduction, parasitic heat loads, and property variations". *Cryogenics*. vol. 43, p. 523–38.
doi: 10.1016/S0011-2275(03)00132-2.

[61] Ogura, T., Koseki, K. 2007. "SHI Cryocooler Specification – Model SRDK-415D-F50H". Data Sheet/Product Specification. Cryogenics Division, Precision Equipment Group, Sumitomo Heavy Industries, Ltd. Shinagawa, Tokio, Japan.

[62] Thompson, C. A., Manganaro, W. M., and Ficket, F. R. 1990. "Cryogenic Properties of Copper - Thermal Conductivity of Alloys". Copper Development Association Inc. Website content.
https://www.copper.org/resources/properties/cryogenic/images/Thermal-Conductivity-of-Alloys.gif. Last accessed 23 Aug 2019.

[63] KME Germany AG & Co. KG. 2008. "TECTUBE_fin, Inner-grooved tubes, Thermal performance test laboratory". Data Sheet/Product Specification. KME Germany AG & Co. KG. Menden, Germany.
https://www.kme.com/fileadmin/DOWNLOADCENTER/COPPER%20DIVISON/5%20Industrial%20Tubes/1%20TECTUBE%C2%AE/TECTUBE_Inner_grooved%20tubes/TECTUBE_fin_Inner_grooved%20tubes_2016.pdf. Last accessed 23 Aug 2019.

[64] Alexeyev, A. I., Filippov, Y. P. and Mamedov, I. S. 1991. "Flow patterns of two-phase helium in horizontal channels," *Cryogenics*, vol. 31, no. 5, pp. 330–7.
doi: 10.1016/0011-2275(91)90105-6.

[65] Filina, N. N. and Weisend, J. G. 1996. "Cryogenic two-phase flow: applications to large-scale systems". Cambridge University Press, Cambridge, England.
ISBN 9780521481922.

[66] Filippov, Y. P. 1999. "Characteristics of horizontal two-phase helium flows - Part1 - Flow patterns and void fraction". *Cryogenics*. vol. 39, no. 1, pp. 59–68.
doi: 10.1016/S0011-2275(98)00114-3.

[67] Sauvage-Boutar, E., Meuris, C., Poivilliers, J. and Francois, M. X. 1988. "Observation of Two-Phase Helium Flows in a Horizontal Pipe". *Advances in Cryogenic Eng.* vol. 33, pp. 441–7.
doi: 10.1007/978-1-4613-9874-5_54.

[68] Theilacker, J. C. and Rode, C. H. 1988. "An Investigation into Flow Regimes for Two-Phase Helium Flow". *Advances in Cryogenic Eng.* vol. 33, pp. 391–8.
doi: 10.1007/978-1-4613-9874-5_48.

[69] Jakob, M. 2015. "Instrumentation and measurement of a compact cryogenic refrigeration system". Bachelor Thesis. Faculty of Mechatronics and Electrical Engineering, Esslingen University of Applied Sciences. Esslingen, Germany.

[70] Carlsson, Magnus. 2013. "Methods for Early Model Validation: Applied on Simulation Models of Aircraft Vehicle Systems." PhD Thesis. Department of Management and Engineering, Linköping University. Linköping, Sweden.
ISBN 978-91-7519-627-5.

[71] Joint Committee for Guides in Metrology. 2008. "Evaluation of Measurement Data - Guide to the Expression of Uncertainty in Measurement". JCGM 100:2008. Bureau International des Poids et Mesures. Sèvres, France.

[72] American Society of Mechanical Engineers. 2009. "Standard for Verification and Validation in Computational Fluid Dynamics and Heat Transfer: An American National Standard". ASME V&V 20–2009. American Society of Mechanical Engineers. New York, United States of America.

[73] Coleman, H. W. and Steele, W. Glenn. 2009. "Experimentation, Validation, and Uncertainty Analysis for Engineers". John Wiley & Sons, Hoboken (NJ), United States of America.
ISBN 978-0-4701-6888-2.

[74] Coleman, H. W. and Stern, F. 1997. "Uncertainties and CFD Code Validation". *Journal of Fluids Engineering*, vol. 119, no. 4, pp. 795-803.
doi: 10.1115/1.2819500.

[75] Kiusalaas, Jaan. 2013. "Numerical Methods in Engineering with Python 3". 3rd ed. Cambridge University Press, Cambridge, England.
ISBN 978-1-139-62058-1.

[76] OriginLab Corp. 2018. "OriginPro". Data-analysis software, version 2018. Northampton (MA), United States of America.
https://www.originlab.com/index.aspx?go=Products/Origin. Last accessed 23 Aug 2019.

[77] De Levie, R. 2004. "Advanced Excel for Scientific Data Analysis". Oxford University Press, Oxford, England.
ISBN 978-0-1951-5275-3.

[78] Constantinides, Ch. 2016. "Magnetic Resonance Imaging: The Basics".CRC Press, Taylor & Francis Group, Boca Raton (FL), United States of America.
ISBN 978-1-4822-1732-2.

[79] Papanicolaou, A. C. 2009. "Clinical Magnetoencephalography and Magnetic Source Imaging". Cambridge University Press. Cambridge, England.
ISBN 978-0-5218-7375-8.

[80] Weisend, J. 2011. "Defining Cryogenics: Zero Boiloff". Online article, website of the Cryogenic Society of America, Inc. Oak Park (Illinois), United States of America.
https://cryogenicsociety.org/resources/defining_cryogenics/zero_boil_off_cryostats/.
Last accessed 23 Aug 2019.

[81] Siemens Healthcare GmbH. 2019. "MAGNETOM Altea with BioMatrix". Product brochure. Siemens Healthcare GmbH. Erlangen, Germany.
https://www.siemens-healthineers.com/magnetic-resonance-imaging/0-35-to-1-5t-mri-scanner/magnetom-altea. Last accessed 23 Aug 2019.

Appendices

The following appendix contains tables and data sheets for this work.

The appendix is excluded from the normal numbering.

A1. Calculated values obtained for the analysis of possible refrigeration cycles

Calculated data points

Table A1.2. Data set of calculated values for configuration CFG0.

#	p	$\dot{Q}$	T	x_7	η^{II}_{TP}	$\dot{Q}^{II}_R$	$\dot{m}$	6	7		$5\rightarrow6$	$6\rightarrow7$	$8\rightarrow9$	$6\rightarrow8$		δT	$\dot{Q}$	ε
		2nd Stage						h			Δh					HX2		
-	bar	W	K	J/g-K	-	W	g/s	J/g	J/g		J/g	J/g	J/g	J/g		K	W	K
1	1.30	1.45	4.30	0.00	1.00	1.45	0.08	30.47	11.64	245.13	18.82	245.13	0.00	0.00	18.92	1.00	1.30	1.45
2	1.30	1.45	4.30	0.00	0.97	1.41	0.08	30.99	11.64	244.61	19.34	244.61	0.52	0.10	18.37	1.00	1.30	1.45
3	1.30	1.45	4.30	0.00	0.95	1.38	0.07	31.51	11.64	244.09	19.86	244.09	1.04	0.20	17.85	1.00	1.30	1.45
4	1.30	1.45	4.30	0.00	0.92	1.34	0.07	32.03	11.64	243.57	20.38	243.57	1.56	0.30	17.36	0.99	1.30	1.45
5	1.30	1.45	4.30	0.00	0.90	1.31	0.07	32.55	11.64	243.05	20.90	243.05	2.08	0.40	16.89	0.99	1.30	1.45
6	1.30	1.45	4.30	0.00	0.88	1.28	0.07	33.07	11.64	242.53	21.42	242.53	2.60	0.50	16.44	0.99	1.30	1.45
7	1.30	1.45	4.30	0.00	0.86	1.25	0.07	33.59	11.64	242.01	21.94	242.01	3.12	0.60	16.02	0.99	1.30	1.45
8	1.30	1.45	4.30	0.00	0.84	1.22	0.06	34.11	11.64	241.49	22.46	241.49	3.64	0.70	15.62	0.98	1.30	1.45
9	1.30	1.45	4.30	0.00	0.82	1.19	0.06	34.63	11.64	240.97	22.98	240.97	4.16	0.80	15.23	0.98	1.30	1.45
10	1.30	1.45	4.30	0.00	0.80	1.16	0.06	35.15	11.64	240.45	23.50	240.45	4.68	0.90	14.86	0.98	1.30	1.45
11	1.30	1.45	4.30	0.00	0.78	1.14	0.06	35.67	11.64	239.93	24.02	239.93	5.20	1.00	14.51	0.98	1.30	1.45

Table A1.3. Data set of calculated values for configuration CFG1.

#	p_{HP}	2nd Stage $\dot{Q}$	T	x_8	η_{TP}^{II}	$\dot{Q}_R^{II}$	$\dot{m}$	$T_{7,INV}$	h 5	7	Δh 5→6	6→7	8→9	HX2 δT	$\dot{Q}$	ε
-	bar	W	K	J/g-K	-	W	g/s	K	J/g	J/g	J/g	J/g	J/g	K	W	K
1	1.88	1.48	4.32	0.00	0.88	1.30	0.069	4.52	275.67	11.72	242.53	21.41	18.75	0.50	16.77	0.99
2	2.00	1.52	4.35	0.01	0.87	1.33	0.071	4.55	275.68	11.90	242.53	21.25	18.57	0.50	17.34	0.99
3	2.25	1.61	4.43	0.04	0.87	1.40	0.077	4.63	275.71	12.30	242.53	20.88	18.16	0.50	18.68	0.99
4	2.50	1.69	4.49	0.05	0.87	1.46	0.082	4.69	275.74	12.66	242.53	20.55	17.80	0.50	19.94	0.99
5	2.75	1.78	4.56	0.08	0.86	1.54	0.088	4.76	275.77	13.07	242.53	20.17	17.40	0.50	21.45	0.99
6	3.00	1.87	4.62	0.09	0.86	1.61	0.094	4.82	275.80	13.43	242.53	19.84	17.04	0.50	22.87	0.99
7	3.25	1.97	4.69	0.12	0.85	1.68	0.101	4.89	275.83	13.84	242.53	19.46	16.63	0.50	24.57	0.99
8	3.50	2.06	4.75	0.14	0.85	1.76	0.108	4.95	275.86	14.20	242.53	19.13	16.27	0.50	26.17	0.99
9	3.75	2.17	4.82	0.16	0.85	1.84	0.116	5.02	275.89	14.61	242.53	18.75	15.86	0.50	28.08	0.99
10	4.00	2.27	4.89	0.18	0.84	1.91	0.123	5.09	275.92	14.97	242.53	18.42	15.49	0.50	29.88	0.99
11	4.25	2.38	4.96	0.20	0.84	1.99	0.132	5.16	275.95	15.38	242.53	18.04	15.08	0.50	32.03	0.99
12	4.50	2.48	5.02	0.22	0.83	2.07	0.140	5.22	275.98	15.75	242.53	17.70	14.72	0.50	34.05	0.99
13	4.75	2.60	5.09	0.24	0.83	2.15	0.150	5.29	276.01	16.16	242.53	17.32	14.31	0.50	36.46	0.99
14	5.00	2.71	5.15	0.26	0.82	2.23	0.160	5.35	276.04	16.52	242.53	16.99	13.94	0.50	38.73	0.99
15	5.25	2.84	5.22	0.28	0.81	2.31	0.171	5.42	276.07	16.93	242.53	16.60	13.53	0.50	41.45	0.99
16	5.50	2.95	5.28	0.30	0.81	2.39	0.181	5.48	276.10	17.30	242.53	16.27	13.16	0.50	44.00	0.99
17	5.75	3.08	5.35	0.32	0.80	2.47	0.194	5.55	276.13	17.71	242.53	15.88	12.75	0.50	47.06	0.99
18	6.00	3.20	5.42	0.34	0.80	2.55	0.206	5.62	276.16	18.08	242.53	15.55	12.38	0.50	49.94	0.99
19	6.25	3.34	5.49	0.36	0.79	2.63	0.220	5.69	276.19	18.50	242.53	15.16	11.97	0.50	53.39	0.99
20	6.50	3.46	5.55	0.38	0.78	2.71	0.233	5.75	276.22	18.87	242.53	14.82	11.60	0.50	56.63	0.99
21	6.75	3.60	5.62	0.41	0.77	2.79	0.250	5.82	276.25	19.28	242.53	14.44	11.18	0.50	60.52	0.99
22	7.00	3.75	5.69	0.43	0.77	2.87	0.267	5.89	276.28	19.70	242.53	14.05	10.77	0.50	64.68	0.99
23	7.25	3.88	5.75	0.45	0.76	2.94	0.283	5.95	276.31	20.07	242.53	13.71	10.40	0.50	68.60	0.99
24	7.50	4.03	5.82	0.47	0.75	3.02	0.302	6.02	276.34	20.48	242.53	13.33	9.98	0.50	73.31	0.99
25	7.75	4.18	5.89	0.49	0.74	3.09	0.323	6.09	276.37	20.90	242.53	12.94	9.56	0.50	78.36	0.99
26	8.00	4.32	5.96	0.51	0.73	3.15	0.343	6.16	276.40	21.27	242.53	12.60	9.19	0.50	83.12	0.99
27	8.25	4.47	6.03	0.53	0.72	3.21	0.366	6.23	276.43	21.69	242.53	12.21	8.77	0.50	88.88	0.99
28	8.50	4.63	6.10	0.56	0.71	3.27	0.392	6.30	276.46	22.11	242.53	11.82	8.35	0.50	95.06	0.99
29	8.75	4.78	6.16	0.58	0.70	3.32	0.416	6.36	276.50	22.48	242.53	11.48	7.98	0.50	100.92	0.99
30	9.00	4.94	6.23	0.60	0.68	3.37	0.445	6.43	276.53	22.90	242.53	11.09	7.56	0.50	108.03	0.99
31	9.25	5.11	6.30	0.62	0.67	3.41	0.477	6.50	276.56	23.33	242.53	10.70	7.14	0.50	115.71	0.99
32	9.50	5.27	6.37	0.64	0.65	3.44	0.511	6.57	276.59	23.75	242.53	10.31	6.72	0.50	124.02	0.99
33	9.75	5.42	6.43	0.66	0.64	3.45	0.544	6.63	276.62	24.12	242.53	9.97	6.34	0.50	131.95	0.99
34	10.00	5.59	6.50	0.69	0.62	3.46	0.584	6.70	276.65	24.54	242.53	9.58	5.92	0.50	141.65	0.99
35	10.02	5.61	6.51	0.69	0.62	3.46	0.589	6.71	276.65	24.59	242.53	9.53	5.87	0.50	142.79	0.99
36	10.25	5.76	6.57	0.71	0.60	3.45	0.628	6.77	276.68	24.97	242.53	9.18	5.50	0.50	152.23	0.99
37	10.50	5.94	6.64	0.73	0.58	3.43	0.675	6.84	276.71	25.39	242.53	8.79	5.07	0.50	163.80	0.99
38	10.75	6.11	6.71	0.75	0.55	3.38	0.728	6.91	276.74	25.82	242.53	8.40	4.65	0.50	176.50	0.99
39	11.00	6.29	6.78	0.78	0.53	3.32	0.785	6.98	276.78	26.24	242.53	8.01	4.23	0.50	190.49	0.99
40	11.25	6.46	6.85	0.80	0.50	3.23	0.849	7.05	276.81	26.66	242.53	7.61	3.80	0.50	205.98	0.99
41	11.50	6.64	6.93	0.82	0.47	3.11	0.920	7.13	276.84	27.09	242.53	7.22	3.38	0.50	223.20	0.99
42	11.75	6.82	7.00	0.84	0.43	2.95	1.000	7.20	276.87	27.52	242.53	6.82	2.95	0.50	242.46	0.99
43	12.00	7.00	7.07	0.87	0.39	2.75	1.089	7.27	276.90	27.94	242.53	6.43	2.52	0.50	264.13	0.99
44	12.25	7.18	7.14	0.89	0.35	2.49	1.190	7.34	276.93	28.37	242.53	6.03	2.10	0.50	288.67	0.99
45	12.50	7.36	7.21	0.91	0.30	2.18	1.306	7.41	276.97	28.80	242.53	5.64	1.67	0.50	316.71	0.99
46	12.75	7.54	7.28	0.93	0.24	1.78	1.439	7.48	277.00	29.23	242.53	5.24	1.24	0.50	349.03	0.99
47	13.00	7.72	7.35	0.96	0.17	1.29	1.594	7.55	277.03	29.65	242.53	4.84	0.81	0.50	386.69	0.99
48	13.25	7.93	7.43	0.98	0.08	0.60	1.801	7.63	277.06	30.13	242.53	4.40	0.33	0.50	436.89	0.99
49	13.44	8.07	7.48	1.00	0.00	0.00	1.972	7.68	277.09	30.46	242.53	4.09	0.00	0.50	478.38	0.99

Table A1.4. Data set of calculated values for configuration CFG2.

| # | p_{HP} | 2nd Stage | | x_9 | $\dot{Q}_R^{II}$ | $\dot{m}$ | η_{TP}^{II} | $T_{8,INV}$ | h | | ... |
| | | $\dot{Q}$ | T | | | | | | 7 | 8 | |
-	bar	W	K	J/g-K	W	g/s	-	K	J/g	J/g	...
1	2.74	2.63	5.10	0.07	2.27	0.13	0.86	4.75	17.92	13.02	...
2	2.75	2.64	5.11	0.08	2.28	0.13	0.86	4.76	18.02	13.07	...
3	3.00	2.88	5.24	0.09	2.47	0.15	0.86	4.82	19.38	13.43	...
4	3.25	3.14	5.38	0.12	2.68	0.16	0.85	4.89	20.79	13.84	...
5	3.50	3.40	5.52	0.14	2.89	0.18	0.85	4.95	22.10	14.20	...
6	3.75	3.71	5.67	0.16	3.14	0.20	0.85	5.02	23.56	14.61	...
7	4.00	4.04	5.83	0.18	3.40	0.22	0.84	5.09	24.97	14.97	...
8	4.25	4.42	6.00	0.20	3.69	0.24	0.84	5.16	26.48	15.38	...
9	4.50	4.82	6.18	0.22	4.00	0.27	0.83	5.22	27.95	15.75	...
10	4.75	5.28	6.37	0.24	4.36	0.30	0.83	5.29	29.61	16.16	...
11	5.00	5.77	6.58	0.26	4.74	0.34	0.82	5.35	31.22	16.52	...
12	5.25	6.33	6.80	0.28	5.16	0.38	0.81	5.42	32.98	16.93	...
13	5.50	6.92	7.03	0.30	5.60	0.43	0.81	5.48	34.75	17.30	...
14	5.75	7.57	7.29	0.32	6.08	0.48	0.80	5.55	36.66	17.71	...
15	6.00	8.24	7.55	0.34	6.57	0.53	0.80	5.62	38.53	18.08	...
16	6.25	9.00	7.84	0.36	7.10	0.59	0.79	5.69	40.65	18.50	...
17	6.50	9.75	8.14	0.38	7.63	0.66	0.78	5.75	42.72	18.87	...
18	6.75	10.56	8.46	0.41	8.18	0.73	0.77	5.82	44.98	19.28	...
19	7.00	11.40	8.82	0.43	8.74	0.81	0.77	5.89	47.40	19.70	...
20	7.25	12.20	9.17	0.45	9.25	0.89	0.76	5.95	49.72	20.07	...
21	7.50	13.05	9.56	0.47	9.77	0.98	0.75	6.02	52.33	20.48	...
22	7.75	13.89	9.99	0.49	10.27	1.07	0.74	6.09	55.10	20.90	...
23	8.00	14.66	10.41	0.51	10.69	1.16	0.73	6.16	57.77	21.27	...
24	8.25	15.43	10.88	0.53	11.08	1.26	0.72	6.23	60.74	21.69	...
25	8.50	16.17	11.38	0.56	11.42	1.37	0.71	6.30	63.91	22.11	...
26	8.75	16.81	11.88	0.58	11.69	1.46	0.70	6.36	66.98	22.48	...
27	9.00	17.44	12.44	0.60	11.89	1.57	0.68	6.43	70.45	22.90	...
28	9.25	18.02	13.04	0.62	12.02	1.68	0.67	6.50	74.08	23.33	...
29	9.50	18.53	13.66	0.64	12.07	1.80	0.65	6.57	77.85	23.75	...
30	9.61	18.74	13.96	0.65	12.07	1.85	0.64	6.60	79.63	23.93	...
31	9.75	18.95	14.28	0.66	12.06	1.90	0.64	6.63	81.52	24.12	...
32	10.00	19.36	14.98	0.69	11.97	2.02	0.62	6.70	85.69	24.54	...
33	10.25	19.72	15.73	0.71	11.80	2.15	0.60	6.77	90.12	24.97	...
34	10.50	20.05	16.52	0.73	11.57	2.28	0.58	6.84	94.69	25.39	...
35	10.75	20.62	17.36	0.75	11.42	2.46	0.55	6.91	99.57	25.82	...
36	11.00	21.23	18.25	0.78	11.21	2.65	0.53	6.98	104.69	26.24	...
37	11.25	21.88	19.19	0.80	10.93	2.87	0.50	7.05	110.11	26.66	...
38	11.50	22.57	20.20	0.82	10.55	3.13	0.47	7.13	115.84	27.09	...
39	11.75	23.31	21.27	0.84	10.07	3.42	0.43	7.20	121.92	27.52	...
40	12.00	24.09	22.41	0.87	9.45	3.75	0.39	7.27	128.34	27.94	...
41	12.25	24.93	23.64	0.89	8.66	4.13	0.35	7.34	135.22	28.37	...
42	12.50	25.82	24.95	0.91	7.64	4.58	0.30	7.41	142.50	28.80	...
43	12.75	26.79	26.36	0.93	6.34	5.11	0.24	7.48	150.33	29.23	...
44	13.00	27.83	27.88	0.96	4.66	5.75	0.17	7.55	158.70	29.65	...
45	13.25	29.08	29.70	0.98	2.21	6.61	0.08	7.63	168.68	30.13	...
46	13.44	30.00	31.09	1.00	0.00	7.34	0.00	7.68	176.26	30.46	...

#	...	Δh				HX2			HX3			
		5→6	6→7	7→8	9→10	δT	$\dot{Q}$	ε	δT	δT_{CS}	$\dot{Q}$	ε
-	...	J/g	J/g	J/g	J/g	K	W	K	K	K	W	-
1	...	237.63	20.21	4.90	17.44	0.50	30.88	0.99	0.25	0.25	0.64	0.69
2	...	237.58	20.17	4.95	17.40	0.50	31.08	0.99	0.25	0.26	0.65	0.69
3	...	236.58	19.84	5.95	17.04	0.50	34.33	0.99	0.25	0.32	0.86	0.73
4	...	235.58	19.46	6.95	16.63	0.50	37.96	0.99	0.25	0.39	1.12	0.77
5	...	234.63	19.13	7.90	16.27	0.50	41.75	0.99	0.25	0.45	1.41	0.79
6	...	233.58	18.75	8.95	15.86	0.50	46.22	0.99	0.25	0.52	1.77	0.82
7	...	232.53	18.42	10.00	15.49	0.50	51.03	0.99	0.25	0.59	2.19	0.84
8	...	231.43	18.04	11.10	15.08	0.50	56.65	0.99	0.25	0.66	2.72	0.85
9	...	230.33	17.70	12.20	14.72	0.50	62.66	0.99	0.25	0.72	3.32	0.86
10	...	229.08	17.32	13.45	14.31	0.50	69.84	0.99	0.25	0.79	4.10	0.88
11	...	227.83	16.99	14.70	13.94	0.50	77.44	0.99	0.25	0.85	5.00	0.89
12	...	226.48	16.60	16.05	13.53	0.50	86.33	0.99	0.25	0.92	6.12	0.90
13	...	225.08	16.27	17.45	13.16	0.50	95.74	0.99	0.25	0.98	7.42	0.91
14	...	223.58	15.88	18.95	12.75	0.50	106.61	0.99	0.25	1.05	9.04	0.92
15	...	222.08	15.55	20.45	12.38	0.50	117.74	0.99	0.25	1.12	10.84	0.92
16	...	220.38	15.16	22.15	11.97	0.50	130.74	0.99	0.25	1.19	13.14	0.93
17	...	218.68	14.82	23.85	11.60	0.50	143.80	0.99	0.25	1.25	15.68	0.93
18	...	216.83	14.44	25.70	11.18	0.50	158.56	0.99	0.25	1.32	18.79	0.94
19	...	214.83	14.05	27.70	10.77	0.50	174.33	0.99	0.25	1.39	22.48	0.94
20	...	212.88	13.71	29.65	10.40	0.50	189.41	0.99	0.25	1.45	26.38	0.95
21	...	210.68	13.33	31.85	9.98	0.50	206.31	0.99	0.25	1.52	31.19	0.95
22	...	208.33	12.94	34.20	9.56	0.50	223.68	0.99	0.25	1.59	36.72	0.96
23	...	206.03	12.60	36.50	9.19	0.50	239.68	0.99	0.25	1.66	42.46	0.96
24	...	203.48	12.21	39.05	8.77	0.50	257.08	0.99	0.25	1.73	49.34	0.96
25	...	200.73	11.82	41.80	8.35	0.50	274.49	0.99	0.25	1.80	57.16	0.96
26	...	198.03	11.48	44.50	7.98	0.50	289.96	0.99	0.25	1.86	65.16	0.97
27	...	194.98	11.09	47.55	7.56	0.50	306.67	0.99	0.25	1.93	74.79	0.97
28	...	191.78	10.70	50.75	7.14	0.50	322.89	0.99	0.25	2.00	85.44	0.97
29	...	188.43	10.31	54.10	6.72	0.50	338.60	0.99	0.25	2.07	97.21	0.97
30	...	186.83	10.14	55.70	6.53	0.50	345.43	0.99	0.25	2.10	102.98	0.97
31	...	185.13	9.97	57.40	6.34	0.50	352.06	0.99	0.25	2.13	109.16	0.97
32	...	181.38	9.58	61.15	5.92	0.50	366.71	0.99	0.25	2.20	123.63	0.98
33	...	177.38	9.18	65.15	5.50	0.50	380.82	0.99	0.25	2.27	139.87	0.98
34	...	173.23	8.79	69.30	5.07	0.50	395.08	0.99	0.25	2.34	158.05	0.98
35	...	168.78	8.40	73.75	4.65	0.50	414.48	0.98	0.25	2.41	181.11	0.98
36	...	164.08	8.01	78.45	4.23	0.50	435.20	0.98	0.25	2.48	208.08	0.98
37	...	159.08	7.61	83.45	3.80	0.50	457.31	0.98	0.25	2.55	239.90	0.98
38	...	153.78	7.22	88.75	3.38	0.50	480.89	0.98	0.25	2.63	277.53	0.98
39	...	148.13	6.82	94.40	2.95	0.50	505.96	0.98	0.25	2.70	322.43	0.99
40	...	142.13	6.43	100.40	2.52	0.50	532.58	0.98	0.25	2.77	376.21	0.99
41	...	135.68	6.03	106.85	2.10	0.50	560.65	0.98	0.25	2.84	441.51	0.99
42	...	128.83	5.64	113.70	1.67	0.50	590.17	0.98	0.25	2.91	520.86	0.99
43	...	121.43	5.24	121.10	1.24	0.50	620.74	0.98	0.25	2.98	619.05	0.99
44	...	113.48	4.84	129.05	0.81	0.50	651.97	0.98	0.25	3.05	741.42	0.99
45	...	103.98	4.40	138.55	0.33	0.50	687.19	0.98	0.25	3.13	915.65	0.99
46	...	96.73	4.09	145.80	0.00	0.50	710.22	0.97	0.25	3.18	1070.49	0.99

Table A1.5. Data set of calculated values for configuration CFG3.

#	p_{HP}	2nd Stage $\dot{Q}$	2nd Stage T	x_9	$\dot{Q}_R^{II}$	$\dot{m}$	η_{TP}^{II}	T 7,INV	T 8,INV	h 7	h 8	...
-	bar	W	K	J/g-K	W	g/s	-	K	K	J/g	J/g	...
1	2.74	1.77	4.55	0.07	1.53	0.09	0.86	4.75	4.75	13.02	13.02	...
2	3.00	1.87	4.62	0.07	1.61	0.09	0.86	4.82	4.75	13.43	13.02	...
3	3.50	2.06	4.75	0.07	1.78	0.10	0.86	4.95	4.75	14.20	13.02	...
4	4.00	2.27	4.89	0.07	1.95	0.11	0.86	5.09	4.75	14.97	13.02	...
5	4.50	2.48	5.02	0.07	2.12	0.12	0.85	5.22	4.75	15.75	13.02	...
6	5.00	2.71	5.15	0.07	2.31	0.13	0.85	5.35	4.75	16.52	13.02	...
7	5.50	2.95	5.28	0.07	2.51	0.14	0.85	5.48	4.75	17.30	13.02	...
8	6.00	3.20	5.42	0.07	2.71	0.16	0.85	5.62	4.75	18.08	13.02	...
9	6.50	3.46	5.55	0.07	2.92	0.17	0.84	5.75	4.75	18.87	13.02	...
10	7.00	3.75	5.69	0.07	3.16	0.18	0.84	5.89	4.75	19.70	13.02	...
11	7.50	4.03	5.82	0.07	3.39	0.19	0.84	6.02	4.75	20.48	13.02	...
12	8.00	4.32	5.96	0.07	3.61	0.21	0.84	6.16	4.75	21.27	13.02	...
13	8.50	4.63	6.10	0.07	3.87	0.22	0.84	6.30	4.75	22.11	13.02	...
14	9.00	4.94	6.23	0.07	4.11	0.24	0.83	6.43	4.75	22.90	13.02	...
15	9.50	5.27	6.37	0.07	4.38	0.25	0.83	6.57	4.75	23.75	13.02	...
16	10.00	5.59	6.50	0.07	4.63	0.27	0.83	6.70	4.75	24.54	13.02	...
17	10.50	5.94	6.64	0.07	4.90	0.28	0.83	6.84	4.75	25.39	13.02	...
18	11.00	6.29	6.78	0.07	5.17	0.30	0.82	6.98	4.75	26.24	13.02	...
19	11.50	6.64	6.93	0.07	5.46	0.31	0.82	7.13	4.75	27.09	13.02	...
20	12.00	7.00	7.07	0.07	5.73	0.33	0.82	7.27	4.75	27.94	13.02	...
21	12.50	7.36	7.21	0.07	6.00	0.34	0.82	7.41	4.75	28.80	13.02	...
22	13.00	7.72	7.35	0.07	6.27	0.36	0.81	7.55	4.75	29.65	13.02	...
23	13.50	8.11	7.50	0.07	6.58	0.38	0.81	7.70	4.75	30.56	13.02	...
24	14.00	8.47	7.64	0.07	6.84	0.39	0.81	7.84	4.75	31.42	13.02	...
25	14.50	8.85	7.78	0.07	7.14	0.41	0.81	7.98	4.75	32.33	13.02	...
26	15.00	9.23	7.93	0.07	7.43	0.43	0.81	8.13	4.75	33.24	13.02	...
27	15.50	9.61	8.08	0.07	7.70	0.44	0.80	8.28	4.75	34.16	13.02	...
28	16.00	10.00	8.24	0.07	7.99	0.46	0.80	8.44	4.75	35.12	13.02	...
29	16.50	10.37	8.39	0.07	8.27	0.47	0.80	8.59	4.75	36.04	13.02	...
30	17.00	10.75	8.54	0.07	8.54	0.49	0.79	8.74	4.75	37.01	13.02	...
31	17.50	11.10	8.69	0.07	8.78	0.50	0.79	8.89	4.75	37.93	13.02	...
32	18.00	11.49	8.85	0.07	9.09	0.52	0.79	9.05	4.75	38.95	13.02	...
33	18.50	11.85	9.01	0.07	9.35	0.54	0.79	9.21	4.75	39.92	13.02	...
34	19.00	12.20	9.17	0.07	9.55	0.55	0.78	9.37	4.75	40.89	13.02	...
35	19.50	12.56	9.33	0.07	9.83	0.56	0.78	9.53	4.75	41.92	13.02	...
36	20.00	12.91	9.50	0.07	10.06	0.58	0.78	9.70	4.75	42.95	13.02	...
37	20.50	13.24	9.66	0.07	10.29	0.59	0.78	9.86	4.75	43.97	13.02	...
38	21.00	13.59	9.83	0.07	10.56	0.61	0.78	10.03	4.75	45.05	13.02	...
39	21.50	13.92	10.00	0.07	10.75	0.62	0.77	10.20	4.75	46.13	13.02	...
40	22.00	14.24	10.18	0.07	10.98	0.63	0.77	10.38	4.75	47.21	13.02	...
41	22.50	14.55	10.35	0.07	11.15	0.64	0.77	10.55	4.75	48.30	13.02	...
42	23.00	14.86	10.53	0.07	11.39	0.65	0.77	10.73	4.75	49.43	13.02	...
43	23.50	15.16	10.71	0.07	11.55	0.66	0.76	10.91	4.75	50.56	13.02	...
44	24.00	15.45	10.89	0.07	11.79	0.68	0.76	11.09	4.75	51.75	13.02	...
45	24.50	15.74	11.08	0.07	11.96	0.69	0.76	11.28	4.75	52.93	13.02	...
46	25.00	16.01	11.27	0.07	12.12	0.70	0.76	11.47	4.75	54.12	13.02	...
47	25.31	16.17	11.39	0.07	12.22	0.70	0.76	11.59	4.75	54.86	13.02	...

Continuation of Table A1.5.

#	...	Δh				HX2			JTHX			
		5→6	6→7	7→8	9→10	δT	$\dot{Q}$	ε	δT	δT_{CS}	$\dot{Q}$	ε
-	...	J/g	J/g	J/g	J/g	K	W	K	K	K	W	-
1	...	242.53	20.21	0.00	17.44	0.50	21.28	0.99	K	0.25	0.00	0.00
2	...	242.13	20.24	0.41	17.44	0.50	22.38	0.99	0.25	0.25	0.04	0.11
3	...	241.38	20.28	1.18	17.44	0.50	24.57	0.99	0.28	0.25	0.12	0.24
4	...	240.63	20.32	1.95	17.44	0.50	26.87	0.99	0.34	0.25	0.22	0.32
5	...	239.83	20.40	2.72	17.44	0.50	29.21	0.99	0.39	0.25	0.33	0.39
6	...	239.03	20.49	3.50	17.44	0.50	31.65	0.99	0.44	0.25	0.46	0.44
7	...	238.28	20.52	4.28	17.44	0.50	34.28	0.99	0.48	0.25	0.62	0.47
8	...	237.48	20.60	5.06	17.44	0.50	36.91	0.99	0.51	0.25	0.79	0.51
9	...	236.68	20.67	5.84	17.44	0.50	39.63	0.99	0.55	0.25	0.98	0.54
10	...	235.88	20.70	6.67	17.44	0.50	42.70	0.99	0.57	0.25	1.21	0.57
11	...	235.13	20.73	7.46	17.44	0.50	45.70	0.99	0.60	0.25	1.45	0.59
12	...	234.28	20.85	8.25	17.44	0.50	48.52	0.99	0.62	0.25	1.71	0.61
13	...	233.48	20.87	9.09	17.44	0.50	51.83	0.99	0.64	0.25	2.02	0.63
14	...	232.68	20.94	9.88	17.44	0.50	54.89	0.99	0.65	0.25	2.33	0.65
15	...	231.83	21.01	10.72	17.44	0.50	58.17	0.99	0.67	0.25	2.69	0.67
16	...	231.03	21.08	11.52	17.44	0.50	61.30	0.99	0.68	0.25	3.06	0.69
17	...	230.18	21.14	12.37	17.44	0.50	64.65	0.99	0.69	0.25	3.47	0.70
18	...	229.33	21.21	13.22	17.44	0.50	68.00	0.99	0.69	0.25	3.92	0.72
19	...	228.53	21.22	14.07	17.44	0.50	71.55	0.99	0.70	0.25	4.40	0.73
20	...	227.63	21.33	14.92	17.44	0.50	74.72	0.99	0.70	0.25	4.90	0.74
21	...	226.78	21.39	15.77	17.44	0.50	78.06	0.99	0.70	0.25	5.43	0.76
22	...	225.88	21.49	16.63	17.44	0.50	81.17	0.99	0.70	0.25	5.98	0.77
23	...	225.03	21.50	17.54	17.44	0.50	84.84	0.99	0.70	0.25	6.61	0.78
24	...	224.13	21.61	18.40	17.44	0.50	87.86	0.99	0.70	0.25	7.21	0.79
25	...	223.28	21.61	19.31	17.44	0.50	91.45	0.99	0.69	0.25	7.91	0.80
26	...	222.38	21.66	20.22	17.44	0.50	94.76	0.99	0.69	0.25	8.62	0.81
27	...	221.43	21.76	21.13	17.44	0.50	97.74	0.99	0.68	0.25	9.33	0.82
28	...	220.48	21.81	22.10	17.44	0.50	101.06	0.99	0.67	0.25	10.13	0.83
29	...	219.58	21.86	23.01	17.44	0.50	104.12	0.99	0.66	0.25	10.91	0.84
30	...	218.58	21.96	23.98	17.44	0.50	106.97	0.99	0.65	0.25	11.74	0.85
31	...	217.63	22.06	24.90	17.44	0.50	109.56	0.99	0.63	0.25	12.54	0.86
32	...	216.68	22.05	25.92	17.44	0.50	112.89	0.99	0.62	0.25	13.51	0.86
33	...	215.73	22.10	26.90	17.44	0.50	115.68	0.99	0.60	0.25	14.42	0.87
34	...	214.63	22.29	27.87	17.44	0.50	117.47	0.99	0.59	0.25	15.25	0.88
35	...	213.68	22.28	28.90	17.44	0.50	120.43	0.99	0.57	0.25	16.29	0.89
36	...	212.63	22.37	29.92	17.44	0.50	122.67	0.99	0.55	0.25	17.26	0.90
37	...	211.58	22.46	30.95	17.44	0.50	124.77	0.99	0.53	0.25	18.25	0.91
38	...	210.58	22.45	32.03	17.44	0.50	127.46	0.99	0.51	0.25	19.39	0.91
39	...	209.43	22.59	33.11	17.44	0.50	129.07	0.99	0.49	0.25	20.40	0.92
40	...	208.38	22.62	34.19	17.44	0.50	131.16	0.99	0.46	0.25	21.52	0.92
41	...	207.23	22.76	35.27	17.44	0.50	132.46	0.99	0.44	0.25	22.55	0.93
42	...	206.18	22.75	36.40	17.44	0.50	134.69	0.99	0.41	0.25	23.78	0.94
43	...	204.98	22.88	37.54	17.44	0.50	135.78	0.99	0.39	0.25	24.87	0.94
44	...	203.88	22.87	38.72	17.44	0.50	137.79	0.99	0.36	0.25	26.17	0.95
45	...	202.68	22.95	39.91	17.44	0.50	138.99	0.99	0.33	0.25	27.37	0.95
46	...	201.48	23.03	41.10	17.44	0.50	140.04	0.99	0.30	0.25	28.56	0.96
47	...	200.73	23.08	41.84	17.44	0.50	140.63	0.99	0.27	0.25	29.31	0.96

Table A1.6. Data set of calculated values for configuration CFG4.

	p		2nd Stage						T			
#	HP	MP	$\dot{Q}$	T	x_{10}	$\dot{Q}_R^{II}$	$\dot{m}$	η_{TP}^{II}	7	8,INV	9,INV	...
-	bar	bar	W	K	J/g-K	W	g/s	-	K	K	K	...
1	2.74	2.74	2.63	5.10	0.07	2.27	0.13	0.86	5.30	4.75	4.75	...
2	3.00	2.74	2.82	5.21	0.07	2.43	0.14	0.86	5.41	4.82	4.75	...
3	4.00	2.74	3.65	5.64	0.07	3.14	0.18	0.86	5.84	5.09	4.75	...
4	5.00	2.74	4.59	6.08	0.07	3.91	0.22	0.85	6.28	5.35	4.75	...
5	6.00	2.74	5.63	6.52	0.07	4.77	0.27	0.85	6.72	5.62	4.75	...
6	7.00	2.74	6.73	6.96	0.07	5.67	0.33	0.84	7.16	5.89	4.75	...
7	8.00	2.74	7.80	7.38	0.07	6.52	0.37	0.84	7.58	6.16	4.75	...
8	9.00	2.74	8.89	7.80	0.07	7.40	0.42	0.83	8.00	6.43	4.75	...
9	10.00	2.74	9.88	8.19	0.07	8.18	0.47	0.83	8.39	6.70	4.75	...
10	11.00	2.74	10.79	8.56	0.07	8.88	0.51	0.82	8.76	6.98	4.75	...
11	12.00	2.74	11.63	8.92	0.07	9.51	0.55	0.82	9.12	7.27	4.75	...
12	13.00	2.74	12.34	9.23	0.07	10.01	0.57	0.81	9.43	7.55	4.75	...
13	14.00	2.74	13.01	9.55	0.07	10.51	0.60	0.81	9.75	7.84	4.75	...
14	15.00	2.74	13.67	9.87	0.07	11.01	0.63	0.81	10.07	8.13	4.75	...
15	16.00	2.74	14.15	10.13	0.07	11.31	0.65	0.80	10.33	8.44	4.75	...
16	17.00	2.74	14.58	10.36	0.07	11.58	0.66	0.79	10.56	8.74	4.75	...
17	18.00	2.74	15.00	10.61	0.07	11.86	0.68	0.79	10.81	9.05	4.75	...
18	19.00	2.74	15.19	10.73	0.07	11.89	0.68	0.78	10.93	9.37	4.75	...
19	20.00	2.74	15.52	10.94	0.07	12.10	0.69	0.78	11.14	9.70	4.75	...
20	21.00	2.74	15.81	11.13	0.07	12.29	0.70	0.78	11.33	10.03	4.75	...
21	22.00	2.74	15.95	11.22	0.07	12.29	0.70	0.77	11.42	10.38	4.75	...
22	23.00	2.74	16.10	11.33	0.07	12.35	0.71	0.77	11.53	10.73	4.75	...
23	24.00	2.74	16.22	11.42	0.07	12.37	0.71	0.76	11.62	11.09	4.75	...
24	24.89	2.74	16.29	11.47	0.07	12.37	0.71	0.76	11.67	11.43	4.75	...
25	25.00	2.74	16.23	11.43	0.07	12.29	0.70	0.76	11.63	11.47	4.75	...
26	25.31	2.74	16.22	11.42	0.07	12.25	0.70	0.76	11.62	11.59	4.75	...

Continuation of Table A1.6.

		Δh					HX2			HX3				JTHX			
#	...	5→6	6→7	7→8	8→9	10→11	δT	$\dot{Q}$	ε	δT	$\dot{Q}$	ε	δT_m	δT	$\dot{Q}$	ε	δT_m
-	...	J/g	J/g	J/g	J/g	J/g	K	W	K	K	W	-	K	K	W	-	K
1	...	237.63	20.21	4.90	0.00	17.44	0.50	30.88	0.99	0.25	0.64	0.69	0.31	0.25	0.00	0.00	0.00
2	...	236.83	20.24	5.30	0.41	17.44	0.50	32.97	0.99	0.25	0.74	0.71	0.33	0.28	0.06	0.11	0.21
3	...	233.78	20.32	6.85	1.95	17.44	0.50	42.03	0.99	0.25	1.23	0.78	0.40	0.39	0.35	0.32	0.30
4	...	230.93	20.49	8.10	3.50	17.44	0.50	51.76	0.99	0.25	1.82	0.82	0.43	0.48	0.78	0.44	0.35
5	...	228.18	20.60	9.30	5.06	17.44	0.50	62.40	0.99	0.25	2.54	0.85	0.46	0.55	1.38	0.51	0.39
6	...	225.53	20.70	10.35	6.67	17.44	0.50	73.30	0.99	0.25	3.36	0.87	0.47	0.60	2.17	0.57	0.42
7	...	223.08	20.85	11.20	8.25	17.44	0.50	83.45	0.99	0.25	4.19	0.88	0.48	0.64	3.09	0.61	0.45
8	...	220.63	20.94	12.05	9.88	17.44	0.50	93.62	0.99	0.25	5.11	0.89	0.49	0.67	4.19	0.65	0.48
9	...	218.38	21.08	12.65	11.52	17.44	0.50	102.39	0.99	0.25	5.93	0.89	0.49	0.69	5.40	0.69	0.50
10	...	216.28	21.21	13.05	13.22	17.44	0.50	110.10	0.99	0.25	6.64	0.90	0.49	0.70	6.73	0.72	0.52
11	...	214.28	21.33	13.35	14.92	17.44	0.50	116.89	0.99	0.25	7.28	0.90	0.49	0.70	8.14	0.74	0.53
12	...	212.53	21.49	13.35	16.63	17.44	0.50	122.01	0.99	0.25	7.66	0.90	0.48	0.70	9.55	0.77	0.55
13	...	210.78	21.61	13.35	18.40	17.44	0.50	126.96	0.99	0.25	8.04	0.90	0.47	0.69	11.08	0.79	0.56
14	...	208.98	21.66	13.40	20.22	17.44	0.50	131.87	0.99	0.25	8.46	0.90	0.47	0.68	12.76	0.81	0.57
15	...	207.58	21.81	12.90	22.10	17.44	0.50	134.66	0.99	0.25	8.37	0.90	0.45	0.66	14.33	0.83	0.57
16	...	206.28	21.96	12.30	23.98	17.44	0.50	136.93	0.99	0.25	8.16	0.90	0.44	0.63	15.92	0.85	0.58
17	...	204.93	22.05	11.75	25.92	17.44	0.50	139.37	0.99	0.25	7.99	0.89	0.42	0.60	17.63	0.86	0.58
18	...	204.28	22.29	10.35	27.87	17.44	0.50	139.27	0.99	0.25	7.06	0.88	0.40	0.57	19.00	0.88	0.58
19	...	203.13	22.37	9.50	29.92	17.44	0.50	140.97	0.99	0.25	6.59	0.87	0.38	0.53	20.77	0.90	0.58
20	...	202.08	22.45	8.50	32.03	17.44	0.50	142.34	0.99	0.25	5.99	0.86	0.37	0.49	22.56	0.91	0.57
21	...	201.58	22.62	6.80	34.19	17.44	0.50	142.08	0.99	0.25	4.79	0.83	0.34	0.44	24.10	0.92	0.57
22	...	200.98	22.75	5.20	36.40	17.44	0.50	142.27	0.99	0.25	3.68	0.79	0.32	0.39	25.77	0.94	0.55
23	...	200.53	22.87	3.35	38.72	17.44	0.50	142.21	0.99	0.25	2.38	0.71	0.29	0.33	27.46	0.95	0.54
24	...	200.23	22.97	1.55	40.85	17.44	0.50	142.05	0.99	0.25	1.10	0.53	0.26	0.28	28.98	0.96	0.51
25	...	200.48	23.03	1.00	41.10	17.44	0.50	141.25	0.99	0.25	0.70	0.42	0.25	0.27	28.95	0.96	0.51
26	...	200.53	23.08	0.20	41.84	17.44	0.50	140.87	0.99	0.25	0.14	0.13	0.20	0.25	29.39	0.96	0.50

Comparison of Region II configurations
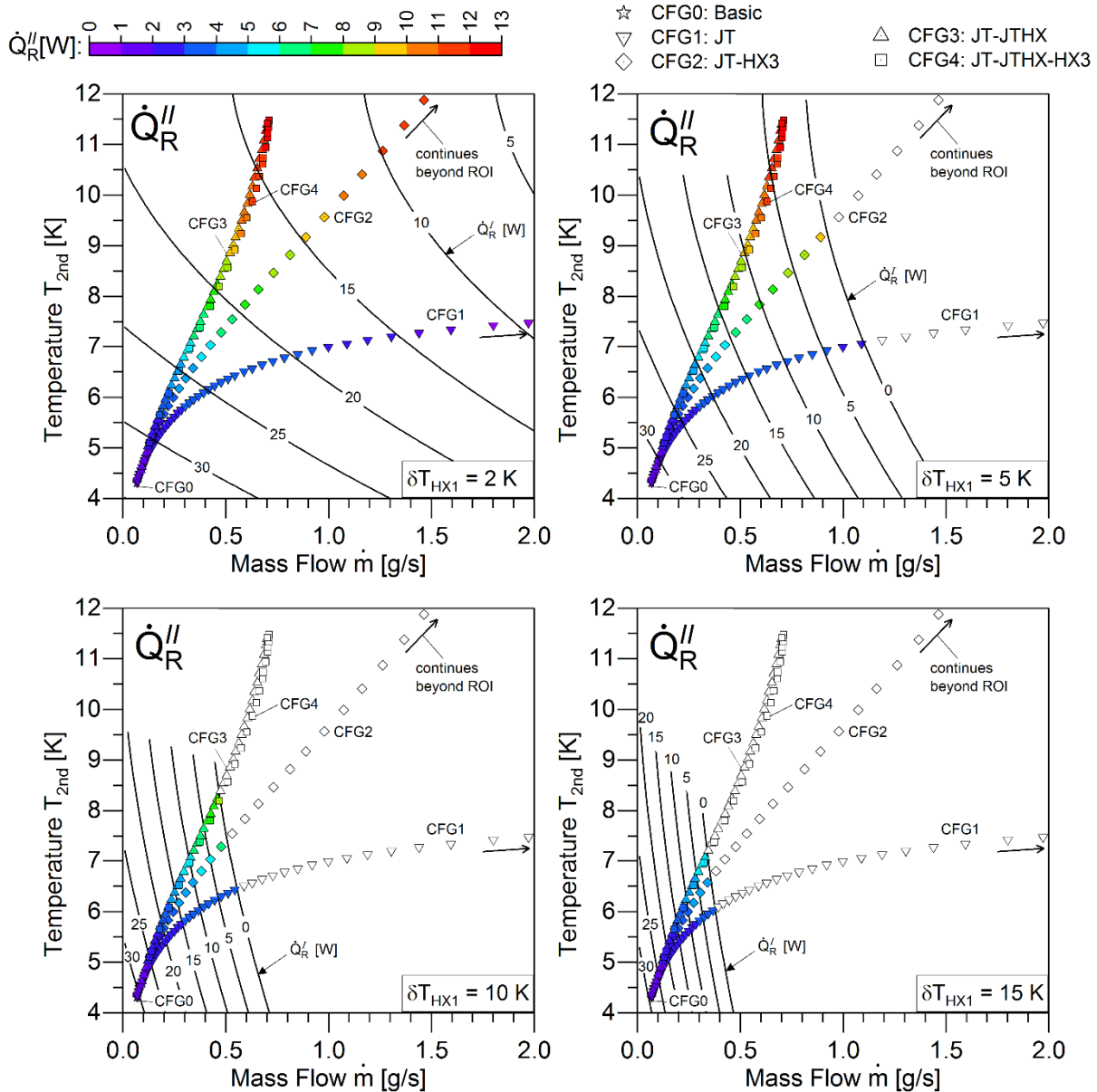
Figure A1.1. Refrigeration power delivered to Circuit I $\dot{Q}_R^I$ (solid lines) and Circuit II $\dot{Q}_R^{II}$ (colour scale in data points) for a given pair of mass flow $\dot{m}$ and 2nd stage temperature T_{2nd}. Each plot corresponds to a different local temperature difference δT_{HX1} at the cold side of recuperator HX1, limiting the design parameter range at which both, $\dot{Q}_R^I$ and $\dot{Q}_R^{II}$, are greater than zero. The shown region of interest (ROI) excludes non-relevant values for CFG1 and CFG2.
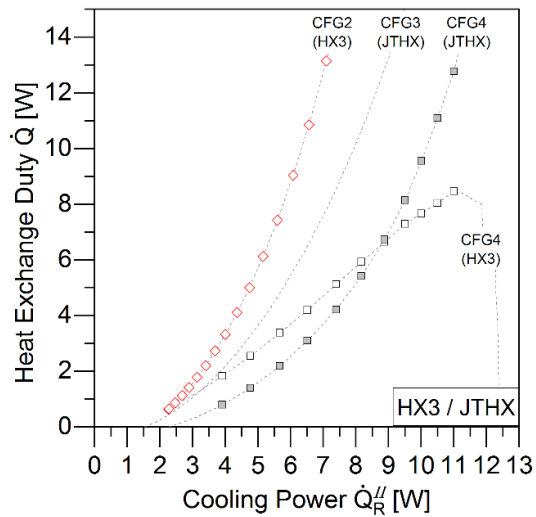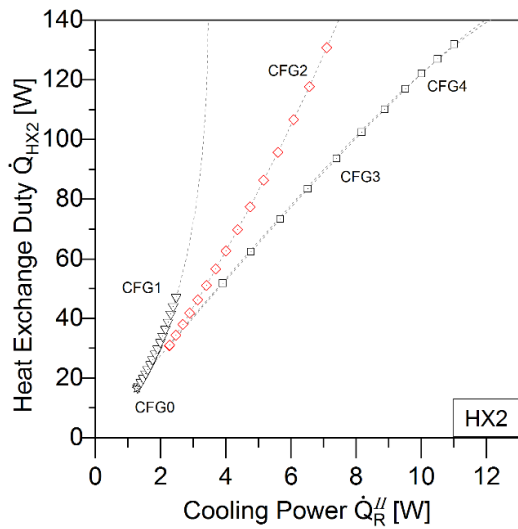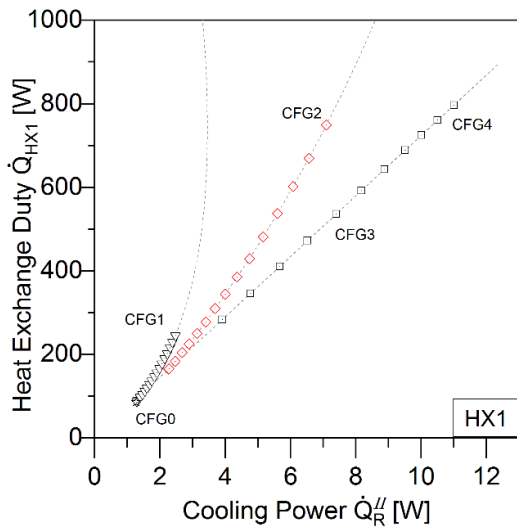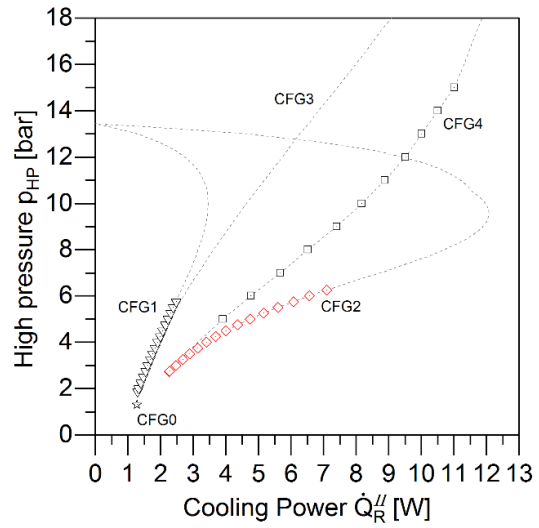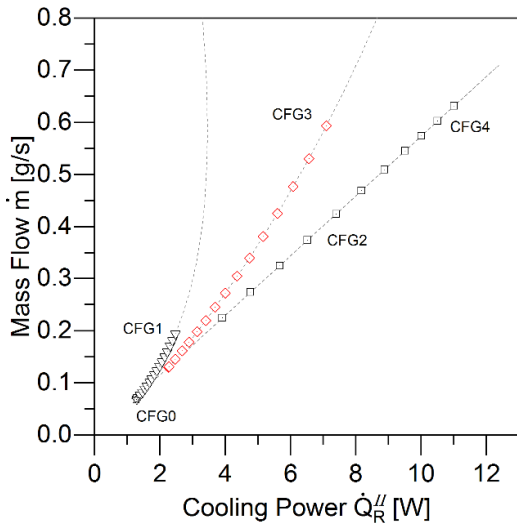
Figure A1.2. Comparison of process parameters for the different Region II configurations. Data points are shown at the operational regions of a configuration that are considered of relative superiority in providing cooling power $\dot{Q}_R^{II}$ for Circuit II.
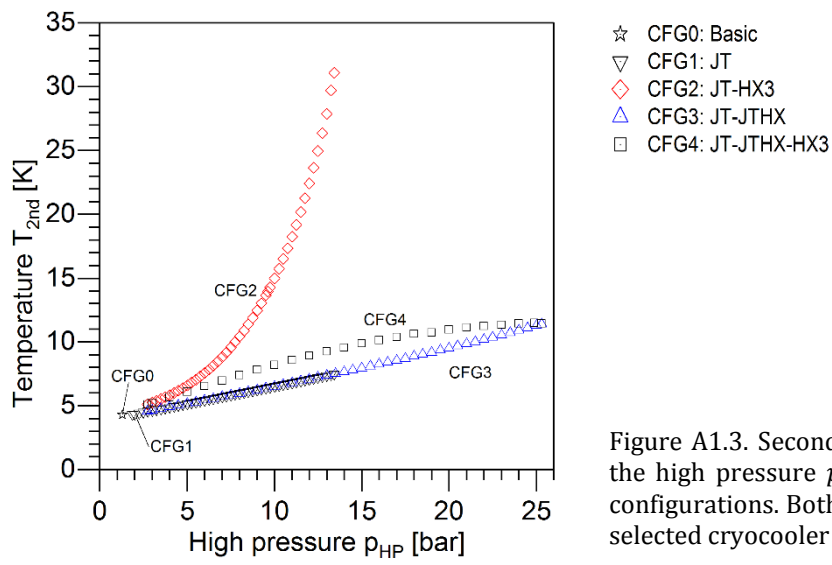
Figure A1.3. Second stage temperature T_{2nd} over the high pressure p_{HP} for the different Region II configurations. Both terms are independent of the selected cryocooler device.

A2. Calculated values for the design of the Cryo Supply System (CSS)

Thermo-Hydraulic Design

Table A2.1. Fluid state values calculated for the CSS design. Design values and boundary conditions are in bold.

Point	p	T	s	h	v	x	e
Unit	kPa	K	J/(g·K)	J/g	cm³/g	-	J/g
1	130.26	**293.15**	30.94	1538.04	4677.70	shg	-7533
2	130.26	**150.00**	27.46	794.65	2395.09	shg	-7256
3	130.26	52.47	22.00	287.92	839.34	shg	-6163
4	130.26	40.00	20.59	223.02	640.05	shg	-5814
5	130.26	89.71	24.79	481.47	1433.54	shg	-6786
6	130.26	40.00	20.59	223.02	640.05	shg	-5814
7	130.26	4.77	8.63	33.07	53.50	shg	-2497
8	130.26	**4.50**	4.31	13.53	12.09	**0.10**	-1250
9	130.26	4.50	8.07	30.47	45.20	**1.00**	-2334
10	130.26	39.50	20.53	220.41	632.05	shg	-5797
11	130.26	137.00	26.99	727.13	2187.79	shg	-7186
12	130.26	280.15	30.71	1470.53	4470.39	shg	-7531

shg = superheated gas.
Values valid for a mass flow of 0.0770 g/s.

Table A2.2. Summary of heat exchange values calculated for the CSS design. Design values are in bold.

Section	Name	Δh	$\Delta \dot{Q}$
Unit	-	J/g	W
1-2	HX1A	-743.39	-57.26
2-3	HX1B	-506.72	-39.03
3-4	HX1stA	-64.91	**-5.00**
4-5	Circuit I	258.45	19.91
5-6	HX1stB	-258.45	-19.91
6-7	HX2	-189.95	-14.63
7-8	HX2nd	-19.54	-1.51
8-9	Circuit II	16.94	1.30
9-10	HX2	189.95	14.63
10-11	HX1B	506.72	39.03
11-12	HX1A	743.39	57.26
-	1st Stage	-	24.91
-	2nd Stage	-	1.51

Values valid for a mass flow of 0.0770 g/s.

Table A2.3. Geometrical values of heat exchangers calculated for the CSS design.

Name	Material	L	L_M	D	D_h	A_h	A_wall
Unit	-	m	m	mm	mm	mm²	mm²
HX1A *	AISI316	4.17	5.62	8/13	8/3	50.27/54.19	28.27/43.98
HX1B *	AISI316	4.77	5.43	6/10	6/2	28.27/28.27	21.99/34.56
HX2 *	CuRRR50	46.51	55.8	4/8	4/2	12.57/21.99	15.71/28.27
HX1stA	CuRRR50	2.54	4.1	6	6	28.27	-
HX1stB	CuRRR50	3.35	4.6	6	6	28.27	-
HX2nd	CuRRR50	2.941	4.4	8.32	8.32	54.37	-

* Coaxial heat exchanger with values for inner / outer pipe.

Table A2.4. Thermo-hydraulic values of heat exchangers calculated for the CSS design. All values with respect to the thermal design length L.

Name	$\dot{Q}$	$U_m \cdot A$	A	δT_m	$\dot{C}_h; \dot{C}_c$	$\dot{C}^*$	$\Delta \dot{E}_h$	$\dot{E}_d$
Unit	W	W/K	m2	K	J/(kg·K)	-	W	W
HX1A	57.26	4.40	0.12	13.00	5193; 5193	1.000	21.31	-5.31
HX1B	39.03	3.00	0.10	12.99	5196; 5197	1.000	84.22	-22.75
HX2	14.63	30.63	0.73	0.48	5391; 5427	0.993	255.50	-11.23
HX1stA	5.00	1.92	0.05	2.61	5205	-	26.89	-4.84
HX1stB	19.91	2.46	0.06	8.10	5200	-	74.94	-51.42
HX2nd	1.50	7.17	0.08	0.21	72873	-	96.03	-5.10

Values valid for a mass flow of 0.0770 g/s

Table A2.5. Dimensionless performance values of heat exchangers calculated for the CSS design. All values with respect to the thermal design length L.

Name	ε	NTU	ζ	Λ	S_A
Unit	-	-	-	10⁻⁴	-
HX1A	91.7%	11.01	80.0%	6.5	1.35
HX1B	88.3%	7.51	78.7%	3.3	1.14
HX2	99.2%	73.29	95.8%	2.7	1.20
HX1stA	99.2%	4.78	84.8%	-	1.90
HX1stB	99.8%	6.13	59.3%	-	1.24
HX2nd	57.3%	13.41	95.0%	-	1.53

Values valid for a mass flow of 0.0770 g/s.

Table A2.6. Thermal and hydraulic losses at the heat exchangers calculated for the CSS design.

Name	$\dot{Q}_{surr,cond}$	$\dot{Q}_{surr,rad}$	$\dot{Q}_{long}$ †	Δp †
Unit	mW	mW	mW	mbar
HX1A *	-	-	13.76/21.41	1.77/12.84
HX1B *	-	-	4.39/6.90	1.88/18.42
HX2 *	-	-	1.44/2.59	28.09/24.58
HX1stA	-	-	-	0.42
HX1stB	-	-	-	0.81
HX2nd	-	-	-	n/a

* Coaxial heat exchanger with values for inner / outer pipe.
† Values with respect to the thermal design length L.
Values valid for a mass flow of 0.0770 g/s.

Geometry Tolerances

Table A2.7. Geometrical tolerances for the manufacturing of the recuperators HX1A, HX1B and HX2.

	HX1A	HX1B	HX2
Pipe material	Stainless Steel AISI 316L	Stainless Steel AISI 316L	Copper (DHP) C12200
Pipe diameter (OP/IP) [mm] *	13/8	10/6	8/4
Pipe Length L_M			
Nominal value [m]	5.62	5.43	55.8
Tolerance [m]	±0.1	±0.1	±0.5
Winding diameter D			
Nominal value [mm]	150/342	272	90/150/210/270
Tolerance [mm]	-3; +3	-3; +3	-3; +3
Windings			
Nominal value [-]	1.7/3.3	6	23/23/23/23
Tolerance (in degrees)	-5°; +5°	-3°; +3°	-3°; +3°
Space between windings			
Nominal [mm]	3	3	3
Tolerance [mm]	-1 ; +2	-1 ; +2	-1 ; +2
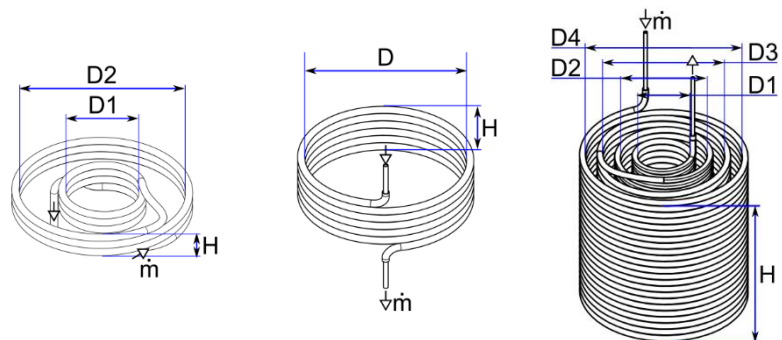
OP: Outer pipe (hotter stream); IP: Inner pipe (colder stream).
* Corresponds to pipe innerdiameter with a wall thickness of 1 mm.

Sensitivity evaluation

Table A2.8. Numerical evaluation for the system sensitivity to deviations from design values. The influence of input to output variations is normalised by the design values (X_0, Y_0).

| Input variations $\Delta X_i/X_0 = i \cdot 0.05 \cdot X_0$ | i | Output variations $\Delta Y_i/Y_0$ [%] | | | | |
| | | Refrigeration power | | Process efficiency | | Mass flow |
		$\dot{Q}_R^I$	$\dot{Q}_R^{II}$	η_{TP}^I	η_{TP}^{II}	$\dot{m}$
Available cooling for Region I $\dot{Q}_{avail}^I$	$-1; +1$	-6.3 ; 6.3	0 ; 0	-1.3 ; 1.2	0 ; 0	0 ; 0
	$-2; +2$	-12.5 ; 12.5	0 ; 0	-2.8 ; 2.3	0 ; 0	0 ; 0
	$-3; +3$	-18.8 ; 18.8	0 ; 0	-4.4 ; 3.3	0 ; 0	0 ; 0
	$-4; +4$	-25.0 ; 25.0	0 ; 0	-6.3 ; 4.2	0 ; 0	0 ; 0
	$\text{MF}_{Y,X}$	1.25	0.00	0.26	0.00	0.00
	R^2	1.00	-	0.99	-	-
Available cooling for Region II $\dot{Q}_{avail}^{II}$	$-1; +1$	2.1 ; -2.2	-4.9 ; 4.9	2.1 ; -2.2	0.1 ; -0.1	-4.9 ; 4.9
	$-2; +2$	4.3 ; -4.4	-9.8 ; 9.8	4.3 ; -4.4	0.3 ; -0.2	-9.8 ; 9.8
	$-3; +3$	6.3 ; -6.7	-14.7 ; 14.7	6.3 ; -6.7	0.4 ; -0.3	-14.7 ; 14.7
	$-4; +4$	8.3 ; -8.9	-19.6 ; 19.6	8.3 ; -8.9	0.5 ; -0.4	-19.6 ; 19.6
	$\text{MF}_{Y,X}$	-0.43	0.98	-0.43	-0.02	0.98
	R^2	1.00	1.00	1.00	0.99	1.00
Thermal design length L	$-1; +1$	-0.9 ; 0.8	-0.8 ; 0.7	-0.9 ; 0.8	-0.8 ; 0.7	-0.8 ; 0.7
	$-2; +2$	-1.8 ; 1.6	-1.7 ; 1.4	-1.8 ; 1.6	-1.7 ; 1.4	-1.7 ; 1.4
	$-3; +3$	-2.8 ; 2.4	-2.6 ; 2.0	-2.8 ; 2.4	-2.6 ; 2	-2.6 ; 2.0
	$-4; +4$	-3.9 ; 3.1	-3.7 ; 2.5	-3.9 ; 3.1	-3.7 ; 2.5	-3.7 ; 2.5
	$\text{MF}_{Y,X}$	0.17	0.15	0.17	0.15	0.15
	R^2	1.00	0.99	1.00	0.99	0.99
Fluid-domain area A_{cross}	$-1; +1$	0.9 ; -0.8	0.8 ; -0.7	0.9 ; -0.8	0.8 ; -0.7	0.8 ; -0.7
	$-2; +2$	1.8 ; -1.6	1.5 ; -1.5	1.8 ; -1.6	1.5 ; -1.5	1.5 ; -1.5
	$-3; +3$	2.7 ; -2.4	2.3 ; -2.2	2.7 ; -2.4	2.3 ; -2.2	2.3 ; -2.2
	$-4; +4$	3.7 ; -3.2	3.0 ; -3.0	3.7 ; -3.2	3.0 ; -3.0	3.0 ; -3.0
	$\text{MF}_{Y,X}$	-0.17	-0.15	-0.17	-0.15	-0.15
	R^2	1.00	1.00	1.00	1.00	1.00
Local thermal conductance $d(U \cdot A)$	$-1; +1$	-0.9 ; 0.8	-0.8 ; 0.7	-0.9 ; 0.8	-0.8 ; 0.7	-0.8 ; 0.7
	$-2; +2$	-1.8 ; 1.6	-1.7 ; 1.4	-1.8 ; 1.6	-1.7 ; 1.4	-1.7 ; 1.4
	$-3; +3$	-2.8 ; 2.4	-2.6 ; 2.0	-2.8 ; 2.4	-2.6 ; 2.0	-2.6 ; 2.0
	$-4; +4$	-3.9 ; 3	-3.7 ; 2.5	-3.9 ; 3	-3.7 ; 2.5	-3.7 ; 2.5
	$\text{MF}_{Y,X}$	0.17	0.15	0.17	0.15	0.15
	R^2	1.00	0.99	1.00	0.99	0.99

$\text{MF}_{Y,X}$: the magnification factor is obtained by simple linear regression; it corresponds to the "slope" with the condition that $Y_0 = Y(X_0)$.
R^2: coefficient of determination for the linear regression.

Table A2.9. Analytical evaluation for the system sensitivity to deviations from design values. The sensitivity is evaluated at the design working point of the CSS (X_0, Y_0).

Governing Equations $Y = f(X)$	Sensitivity Coefficient $\theta_{Y,X} = \partial Y/\partial X$		Magnification Factor $\mathrm{MF}_{Y,X} = \theta_{Y,X} \cdot X_0/Y_0$	
	Partial differential	$\theta_{Y,X}$ at X_0	X_0/Y_0	$\mathrm{MF}_{Y,X}$
$\eta_{\mathrm{TP}}^{I} = \dfrac{\dot{Q}_{\mathrm{R}}^{I}}{\dot{Q}_{\mathrm{avail}}^{I}}$	$\dfrac{\partial \eta_{\mathrm{TP}}^{I}}{\partial \dot{Q}_{\mathrm{avail}}^{I}} = \dfrac{\partial \dot{Q}_{\mathrm{R}}^{I}}{\partial \dot{Q}_{\mathrm{avail}}^{I}} \cdot \dfrac{1}{\dot{Q}_{\mathrm{avail}}^{I}} - \dfrac{\dot{Q}_{\mathrm{R}}^{I}}{\left(\dot{Q}_{\mathrm{avail}}^{I}\right)^{2}}$	0.0080 W-1	31.17 s/J	0.25
	$\dfrac{\partial \eta_{\mathrm{TP}}^{I}}{\partial \dot{Q}_{\mathrm{avail}}^{II}} = \dfrac{\partial \eta_{\mathrm{TP}}^{I}}{\partial \dot{Q}_{\mathrm{R}}^{I}} \cdot \dfrac{\partial \dot{Q}_{\mathrm{R}}^{I}}{\partial \dot{Q}_{\mathrm{avail}}^{II}}$	$-0.66\,a$ s/J	1.51 W	$-a$
	$\dfrac{\partial \eta_{\mathrm{TP}}^{I}}{\partial \dot{Q}_{\mathrm{R}}^{I}} = \dfrac{1}{\dot{Q}_{\mathrm{avail}}^{I}}$	0.04 s/J	24.91 W	1.00
$\eta_{\mathrm{TP}}^{II} \neq f(\dot{Q}_{\mathrm{avail}}^{I}, \dot{Q}_{\mathrm{avail}}^{II})$	$\dfrac{\partial \eta_{\mathrm{TP}}^{II}}{\partial \dot{Q}_{\mathrm{avail}}^{I}} = 0$	0	-	0
	$\dfrac{\partial \eta_{\mathrm{TP}}^{II}}{\partial \dot{Q}_{\mathrm{avail}}^{II}} = 0$	0	-	0
$\dot{Q}_{\mathrm{R}}^{I} \approx \dot{Q}_{\mathrm{avail}}^{I} - \dot{Q}_{\mathrm{HX1stA}}$	$\dfrac{\partial \dot{Q}_{\mathrm{R}}^{I}}{\partial \dot{Q}_{\mathrm{avail}}^{I}} = 1$	1	1.25	1.25
	$\dfrac{\partial \dot{Q}_{\mathrm{R}}^{I}}{\partial \dot{Q}_{\mathrm{avail}}^{II}} = \dfrac{\partial \dot{Q}_{\mathrm{R}}^{I}}{\partial \dot{m}} \cdot \dfrac{\partial \dot{m}}{\partial \dot{Q}_{\mathrm{avail}}^{II}}$	$-8.73\,a$	7.59 %	$-a$
	$\dfrac{\partial \dot{Q}_{\mathrm{R}}^{I}}{\partial \dot{m}}$	$-285.57\,a$	0.00387 g/J	$-a$
$\dot{Q}_{\mathrm{R}}^{II} = \eta_{\mathrm{TP}}^{II} \cdot \dot{Q}_{\mathrm{avail}}^{II}$	$\dfrac{\partial \dot{Q}_{\mathrm{R}}^{II}}{\partial \dot{Q}_{\mathrm{avail}}^{I}} = 0$	0	-	0
	$\dfrac{\partial \dot{Q}_{\mathrm{R}}^{II}}{\partial \dot{Q}_{\mathrm{avail}}^{II}} = \eta_{\mathrm{TP}}^{II}$	86.7 %	1.16	1.00
$\dot{m} = \dot{Q}_{\mathrm{avail}}^{II}/(h_7 - h_8)$	$\dfrac{\partial \dot{m}}{\partial \dot{Q}_{\mathrm{avail}}^{II}} = 1/(h_7 - h_8)$	5.11 %	19.61 J/g	1.00
	$\dfrac{\partial \dot{m}}{\partial \dot{Q}_{\mathrm{avail}}^{I}} = 0$	0	-	0

The numerical evaluation (Table A2.7) shows that $a \approx 0.43$.

A3. Calculated values for the estimation of the overall cryogenic system

Thermo-Hydraulic Values

Table A3.1. Fluid state values calculated for the overall cryogenic system. Design values and boundary conditions are in bold.

Point	p	T	s	h	v	x	e
Unit	kPa	K	J/(g·K)	J/g	cm³/g	-	J/g
1	n/a	n/a	n/a	3581.12	n/a	n/a	n/a
2	130	**293.15**	30.94	1538.04	4677.70	shg	-7533
3	130	293.15	30.94	1538.04	4677.70	shg	-7533
4	130	293.15	30.94	1538.04	4677.70	shg	-7533
5	130	293.15	30.94	1538.04	4677.70	shg	-7533
6	130	147.86	27.39	783.53	2360.96	shg	-7245
7	130	52.03	21.96	285.64	832.34	shg	-6152
8	130	40.00	20.59	223.02	640.05	shg	-5814
9	130	40.77	20.69	227.01	652.32	shg	-5839
10	130	61.58	22.84	335.29	984.77	shg	-6359
11	130	81.50	24.29	438.85	1302.69	shg	-6683
12	130	86.92	24.63	467.02	1389.19	shg	-6753
13	130	87.78	24.68	471.48	1402.87	shg	-6763
14	130	40.00	20.59	223.02	640.05	shg	-5814
15	130	4.73	8.55	32.70	52.32	shg	-2474
16	130	**4.50**	4.31	13.53	12.09	**0.10**	-1250
17	130	4.50	4.31	13.53	12.09	0.10	-1250
18	130	4.50	4.36	13.75	12.54	0.11	-1265
19	130	4.50	4.83	15.86	16.65	0.22	-1399
20	130	4.50	7.48	27.82	40.02	0.86	-2165
21	130	4.50	8.02	30.25	44.78	0.99	-2320
22	130	4.50	8.07	30.47	45.20	**1.00**	-2334
23	130	39.57	20.54	220.78	633.19	shg	-5799
24	130	135.37	26.93	718.67	2161.80	shg	-7176
25	130	280.66	30.72	1473.18	4478.53	shg	-7531
26	130	**293.15**	30.94	1538.04	4677.70	shg	-7533

shg = superheated gas.
Values valid for a mass flow of 0.0979 g/s.

Table A3.2. Summary of heat exchange values calculated for the overall cryogenic system. Design values are in bold.

Section	Name	Δh	$\Delta \dot{Q}$
Unit	-	J/g	W
5-6	HX1A	-754.51	-73.86
6-7	HX1B	-497.89	-48.74
7-8	HX1stA	-62.63	-6.13
8-9	GHe feed	3.99	**0.39**
9-10	GHe feed	108.28	**10.60**
10-11	HX TS	103.56	10.14
11-12	GHe return	28.17	**2.76**
12-13	GHe return	4.46	**0.44**
13-14	HX1stB	-248.46	-24.32
14-15	HX2	-190.31	-18.63
15-16	HX2nd	-19.17	-1.88
16-17	Pipe element	0.00	**0.00**
17-18	LHe feed	0.23	**0.02**
18-19	LHe feed	2.10	**0.21**
19-20	SC Coils	11.96	1.17
20-21	LHe return	2.43	**0.24**
21-22	LHe return	0.22	**0.02**
22-23	HX2	190.31	18.63
23-24	HX1B	497.89	48.74
24-25	HX1A	754.51	73.86
25-26	Pipe element	64.86	6.35
-	$\dot{Q}_{CSS}^{I}$	-	**1.55**
-	$\dot{Q}_{CSS}^{II}$	-	**0.023**
8-13	Circuit I	248.46	24.32
17-22	Circuit II	16.94	1.66
-	1st Stage	-	**32.00**
-	2nd Stage	-	**1.90**

Values valid for a mass flow of 0.0979 g/s.

Table A3.3. Geometrical values of relevant pipes.

Section	Name	Name	L †	D_h	A_h
Unit	Unit	Unit	m	mm	mm²
		HX1A *	5.62	8/3	50.27/54.19
		HX1B *	5.43	6/2	28.27/28.27
		HX2 *	55.8	4/2	12.57/21.99
	CSS	HX1stA	4.83	6	28.27
		HX1stB	4.16	6	28.27
		HX2nd	4.48	8.32	54.76
		Pipe-16to17	1.5	6	28.27
		GHe feed	3.50	6	28.27
	TFL	GHe return	3.50	6	28.27
		LHe feed	3.50	6	28.27
		LHe return	3.50	6	28.27
		GHe feed	0.20	6	28.27
	Connector Box	GHe return	0.20	6	28.27
		LHe feed	0.20	4	12.57
		LHe return	0.50	4	12.57
	Cyclotron	Thermal shield	1.60	4	12.57
		Superconducting magnets	3.06	4.6	30.00

* Coaxial heat exchanger with values for inner / outer pipe.

† For CSS heat exchangers, the values correspond to the manufacturing length L_M.

Table A2.7. Thermo-hydraulic values of heat exchangers calculated for the overall cryogenic system. All values correspond to the thermal design length L.

Name	$\dot{Q}$	$U_m \cdot A$	A	δT_m	$\dot{C}_h; \dot{C}_c$	$\dot{C}^*$	$\Delta \dot{E}_h$	$\dot{E}_d$
Unit	W	W/K	m2	K	J/(kg·K)	-	W	W
HX1A	73.86	5.91	0.20	12.49	5193; 5193	1.000	28.14	-6.66
HX1B	48.74	3.90	0.15	12.48	5196; 5197	1.000	107.00	-27.74
HX2	18.63	45.47	1.23	0.41	5395; 5427	0.994	326.88	-12.31
HX1stA	6.18	5.58	0.09	1.11	5206	-	33.47	-5.76
HX1stB	24.37	4.63	0.08	5.26	5200	-	93.29	-61.40
HX2nd	1.88	14.03	0.12	0.13	84709	-	119.82	-4.12

Values valid for a mass flow of 0.0979 g/s.

Table A3.4. Dimensionless performance values of heat exchangers calculated for the overall cryogenic system. All values correspond to the thermal design length L.

Name	ε	NTU	ζ	Λ	S_A
Unit	-	-	-	10^{-6}	-
HX1A	92.1%	11.63	80.9%	0.04	1.00
HX1B	88.5%	7.68	79.4%	0.02	1.00
HX2	99.4%	85.52	96.4%	0.02	1.00
HX1stA	~100.0%	10.95	85.3%	1.02	1.00
HX1stB	~100.0%	9.09	60.3%	1.19	1.00
HX2nd	64.0%	20.76	96.7%	0.03	1.00

Values valid for a mass flow of 0.0979 g/s.

Thermal and Hydraulical Losses

Table A3.5. Thermal loads on the cryocooler's 1st stage for the overall cryogenic system.

	Name	$\dot{Q}_{surr,cond}$	$\dot{Q}_{surr,rad}$	$\dot{Q}_{long}$ [†]	$\dot{Q}_{others}$
	Unit	mW	mW	mW	mW
CSS	Thermal Shield	~ 0 [1]	1337.58	-	-8.19 [2]
	HX1A *	88.1	~ 0	9.37/14.97	-
	HX1B *	16.2	-	3.21/5.48	-
	HX2 *	66.6	-	-	-
	HX1stA	-	-	-	-
	HX1stB	-	-	-	-
	HX2nd	-	-	-	-
Transfer Line	Thermal Shield	-	215	-	-
	GHe pipes (feed)	176	-	-	-
	GHe pipes (return)	364	72.2	-	-
	LHe pipes (feed)	-	-	-	-
	LHe pipes (return)	-	-	-	-
Connector Box	Thermal Shield	2500	258	-	-
	GHe pipes (feed)	-	-	-	-
	GHe pipes (return)	-	-	-	-
	LHe pipes (feed)	-	-	-	-
	LHe pipes (return)	-	-	-	-
Current Leads	Current Leads	-	-	-	10600 [3]
Cyclotron	Thermal Shield	800	6850	-	-

*   Coaxial heat exchanger with values for inner / outer pipe.

†   Values with respect to the thermal design length L.

1)   It is supported to the cryocooler and therefore conduction loads are neglected.

2)   Thermal radiation from thermal shield to all cold masses inside it.

3)   Load for self-heating and longitudinal cable conduction.

Table A3.6. Thermal loads on the cryocooler's 2nd stage for the overall cryogenic system.

	Name	$\dot{Q}_{surr,cond}$	$\dot{Q}_{surr,rad}$	$\dot{Q}_{long}$ †	$\dot{Q}_{others}$
	Unit	mW	mW	mW	mW
CSS	Cold Masses	∼ 0 [1]	8.19 [2]	-	-
	HX1A *	-	-	-	-
	HX1B *	-	-	-	-
	HX2 *	10.74	-	1.18/2.14	-
	HX1stA	-	-	-	-
	HX1stB	-	-	-	-
	HX2nd	-	-	-	-
Transfer Line	Cold Masses	-	-	-	-
	GHe pipes (feed)	-	-	-	-
	GHe pipes (return)	-	-	-	-
	LHe pipes (feed)	18.56	3.8	-	-
	LHe pipes (return)	17.48	3.8	-	-
Connector Box	Cold Masses	-	-	-	-
	GHe pipes (feed)	-	-	-	-
	GHe pipes (return)	-	-	-	-
	LHe pipes (feed)	200	6	-	-
	LHe pipes (return)	200	6	-	-
Current Leads	Current Leads	-	-	-	32 [3]
Cyclotron	Cold Mass	120	6	-	264 [4]

*   Coaxial heat exchanger with values for inner / outer pipe.

†   Values with respect to the thermal design length *L*.

1)   It is supported to the cryocooler and therefore conduction loads are neglected.

2)   Thermal radiation from thermal shield to all cold masses inside it.

3)   Load for self-heating and longitudinal cable conduction.

4)   Load for residual gas conduction and radiative particles on coil and caising.

Table A3.8. Hydraulic losses on the overall cryogenic system.

	Name	Δp
	Unit	bar
CSS	HX1A *	3.02/21.84
	HX1B *	2.8/26.07
	HX2 *	51.36/37.85
	HX1stA	1.47
	HX1stB	1.35
	HX2nd	n/a
Transfer Line	GHe pipes (feed)	0.92
	GHe pipes (return)	1.37
	LHe pipes (feed)	0.01
	LHe pipes (return)	0.04
Connector Box	GHe pipes (feed)	0.07
	GHe pipes (return)	0.08
	LHe pipes (feed)	0.005
	LHe pipes (return)	0.04
Cyclotron	Thermal Shield	5.56
	Cold Mass	0.02

* Coaxial heat exchanger with values for inner / outer pipe.

Table A3.9. Destroyed exergetic power $\dot{E}_d$ on the overall cryogenic system, as a result from heat exchange with a non-zero temperature difference, frictional pressure loss from of the flowing fluid and heat conduction along the pipes wall.

		Destroyed exergetic power $\dot{E}_d$ [W]			
	Cause	Heat exchange	Pressure drop	Long. heat conduction	Total
CSS	HX1A	6.66	1.15	0.03	7.84
	HX1B	27.74	1.34	0.05	29.13
	HX2	12.31	3.28	0.21	15.80
	HX1stA	5.76	0.07	-	5.83
	HX1stB	61.40	0.06	-	61.46
	HX2nd	4.12	<0.01	-	4.12
Other	Circuit I	92.98	0.37	-	93.35
	Circuit II	106.13	<0.01	-	106.13
	Total	318.00	6.27	0.29	324.56

A4. Fluid properties of Helium

Figure A4.1 was created using the fluid state values of helium according to the specialised library HePak©:

- Cryodata, Inc. 1999. "HePak". Database software. Version 3.4.
  http://www.htess.com/hepak.htm.

All remaining figures in Appendix A4 were obtained from:

- Jensen, J.E., W.A. Tuttle, R.B. Stewart, H. Bréchna, and Prodell A.G. "Brookhaven National Laboratory Selected Cryogenic Data Notebook." Worcester Polytechnic Inst. and National Bureau of Standards, 1980.

Figures A4.5-6 require the following conversion of pressure-units:

- 1 atm ≈ 1.013 bar.
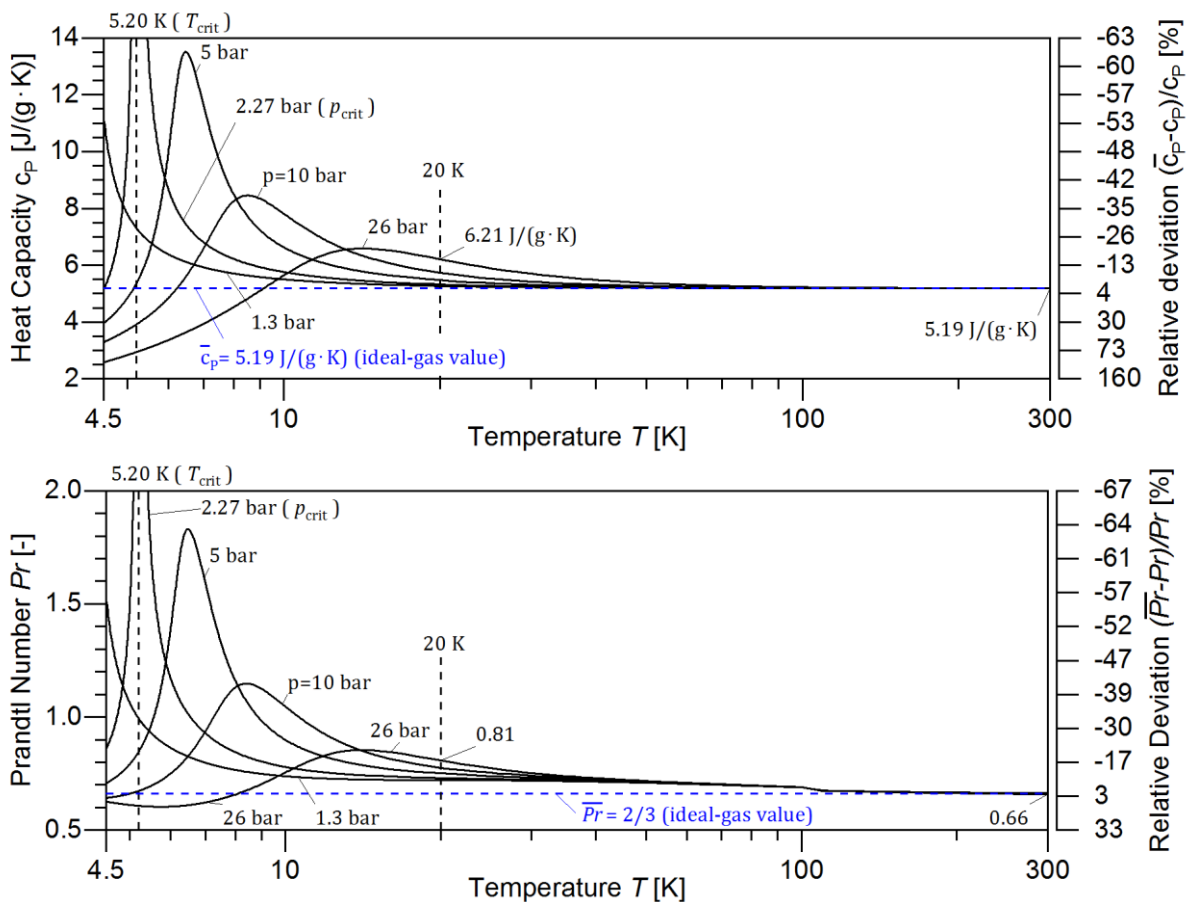
Figure A4.1. Heat capacity at constant pressure c_p (upper graph) and Prandtl number Pr (lower graph) as a function of temperature T for different pressures p. The relative deviation is introduced when the ideal-gas value is used instead of the real-gas values of helium. Note the non-linear scale of the right ordinates.
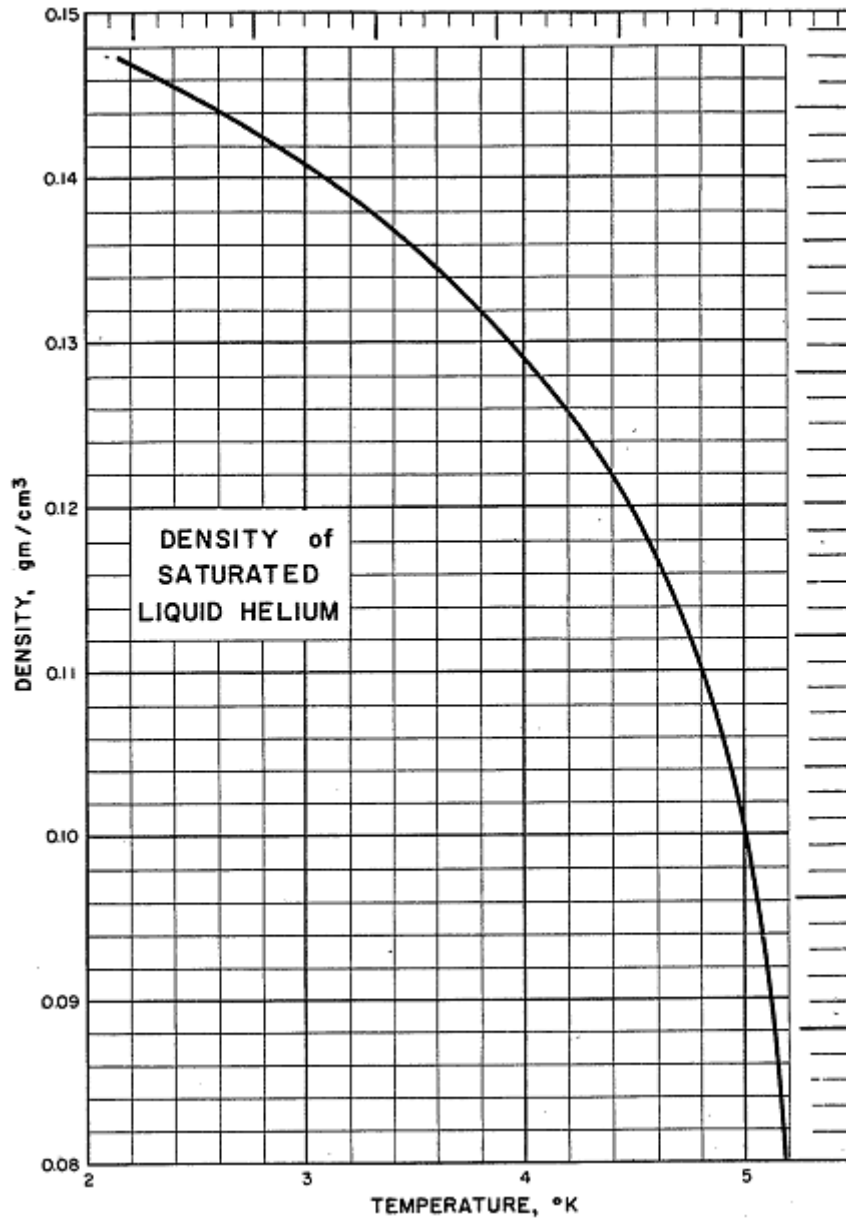
Figure A4.2. Density of saturated liquid helium.
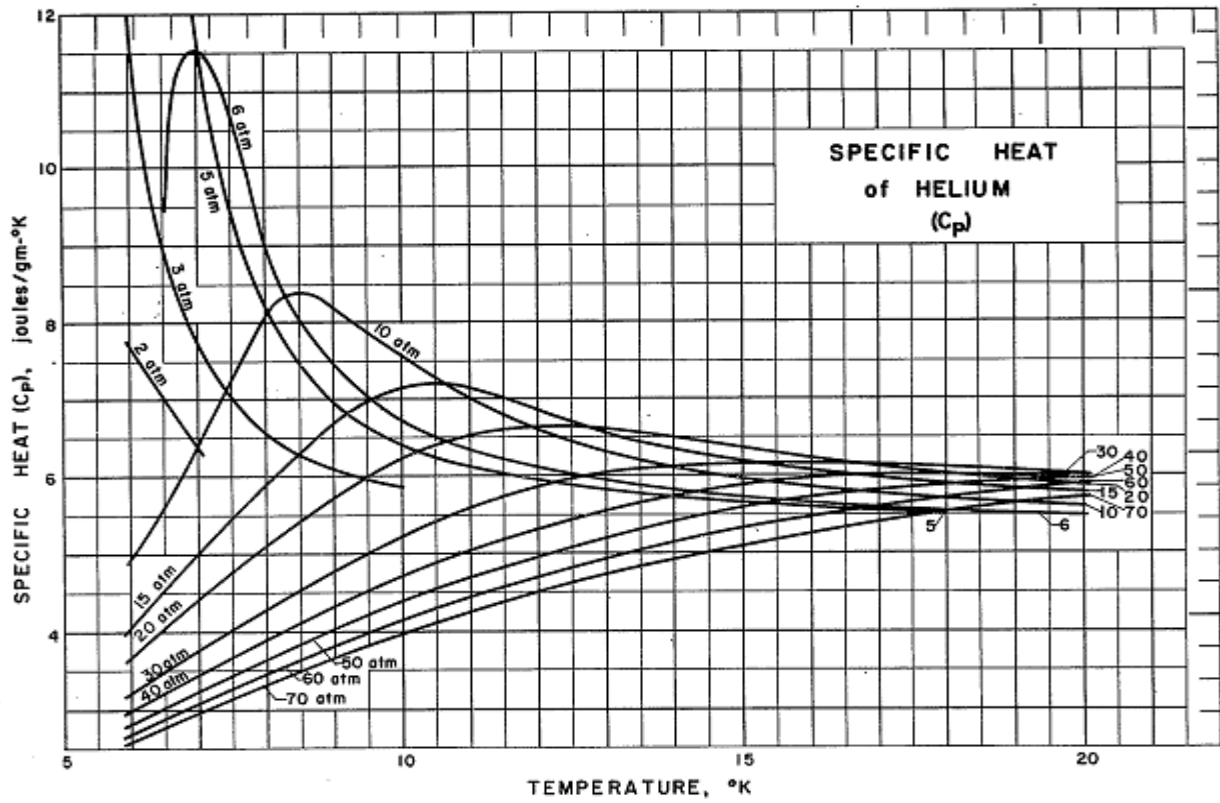
Figure A4.3. Specific heat of helium.
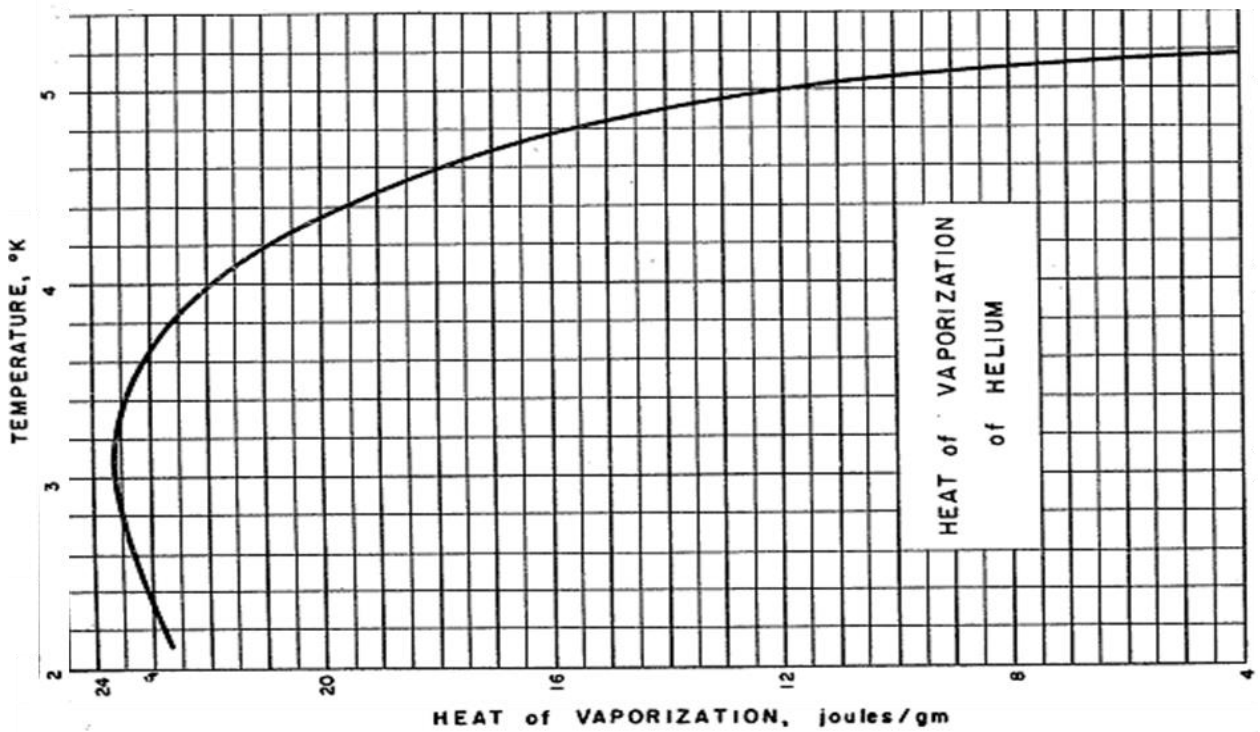
Figure A4.4. Specific heat of liquid helium at saturation.
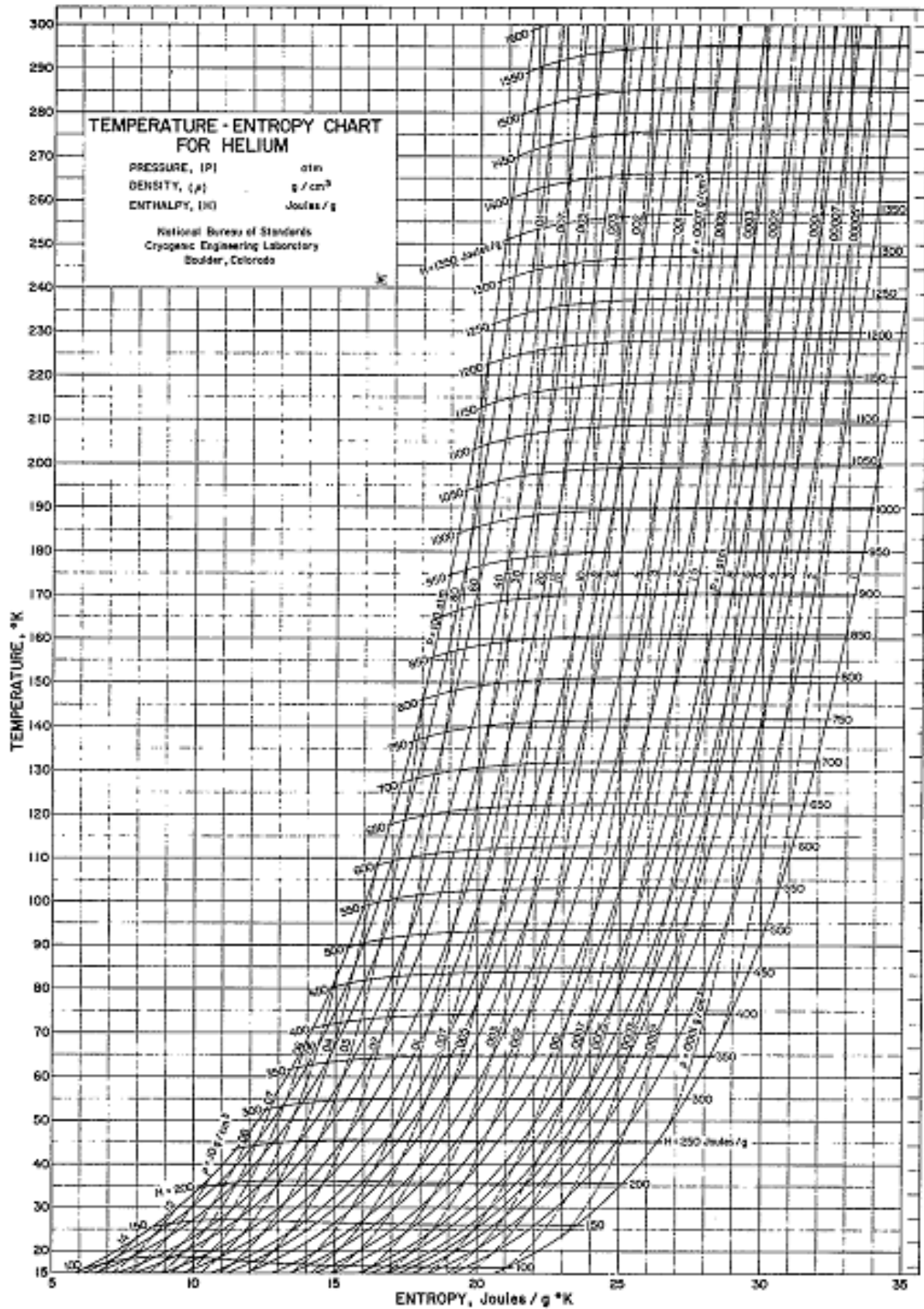
Figure A4.5. Temperature-entropy chart for Helium. For the temperature range 15 K to 300 K.
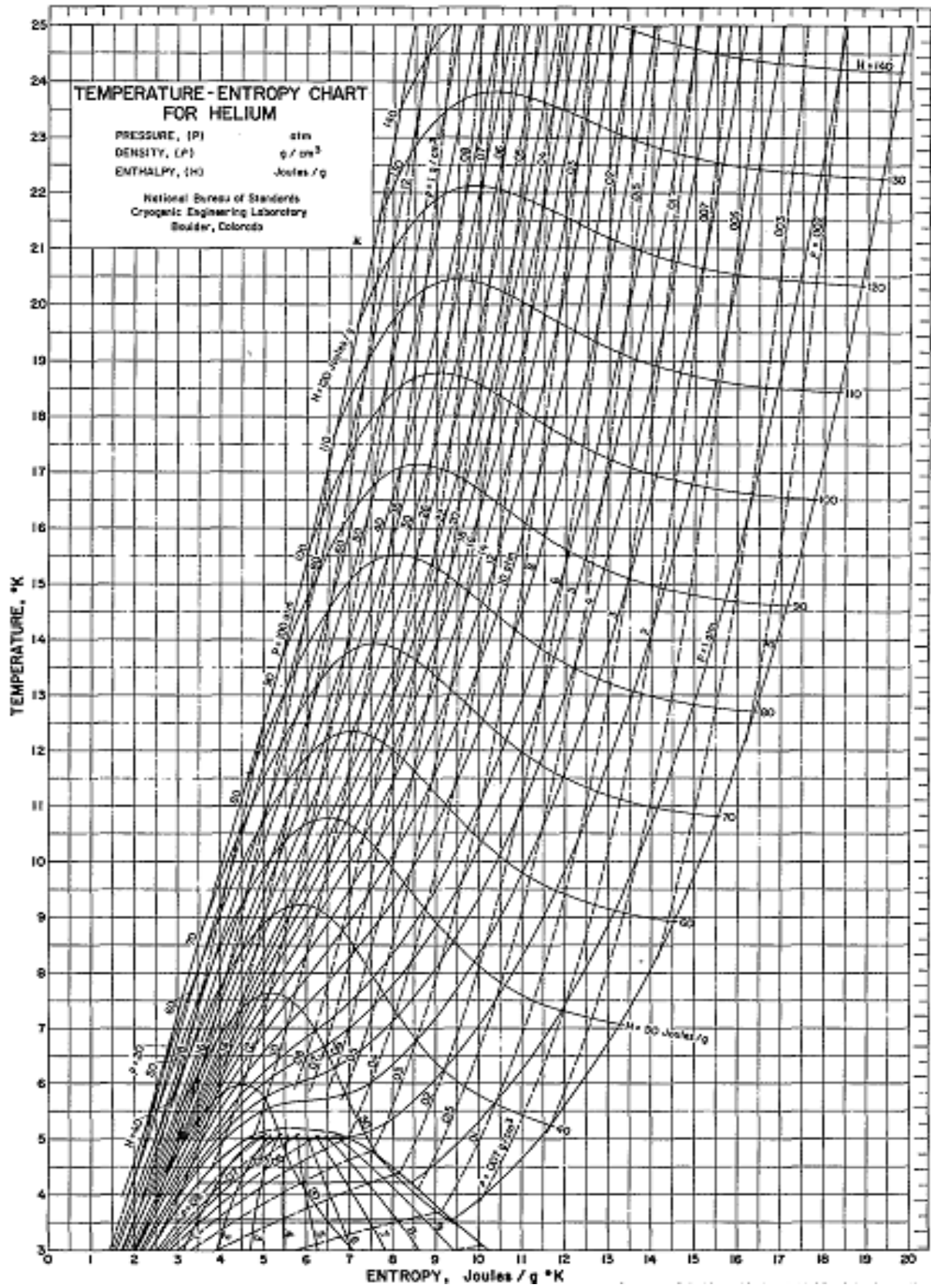
Figure A4.6. Temperature-entropy chart for Helium. For the temperature range 3 K to 25 K

A5. Data sheet of selected cryocooler system

Data for GM-cryocooler, model SRDK-415D-F50H, from the company Sumitomo Heavy Industries, Ltd.
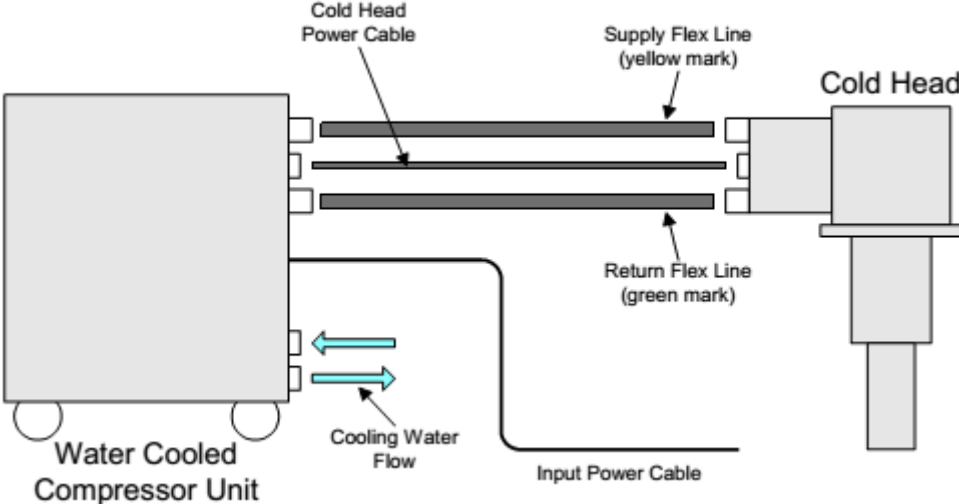
Figure A5.1. System configuration of GM-cryocooler from type SRDK-41D from the company Sumitomo.

Cooling Cycle	Modified Gifford-McMahon (2-Stage)
Site Condition	Indoor
Cooling Capacity (Vertical Position)	1st 35 / 45 W at 50 K (50/60Hz) 2nd 1.5 W at 4.2 K (50/60Hz)
Lowest Temperature	< 3.5 K -- for reference only
Cool Down Time (300K to 4.2K, 2nd Stage)	< 60 min. -- for reference only
Cooling Capacity Degradation (10,000Hrs.)	< 10 % -- for reference only
Orientation	Free (Cooling Capacity Loss: max. 15 %)
Ambient Temperature Range	5 to 35 deg.C (28 to 35 deg.C with cooling capacity loss max. 5%)
Dimension	H: 557 x W: 180 x L: 294 mm -- approx.
Weight	18.5 kg -- approx.
Maintenance	Shown in Table 1

Table 1   MAINTENANCE SCHEDULE FOR THE COLD HEAD UNIT

Maintenance	Frequency	Remark
Replace the Inside sliding parts	Every 10,000 Hrs.	"SHI maintenance" Return the Cold Head Unit to SHI, Ltd.

Notes
- The cooling capacity depends on the Flexible Gas Line length.
- The cooling capacity depends on the ambient temperature.
- The Heat Station Plated with nickel is available upon the request.
- The room should be provided to install the Cold Head Unit.

Figure A5.2. Cryocooler specification for the cold head unit (Model: RDK-415D).

Cooling system	Water Cooled
Site Condition	Indoor

Electrical Requirement
Power Line Voltage	3 phase (3W+PE),
50Hz	AC 380, 400, 415 V (+/- 10%)
60Hz	AC 460, 480 V (+/- 10%)

Power Requirement	
Minimum	9 kVA
Recommended	12 kVA

Power Consumption	Steady	Maximum	
50Hz	6.5 kW	7.2 kW	-- approx.
60Hz	7.5 kW	8.3 kW	-- approx.

Operating Current		
Maximum	13 A (50/60Hz)	-- approx.

Starting Current	75/80A (50/60 Hz)	-- approx.

Built-in Circuit Breaker Setting	16 A

Ambient Temperature Range	5 to 35 deg.C
	(28 to 35 deg.C with cooling capacity loss max. 5%)

Cooling Water Requirement*
Temperature Range	4 to 28 deg.C
Minimum Flow Rate	7 liter / min.
Quality Requirement	Refer to the ANNEX.

*See the ANNEX. for more detail.

Figure A5.3a. Cryocooler specification for the compressor unit (Model: F-50H).

Noise Level (1m distance)

Compressor Unit Only   Max. 60 dBA   -- approx.

*Noise level of the whole equipment may exceed 70dBA depending on the environment it is used in.

Dimension   H: 591 x W: 450 x L: 485 mm*

-- approx.

* without Terminal Cover , Connectors and Screw Head.

Weight   120 kg   -- approx.

Required Space*   Refer to the ANNEX.

*with maintenance space.

Maintenance   Shown in Table 2

Table 2 MAINTENANCE SCHEDULE FOR THE COMPRESSOR UNIT

Maintenance	Frequency	Remark
Replace the Adsorber	Every 30,000 Hrs.	"USER maintenance"
Charge the Helium Gas	As required	"USER maintenance" Purity of 99.999% up
Reset the circuit protector(s)	As required	"USER maintenance"
Cleaning the Water Line	As required	"USER maintenance" Depending on the water conditions

Notes

·While carrying the compressor unit, do not tilt it by more than 30 degrees.

·While setting the compressor unit, do not tilt it by more than 5 degrees.

Figure A5.3b. Cryocooler specification for the compressor unit (Model: F-50H).
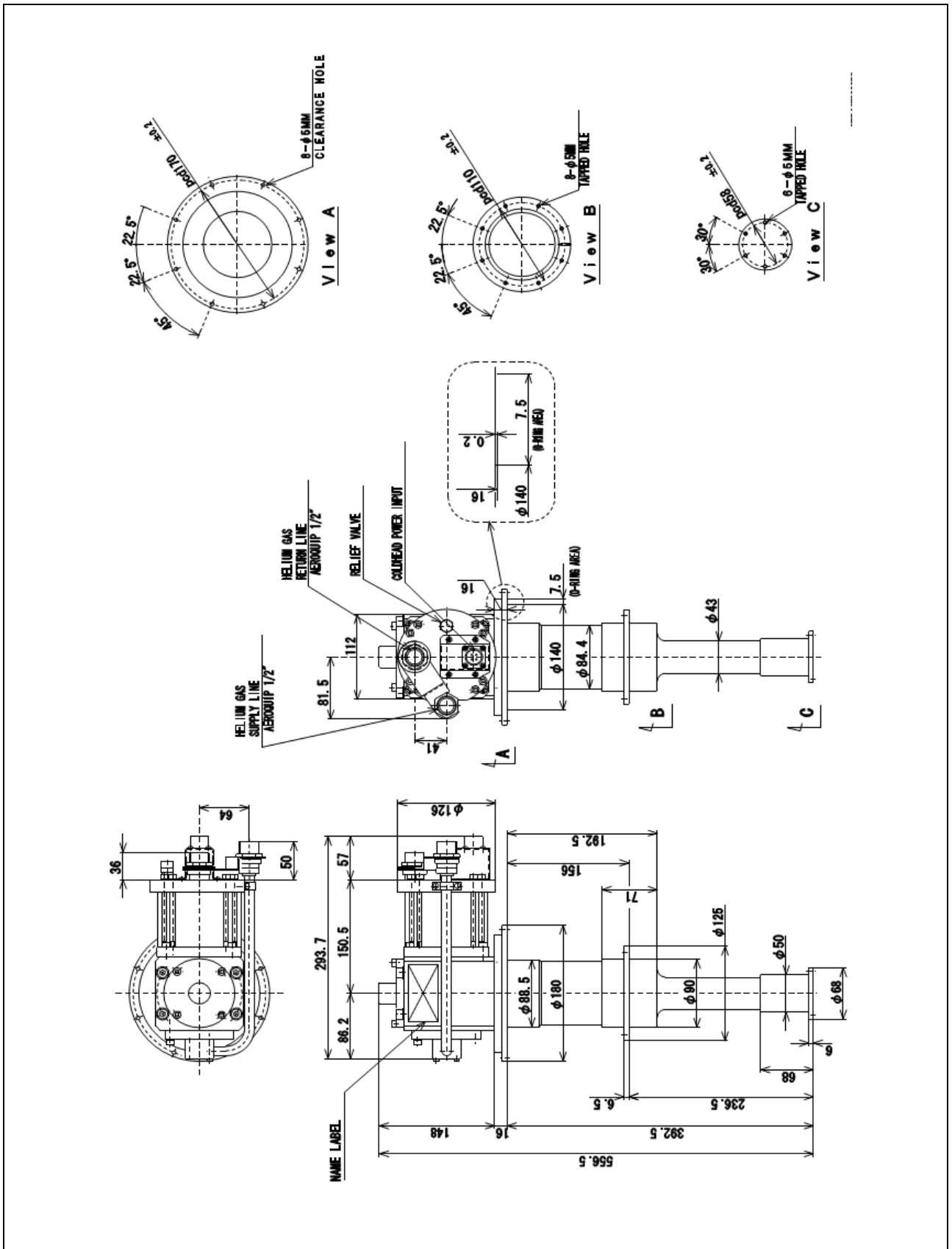
Figure A5.4. Cold head unit. The dimensions are in millimetres.

A6. Uncertainty Estimations

The Normal Distribution

Figure A6.1 is computed based on:

- Faber, M. 2012. "Statistics and Probability Theory: In Pursuit of Engineering Decision Support". Springer. New York, USA. ISBN 978-94-007-4056-3.

Probability density function

$$f(x) = \frac{1}{2\pi\sigma^2} e^{-(x-\mu)^2/2\sigma^2}$$

Cumulative distribution function

$$F(x) = \int_{-\infty}^{x} f(x)\, dx$$
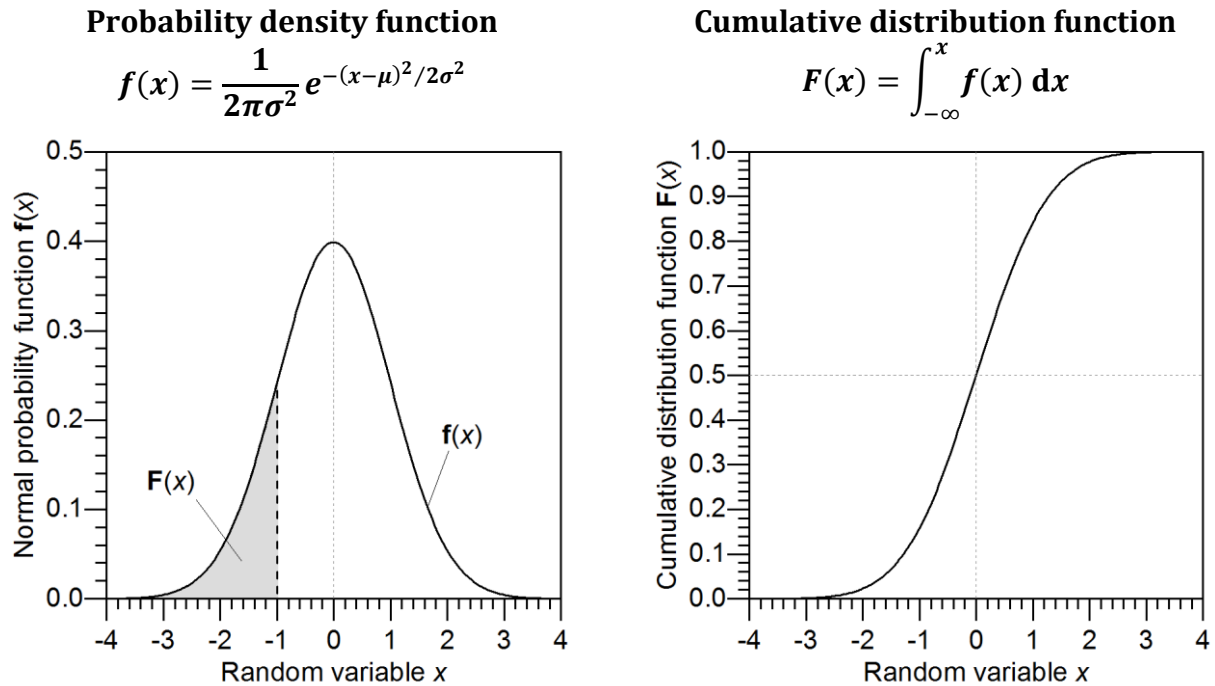
Figure A6.1. Graphic representations of the *standard* normal distribution ($\mu = 0$; $\sigma = 1$).

Uncertainty estimation for the cryocooler power

The cooling power of the cryocooler stages ($\dot{Q}_{1st}$, $\dot{Q}_{2nd}$) employed in chapter 5 is estimated based on the capacity maps available in the cryocooler's data sheets. The capacity maps are introduced in chapter 4.2 (Figure 4.11 and Figure 4.12), and were obtained from:

- SHI Cryogenics Group. 2014. "Cryocooler Product Catalogue". Sumitomo Heavy Industries ltd.
- Ogura, T., Koseki, K. 2007. "SHI Cryocooler Specification – Model SRDK-415D-F50H". Data Sheet. Sumitomo Heavy Industries, Ltd.

First, data points are collected as a function of the 2nd stage temperature T_{2nd} for a constant 1st stage temperature of T_{1st} = 50 K. Since the data sheets only contain information in "graph form", a *reading error* is introduced for each read-out. The magnitude of this reading error is considered to be no greater than 0.1 K for T_{2nd}, 0.5 W for $\dot{Q}_{1st}$, and 0.1 W for $\dot{Q}_{2nd}$. The collected data points are summarised in Table A6.1.

Table A6.1. Data points obtained from the capacity maps available in the data sheets of the cryocooler model. The uncertainty introduced by the *reading error* is expressed in terms of the 95 % confidence intervals.

	T_{2nd} [K]	$\dot{Q}_{1st}$ [W]	$\dot{Q}_{2nd}$ [W]
95 % confidence interval:	±0.1	±0.5	±0.1
Data points:	2.65	0	39
	3.75	1	37
	4.19	1.5	36
	6.35	5	27
	8.17	10	23
	10.65	15	20
	16.43	20	22

The data is inspected systematically to determine the fitting model. This is accomplished with the specialised data-analysis software "OriginPro" (OriginLab, Northampton, MA), which contains an extensive library of fitting functions and tools. The models that come into consideration are summarised in Table A6.2, where two suitable functions, one for each stage power, are chosen based on two *information criteria*: Bayesian and Akayke`s. In principle, both information criteria attempt to avoid overfitting by penalizing models with a higher amount of parameters; hence lower values are better.

Table A6.2. Models considered for fitting the data-points.

Fitting function and form	# of parameters	BIC-value *	AIC-value *	Comment
Models for $\dot{Q}_{1st}$:				
Quadratic polynom: $y = c_2 \cdot x^2 + c_1 \cdot x + c_0$	3	16.56	36.78	Favoured by BIC and AIC tests
Exponential decay: $y = c_1 \cdot e^{-x/n} + c_0$	3	25.34	45.55	-
Models for $\dot{Q}_{2nd}$:				
Hill function: $y = (c_1 \cdot x^n)/(c_2{}^n + x^n)$	3	14.63	34.85	Favoured by BIC and AIC tests
Cubic polynom: $y = c_2 \cdot x^2 + c_1 \cdot x + c_0$	4	22.28	82.55	-

* The lower, the better; BIC: Bayesian Information Criterion; AIC: Akayke`s Information Criterion.

Then, two separate functions are obtained by fitting the collected data points; one for each stage power. The fitting results are summarised in Table A6.3, where the fitted functions correspond to Eq. (5.11) in chapter 5.2.1. The uncertainty of the fitting parameters considers

both, the *intrinsic fitting errors* and the *reading errors* [*]. In both cases the fittings where obtained from 7 data points and have 4 degrees of freedom. The t-values and p-values result from the statistical hypothesis test performed by the software on each fitting parameter. The different p-values extend from 0.11 % to values well below 10^{-6}, which is consistently lower than the commonly used threshold of 5 %, and suggests a high statistical significance. The coefficient of determination R^2 is 98.4 % for the $\dot{Q}_{1st}$-function and 99.9 % for the $\dot{Q}_{2nd}$-function, indicating that both regression models fit the data very well.

Table A6.3. Fitting results obtained with the software "OriginPro 2018b" from OriginLab Corporation. It includes the functions and parameters for the collected data points.

	$\dot{Q}_{1st}$ [W] as a function of T_{2nd} [K]	$\dot{Q}_{2nd}$ [W] as a function of T_{2nd} [K]
Fitting function:	Quadratic	Hill
General form:	$y = c_2 \cdot x^2 + c_1 \cdot x + c_0$	$y = \dfrac{c_1 \cdot x^n}{(c_2)^n + x^n}$
Fitting parameters:	$c_0 = 53.27$	$c_1 = 21.68$
	$c_1 = -5.38$	$c_2 = 8.58$
	$c_2 = 0.21$	$n = 3.81$
Statistical Summary		
Number of data points:	7	7
Degrees of freedom:	4	4
t-value (on parameters):	c_0: 28.3; c_1: -11.0; c_2: 8.36	c_1: 54.7; c_2: 69.3; n: 25.9
p-value (on parameters):	c_0: <10^{-5}; c_1: <10^{-3}; c_2: 0.11%	c_1: <10^{-6}; c_1: <10^{-6}; c_2: <10^{-4}
Coefficient of determination R^2:	0.984	0.999
Weighting method:	considers y-error-bars	considers y-error-bars
Parameter uncertainties:	$u_{c_0} = 1.88$	$u_{c_1} = 0.40$
	$u_{c_1} = 0.49$	$u_{c_2} = 0.12$
	$u_{c_2} = 0.025$	$u_n = 0.15$
Covariances between parameters:	$u_{c_0 c_1} = -0.87$	$u_{n c_1} = -0.0435$
	$u_{c_0 c_2} = 0.042$	$u_{n c_2} = -0.0126$
	$u_{c_1 c_2} = -0.012$	$u_{c_1 c_2} = 0.043$

Finally, the two fitted functions and the collected data points are plotted in Figure A6.2. The uncertainties are shown in terms of 95 % confidence intervals; data-points exhibit error bars due to reading errors, and fitted curves exhibit error bands due to fitting errors. Table A6.4 contains the corresponding values in tabulated form.

Table A6.5 contains the tabulated values of the fitted functions considering *all* error sources (fitting and data-sheet errors). The values are plotted in Figure 5.5 (chapter 5.2.1).

---

[*] More precisely, it only considers the reading errors of the dependent variables $\dot{Q}_{1st}$ and $\dot{Q}_{2nd}$. The reading errors of the independent variable T_{2nd} can not be considered with the employed software, since this is only supported for simple linear regressions ($y = c_1 \cdot x + c_0$).

Cryocooler Stage Power :		
Stage	1st	2nd
Data	▲	◆
Data Fit		
Curve	—··—··—	– – – –
Function	Quadratic	Hill
	$y = c_0 + c_1 x + c_2 x^2$	$y = c_1 x^n / (c_2^n + x^n)$
c_0; c_1; c_2	53.27; -5.38; 0.21	- ; 21.68; 8.58
n	-	3.81
R^2	0.984	0.999

Figure A6.2. Fitting of the refrigeration power of the cryocooler stages as a function of the 2nd stage temperature T_{2nd} for a constant 1st stage temperature T_{1st} of 50 K. The curves correspond to the fitting of data points as provided by the supplier (Table A6.1). The 95 % confidence intervals (error bands) consider fitting errors only, and correspond to the tabulated values in Table A6.4.

Table A6.4. Tabulated values of the stage-power functions. The standard uncertainty u and the corresponding 95 % confidence interval consider *fitting errors* only. The values are plotted in Figure A6.2.

T_{2nd} [K]	$\dot{Q}_{1st}$ [W]				$\dot{Q}_{2nd}$ [W]			
			95 % confidence interval				95 % confidence interval	
	Nominal	$\pm u$	from	to	Nominal	$\pm u$	from	to
2.65	40.51	0.89	38.73	42.28	0.24	0.04	0.17	0.32
2.75	40.08	0.86	38.36	41.80	0.28	0.04	0.20	0.36
3.00	39.04	0.80	37.45	40.64	0.39	0.05	0.29	0.49
3.25	38.03	0.74	36.55	39.51	0.52	0.06	0.40	0.65
3.50	37.04	0.69	35.66	38.42	0.69	0.08	0.54	0.84
3.75	36.08	0.64	34.79	37.37	0.89	0.09	0.71	1.06
4.00	35.14	0.61	33.93	36.36	1.12	0.10	0.92	1.32
4.25	34.24	0.58	33.07	35.40	1.39	0.11	1.17	1.62
4.50	33.35	0.56	32.23	34.48	1.71	0.12	1.46	1.95
4.75	32.50	0.55	31.40	33.60	2.06	0.13	1.79	2.33
5.00	31.67	0.55	30.58	32.76	2.45	0.14	2.17	2.74
5.25	30.86	0.55	29.77	31.96	2.89	0.15	2.59	3.18
5.50	30.09	0.55	28.98	31.20	3.36	0.15	3.06	3.66
5.75	29.34	0.57	28.21	30.47	3.87	0.15	3.57	4.18
6.00	28.61	0.58	27.45	29.77	4.42	0.15	4.11	4.72
6.25	27.92	0.60	26.72	29.11	4.99	0.15	4.68	5.29
6.50	27.24	0.62	26.01	28.48	5.58	0.15	5.28	5.89
6.75	26.60	0.64	25.33	27.87	6.20	0.15	5.91	6.50
7.00	25.98	0.66	24.67	27.29	6.83	0.15	6.54	7.12
7.25	25.39	0.68	24.04	26.74	7.47	0.14	7.19	7.76
7.50	24.82	0.69	23.44	26.21	8.12	0.14	7.83	8.41
7.75	24.28	0.71	22.86	25.71	8.76	0.14	8.47	9.05
8.00	23.77	0.73	22.31	25.23	9.40	0.15	9.11	9.69
8.25	23.29	0.74	21.80	24.77	10.03	0.15	9.73	10.33
8.50	22.83	0.76	21.31	24.34	10.64	0.15	10.34	10.95
8.75	22.39	0.77	20.85	23.93	11.24	0.16	10.93	11.56
9.00	21.98	0.78	20.42	23.55	11.82	0.16	11.50	12.14
9.25	21.60	0.79	20.02	23.18	12.38	0.16	12.05	12.71
9.50	21.25	0.80	19.65	22.85	12.92	0.17	12.58	13.25
9.75	20.92	0.80	19.31	22.53	13.43	0.17	13.09	13.77
10.00	20.62	0.81	19.00	22.24	13.91	0.17	13.57	14.26
10.25	20.34	0.81	18.72	21.97	14.38	0.17	14.03	14.72
10.50	20.09	0.81	18.47	21.72	14.81	0.17	14.47	15.16
10.75	19.87	0.81	18.24	21.50	15.23	0.17	14.89	15.57
11.00	19.68	0.81	18.05	21.30	15.62	0.17	15.28	15.95
11.25	19.51	0.81	17.88	21.13	15.98	0.17	15.65	16.32
11.50	19.36	0.81	17.74	20.99	16.33	0.17	16.00	16.66
11.75	19.24	0.81	17.62	20.86	16.65	0.16	16.32	16.98
12.00	19.15	0.81	17.54	20.77	16.95	0.16	16.63	17.28
12.25	19.09	0.81	17.48	20.70	17.24	0.16	16.92	17.56
12.50	19.05	0.81	17.44	20.66	17.50	0.16	17.18	17.82
12.75	19.04	0.81	17.43	20.65	17.75	0.16	17.43	18.07
13.00	19.06	0.81	17.44	20.67	17.98	0.16	17.66	18.30
13.25	19.10	0.81	17.47	20.73	18.20	0.16	17.88	18.52
13.50	19.16	0.82	17.52	20.81	18.40	0.16	18.08	18.73
13.75	19.26	0.83	17.59	20.92	18.59	0.16	18.26	18.92
14.00	19.38	0.85	17.68	21.07	18.77	0.17	18.43	19.10
14.25	19.52	0.87	17.79	21.26	18.93	0.17	18.59	19.27
14.50	19.70	0.89	17.92	21.47	19.09	0.17	18.74	19.44
14.75	19.90	0.92	18.07	21.73	19.23	0.18	18.88	19.59
15.00	20.12	0.95	18.23	22.02	19.37	0.18	19.00	19.73
15.25	20.38	0.99	18.40	22.35	19.49	0.19	19.12	19.87
15.50	20.65	1.03	18.60	22.71	19.61	0.19	19.23	20.00
15.75	20.96	1.08	18.80	23.12	19.72	0.20	19.33	20.12
16.00	21.29	1.13	19.03	23.55	19.83	0.20	19.42	20.23
16.25	21.65	1.19	19.27	24.03	19.92	0.21	19.51	20.34
16.43	21.92	1.24	19.45	24.40	19.99	0.21	19.57	20.41

Table A6.5. Tabulated values of the stage-power functions. The standard uncertainty u and the corresponding 95 % confidence interval consider *fitting errors* and *data-sheet errors*. The values are plotted in Figure 5.5 (chapter 5.2.1).

T_{2nd} [K]	$\dot{Q}_{1st}$ [W]				$\dot{Q}_{2nd}$ [W]			
			95 % confidence interval				95 % confidence interval	
	Nominal	$\pm u$	from	to	Nominal	$\pm u$	from	to
2.65	40.51	2.21	40.14	48.98	0.24	0.04	0.19	0.34
2.75	40.08	2.18	39.73	48.45	0.28	0.04	0.22	0.39
3.00	39.04	2.11	38.73	47.16	0.39	0.05	0.32	0.54
3.25	38.03	2.04	37.75	45.91	0.52	0.07	0.44	0.71
3.50	37.04	1.98	36.79	44.70	0.69	0.08	0.59	0.92
3.75	36.08	1.92	35.86	43.52	0.89	0.10	0.78	1.17
4.00	35.14	1.86	34.94	42.38	1.12	0.11	1.00	1.46
4.25	34.24	1.81	34.04	41.27	1.39	0.13	1.27	1.80
4.50	33.35	1.76	33.17	40.21	1.71	0.15	1.58	2.18
4.75	32.50	1.72	32.32	39.18	2.06	0.17	1.93	2.60
5.00	31.67	1.67	31.49	38.18	2.45	0.19	2.33	3.07
5.25	30.86	1.64	30.68	37.23	2.89	0.21	2.76	3.59
5.50	30.09	1.60	29.89	36.30	3.36	0.23	3.25	4.15
5.75	29.34	1.57	29.13	35.42	3.87	0.25	3.77	4.75
6.00	28.61	1.54	28.39	34.56	4.42	0.27	4.32	5.39
6.25	27.92	1.52	27.67	33.74	4.99	0.29	4.90	6.07
6.50	27.24	1.50	26.98	32.96	5.58	0.32	5.51	6.78
6.75	26.60	1.47	26.31	32.21	6.20	0.34	6.13	7.51
7.00	25.98	1.46	25.67	31.49	6.83	0.37	6.77	8.26
7.25	25.39	1.44	25.05	30.80	7.47	0.40	7.42	9.02
7.50	24.82	1.42	24.46	30.15	8.12	0.43	8.07	9.79
7.75	24.28	1.41	23.90	29.53	8.76	0.46	8.72	10.56
8.00	23.77	1.39	23.36	28.94	9.40	0.49	9.36	11.33
8.25	23.29	1.38	22.85	28.38	10.03	0.52	9.99	12.08
8.50	22.83	1.37	22.37	27.85	10.64	0.55	10.60	12.82
8.75	22.39	1.36	21.91	27.35	11.24	0.58	11.20	13.54
9.00	21.98	1.35	21.49	26.88	11.82	0.61	11.78	14.23
9.25	21.60	1.34	21.09	26.44	12.38	0.64	12.34	14.90
9.50	21.25	1.33	20.72	26.03	12.92	0.67	12.87	15.54
9.75	20.92	1.32	20.37	25.65	13.43	0.69	13.39	16.15
10.00	20.62	1.31	20.06	25.30	13.91	0.72	13.87	16.74
10.25	20.34	1.30	19.77	24.98	14.38	0.74	14.34	17.29
10.50	20.09	1.29	19.52	24.69	14.81	0.76	14.78	17.82
10.75	19.87	1.28	19.29	24.43	15.23	0.78	15.19	18.31
11.00	19.68	1.28	19.09	24.20	15.62	0.80	15.58	18.78
11.25	19.51	1.27	18.92	24.00	15.98	0.82	15.95	19.21
11.50	19.36	1.26	18.77	23.82	16.33	0.83	16.29	19.63
11.75	19.24	1.26	18.65	23.68	16.65	0.85	16.62	20.01
12.00	19.15	1.25	18.56	23.58	16.95	0.86	16.92	20.37
12.25	19.09	1.25	18.50	23.50	17.24	0.88	17.21	20.71
12.50	19.05	1.25	18.46	23.45	17.50	0.89	17.47	21.03
12.75	19.04	1.25	18.45	23.44	17.75	0.90	17.72	21.33
13.00	19.06	1.25	18.46	23.46	17.98	0.91	17.95	21.61
13.25	19.10	1.25	18.50	23.52	18.20	0.92	18.17	21.87
13.50	19.16	1.26	18.56	23.60	18.40	0.93	18.37	22.11
13.75	19.26	1.27	18.64	23.73	18.59	0.94	18.56	22.34
14.00	19.38	1.29	18.74	23.89	18.77	0.95	18.74	22.55
14.25	19.52	1.30	18.87	24.09	18.93	0.96	18.90	22.75
14.50	19.70	1.33	19.02	24.32	19.09	0.97	19.06	22.94
14.75	19.90	1.35	19.18	24.59	19.23	0.98	19.20	23.11
15.00	20.12	1.38	19.37	24.90	19.37	0.99	19.33	23.28
15.25	20.38	1.42	19.58	25.25	19.49	0.99	19.46	23.43
15.50	20.65	1.46	19.80	25.64	19.61	1.00	19.57	23.57
15.75	20.96	1.50	20.05	26.06	19.72	1.01	19.68	23.71
16.00	21.29	1.55	20.31	26.53	19.83	1.01	19.79	23.83
16.25	21.65	1.61	20.60	27.03	19.92	1.02	19.88	23.95
16.43	21.92	1.65	20.81	27.42	19.99	1.02	19.95	24.03

A7. Validation procedure

Experimental estimation of model uncertainty; outline of a standardised validation approach

The following outlines a validation approach in accordance to the *standard for verification and validation* (V&V standard):

- American Society of Mechanical Engineers. 2009. "Standard for Verification and Validation in Computational Fluid Dynamics and Heat Transfer: An American National Standard". ASME V&V 20–2009. American Society of Mechanical Engineers. New York, USA.

According to the V&V standard, the concern of a validation process is to determine the accuracy of calculation results in representing the "real world" from the perspective of the intended use, and its primary objective is to estimate the error introduced through the calculation model.

Figure A7.1 illustrates the error estimates considered during a validation process as per the V&V standard[*]. For a parameter of interest $P[X]$ at the validaton set-point X_0, the comparison error ϵ_{com} is the difference between the values of the calculation result P_{calc} and the experimental data P_{data}. Their actual difference with respect to the unknown true value P_{true} is given by the errors ϵ_{calc} and ϵ_{data}. The equations derived from these definitions are:

$$\epsilon_{\text{calc}} \equiv P_{\text{calc}} - P_{\text{true}} \quad , \tag{A7.1}$$

$$\epsilon_{\text{data}} \equiv P_{\text{data}} - P_{\text{true}} \quad , \tag{A7.2}$$

and

$$\epsilon_{\text{com}} \equiv P_{\text{calc}} - P_{\text{data}} = \epsilon_{\text{calc}} - \epsilon_{\text{data}} \quad . \tag{A7.3}$$

Eq. A7.3 shows that the comparison error ϵ_{com} is known once the calculation and experimental results are obtained, and that it represents the combination of all calculation and experimental errors.

The calculation error ϵ_{calc} is considered the combination of three types of error:

$$\epsilon_{\text{calc}} = \epsilon_{\text{model}} + \epsilon_{\text{input}} + \epsilon_{\text{num}} \quad , \tag{A7.4}$$

where ϵ_{model} is the error originated from model assumptions and approximations, ϵ_{input} is the error coming from input-parameter values, and ϵ_{num} is the error generated by solving equations numerically. Their corresponding standard uncertainties are u_{model}, u_{input}, and u_{num}.

---

[*] Note that in the V&V standard, the "calculation result" is referred to as the "simulation solution".

It is not possible to independently observe the specific effects of the model error ϵ_{model}, but there are ways to estimate the remaining errors. Using Eqs. (A7.3) and (A7.4) yields

$$\epsilon_{\text{model}} = \epsilon_{\text{com}} - \left(\epsilon_{\text{input}} + \epsilon_{\text{num}} - \epsilon_{\text{data}}\right) \, , \tag{A7.5}$$

showing that the model error ϵ_{model} can be estimated indirectly from the combination of the other errors. Consequently, the model error ϵ_{model} is estimated to lay within the interval

$$\epsilon_{\text{model}} \in \left[\epsilon_{\text{com}} - u_{\text{val}}; \epsilon_{\text{com}} + u_{\text{val}}\right] \, , \tag{A7.6}$$

where

$$u_{\text{val}} = \boldsymbol{f}\left[u_{\text{input}}, u_{\text{num}}, u_{\text{data}}\right] \tag{A7.7}$$

corresponds to the *validation uncertainty* defined as the estimate of the error combination: $\epsilon_{\text{input}} + \epsilon_{\text{num}} - \epsilon_{\text{data}}$.
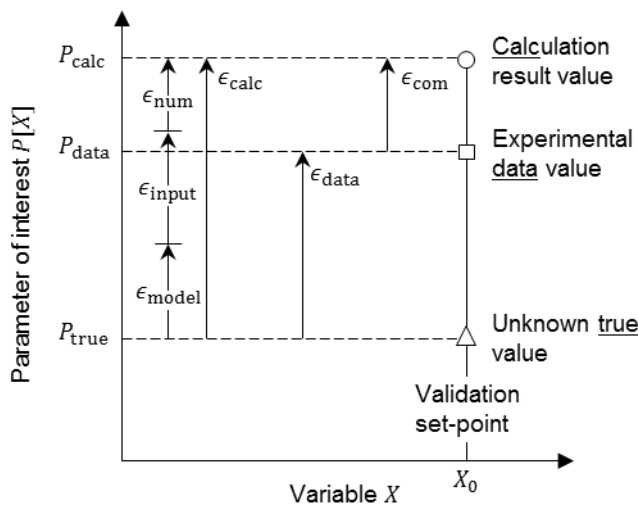

Figure A7.1. Schematic showing of errors according to the validation approach of the V&V standard [72]. The unknown true value P_{true} of a parameter $P[X]$ at the validation set-point X_0 differs from the calculation result P_{calc} and its experimental value P_{data}. These differences result in the calculation error ϵ_{calc}, the experimental error ϵ_{data}, and the comparison error ϵ_{com}. The calculation error ϵ_{calc} is the combination of numerical, input and model errors (ϵ_{num}, ϵ_{input}, ϵ_{model}).